POLITECNICO
DI MILANO

DIPARTIMENTO DI CHIMICA, MATERIALI
E INGEGNERIA CHIMICA "G. NATTA"

Mechanical characterization of elastomers under quasi-static and dynamic biaxial loading conditions

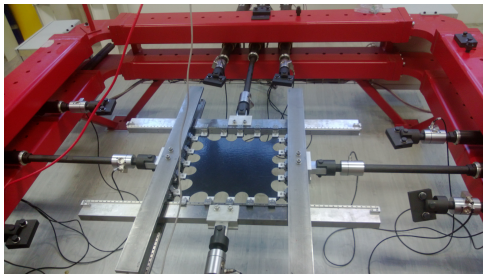

Author:
Roberto Calabrò

Supervisor:
Prof. Marta Rink

PhD in Materials Engineering, XXV cycle

POLITECNICO
DI MILANO

Dipartimento di Chimica, Materiali e Ingegneria Chimica "G. Natta"

Mechanical characterization of elastomers under quasi-static and dynamic biaxial loading conditions

PhD in Materials Engineering, XXV cycle

Supervisor:
Prof. Marta Rink

Candidate:
Roberto Calabrò

Coordinator of the doctoral program: Prof. Chiara Castiglioni

To Angela and all my family, your love and support
helped me to overcome the most difficult times
Roberto

Acknowledgements

First and foremost I want to thank my supervisor Marta Rink. Her suggestions and guidance were fundamental to me during these years; it has been for me a pleasure and an honour to be one of her Ph.D. students. In regards of "Politecnico di Milano" I want to thank Francesco Caimmi for the help with FE simulations and in material parameters determination, as well as for the friendship that has always shown; and Claudia Marano for the fundamental help given in understand physical phenomena and in the work organization. I would like to thanks Josè Silicani, Salvatore Cotugno and all the staff of the Bridgestone TCE for the support, know-how exchange, material supply, and opportunities that they have given to me. I also would like to thanks Konrad Schneider and Thomas Horst for the wonderful welcome and the technical support during my stay at the IPF in Dresden. Finally I would like to thank my brother, Alessandro Calabrò, for the support in the design of the clamping system used in this work.

Contents

Abstract

The research activity was focused on the determination of a fracture mechanics energy based parameter suitable for elastomers when subjected to biaxial loading conditions. Although for some simple geometries such as SENT or pure shear, simple experimental methods for evaluating the energy release rate or the J-integral for highly non-linear materials as elastomers can be found in the literature, for the case of biaxial test configurations these are not available. Two specific techniques were developed to evaluate the tearing energy, which can be used for this test configuration, by using direct and indirect calculation methods. Both calculation techniques require an accurate calibration of the constitutive model of the material. Constitutive equations for hyperelastic materials, which can describe the behaviour under different stress states and high strains generally contain a large number of parameters. Therefore in order to obtain a sound parameters set experimental data under different stress states and high strains are required. Two loading conditions were considered, dynamic and quasi-static. For dynamic stress-strain characterization and fatigue crack propagation tests a biaxial testing machine purposely designed for rubbers was used during a six months stay at "Leibnitz Institut fur Polymerforshung Dresden e. V. (IPF)". A direct technique for tearing energy evaluation, based on full-field strain measurements performed with the digital image correlation technique, was proposed and successfully tested, although the obtained results need to be confirmed with further stress-strain and fatigue characterization tests. For quasi-static tests a biaxial dynamometer designed for textiles was adapted for testing elastomers up to high strains by designing an ad hoc clamping system . In this case an indirect technique based on finite element simulations was

used to determine the tearing energy. Unfortunately, the production of the clamping system has taken longer time than expected, and was available for testing only from April 2013. For this reason it was possible to perform a stress-strain characterization but only a few fracture tests. The determination of material parameters even using characterization data from different biaxial load configurations is still not satisfactory. Nevertheless, lately some attempt to calculate the tearing energy with the finite element method has been done and the results obtained are encouraging. Much attention has also been devoted to obtain an optimal speckles pattern for digital image correlation. It was then possible to extensively apply this technique in the thesis work.

Chapter 1

Generalities on elastomers

1.1 Some information about natural rubber as a natural renewable material

Natural rubber is a natural renewable material extracted from Havea brasiliensis tree latex. Until the 20th century almost all natural rubber used in the world comes from wild trees in Brazil, with an annual maximum production of 52,000 tonnes. However, the introduction of electricity (cables), bicycles and cars (tyres) makes rubber consumption to be doubled every 10 years. As reported in figure1.1 Hevea seeds were planted in many countries. Rubber planting in south-east Asia began seriously in 1898. By 1910, there was a boom in rubber production, and Malaya became the leading producer, a position that still retain nowadays as shown in figure1.2. South-East Asia still produces 92% of the world's supply, with Malaya, Indonesia and Thailand being the largest producers.

Rubber global market today seems to be one of the few markets that never satisfy the demand with enough offer. Havea Brasiliensis is still the most used plant to produce natural rubber, but due to the harvesting problem it is not the only one. Many studies are carried out in order to create new genetically modified species that can be harvested outside the tropical regions, in fact many countries such as USA are great consumer of rubber even if they have not the possibility to grow up Havea. In figure1.3 Cornish [1] gives a complete description of this phenomenon in terms of

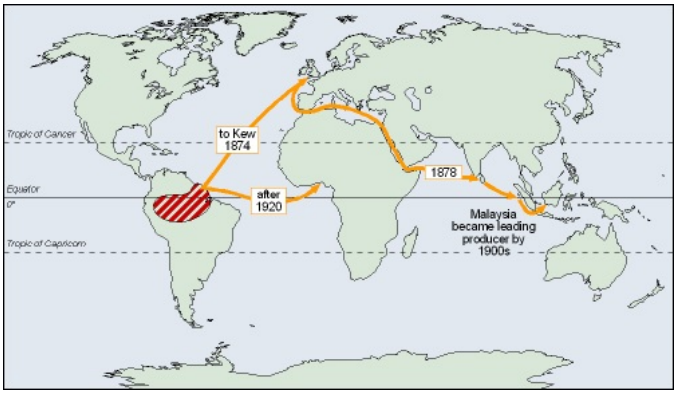

Figure 1.1: *Historical movement of Havea Brasiliensis seeds.*

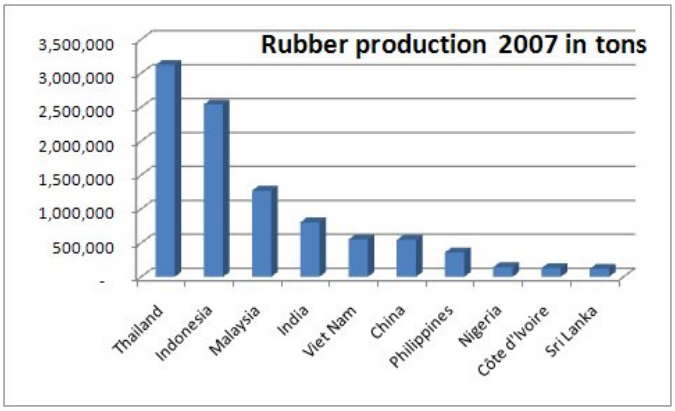

Figure 1.2: *Major natural rubber producer in 2007.*

rubber production-consumption, highlighting how during World War II the production of synthetic rubber sows a great increase caused by difficulties in rubber production in South-East Asia (figure1.4). The author gives an overview of the differences between the polymer synthesis process and final properties as a function of the plant used to produce it.

All this needing in rubber, and so all the energies spent into research on new plant species, comes from the practical fact that elastomers (i.e. rubbers) are definitively irreplaceable for many application. As an example of the variety of rubbery items in figure 1.5 it can be seen how the great part of the total amount of rubber produced worldwide goes in tire production, as can be easily expected, but 31% of the total amount goes in non-tyre

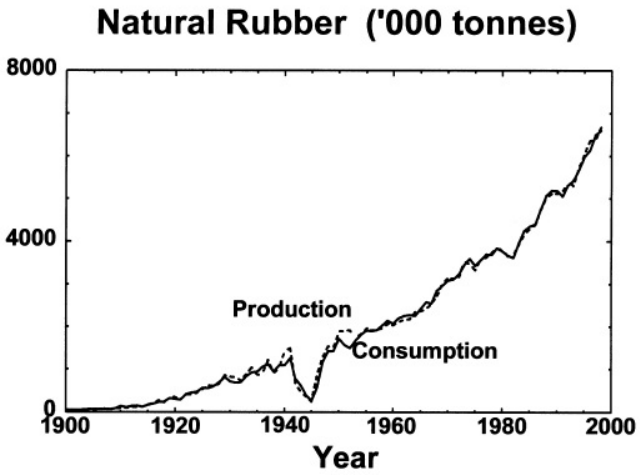

Figure 1.3: *Global production (dashed line) and consumption (solid line) of natural rubber during the twentieth century. Rubber consumption figures have closely tracked production.*

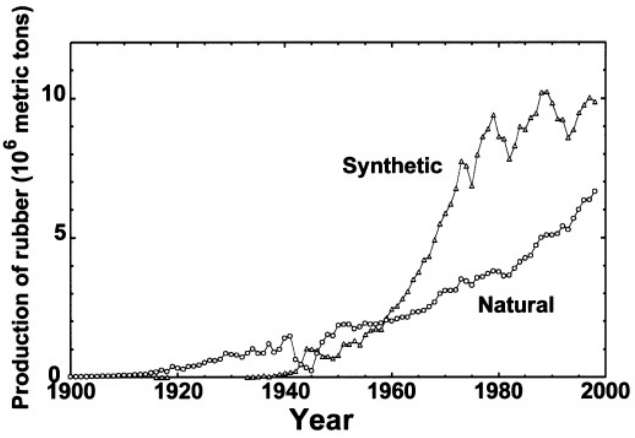

Figure 1.4: *Global production of natural ◯ and synthetic △ rubber during the twentieth century. Synthetic rubber production was established largely because of the drop in natural rubber production during World War II.*

non-automotive objects.

1.2 Definition of elastomer

The term elastomer is derived from "elastic polymer" and is often used interchangeably with the term rubber. Elastomers are amorphous polymers with

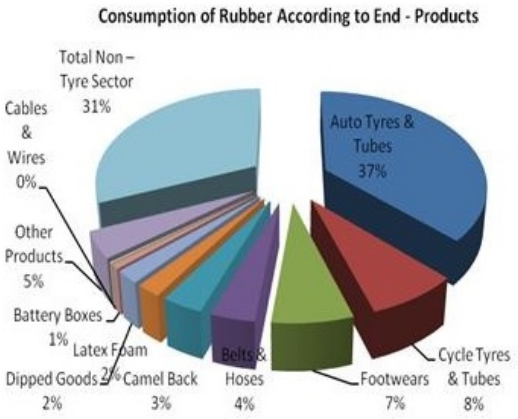

Figure 1.5: *Rubber consumption for different items production.*

glass transition temperature below ambient, so that considerable polymeric chain motion is possible. At ambient temperatures, rubbers have low elastic modulus ($\approx 3MPa$) and high failure strain. Their primary uses are for seals, adhesives, moulded flexible parts and, of course, tyres. It exist many definition of elastomer even if no one is universally accepted. Here we will give the following: "*Amorphous polymeric materials with a glass transition temperature below ambient, capable to experience large deformations when subjected to moderate stresses and to return to it's original configuration when the stresses are removed.*"

1.3 Elasticity

1.3.1 Stress and strain

The mechanical behaviour of a solid is analytically described as the relation between the applied deformation, called strain and indicated by ε, and the internal reactive force acting across a unit area, called stress and indicated by σ. Strains are pure numbers (dimensionless) and are expressed as percentage of the original length, stresses are pressures (forces acting across an area) and so are expressed in Pascal Pa or more frequently in MPa. When dealing with elastic solid stress and strain are bijectively related, it means that stress is a function of the strain only. The stress and/or strain state at which a

certain unitary volume of material is subjected must be expressed by all the components of the acting stress as shown in figure1.6. The stress and

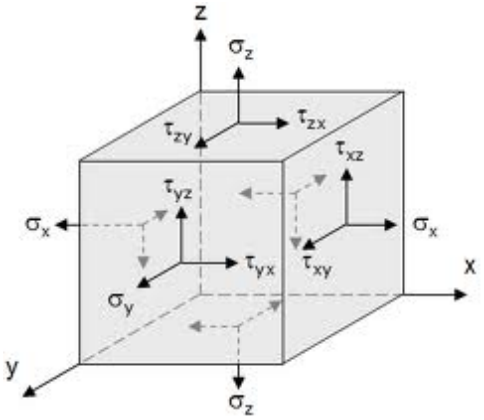

Figure 1.6: *Elementary cube of material subjected to all stress components.*

strain state is expressed by 9 components second order symmetric tensors[1] called respectively stress (equation (1.1)) and strain (equation (1.2)) tensors. Stress and strain tensors must be symmetric ($\tau_{ij} = \tau_{ji}$ and $\gamma_{ij} = \gamma_{ji}$) to guarantee the elementary volume equilibrium to rotation in respect of the second Euler law, so that the independent component of the stress and strain tensors reduces from 9 to 6. The following are common conventions used to represent the components:

$$\sigma_{i,j} = \begin{bmatrix} \sigma_{xx} & \tau_{xy} & \tau_{xz} \\ \tau_{yx} & \sigma_{yy} & \tau_{yz} \\ \tau_{zx} & \tau_{zy} & \sigma_{zz} \end{bmatrix} \tag{1.1}$$

$$\varepsilon_{i,j} = \begin{bmatrix} \varepsilon_{xx} & \gamma_{xy} & \gamma_{xz} \\ \gamma_{yx} & \varepsilon_{yy} & \gamma_{yz} \\ \gamma_{zx} & \gamma_{zy} & \varepsilon_{zz} \end{bmatrix} \tag{1.2}$$

[1] A tensor, expressed with respect to a particular reference system, is a more general "n-dimensional table of numbers" that generalizes the cases $n = 1$ (a sequence) and $n = 2$ (a matrix); n represents the tensor order. with changing of the reference system the components of a tensor are modified by specific laws. The physical notion of tensor as an object whose coordinates depend on the reference system according to fixed laws (called covariance and contra variance), it is useful to express many physical laws.

Thanks to tensors properties respect to the rotation of the reference system it is always possible to find a suitable orthogonal reference system with respect to which the shear components τ_{ij} and γ_{ij} are null. Therefore in this reference system, whose directions are called *principal* and indicated by $1-2-3$, the elementary volume is only subject to tensile stresses. With respect to the principal reference system the stress and strain tensors are diagonal and the components can be expressed as:

$$\sigma_i = \begin{bmatrix} \sigma_1 & 0 & 0 \\ 0 & \sigma_2 & 0 \\ 0 & 0 & \sigma_3 \end{bmatrix} \tag{1.3}$$

$$\epsilon_i = \begin{bmatrix} \varepsilon_1 & 0 & 0 \\ 0 & \varepsilon_2 & 0 \\ 0 & 0 & \varepsilon_3 \end{bmatrix} \tag{1.4}$$

Note that the single index $i = 1;3$ indicates the three principal directions.

When dealing with finite strains it is always useful to remind that strain measure must be independent by rigid rotation of the elementary cube, so that it is useful in what follows to refer to the principal axes and strains. Another way to identify the strain state of an elementary cube is to describe it by the stress and strain *invariants*. Thanks to the properties of tensors with respect to the change of reference system, there are three combinations of a tensor components that do not change value if calculated in different reference system, those three scalars are called *invariants* of the tensor. Referring to the strain tensor those invariants can be expressed as:

$$\begin{aligned} I_1 &= \mathrm{tr}\overline{\varepsilon} = \varepsilon_{xx} + \varepsilon_{yy} + \varepsilon_{zz} = \varepsilon_1 + \varepsilon_2 + \varepsilon_3 \\ I_2 &= \frac{1}{2}((\mathrm{tr}\overline{\varepsilon})^2 - \mathrm{tr}(\overline{\varepsilon})^2) = ... = \varepsilon_1\varepsilon_2 + \varepsilon_2\varepsilon_3 + \varepsilon_3\varepsilon_1 \\ I_3 &= \mathrm{det}\overline{\varepsilon} = ... = \varepsilon_1\varepsilon_2\varepsilon_3 \end{aligned} \tag{1.5}$$

where $\overline{\varepsilon}$ represents the strain tensor. Stress invariants can be derived in a similar manner. Stress and strain can be expressed in many different ways, the most common of which are referred to the reference (undeformed) or present (deformed) configuration. The corresponding descriptions of the

mechanical behaviour are called Lagrangian and Eulerian respectively.

Referring to the undeformed configuration it is possible to define the stress tensor components as the ratio between the force F_i applied to i-face of the elementary cube and the undeformed cross-sectional area normal to the same face A_0. This is called **Engineering stress tensor** and, referring to the principal directions, stresses can be evaluated as:

$$\sigma_i = \frac{F_i}{A_0} \tag{1.6}$$

Strains with respect to the undeformed configuration are defined as the ratio between the variation in length of the elementary cube in i direction ΔL_i and the corresponding unstrained length L_0. This is called **Engineering strain tensor** and referring another time to the principal directions, strain components can be evaluated as:

$$\varepsilon_i = \frac{\Delta L_i}{L_{i0}} = \frac{L_i - L_{i0}}{L_{i0}} \tag{1.7}$$

When dealing with elastomers usually principal *draw ratios* (also called stretches) λ_i are used instead of principal strains. Draw ratios are defined as the ratio between the deformed length L_i of the elementary cube in i direction and the corresponding undeformed length:

$$\lambda_i = \frac{L_i}{L_{i0}} = \varepsilon_i + 1 \tag{1.8}$$

When dealing with finite strains the Lagrangian description is no more accurate to express stress and strain due to the reduction of cross sectional area regarding the stresses and due to the strong change of the current length of each element regarding strains. In this case the **true (or Cauchy) stress tensor** and the **true (or Hencky) strain tensor** are commonly used, that are both referred to the current configuration instead to the reference one. Principal Cauchy stress tensor components are defined in a similar manner to the corresponding components of the principal Engineering stress tensor previously defined, but the force acting on the i-face is divided by the de-

formed cross-sectional area A:

$$\sigma_{ti} = \frac{F_i}{A_i} \tag{1.9}$$

Principal Hencky strain tensor components are defined as the sum of the infinitesimal strains referred to the current length:

$$d\varepsilon_{ti} = \frac{dl_1}{l_i} \tag{1.10}$$

And so can be obtained integrating differential increments from the reference length L_0 to the current length L:

$$\varepsilon_{ti} = \int_{L_{0i}}^{L_i} \frac{dl_1}{l_i} = \ln \frac{L_i}{L_{0i}} = \ln \lambda_i \tag{1.11}$$

When dealing with constant volume deformations engineering and true measures of stress and strain can be related. Elastomers have the peculiarity to deform without changes in volume, and this property can be expressed by use of (1.8) considering a cube of side l_0 which deforms in a parallelepiped of sides l_1 l_2 and l_3, equating the volumes in the reference and deformed configuration:

$$\begin{aligned} l_1 l_2 l_3 &= l_0^3 \\ \frac{l_1 l_2 l_3}{l_0^3} &= 1 \\ \lambda_1 \lambda_2 \lambda_3 &= 1 \end{aligned} \tag{1.12}$$

or similar with respect to (1.11):

$$\varepsilon_{t1} + \varepsilon_{t2} + \varepsilon_{t3} = 0 \tag{1.13}$$

Gent [2] highlights how elastomers when subjected to severe triaxial tension develops internal fractures cavities instead of expanding volume. Being equation (1.12) a link between the three principal draw ratios it implies a reduction of independent principal strain tensor components from 3 to only 2. The imposition of this boundary to the problem in most cases is not so far from reality.

It is easy to demonstrate that due to constance of volume the following relation exists between undeformed and deformed cross-sectional area:

$$A_i = \frac{A_{0i}}{\lambda_i} \tag{1.14}$$

And consequently the Cauchy and Engineering principal stress tensors components are linked by the following relation:

$$\sigma_{ti} = \lambda_i \sigma_i \tag{1.15}$$

The relationship between the true and engineering principal strain can be easily derived combining (1.8) with (1.11):

$$\varepsilon_{ti} = \ln(\varepsilon_i + 1) \tag{1.16}$$

Rebus sic stantibus many advantages can be achieved by describing stresses and strain in one or the other manner from case to case, in this work Engineering stress and strain will be used were not specified.

1.3.2 Simple, pure shear and equibiaxial tension

In the course of this work we will often refer to some particular configurations that now will be briefly described in the framework of constant volume deformations expressed in equation (1.12) and plane stress (i.e., $\sigma_3 = 0$ and principal axis 3 always in thickness direction).

The state of simple or uniaxial tension (U) depicted in figure 1.7(a) is such that the elementary cube of material is deformed along one direction and left free to contract in the remaining two. In terms of draw ratios as defined in equation (1.8) it can be described as:

$$\begin{aligned} \lambda_1 &= \frac{l}{l_0} = \lambda_U \\ \lambda_2 &= \lambda_3 = \lambda_t = \frac{1}{\sqrt{\lambda_1}} \end{aligned} \tag{1.17}$$

The state of pure shear tension (PS) is the simplest state of biaxial deformation that can be achieved and is schematically shown in figure 1.7(b). Gent

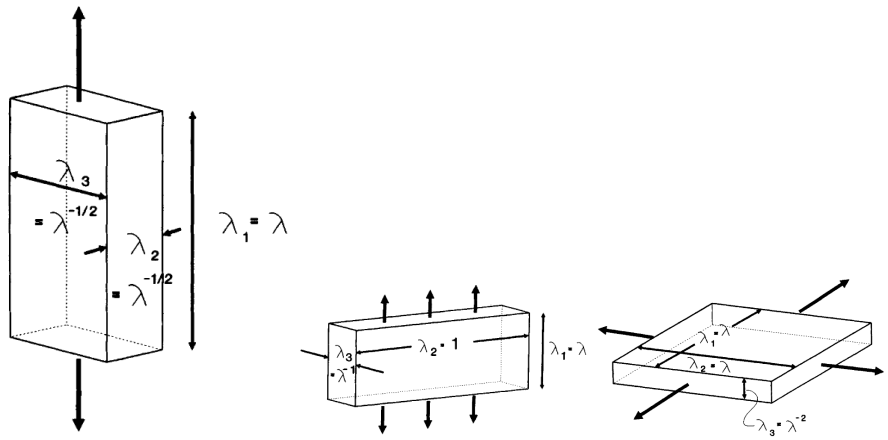

(a) (b) (c)

Figure 1.7: *Elementary cubes deformed in uniaxial (a), pure shear (b) and equibiaxial (c) configurations. (Images from [3]).*

in [3] gives a simple and effective explanation of this state of deformation, defining it as a "constrained tension", i.e. a state of uniaxial tension in which one of the two transverse directions is constrained not to change in length. In terms of draw ratios it can be described as:

$$\begin{aligned} \lambda_1 &= \frac{l}{l_0} = \lambda_{PS} \\ \lambda_2 &= 1 \\ \lambda_3 &= \frac{1}{\lambda_{PS}} \end{aligned} \tag{1.18}$$

The reason for the name *"pure shear"* is that *"shear"* is defined as a state of deformation in which parallel lines to one of the principal strain axes do not change length, and this is the case along the 2nd axis. The prefix *"pure"* refers to the fact that the principal axes do not rotate during the deformation process. Finally in figure 1.7(c) the equibiaxial tension (E) is reported. As the name suggests this is a state of deformation in which two of the three principal strains are equal to each other, and the third can be obtained by imposing, as usual, the constancy of the volume. In terms of draw ratios this state of deformation can be described by the following

relationships:

$$\begin{aligned} \lambda_1 &= \lambda_2 = \lambda_E \\ \lambda_3 &= \frac{1}{\lambda_E^2} \end{aligned} \tag{1.19}$$

A general biaxial deformation can be described in a similar manner.

Biaxiality In order to describe the deformation state by means of a single number it is possible to define a quantity, here named **biaxiality**, as follows:

$$Biaxiality = \frac{\varepsilon_1 - \varepsilon_2}{\varepsilon_1} \tag{1.20}$$

Where ε_1 and ε_2 are the first and second component of the principal engineering strain tensor. As an example a PS strain state have a biaxiality equal to 1 and an E strain state have a biaxiality equal to 0. All the biaxial deformation states have a biaxiality between 0 and 1 and will be indicated in what follows as a capital B followed by the biaxiality value without comma. As an example "$B05$" indicates an element subjected to:

$$\begin{aligned} \lambda_1 &= \lambda \\ \lambda_2 &= \frac{\lambda}{2} \\ \lambda_3 &= \frac{2}{\lambda^2} \end{aligned}$$

In order to evaluate the biaxiality of an element deformed in simple tension the *Poisson ratio* must be first defined.

Poisson ratio The Poisson ratio is a characteristic of each material that measures the degree of transversal shrinkage (or expansion) that the material experiences when subjected to unidirectional longitudinal strain as:

$$\nu = -\frac{\varepsilon_t}{\varepsilon_U} \tag{1.21}$$

This classic definition of Poisson ratio can be extended to finite strain in accordance with the definition arbitrary given by Chevalier in [4], knowing the relationship between the longitudinal and transverse draw ratio for uni-

axially stressed elastomer from equation (1.17), we can rewrite the Poisson ratio as a function of applied strain in the longitudinal direction:

$$\nu(\varepsilon_U) = \frac{1}{\varepsilon_U}\left(1 - \frac{1}{\sqrt{\varepsilon_U + 1}}\right) \tag{1.22}$$

This definition of the Poisson ratio as a function of the applied longitudinal strain is not in contrast with the classical theory, in fact for infinitesimal strains we found:

$$\lim_{\varepsilon \to 0} \nu(\varepsilon) = 0.5$$

that is the usual value of Poisson ratio attributed to constance of volume, as well as the maximum possible value. In fact, as you can see in figure 1.8 the function described by equation (1.22) divides the $\nu(\varepsilon) - \varepsilon$ plane in two distinct areas: the upper area that characterizes deformation with volume contraction and which is therefore prohibited, and a lower area that characterizes deformation with volume expansion. The transverse strain of

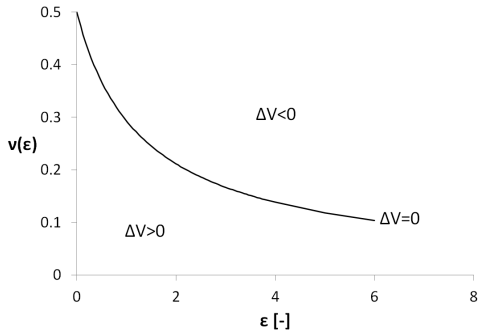

Figure 1.8: *Poisson ratio ν versus applied engineering strain ε in simple tension.*

an element deformed in simple tension results to be:

$$\varepsilon_t = -\nu(\varepsilon_U)\varepsilon_U \tag{1.23}$$

Using the definition of Poisson ratio it is now possible to define the biaxiality of an element in U tension by combining (1.23) and (1.20) as:

$$Biaxiality(U) = \frac{\varepsilon_U + \nu(\varepsilon_U)\varepsilon_U}{\varepsilon_U} = 1 + \nu(\varepsilon_U) \tag{1.24}$$

The biaxiality of an element deformed in simple tension is a decreasing function of the applied longitudinal strain ε_U, whose initial maximum value is 1.5 and that tends asymptotically to 1 when the longitudinal applied strain tends to infinity. In summary:

$$Biaxiality = \begin{cases} 1 < biaxiality \leqslant 1.5, & \text{U} \\ 1, & \text{PS} \\ 0 < biaxiality < 1, & \text{B} \\ 0, & \text{E} \end{cases} \tag{1.25}$$

These boundaries are derived from the choice of using the engineering strain tensor to define the biaxiality of an element, whereas identify the biaxiality using another strain measure the numerical values can change but would maintain the same meaning.

1.3.3 Constitutive relation between stress and strain

As asserted at the beginning of the last paragraph the mechanical behaviour is characterized by the stresses that the material generates when subjected to deformations. The simplest example of elastic behaviour is the linear spring, that is representative of *linear elastic materials*. This device, whose behaviour is described in Figure 1, reacts to tensile \compressive displacements with a force that depends on the imposed deformation by means of a constant, k, said elastic constant or stiffness of the spring. The behaviour

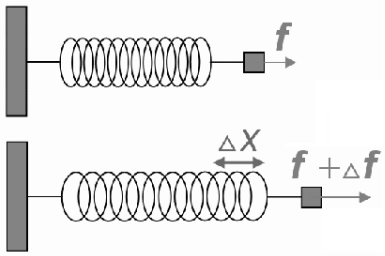

Figure 1.9: *Behaviour of a simple spring.*

of the spring can be described as:

$$\Delta f = k\Delta X \tag{1.26}$$

This is a simple case of linear relation between a force and an applied displacement, when dealing with elementary cubes of materials this linear relation must be written in terms of stress and strain. The stress-strain constitutive relation for linear elastic materials is commonly known as *Hooke law*. In its simplest form, the law defines the Young modulus E in a scalar equation, stating the tensile \compressive stress is proportional to the extended (or contracted) strain:

$$\sigma = E\varepsilon \tag{1.27}$$

It means that the material react to strain ε with a stress σ linearly related to the applied deformation by means of the constant E. Equation (1.27) is valid only when uniaxial stresses are applied. If a general system of forces acts on the material Hooke law is written in the following vectorial form:

$$\sigma_{ij} = C_{ijkl}\varepsilon_{kl} \tag{1.28}$$

where C is the elasticity tensor containing the elastic coefficients of the material. Due to the inherent symmetries of σ, ε, and C, only 21 elastic coefficients of the latter are independent. For isotropic media (which have the same physical properties in any direction), C can be reduced to only two independent parameters, the bulk modulus K and the shear modulus G, that quantifies the material's resistance to changes in volume and to shearing deformations, respectively. When an elastic solid is deformed due to an external force a certain amount of energy is elastically stored inside the material. The stored energy amount for unitary volume of the material is called **strain energy density** W, expressed in Joule for cubic length J/m^3. In the simplest case of an elastic solid deformed in one single direction, W can be evaluated as the area under the stress-strain curve by the integral:

$$W(\varepsilon) = \int_0^{\varepsilon} \sigma d\varepsilon \tag{1.29}$$

If the material is subjected to multiple axis deformation the strain energy density becomes a function of the three principal strains:

$$W(\varepsilon_1; \varepsilon_2; \varepsilon_3) \tag{1.30}$$

Valanis and Landel [5] proposed that the strain energy function W may be expressible as the sum of three functions of the principal stretches, namely the integrals of the stress-strain curves into the three principal directions:

$$W(\lambda_1; \lambda_2; \lambda_3) = w(\lambda_1) + w(\lambda_2) + w(\lambda_3) \tag{1.31}$$

1.4 Hyperelasticity of elastomers

In physics, a Cauchy-elastic material [6] (also known as simple elastic) is one in which exist a bijective relation between the stress at each point and the current state of deformation, with respect to the reference configuration. Even though the stress depends only on the deformation, the work done by stresses may depend on the path of deformation. Therefore a Cauchy elastic material is not necessarily conservative in terms of W as defined in equation (1.30), and the stress cannot be derived from a scalar potential function. Materials that are conservative with respect to the strain energy density are called hyperelastic or Green-elastic [6].

Elastomers behaves mechanically as non-linear elastic isotropic incompressible materials, and are often modelled as hyperelastic. The hyperelastic nature of elastomers directly derived from the properties of the polymer chains of which it is composed and from the structure that they form when they are bound together. The structure of an elastomer is in fact constituted by long flexible polymer chains interconnected by bridges of different kind, called cross-link, to form a network. In the case of natural rubber, the base polymer is the *cis*-1,4 polyisoprene, a highly stereo-regular polymer. The cross-linking of natural rubber is done by using a Sulphur-based process discovered by Charles Goodyear in 1839 and later called "vulcanization". This curing process completely or partially locks the possibility of relative sliding of the polymer chains as shown in figure1.10, giving to vulcanized rubber

the mechanical properties described in section1.2.

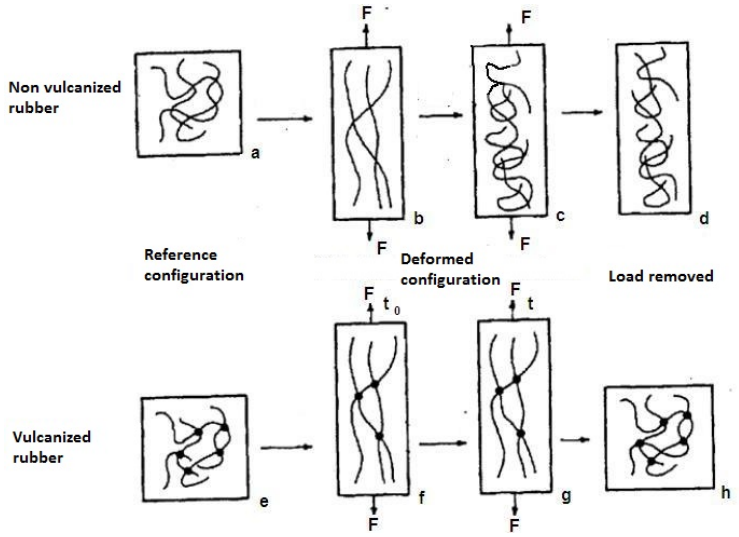

Figure 1.10: *Schematic representation of a loading-unloading cycle performed on unvulcanized (top) and vulcanized (bottom) rubber.*

Single chain elasticity The first example of an analytical approach to the problem of elastomers elasticity is the Rivlin's theory of large elastic deformations [7] [8]. The elasticity of the **single chain** can be described by statistic thermodynamic considerations about the number of configurations that the chain is allowed to assume. In the undeformed condition a very flexible macromolecule, as is the case for the polyisoprene, lies in a state of complete disorder called random coil. The linear size of a random coil is defined by the size of the vector r shown in figure 1.11 joining the beginning and the end of the macromolecule, represented as a set of n rigid sections of length l, freely-to-rotate connected. At least for small values of r, the distribution of end-to-end distances obeys to a Gaussian probability function of the type:

$$P(r) = Cexp(-\beta^2 r^2) \tag{1.32}$$

where β^2 is given by $3/2nl^2$ and the mean square distance between the ends, denoted r^2, is then:

$$\bar{r^2} = nl^2 \tag{1.33}$$

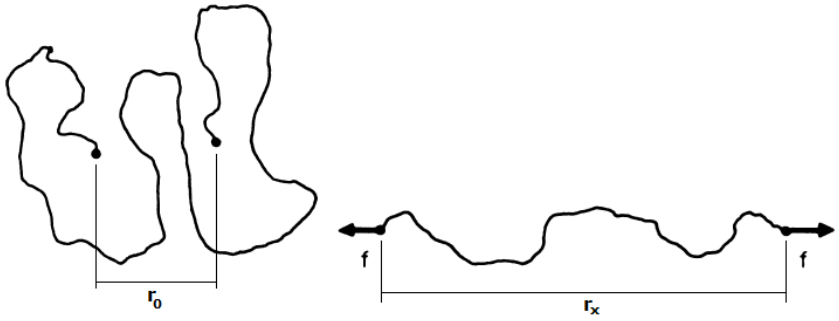

Figure 1.11: *Schematic representation of a macromolecule in unextended or random coil configuration (end-to-end distance r_0) and extended configuration (end-to-end distance r_x)(image adapted from [9]).*

A macromolecule thus described has an Helmholtz free energy w that can be expressed by $-Ts$, where s is the entropy value associated with the dimension r which can be calculated by the Boltzmann's law. This energy can be expressed as follows:

$$w = -kTlnP(r) = kT\beta^2 r^2 = \frac{3kTr^2}{2nl^2} \tag{1.34}$$

where k is the Boltzmann constant and T is the absolute temperature expressed in Kelvin. The elastic behaviour of the macromolecule in terms of reaction force f arising from a linear variation in length δr can now be derived using the relationship:

$$f = \left(\frac{\partial w}{\partial r}\right) = \frac{3kTr}{nl^2} \tag{1.35}$$

If we assume:

$$K = \frac{3kT}{nl^2}$$

It becomes evident how a macromolecule that obeys to the Gaussian probability function behaves mechanically as the ideal spring described in equation (1.26), whose K constant is linearly dependent on the temperature T and is inversely proportional to the number n of sub-chain segments.

Molecular chains network Looking to the elasticity of the molecular network it is again necessary to express the total Helmholtz free energy of

the network as a function of the principal draw ratios (1.8) applied to a unitary cube of material. In order to reach this result some hypothesis must be done:

1. The network contains N chains per unit volume, a chain being defined as the segment of molecule between two crosslinks.

2. The mean-square end-to-end distance for the whole assembly of chains in the unstrained state is the same as for a corresponding set of free chains, and is given by the formula (1.33).

3. There is no change in volume on deformation (1.12).

4. The junction points between chains move on deformation as if they were embedded in an elastic continuum. as a result the components of length of each chain change in the same ratio as the corresponding dimension of the bulk rubber. (Affine deformation)

5. The entropy of the network is the sum of the entropies of the individual chains. (Gaussian chains)

In this framework it is possible to demonstrate that the Helmholtz free energy of the network can be expressed as:

$$W = \frac{G}{2}(\lambda_1^2 + \lambda_2^2 + \lambda_3^2 - 3) \tag{1.36}$$

where G is the *shear modulus*, linked to the network molecular parameters by the relation:

$$G = NkT = \frac{\rho RT}{M_c} \tag{1.37}$$

in which ρ is the density of the rubber, R the gas constant per mole and M_c is the average chain molecular weight between cross-link. Treloar [10] gives the complete derivation of equation (1.34) and (1.36). It is interesting to highlight how a homogeneous isotropic ideal elastomer has a mechanical behaviour that is described by just one elastic constant i.e. the shear modulus G. Equation (1.36) represent the simplest example of hyperelastic strain energy potential, for this reason it is usually referred as Neo-Hookean model. The stress-strain relation of the elastomer can be obtained from equation

(1.36) (or analogue) simply by partial derivation of the strain energy density function W with respect to the principal λ_i. In the case of simple uniaxial traction, in which principal stretches are expressed by equation (1.17) W can be specified as:

$$W = \frac{G}{2}\left(\lambda_U^2 + \frac{2}{\lambda_U} - 3\right) \tag{1.38}$$

And the resulting stress-stretch relation is:

$$\sigma_U = \left(\frac{\partial W}{\partial \lambda_U}\right) = G\left(\lambda_U - \frac{1}{\lambda_U}\right) \tag{1.39}$$

The first interesting result that can be deduced is that the molecular network, although it is composed of Gaussian chains we saw to behave mechanically as ideal springs, results to have a **non-linear behaviour**. As shown in figure 1.12, comparing real experimental data, obtained by uniaxial tensile test, with the mechanical behaviour predicted by the ideal molecular network model expressed in equation (1.39) it can be seen how there is a good agreement only for relatively moderate strains, say $\lambda_U < 2$. For intermediate strains ($2 < \lambda_U < 6$) Neo-Hookean model results to be stiffer with respect to the real behaviour due to network defects. The real network obtained during a curing process results to different with respect to the network assumed by Treloar into the framework of the ideal molecular network model, some possible examples of network defects are shown in figure 1.13. when the applied strain reaches relatively high levels ($\lambda_U = 5$ in figure 1.12), chains reach their maximum extension. In this condition the elastomer becomes progressively more rigid, giving rise to a phenomenon known as **upturn** or **strain hardening**. The Gaussian chain assumption used to derive the constitutive model of the ideal molecular network do not take in account for the chains finite extensibility, for this reason is not able to predict the phenomenon of strain hardening. In the next two sections we will discuss about the proposed constitutive models to address this shortcoming and the peculiar phenomenon of strain induced crystallization, which can occur in elastomers with highly stereoregular chains when subjected to severe deformations.

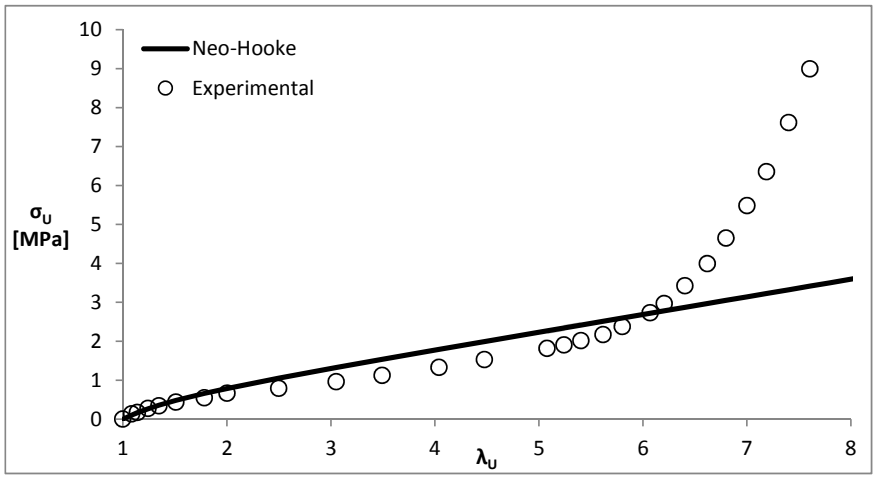

Figure 1.12: *Comparison between experimental data for uniaxial tensile test on natural rubber and the mechanical behavior prediction of the ideal molecular network model (Neo-Hooke) with* $G = 0.45MPa$.

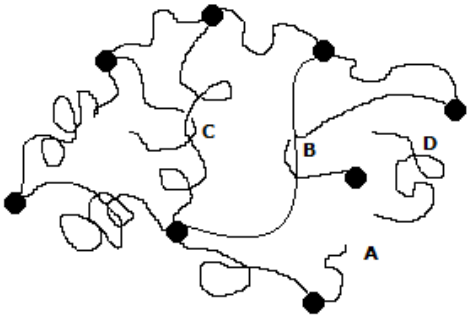

Figure 1.13: *Schematization of a real network of molecular chains with: A) free chain end; B) permanent entanglement; C) simple entanglement; D) uncured chain.*

1.5 Hyperelastic strain energy density models

The effort made by the research community in identifying appropriate constitutive models able to correctly represent the mechanical behaviour of

hyperelastic materials is evident by the number and variety of models proposed over the years. Such models can be divided into three main types of formulation:

1. **Phenomenological models**: purely mathematical formulations aimed at the reproduction of the experimental data without regard to the basic physics of the phenomenon.

2. **Invariant-based models**: formulations based on considerations regarding particular features of mechanical behaviour with respect to strain invariants, aimed at the direct determination of the most appropriate material parameters from the measured $\partial W/\partial I_1$ and $\partial W/\partial I_2$.

3. **Physical models**: formulations based on considerations about the physics of the deformation process using statistical approach. In most cases these models are mathematically quite complicated, but the model parameters are directly related to the physical properties of the model, in relation to the assumptions on which they are based.

For each one of these three classes we will now give a brief description of the most representative model as well as a list of the most popular and efficient.

Phenomenological models - Ogden model In 1972 Ogden [11] proposed a model of hyperelastic potential based on the expression of the elastic strain energy density as the sum of real powers of the draw ratios in the form:

$$W = \sum_{i=1}^{N} \frac{\mu_i}{\alpha_i} \left(\lambda_1^{\alpha_i} + \lambda_2^{\alpha_i} + \lambda_3^{\alpha_i} - 3\right) \tag{1.40}$$

Where μ_i and α_i are material parameters. The number of these parameters is clearly equal to $2N$ where N is the number of terms of the summation used. The parameters must satisfy the stability condition:

$$\mu_i \alpha_i > 0 \tag{1.41}$$

For practical reasons the number of terms of the summation used is usually truncated to a finite number generally between 3 and 6. It should also be

pointed out that:

$$\sum_{i=1}^{N} \mu_i \alpha_i = 2G \tag{1.42}$$

Where G is the shear modulus of the material [12]. This model is one of the most widely used in the context of finite element simulation for the problems of large deformations, although the determination of the parameters is difficult. Ogden [13] also extent the validity of this model to small compressibility.

For plane stress ($\sigma_3 = 0$) the stress-stretch relation in each direction can be obtained from equation (1.40) by partial derivation of W with respect to λ_i:

$$\begin{aligned} \sigma_1 &= \frac{\partial W}{\partial \lambda_1} = \sum_{i=1}^{N} \mu_i \left(\lambda_1^{\alpha_i - 1} - \frac{1}{\lambda_2^{\alpha_i} \lambda_1^{\alpha_i + 1}} \right) \\ \sigma_2 &= \frac{\partial W}{\partial \lambda_2} = \sum_{i=1}^{N} \mu_i \left(\lambda_2^{\alpha_i - 1} - \frac{1}{\lambda_1^{\alpha_i} \lambda_2^{\alpha_i + 1}} \right) \end{aligned} \tag{1.43}$$

As part of this work the Ogden model was used to model the behaviour of the material in quasi-static loading conditions, so it is useful to specify equations (1.43) for U, PS and E configurations substituting equations (1.17) (1.18) and (1.19):

Uniaxial

$$\begin{aligned} \sigma_1 &= \sum_{i=1}^{N} \mu_i \left(\lambda_U^{\alpha_i - 1} - \frac{1}{\lambda_U^{\frac{\alpha_i}{2} + 1}} \right) \\ \sigma_2 &= 0 \end{aligned} \tag{1.44}$$

PureShear

$$\begin{aligned} \sigma_1 &= \sum_{i=1}^{N} \mu_i \left(\lambda_{PS}^{\alpha_i - 1} - \frac{1}{\lambda_{PS}^{\alpha_i + 1}} \right) \\ \sigma_2 &= \sum_{i=1}^{N} \mu_i \left(1 - \lambda_{PS}^{-\alpha_i} \right) \end{aligned} \tag{1.45}$$

Equibiaxial

$$\sigma_1 = \sigma_2 = \sum_{i=1}^{N} \mu_i \left(\lambda_E^{\alpha_i - 1} - \frac{1}{\lambda_E^{1+2\alpha_i}} \right) \tag{1.46}$$

In this category should also be mentioned the Mooney-Rivlin model:

$$W = \sum_{i,j=1}^{N} C_{ij} \left(I_1 - 3\right)^i \left(I_2 - 3\right)^j \tag{1.47}$$

Where C_{ij} are material parameters and I_1 and I_2 are the first and second invariants of the right Cauchy-Green deformation tensor defined as:

$$\begin{aligned} I_1 &= \lambda_1^2 + \lambda_2^2 + \lambda_3^2 \\ I_2 &= \lambda_1^2\lambda_2^2 + \lambda_2^2\lambda_3^2 + \lambda_3^2\lambda_1^2 \end{aligned} \tag{1.48}$$

Invariant-based models - Gent model In order to take into account the chains finite extensibility Gent [14] formulated a model in which the maximum value admissible by the first invariant of the tensor of the right Cauchy-Green deformation tensor as defined in (1.48) is limited to a constant value for all strain configuration. This assumption was lather confirmed by the same author in [15]. On the basis of this assumption Gent proposed to express the strain energy density using the relation:

$$W = -\frac{E}{6} \left(I_m - 3\right) ln \left[1 - \frac{I_1 - 3}{I_m - 3} \right] \tag{1.49}$$

Where E and I_m are two material parameters, in particular I_m represents the limiting value for I_1.

As part of this work the Gent model was used to represent the behaviour of the material in dynamic biaxial loading conditions. The stress-strain relationship can be derived in a similar manner than seen so far in the case of Neo-Hookean and Ogden models.

In this category should also be mentioned the Rivlin and Saunders model [16] and the Hart-Smith model [17], that is an extension of the R-S model for finite extensibility of macromolecules.

Physical models - Extended tube model In carrying out this work physical constitutive models have not been used due to difficulties in imple-

mentation of the models itself in finite elements simulations, so we will just report the model that best represents this category. The extended tube model, proposed by Kaliske and Heinrich [18], provides the hyperelastic potential by the sums of two contributions, one relevant to the finite extensibility of macromolecules and the other relevant to the confinement of the macromolecule within a "tube" formed by the surrounding macromolecules through the entanglements [19]. The hyperelastic strain energy density can be expressed as:

$$W = \frac{G_c}{2}\left[\frac{\left(1-\delta^2\right)(I_1-3)}{1-\delta^2(I_1-3)} + ln\left(1-\delta^2(I_1-3)\right)\right] - \frac{2G_e}{\beta}I^*(-\beta) \quad (1.50)$$

Where G_c, G_e, δ and β are material parameters.

In this category should also be mentioned the 8-chain model, also known as Arruda-Boyce model [20]

Comparison Verron [21] has carried out a detailed study about the capabilities of the constitutive models available in the literature for rubber, comparing twenty hyperelastic models on the basis of their ability to correctly represent the classic data from Treloar [22] and Kawabata [23]. The author proposes a ranking based on some rules accurately described, including the ability of the model to represent complex loading conditions and the simplicity of the model in terms of the number of parameters used. The extended-tube model took the first place, the Ogden model the fourth and the Gent model the ninth.

1.6 Experimental techniques for material parameters identification

As already described in section 1.4 the mechanical behaviour of rubbers is described analytically by the strain energy W stored per unit volume for a given applied state of deformation. In order to correctly determine the coefficients of hyperelastic constitutive models it is of fundamental importance the mechanical characterization of materials. Since the hyperelastic

strain energy potential is a function of the strain state, which can be represented by only two of the three principal strains in the case of constant volume, it can be represented by a surface in the space of the two principal strains towards energy as shown in figure 1.14. The models described

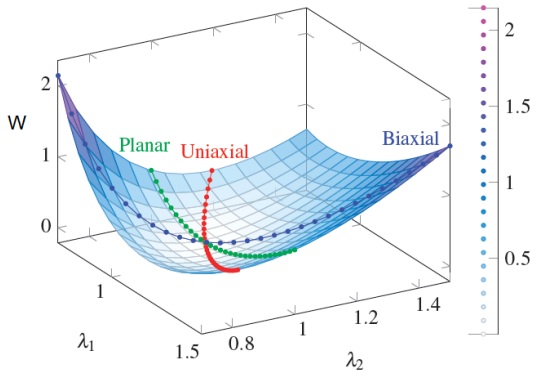

Figure 1.14: *Strain energy density surface versus applied strain state represented by λ_1 and λ_2. (Image adapted from www.axelproducts.com).*

in section 1.5 can contain a large number of parameters and therefore to obtain a good estimate of the whole surface a characterization performing tests in multiple homogeneous states of deformation such as uniaxial, pure shear and equibiaxial is required. It has been reported in literature with various characterization techniques, that can be divided into two main categories: multiple homogeneous strain tests and single heterogeneous strain test methods.

Treloar [22] was the first in 1943 to investigate the mechanical properties of rubber under various loading conditions by means of multiple homogeneous test. He performs stress-strain characterization tests in simple elongation, pure shear and equibiaxial extension. The latter was performed by inflation of rubber circular sheet into the form of a balloon. The bulge test shown in figure 1.15(a) is still commonly used for elastomers characterization both in quasi-static and in dynamic loading condition [24], but this type of test have many shortcoming such as the practical difficulties encountered to measure the real applied strain to the pole of the balloon. In the example of figure 1.15(a) the strain was optically measured using two cameras with a special mounting used to maintain the correct focal distance during bulge

inflation. Woo [25] uses radial extension of rubber circular sheet to obtain equibiaxial loading conditions. He provides an example of the importance of a complete characterization showing how the parameters obtained for the Mooney-Rivlin constitutive model change strongly using uniaxial stress data alone or in combination with equibiaxial data. Extrand and Gent in [26] follows a similar approach to characterization using simple tension, pure shear and equibiaxial test. They obtain biaxial stress-strain data by planar tension on square sheets. In the present work this latter approach to biaxial extension was chosen, because it allows to perform stress-strain characterization tests in general biaxial loading conditions in addition to the equibiaxial test that can be obtained by the bulge test or the radial extension. We can find a completely different approach to the problem of the characterization in the work of Toussaint [27]. Instead of multiple tests on homogeneously deformed specimens, a single test performed on the particular three-branch specimen shown in figure 1.15(b) (tested by means of a suitably modified uniaxial dynamometer) which presents uniaxial, pure shear and equibiaxial deformation at the same time was used. Using digital image correlation to measure the strain field and applying an inverse method for results processing material parameters of a Mooney model (two parameters) were obtained.

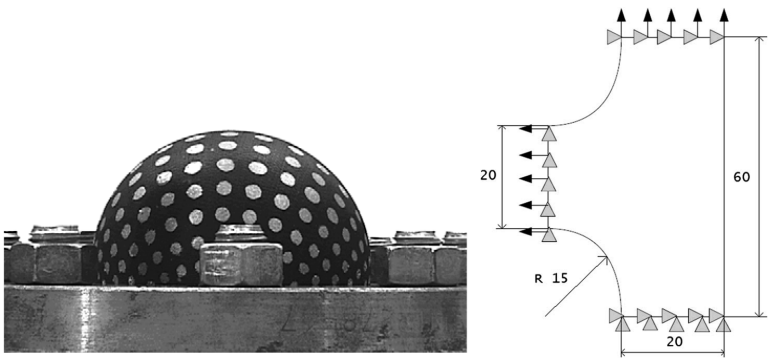

(a) (b)

Figure 1.15: *a) Bulge test (image from [24]); b) Three-branch specimen used in [27].*

1.7 Strain induced orientation and crystallization

Above the melting temperature natural rubber in the undeformed state is an amorphous solid composed from its macromolecules, eventually cross-linked, arranged in the random coil configuration. However if rubber is deformed macromolecules begin to extend and simultaneously to orientate in the direction of the maximum principal strain applied to each elementary volume of material. If the macromolecules are sufficiently stereoregular to form ordered structures, the strain induced orientation leads to the phenomenon of strain induced crystallization (SIC). SIC is a phenomenon in which an initially amorphous solid material undergoes a phase transformation due to the application of strain. Strain crystallization occurs in natural rubber due to the fact that it is constituted of more than 94% of cis 1,4 polyisoprene streoregular macromolecules. The phenomenon has important effects on strength and fatigue properties. There are various techniques for measuring crystallization in rubber the best of which is X-ray diffraction, but can also be observed indirectly through its effects on stress-strain and fatigue behaviour. Chenal [28] asserts that the molecular weight between physical entanglements in natural rubber is a key parameter for strain-induced crystallization. Natural rubber stereoregularity allows its rapid crystallization when it is stretched more than 300% of its original length. The presence of the filler increases the crosslinking density due to the rubber-filler interactions, so it reduces the molecular weight between junction increasing the rate of crystallization [29]. Carbon black also acts as a nucleus of crystallization, and the crystal nuclei behaves as giant cross-links largely responsible for the phenomenon of strain hardening [30]. Murakami by means of X-ray diffraction measurements in constrained cooling and constrained heating establish that crystallites creates a new network structure that adds or strengthens the network formed by vulcanization [31]. Toki in [32,33] found that even at large deformations ($> 500\%$) the amount of rubber crystallized remains around 20%, 5% of the material is still amorphous but is oriented and the remaining 75% is non-oriented amorphous. The author address this unexpected behaviour to the non homogeneity of the real network, as schematically shown in figure 1.16. He also highlights the effect of relaxa-

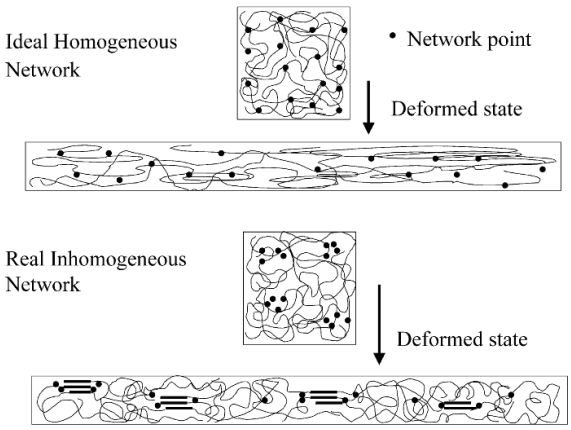

Figure 1.16: *Top - Ideal homogeneous network with affine deformation of molecular chains; Bottom - Real inhomogeneous network with crystals and unoriented amorphous chains. (Image from [33])*

tion time on strain induced orientation and crystallization in [34], measuring the crystallization dynamic by real-time diffraction measurements. He finds very different results than those obtained by measurements on specimens deformed at an earlier time than the experiment. It is emphasized that the macromolecules are oriented during deformation but without there being crystallization up to 400% of applied strain. Beyond this threshold the crystallization increases rapidly.

1.8 Dissipation phenomena and Mullins effect

"Mullins effect consists in a change of the mechanical properties after that the material has been subjected to a deformation. Among the first important works on this subject, Mullins effect was early observed and studied by Mullins (1947) [35] and Mullins and Tobin (1957) [36]. They idealized that rubber could exist in two phases: a "hard phase" and a "soft phase". When the material is virgin it shows only the hard phase, but, when greater and greater deformation is applied, more and more rubber degrades in the soft phase. A typical cyclic loading path where Mullins effect is evident is represented in figure 1.17 in terms of stress strain curves. In particular, on the initial loading (OaA) the virgin material exhibits a relatively

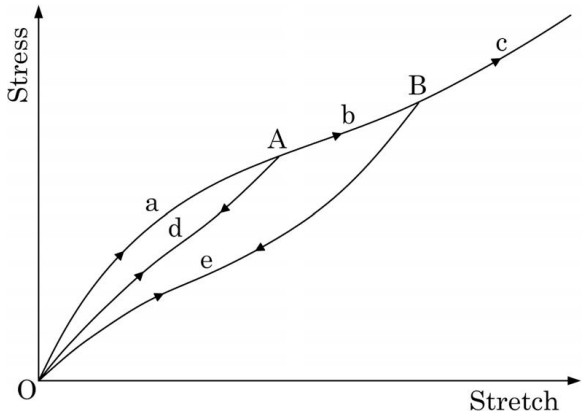

Figure 1.17: *Mullins effect (Image from [24]).*

stiff response. From point A the material is unloaded and then reloaded; in these two phases the material follows two paths (AdO, OdA) that are softer than the primary path, until it reaches for the second time the point A. Increasing further the stretch, the stress strain curve will return to follow the primary path (AbB) until the next unload is performed (BeO), and so on. With "primary path" it is indicated the curve OaAbBc that is the typical hyperelastic path without stress softening effects; this curve can be obtained from monotonic quasi-static stretching tests in the different load distributions." [24]

Chapter 2

Materials and methods

2.1 Laboratory machines

2.1.1 Uniaxial dynamometers

Uniaxial characterization tests were performed on Hounsfield Model H5K-S UTM dynamometer, that is equipped with a mechanical extensometer for large strain measure (Model 100R Long Travel Extensometer), a pneumatic clamping system and $5kN$ load cell. Pure shear characterization and fracture tests were performed on an Instron 1121 screw driven dynamometer equipped with a $10kN$ load cell, using a pneumatic clamping system in combination with the aluminium hand-made clamps described in section 2.3.1.

2.1.2 Biaxial dynamometers

Three different biaxial dynamometers were used in order to perform biaxial tests in this work, two for quasi-static and one for dynamic testing. The three dynamometers will now be described briefly.

LaBS Biaxial tester (Politecnico of Milan) This biaxial dynamometer, shown in figure 2.1(a), located at the **Laboratory of Biological Structure Mechanics (LaBS)**. It was used during the first year of the PhD in order to complete the series of quasi-static fracture tests on cross-shaped specimens carried out during the master degree thesis [37]. The

results were published in [38, 39], full papers with experimental details of this series of tests and the results obtained are in Appendix B.

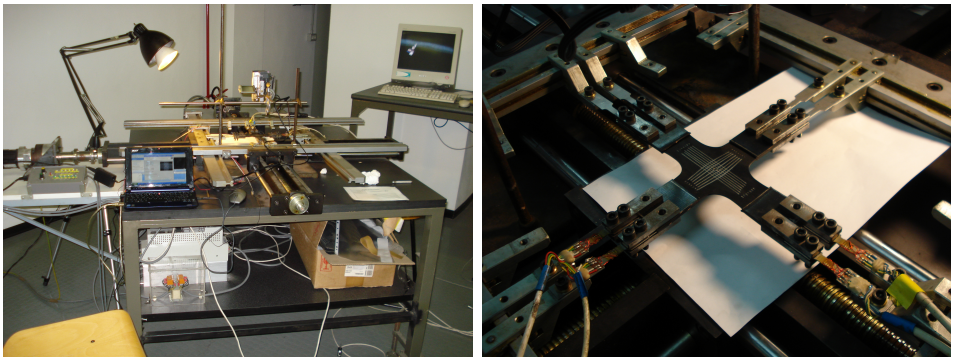

(a) (b)

Figure 2.1: *a) LaBS biaxial tester used for fracture test on cross shaped specimens; b) Cross shaped specimen mounted on the LaBS biaxial tester.*

Coesfeld Biaxial tester (Dresden - Germany) This dynamic biaxial dynamometer designed by Coesfeld Materialtest, shown in figure 2.2, was used for dynamic stress-strain and fatigue characterization tests carried out during a 6 months stay at the **IPF Leibniz-Institute for Polymer Research Dresden**. The work done with this machine has been divided into two periods of 3 months each. In the first one performance and testing optimization of the machine (that at the time was a new prototype) were conducted in order to explore the machine capabilities and optimize the software, during the second period we have focused on the materials characterization and fatigue resistance of compounds in dynamic biaxial loading conditions. The machine, being equipped with four independent motors with the configuration reported in figure 2.3, is able to generate independent load histories in the four directions implemented by pre-set profiles such as sine pulse, triangle, rectangles and saw tooth as well as by user-defined profile. Each engine has a maximum stroke of $30mm$ and can work with frequencies between $0.1Hz$ and $50Hz$. Opposite motors was always used in synchronous mode, so in the following they will be referred in couples as M1-3 and M2-4. Each one of the four directions is equipped with a load

cell ($2kN$) and a position detector. The machine is also equipped with the infra-red video capture system reported in figure 2.4 with trigger synchronized with motor displacement and double light source, one from the bottom of the specimen for crack propagation measurement and one from the top for the acquisition of specimen surface images. The system is provided with a 4 megapixels infra-red camera with integrated trigger connected to the displacement sensor of each engine, that makes it possible to acquire the image of the specimen in a specific position of the displacement cycle. Specimens were connected to the biaxial tester by the clamping system shown in figure 2.5, that is composed of a maximum of 10 individual clamps ($10mm$ wide) for each side, sliding on rails.

Figure 2.2: *The Coesfeld Materialtest biaxial tester used for dynamic characterization and fatigue test.*

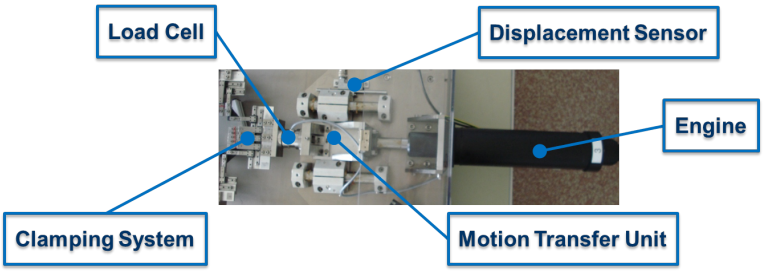

Figure 2.3: *Axis configuration of the Coesfeld Materialtest biaxial tester.*

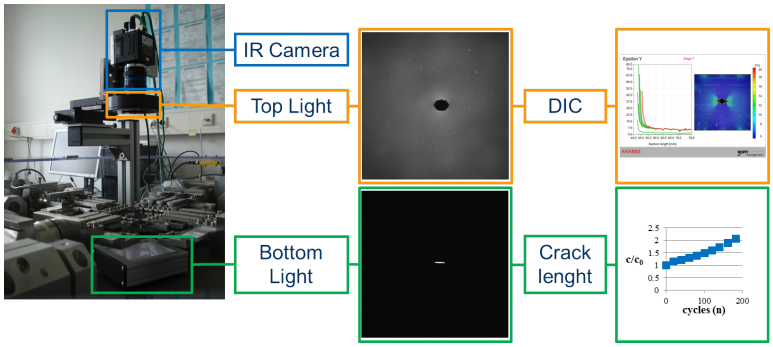

Figure 2.4: *Imaging set-up used on Coesfeld Materialtest biaxial tester.*

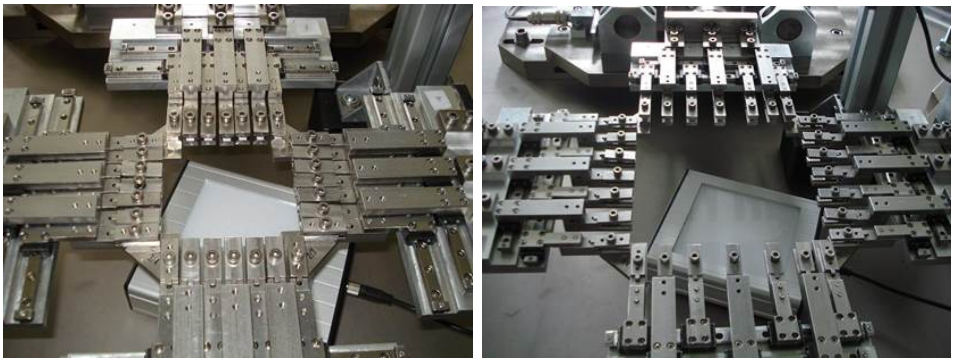

(a) (b)

Figure 2.5: *A detail of the clamping system adopted by Coesfeld. a) closed configuration b) fully extended configuration.*

CLUSTex Biaxial tester (Politecnico of Milan) This biaxial dynamometer was used for characterization and fracture testing in biaxial quasi-static loading conditions and is schematically shown in figure 2.6. The machine was designed for biaxial testing of textiles, and has been adapted to rubber testing by means of a specifically designed clamping system for high strain realized as part of this work (drawings are shown in Appendix A). The machine is equipped with 12 axial motors controlled independently (3 motors for each side), each one has a maximum stroke of $530mm$ and a maximum displacement speed equal to $120mm/min$ (total area covered by the actuators is $1060mm$ on each direction with $240mm/min$ of maximum relative displacement speed), each motor is equipped with a $25kN$ load cell

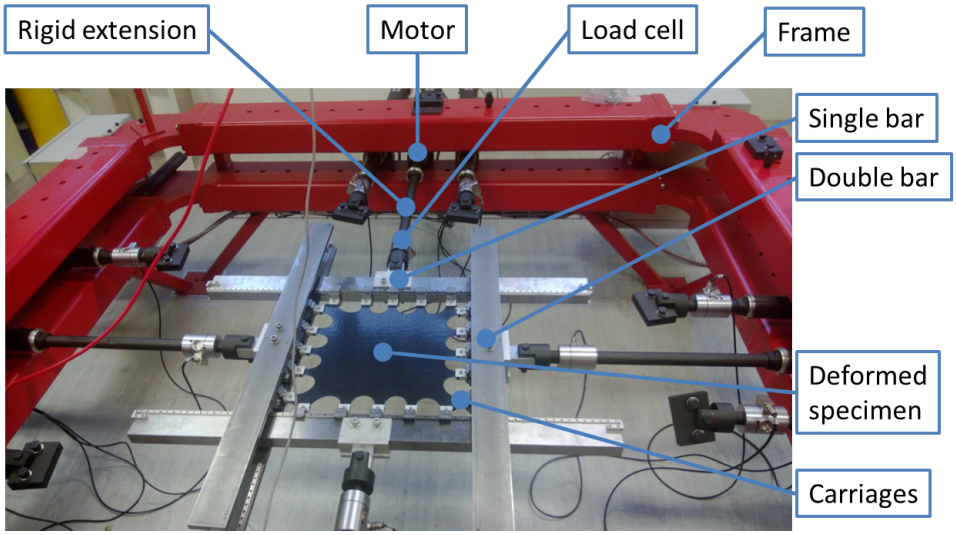

Figure 2.6: *The designed clamping system mounted on the CLUSTex biaxial tester with a specimen stretched in equibiaxial extension.*

and an encoder for displacement measurement. The biaxial machine was equipped with an ad-hoc fixture for the camcorder in order to record the surface of the specimen during the test. Each motor can move along the frame by means of two carriages which slide on linear-guides fixed on the frame. The motor is connected to this sliding system with a pin through which it may also rotate in the loading plane. In our case only one motor on each side was used and the clamping system was fixed on to the four central motors as shown in figure 2.6. The rotation of the motor in the loading plane was locked because this way better results were obtained. The clamping system consists of four bars, two singles ones and two doubles ones to maintain the symmetry with respect to the specimen plane (that is the loading plane). A couple of rails for linear guides are mounted on both side of single bars and in the interior side of double bars. Five clamps for each side are mounted on carts with linear guides that are free to slide on the rails; in this way, similarly to what was seen in the case of the clamping system adopted by Coesfeld, the constraint applied to the specimen in one direction, say x, is free to adapt to the displacement applied in the y direction. The symmetry of the system of carts with respect to the specimen plane ensures that there is no bending moment acting on the linear guides,

condition that ensures maximum smoothness of movement avoiding friction. The clamping system is connected to the four central engines on each side using rigid extensions, with the load cells close to the clamping system. This machine and the clamping system have been available only in the last four months, for this reason experiments are limited and regard mainly material characterization, a few fracture tests was performed too.

2.2 Materials

All the materials used was provided by **Bridgestone Technical Center Europe (TCE)**, with exception of an experimental compound provided by **Technische Universitt (TU) Chemnitz** used for the fatigue crack propagation tests.

Quasi-static testing In order to study the effect of carbon black (CB) content on rubber properties, 4 different compounds of natural rubber (NR) filled with CB type N330 [40] were used in the present research. Details on the formulation of the compounds are reported in Table 2.1. The table reports, in addition to the carbon black content, also the content of *Sulphur* which is the crosslinking agent, *tertButyl2benzothiazole sulfenamide (TBBS)* that is added to the compound as an accelerator of the vulcanization process, *Stearic acid* and *Zinc oxide* which are activators of TBBS [41]. All the ingredients are expressed as *phr* acronym used to indicate the parts by weight per 100 parts of rubber. Materials used was provided in form of not cured sheets. Materials were crosslinked for 15 minutes at 160 ℃ in an electrically heated compression moulding press applying a pressure of $80kg/cm^2$. Dumbbell specimens used for uniaxial tensile test were obtained from a $200x170x3mm$ plate using a cutting die, pure shear and square specimens were instead obtained directly shaped by use of purposely made molds. The compounds density was also measured by immersion method in a solution of ethyl alcohol and distilled water as described in [42], results are shown in Table 2.2.

Table 2.1: *Compounds formulations - Quasi-static testing*

Compound	CB [phr]	CB type	Sulphur [phr]	Stearic acid [phr]	TBBS [phr]	ZnO_2 [phr]
NR0	0	N330	1.3	2	0.8	3
NR25	25	N330	1.3	2	0.8	3
NR50	50	N330	1.3	2	0.8	3
NR75	75	N330	1.3	2	0.8	3

Table 2.2: *Compounds density - Quasi-static testing*

Compound	density $[g/cm^3]$
NR0	0.931
NR25	1.024
NR50	1.102
NR75	1.165

Dynamic testing The materials used in the part of dynamic testing were provided by Bridgestone Technical Center Europe (TCE) in the form of vulcanized plates. All three compounds were filled with the same type and quantity of carbon black, so they differ only in the matrices that are natural rubber (NR), isoprene rubber (IR) and styrene-butadiene rubber (SBR). The main difference between the three matrices is that only NR and IR crystallize when subjected to high strain, and also that IR is supposed to have lower hysteresis. For fatigue crack propagation tests an experimental compound has been used provided by the TU Chemnitz, the composition was unknown. The details of the compounds used are summarized in Table 2.3.

2.3 Test specimens

2.3.1 Quasi-static stress-strain characterization

Dumbbell specimen Dumbbell specimen was adopted for uniaxial tensile test, figure 2.7 reports the geometrical dimension of this type of test

Table 2.3: *Compounds formulations - Dynamic testing*

Compound	Matrix	CB content [phr]	CB type
NR	Natural rubber	50	N550
IR	Isoprene rubber	50	N550
SBR	Styrene-Butadiene copolymer	50	N550
Ch compound	experimental unknown composition		

piece as prescribed by ASTM D638 type B-IV.

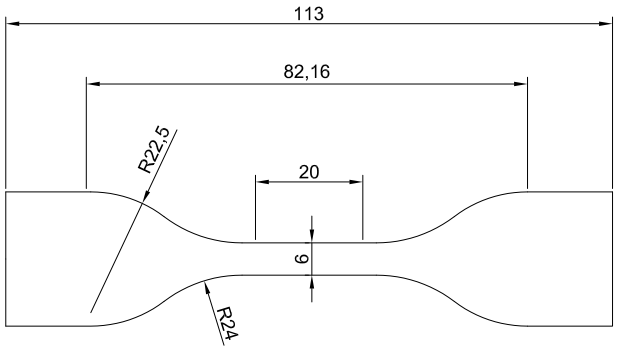

Figure 2.7: *Geometry and dimensions of the Dumbbell specimen used for uniaxial tensile test as prescribed by ASTM D638 type B-IV. Dimensions in millimeters.*

Pure Shear specimen In order to obtain the PS deformation state (see section 1.3.2) in a laboratory test wide strips clamped along the long side and deformed parallel to the short side are generally used, as first suggested by Treloar [22]. An example of this kind of specimen is reported in figure 2.8, in which the width of the strip is denoted by W and the gauge length by h_0.

The dimensions of the pure shear specimen used in this work are shown in figure 2.9(a), section 3.2.1 reports preliminary tests that led to the choice of this particular geometry. Specimens were obtained using a purposely made mold, the long sides of the strips have a square section with increased

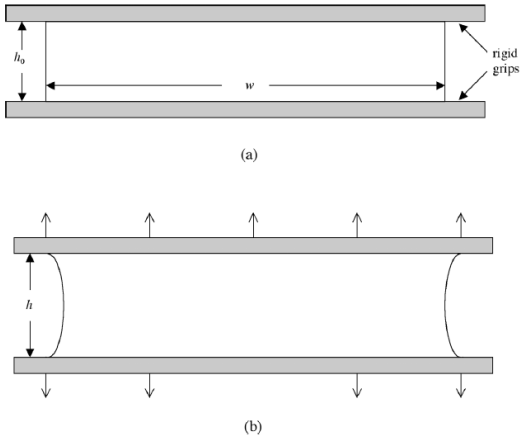

Figure 2.8: *Sketch of a pure shear test piece. a) undeformed; b) deformed. (image from [43]).*

thickness ($5mm$) compared to that of the specimen ($1mm$). The square section is used to clamp the specimen by means of a special hand-made aluminium clamp. This solution, schematically reported in figure 2.9(b) and referred as **interference clamping** in the following, has allowed to avoid problems related to clamping rubber specimens with pneumatic clamps (that works with friction), such as the outflow of the specimen due to the pressure, the increasing of the gauge length during the test and the failure of the specimen near to the clamps. This same solution was adopted for specimens clamping for biaxial tests both in quasi-static and dynamic loading when possible.

Square specimen The square specimen shown in figure 2.10 was designed in combination with the clamping system adopted for rubber testing with the CLUSTex biaxial tester. On the four outer edges there is a larger thickness used for mounting the specimen onto the test machine similarly to that seen for the pure shear specimen. The presence of thick edges, however, change the cross-section of the specimen and contribute to the boundary forces. To overcome this problem 5 separate mounting positions have been created for each side of the specimen, corresponding to the five clamps on each side of the clamping system, by cutting the thick edge and piercing the specimen at the end of each cut to reduce the stress concentration. This

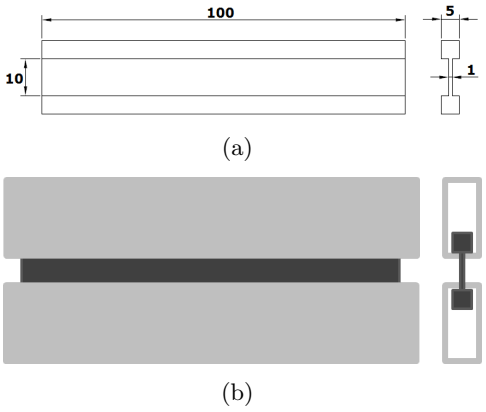

Figure 2.9: *a) Geometry and dimensions of the PS specimen; b) Aluminium clamp for PS specimen. Dimension in millimeters.*

solution has been adopted by several authors in the case of biaxial tensile tests [26, 44]. Preliminary tests performed in order to define the geometry will be described in section 3.3.1.

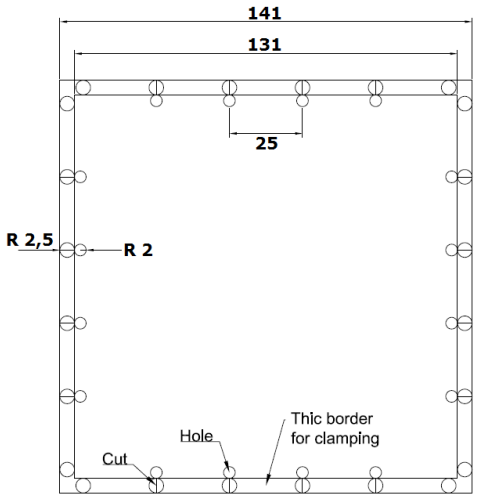

Figure 2.10: *Geometry and dimensions of the square specimen used for biaxial tensile test. Dimensions in millimeters.*

2.3.2 Dynamic stress-strain characterization.

For uniaxial tensile test from the vulcanized plates $2mm$ thick rectangular specimens $100x15mm$ were cut. A gauge length of $85mm$ was used. Pure shear and equibiaxial tests were performed on $100x100mm$ square specimens cut out from the plates, the unclamped specimen is then $85x85mm$. One clamp for each side was used to connect the strip and 7 clamps for side to connect the square specimen.

2.3.3 Fracture characterization

Pure shear Following the considerations of section 2.5.1 it was decided to use a pure shear specimen for fracture test with the same dimensions shown in figure 2.9(a) ($W/h_0 = 10$), introducing an edge crack of $15mm$, which corresponds to 1.5 times h_0. The specimen is shown in figure 2.11.

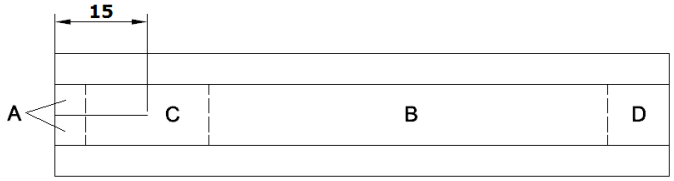

Figure 2.11: *PS fracture specimen with edge crack of* $15mm$*. A) unloaded material; C) stress field determined by the presence of the crack; B) uniform pure shear strain; D) stress field determined by specimen boundary.*

Biaxial The corners of the square specimen shown in figure 2.10 were removed to obtain the shape shown in figure 2.12. A $16mm$ central notch has been introduced using a sharp razor blade. The effect of the original notch length was also investigated, and the results will be shown in section 4.2.1.

2.4 Stress-strain characterization methods

2.4.1 Quasi-static monotonic stress-strain

For materials characterization in quasi-static loading conditions tests were carried out in simple tension, constrained tension (pure shear), biaxial (B05)

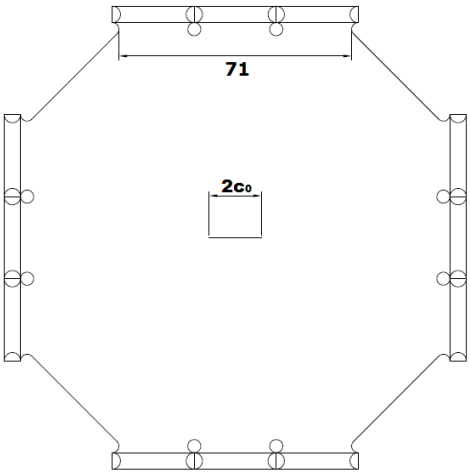

Figure 2.12: *The square specimen without corners with a 2a central crack used for fracture tests in biaxial loading. Measures in millimeters.*

and equibiaxial tension.

Data obtained from stress-strain characterization in different loading conditions were fitted together with a 3^{rd} order Ogden model (1.40), using a minimization technique of the objective function based on genetic algorithms [45] for parameters generation, implemented into a custom Python code built around the solvers provided by [46]. The objective function was defined as:

$$S_F(p) = \|F(\lambda, p) - \tau\|_2^2 = \sum_{j=1}^{n} \sum_{i=1}^{m} [F_j(\lambda_i, p) - \tau_i]^2 \tag{2.1}$$

where

- $S_F(p)$ is the objective function;
- p is the model parameters vector;
- $F(\lambda, p)$ is the model predicted stress values for a given set of draw ratios λ and parameters p;
- τ is the measured stress values corresponding to λ;
- i is the sum index that runs over all the experimental values considered;

- j is the sum index that runs over all the loading conditions considered.

The problem of parameters identification with respect to the objective function as formulated in equation (2.1) reduces to:

$$\min_{p} S_F(p) \tag{2.2}$$

Some boundaries to the parameters values were also given to the minimization procedure, such as:

- $|\alpha_i| > 1$ for thermodynamic consistency;

- $\mu_i \alpha_i > 0$ for physically realistic response and material stability.

These are sufficient conditions for strain energy density to be a polyconvex function[1] [47]. The biggest problem in the determination of the parameters of the constitutive model is that the equation (2.1) admits multiple minima in the parameter space. The identification of the absolute minimum is impossible in practice and the set of parameters obtained from (2.2) depends on the initial population, i.e. a set of randomly generated points in the parameter space used to start the optimization algorithm. The genetic algorithm here used woks iteratively by spawning new populations obtained combining the components of those points that gives lower values of the objective function in each minimization step. In the presence of multiple minima also a set of material parameters which gives a good fit does not guarantee a correct representation of the mechanical behaviour of the material in a stress state different from that used to obtain the parameters, this is why the need to obtain the material parameters by the minimization of multiple sets of experimental data obtained from as more loading conditions as possible.

Material parameters identification and finite element simulations were performed by Eng. Francesco Caimmi.

[1] The notion of polyconvexity is a generalization of the notion of convexity for functions defined on spaces of matrices.

2.4.2 Quasi-static loading-unloading stress-strain

Additional tests were carried out in pure shear and equibiaxial loading-unloading conditions in order to study how the behaviour of the material during monotonic tensile test is approximated by a purely hyperelastic behaviour. Tests were performed on specimens with same geometry used for monotonic stress-strain characterization. Specimens were cyclically deformed up to progressively higher strain levels and then unloaded in order to record the unloading stress-strain behaviour that was considered as elastic. The absorbed energy was obtained integrating the monotonic stress-strain response of the material, the elastically stored energy was indeed obtained integrating the unloading stress-strain curve linearly interpolated up to conjunction with the monotonic curve where necessary. The dissipated energy was considered as the difference between total absorbed energy and the elastically stored energy.

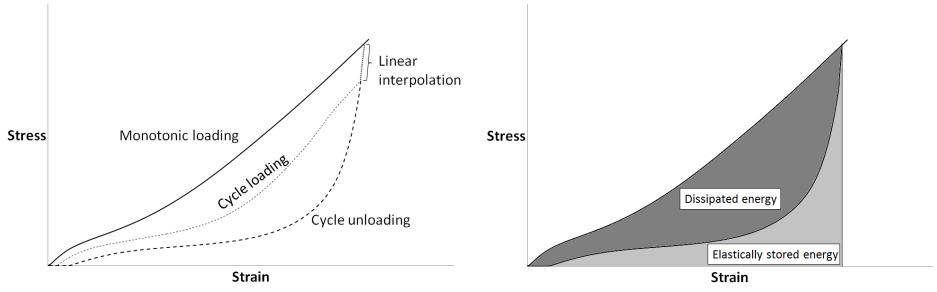

(a) (b)

Figure 2.13: *a)Comparison between a loading-unloading cycle and monotonic loading, unloading curves must be linearly interpolated up to conjunction with monnotonic stress-strain because of cyclic softening of the material; b) Elastically stored and dissipated energy components, total absorbed energy is equal to the sum of the two.*

Elastically stored and dissipated energy components will be reported in chapter 3 for each level of maximum strain tested both as absolute value and as a percentage of the total energy absorbed.

2.4.3 Dynamic stress-strain

Two different approaches was adopted for stress-strain characterization in dynamic loading conditions. For materials provided by Bridgestone TCE (that was not used for fatigue crack propagation tests) only uniaxial, pure shear and equibiaxial loading configuration were tested. Energy components was evaluated from the hysteresis cycle and materials compared on the basis of both stress-strain behaviour and energy dissipation in different loading conditions. For Ch compound, that was used for fatigue tests in biaxial dynamic loading conditions, a more complete characterization of the stress strain behaviour was adopted. 32 biaxial loading configurations were tested in order to obtain as more information as possible regarding the relation between the elastically stored energy and the applied biaxial strain. Obtained data was fitted with a Gent model (1.49) with a minimization method such that described in equation (2.2), but using directly elastic energy instead of stress for the objective function.

The total absorbed (W_t), elastically stored (W_e) and dissipated energies (W_d) were evaluated by integrating the stress-strain curve of each cycle in the positive side of the stress axis (residual strain and consequent compression/bending effects were neglected). In figure 2.14 it is shown a schematic representation of those quantities. Showing results different colours will be associated to energies: W_t will be associated to black, W_e to green and W_d to red.

The total energy density absorbed by the unitary volume of the material during a cycle of biaxial deformation can be calculated using the integral of the stress-strain curves recorded in the two loading directions x and y according to the formula:

$$W_t(\bar{\varepsilon}) = \int_{\varepsilon_{xrl}}^{\varepsilon_{xmax}} \sigma_{xl} d\varepsilon_{xl} + \int_{\varepsilon_{yrl}}^{\varepsilon_{ymax}} \sigma_{yl} d\varepsilon_{yl} \tag{2.3}$$

where ε_{irl} indicates the residual strain relative to the loading curve as shown in figure 2.14.

The elastically stored component of the absorbed energy density can be calculated integrating the unloading stress-strain curves in both x and y

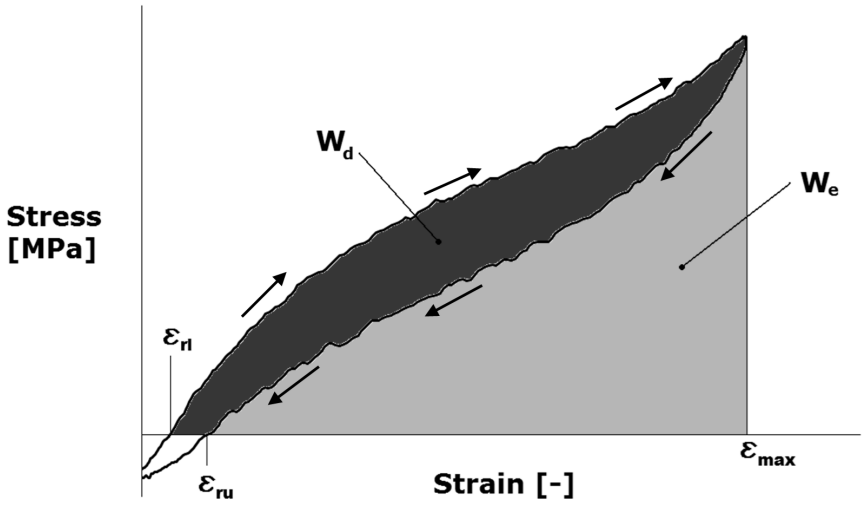

Figure 2.14: *Elastically stored W_e and dissipated W_d energies in a stress-strain cycle. ε_{rl} and ε_{ru} are the residual strains at loading and unloading respectively.*

directions as follows:

$$W_e(\bar{\varepsilon}) = \int_{\varepsilon_{xru}}^{\varepsilon_{xmax}} \sigma_{xu} d\varepsilon_{xu} + \int_{\varepsilon_{yru}}^{\varepsilon_{ymax}} \sigma_{yu} d\varepsilon_{yu} \tag{2.4}$$

where ε_{iru} indicates the residual strain relative to the unloading curve.

The dissipated energy by unitary volume, that is the area inside the hysteresis cycle can be expressed as:

$$W_d(\bar{\varepsilon}) = W_t(\bar{\varepsilon}) - W_e(\bar{\varepsilon}) \tag{2.5}$$

In order to estimate the elasticity of the compound as a function of strain level and loading condition a percentage value of W_e and W_d with respect to W_t was evaluated as:

$$W_{e/d}\% = \frac{W_{e/d}}{W_t} \tag{2.6}$$

2.5 Fracture characterization methods

2.5.1 Quasi-static pure shear loading

The pure shear specimen is well-recognized in literature as one of the best specimens for rubber fracture testing because of the simplicity in the calculation of fracture energy release rate. The specimen reported in figure 2.11 can be divided into four regions: region A which is undeformed, region C which includes the crack tip and results to be in a complicated stress state, region B which is under uniform pure shear stress and region D where boundary determines the stress state. When crack propagates regions C and D does not change size, while B region becomes shorter and A region larger. Rivlin and Thomas in [48] showed that for a pure shear specimen in which the latter geometric conditions are satisfied the tearing energy T (that is a generalization to rubber fracture of the energy release rate G defined by Irwin [49] on the basis of the Griffith energy balance [50]) resulting from an increase of the crack length δc does not depend on the current size of the defect, and can be calculated as:

$$T = W_{PS} * h_0 \tag{2.7}$$

In which W_{PS} is the energy stored in the B-zone at the instant of tearing onset and h_0 is the gauge length in the undeformed configuration. Equation 2.7 is actually valid only if the crack propagates transforming a volume homogeneously deformed in pure shear in an equivalent unloaded volume, i.e. if B-zone and A-zone are actually present. Yeoh [51] has studied the problem of the minimum length of the defect c_0 required for this condition to be verified in the case of edge and central cracks, concluding that the minimum size of the edge crack shall be not less than the size of the gauge length h_0. Both in the case of edge and central cracks the author emphasizes the dependence of T from the crack length for short defects.

Fracture tests in quasi-static pure shear loading conditions were performed on compounds reported in table 2.1 using the specimen reported in figure 2.11, with a crosshead displacement rate of $50mm/min$. The critical tearing energy was evaluated by equation (2.7) at the crack onset using

both the total absorbed energy W_t and the elastically stored energy W_e determined by loading-unloading tests. Each test was video recorded with a 10 megapixels CCD with a frame rate of $3 frame/s$ and a resolution of $82.5 pixels/mm$, the crack onset was visually determined from the video and the strain in the uniform B-zone was obtained by optical strain measure using digital image correlation (section 2.6).

2.5.2 Quasi-static biaxial loading

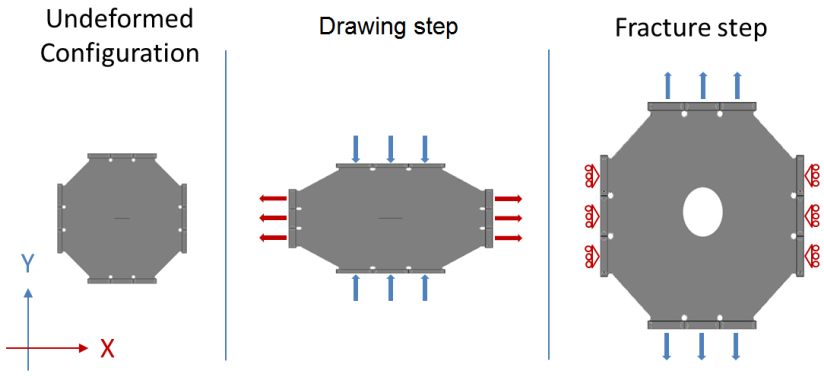

Figure 2.15: *Schematic representation of the fracture test in biaxial loading conditions.*

Fracture tests in quasi-static biaxial loading conditions were performed on compounds reported in table 2.1 using the specimen reported in figure 2.12, with a crosshead relative displacement rate of $60 mm/min$ in both directions. The biaxial fracture tests performed in this work consist of two distinct stages as reported in figure 2.15. In the first stage, the **drawing step**, the specimen was deformed up to a certain draw ratio λ_x in a direction parallel to the notch, named x-direction, unloading the force generated due to Piosson effect in the direction perpendicular to the notch, named y-direction. In the second stage, the **fracture step**, the specimen was elongated in the direction perpendicular to the notch until the fracture occurs, with fixed displacement in the direction parallel to the notch. In order to unload the specimen during the drawing step it was necessary to

adopt a configuration of the clamping system described in section 2.1.2 with 3 carriages on each side by suitably modifying the square specimen used for the stress-strain characterization. Pristine specimens were extended up to different levels of draw ratio λ_x during the drawing step, and the critical tearing energy at crack onset was evaluated using finite element simulations (section 2.7). Tests were video recorded with a 10 mega-pixels CCD with a frame rate of $1 frame/s$ and a resolution of $34 pixels/mm$, the crack onset was visually determined from the video. Strain field was also measured by means of digital image correlation (section 2.6).

2.5.3 Dynamic biaxial loading

The applied tearing energy T in dynamic biaxial loading conditions was evaluated by a new digital image correlation-based technique described in section 5.4.2.2.

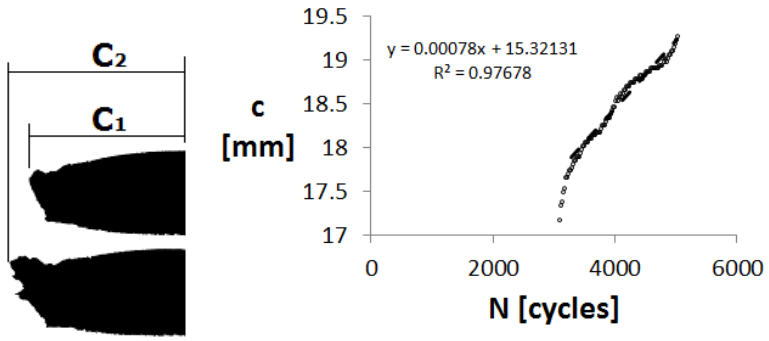

(a) (b)

Figure 2.16: *Measurement of crack growth rate as a function of the cycle number. a) crack length identified by the overall dimension of the defect; b) linear interpolation of the crack size with respect to the cycle number.*

Crack Growth measurement in dynamic loading conditions As mentioned in section 2.1.2, using the video capture system supplied with the dynamic biaxial tester it was possible to capture the crack image using the bottom light. Crack length images were recorded at 10% of the displacement cycle to have the crack open, but still very close to the undeformed length.

In order to determine the crack growth rate dc/dn, images of the crack length was collected every 20 cycles during the fatigue test. As shown in figure 2.16(a) crack size measurement was determined by the overall size of the defect, the crack growth rate has been obtained by linear interpolation the crack size data obtained as a function of the number of cycles in the region of constant propagation rate (figure 2.16(b)).

2.6 Digital Image Correlation (DIC)

The **digital image correlation** (DIC) is the application in the field of mechanical testing of optical motion tracking, and allows to measure the full-field of deformation. DIC is increasingly used in various fields of scientific research in order to measure the deformation of an object subjected to loads in place of the usual contact techniques (such as strain gauges and extensometers). DIC is an optical measuring system of the deformation field and therefore requires that the specimen is photographed during the deformation process, the portion of the specimen of which strain measures are desired must remain within the image and in focus during for the whole duration of the test and takes the name of **area of interest** or **AOI**. The measurement system is based on the determination of the displacement field of the external surface of an object by means of the subdivision of the AOI in distinguishable subimages (i.e., a square region) defined **subsets** or **facets**. The spacing between subimages is said **step**, and defines the measurement grid density. The specimen is photographed (or video-recorded) both before and during the process of deformation, the image of the undeformed specimen is used as a reference for the analysis of movements and takes the name of **reference image**, as schematically shown in figure 2.17 the displacement field is then determined by a comparison process called "correlation" between the reference image and the deformed images. The analytical details of the correlation process can be found in [52].

In this research two different software for digital images correlation were used, **Vic-2D** (Correlated Solutions, inc.) for quasi static test in Milan and **Aramis** (gom mbh, Optical Measuring Techniques) for dynamic test in Dresden.

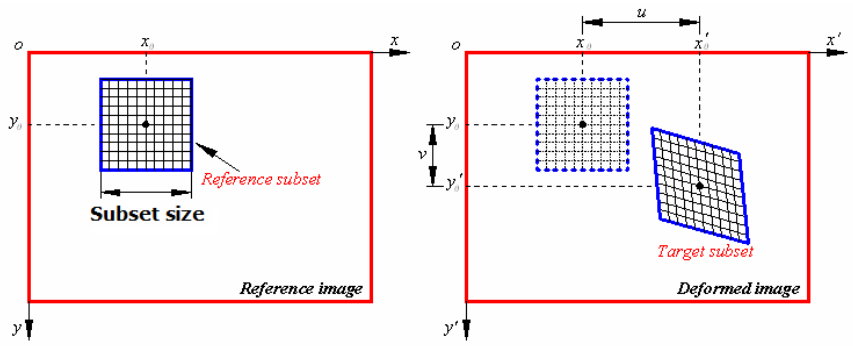

Figure 2.17: *Schematic representation of a single subset displacement from reference to deformed configuration. (Image adapted from [53])*

2.6.1 Specimen patterning

With the DIC technique, the full-field deformation of a planar specimen surface can be obtained through processing the greyscale digital images of the specimen surface captured before and after deformation. In order that the subset can be identified on the reference image and the deformed images they must contain sufficient content of "information". In the case of a digital image, information is determined by the distribution of the gray scale; in other words, each subset must have inside something that makes it unique and optically distinguishable from the other subsets. This result is obtained by drawing on the surface of the specimen regular geometries or random distributions of spots, the latter solution is the most used because of its simplicity in preparing the specimens by means of spray painting. The amount of speckles that can be deposited per unit area depends on the technique used for the application of the pattern, and strongly affects the spacing of the deformation measurements as is reflected directly on the minimum size of the subset that can be used. According to the resolution of the optical system used it is possible to say that the more the surface is structured the greater the density of the measures. In [52] it is suggested to use an optical system resolution that it allows having 3x3 pixels in each speckle and not less than 3x3 speckles within each subset. An example of specimens surface painted with different spots density is reported in figure 2.18. Pan [53] reports a detailed study on the accuracy of the displacements

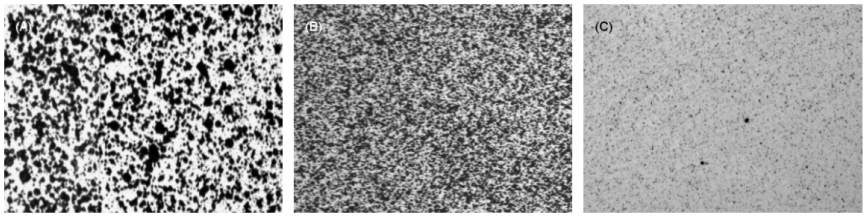

Figure 2.18: *Three different speckles pattern densities, undeformed images. (Image from [53])*

measured with the DIC technique as a function of the subset size chosen for a particular pattern, he also highlights how the measurement accuracy can be increased by using high bit-depth (12 or 16-bit) CCD camera, increasing the contrast of the speckle patterns or decreasing the image noise.

In the course of this research, great attention has been given to the determination of the best paints to be used on rubber, both in terms of adhesion of the pattern to specimen surface and in terms of color and dilution to improve contrast and spraying. Also the pattern application technique was thoroughly tested obtaining patterns with a commercial sprayer, paint gun and airbrush. In the end the choice fell on a water-based metal grey paint diluted 50% and applied with the airbrush, a combination that led to the best outcomes in terms of feature patterns and density of speckles for our application. Concerning the use of the dual action airbrush (air and paint flow controlled separately) it was possible to determine that the size of the speckles applied is directly proportional to the paint flow and inversely proportional to the air flow, allowing to obtain patterns with different structure for the different test conditions according to the density of measurements required. The spray does not allow such an adjustment, while the paint gun works on a range of higher speckle size, making it more suitable for applications on large objects rather than for relatively small test specimens.

2.6.2 Subset step and overlap

Once the correct size of the subset was determined by the pattern used the relative spacing between subsets must be chosen (subset step). Subset step is typically less than subset size, for this reason the subset are to some extent

overlapping. The degree of overlap that can be used again depends on how the surface is structured, as the non-overlapping part of two adjacent subset must contain sufficient features to make them distinguishable. The patterns used in this research are very structured and allow getting reliable correlations using overlapping up to 80%. The step size controls the spacing of the points that are analysed during correlation and thus the density of measuring points of the strain field obtained, obviously at expense of computation time.

2.6.3 Incremental correlation

If the displacements recorded between the deformed and the reference image are large (as is generally the case for elastomers) the correlation often does not reach the convergence and the measurement is impossible. In this case it is necessary to perform an incremental correlation, determining the displacement of each subset with respect to its position in the previous image (i.e. using each image as a reference for the next one) and rebuilding the displacement fields at the end of the analysis. The incremental correlation is a built-in option in Vic2D and Aramis.

2.6.4 Literature survey on application of DIC on rubbers

There are many examples of application of DIC for rubber mechanical testing in literature. Regarding the constitutive model parameters Chevalier [4] uses data obtained from the displacement and deformation fields of rubber in uniaxial and biaxial tensile test as a comparison with the corresponding fields coming from finite element simulations in order to check the material parameters obtained with direct methods of minimization, the author also uses measurements of the deformation field as the basis for calculating the stress field in conjunction with the identified constitutive law. As already mentioned in section 1.6 Toussaint [27] adopt a different approach to rubber stress-strain characterization that implies DIC technique for the determination of the strain full-field on a particular three-branch specimen.

At the moment there are few studies in the literature concerning the application of digital image correlation to rubber fracture mechanics and

about the measurement of the deformation field in the neighbourhood of the crack tip. Fichter [54] investigated the influence of the initial crack tip radius on the strain distribution in the vicinity of the blunted crack tip, and compares these experimental results with the calculations made with the commercial finite element code ABAQUS 6.4-1. He affirms that the optical full-field strain analysis method based on the image correlation technique is an effective tool to determine strains, strain distributions and gradients near the crack tip for elastomeric materials and that the strain gradient can be considered as the driving force for crack growth initiation. The observations also indicate the importance of the crack tip blunting process for good tear strength. Creton [55] in 2011 has used the digital image correlation to determine the strain field in the vicinity of the crack tip on pure shear specimens in dynamic loading conditions. Using high-resolutions images ($\approx 1.6\mu m/pixel$) in combination with pattern obtained by talc powder deposition (average particle size $10\mu m$) observed the presence of a highly oriented zone in the vicinity of the crack tip. Author also proposed a way to calculate a local energy release rate from the highly oriented zone size H_0 as:

$$g_{local} = W_{unloading} H_0$$

where $W_{unloading}$ is the elastically stored energy in uniaxial extension at the maximum strain measured near to the crack tip. Measurements were performed on three SBR compounds differing in carbon black and sulphur content. Surprisingly all the three tested compounds showed the same crack propagation rate as a function of this new parameter, regardless of the amount of filler and Sulphur, while the crack growth rate for the same compounds differs by two orders of magnitude as a function of the macroscopic energy release rate G. The author concludes that rubber toughness depends on the amount of energy needed to form this highly oriented zone near to the crack tip.

2.7 Finite element simulations

The finite element method was used to calculate the tearing energy applied during the fracture tests in quasi-static biaxial loading conditions. Rubber mechanical behaviour was described with a 3^{rd} order Ogden's hyperelastic model with material parameters determined as described in section 2.4.1. ABAQUS FE code (Dassault Systèmes, 2010) was used to perform simulations.

A first attempt was to simulate the fracture test of the whole specimen by imposing the experimental boundary displacements both in x and y directions. For these simulations a 2D plane stress model of the biaxial specimen was used. The clamps were modelled as rigid lines tied to the ends of the specimen. Comparing the force-displacement curves obtained experimentally in both loading directions with those calculated with FEM, as reported in figure 2.19, a stiff response of the simulation was observed. Whether this is due to a problem with finite element model, which could be unable to completely reproduce the complex boundary conditions (see section 2.5.2) or to the identified material parameters is still unclear.

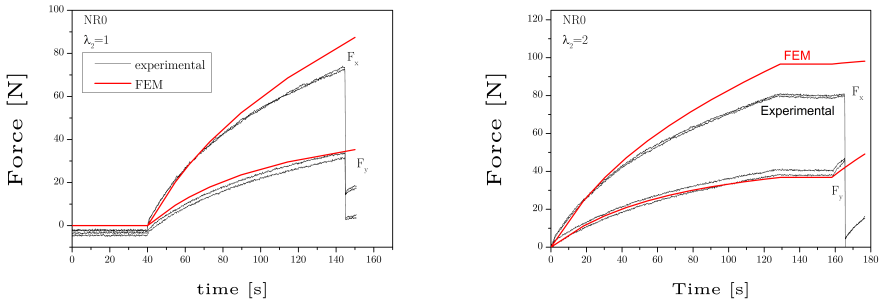

Figure 2.19: *Force-displacement curves comparison between experimental measures and FEM prediction for biaxial fracture tests on natural rubber under two different levels of draw ratio λ_x imposed during the drawing step.*

In order to eliminate any problems of the FE model related to the boundary conditions of the complete specimen it was decided to perform the simulations using a submodel of the central zone of the specimen containing the

crack, shown in figure 2.20(a). Displacements were imposed to the submodel boundaries by the digital image correlation measures of the corresponding point on the real specimen. The model used plane stress quadratic elements with reduced integration away from the crack tip, and fully integrated near the crack tip, for a total of about 27000 degrees of freedom. Figure 2.20(b) reports a comparison between of the experimental vertical displacement field obtained from digital image correlation and the FEM prediction; the black line indicates the submodel boundary; only one half of the FE model is shown to allow comparing the predicted and the measured displacement fields. Inside the black solid line the vertical displacement field obtained with FEM is shown, while outside the displacement field as measured by DIC is plotted. Judging from the contours and the crack shape, the simulated FEM response looks still more stiff than the actual one, but the displacement field seems to be close enough to real measure. This residual difference can be entirely ascribed to the material parameters, that must be determined with more precise material stress-strain characterization and optimizing the minimization procedure. In order to check the results obtained by the submodel simulation of each test it was decided to use the dimensions of the elliptic deformed crack at the fracture onset as a comparison parameter.

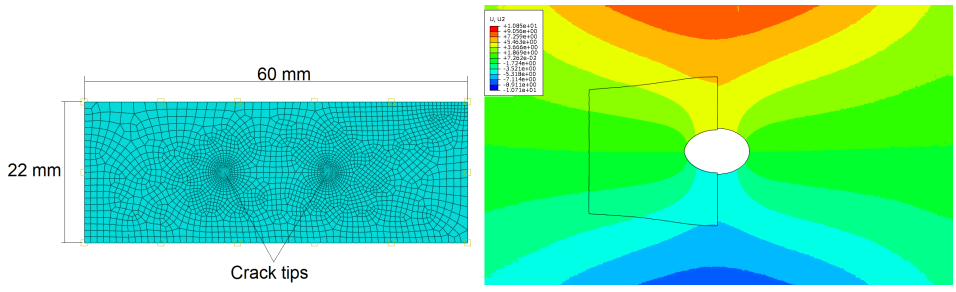

Figure 2.20: *a) Submodel used for finite element simulations of the fracture test in biaxial loading conditions; b) Comparison between the experimental and FEM vertical displacement fields, the black line represents the half-submodel boundary. Inside the boundary the displacement field obtained from FEM is plotted, while outside the experimental field is shown.*

Chapter 3

Stress-strain characterization in quasi static loading conditions

3.1 Uniaxial loading

For simple tension test on the compounds described in table 2.1 the Dumbbell specimen presented in section 2.3.1 was used, tests were performed on the Hounsfield uniaxial dynamometer presented in section 2.1.1 with a displacement rate of $60mm/min$. A pattern of speckles for strain measuring by DIC was printed on the specimen surface. For image acquisition we used a $10Mega-pixel$ CCD with zoom lens (the scale factor $40pixels/mm$). The engineering stress has been calculated in accordance with equation (1.6) using force measured by the load cell and the undeformed area measured before the test, the longitudinal engineering strain was obtained by DIC.

First a check on the reliability of optical strain measurements carried out by the digital image correlation technique was performed. The specimens were prepared printing two dots on the gauge length with speckles pattern for DIC measurements in between of them as shown in figure 3.1(a). Three different strain measurements were made out in the gauge length of the specimen: one using a mechanical extensometer, one by video recording and tracking the position of dots printed on the specimen surface and one using

the DIC technique. For mechanical and video recording measures engineering strain was directly evaluated using equation (1.7), for DIC measure the true strain was first obtained and then engineering stain evaluated in accordance with equation (1.16). Results are shown in figure 3.1(b): it is clear that the three measuring techniques results to be equivalent. It was therefore decided to measure strains by DIC, that compared to the other two techniques allows measuring also the transverse strain.

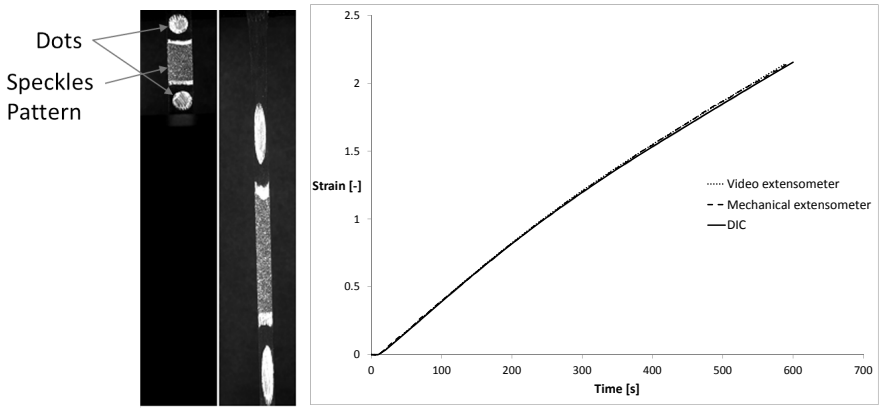

(a) (b)

Figure 3.1: *a) Dots and speckles pattern used for optical strain measures (left - reference image, right - deformed image); b) Longitudinal strain versus time for mechanical and optical strain measures.*

3.1.1 Uniaxial stress-strain behaviour

The stress-strain curves thus obtained are shown in figure 3.2(a). As well known it can be seen the reinforcement effect of CB on natural rubber and the decreasing of elongation at break with increasing CB content. The carbon black has a strengthening effect on the natural rubber, it in fact creates physical links with the rubber acting as a physical cross link, reducing the molecular weight between junctions and so increasing the rubber propensity to physical phenomena such as chains finite extensibility and the strain induced crystallization which leads to the strain hardening. In order to evaluate the strain level at which the upturn of the stress strain curve occur, it was decided use the deviation of the observed behaviour from the

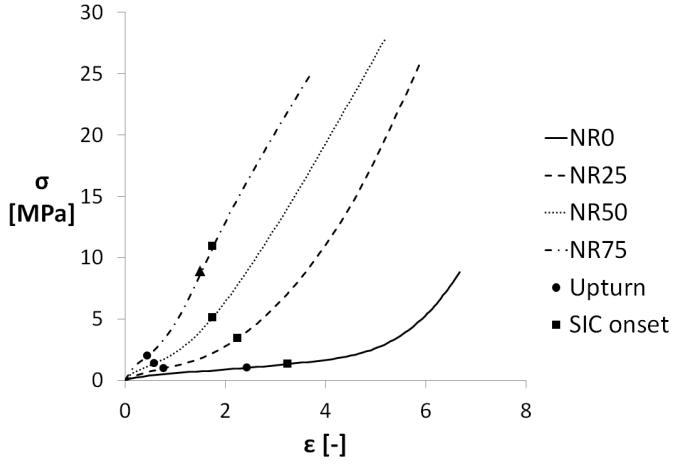

(a)

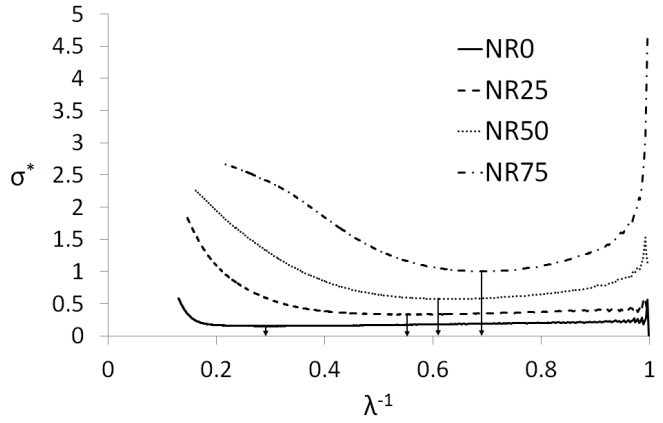

(b)

Figure 3.2: *Simple extension - a) engineering stress σ as a function of longitudinal engineering strain ε; b) reduced stress σ^* (equation (3.2)) as a function of $1/\lambda$*

Mooney-Rivlin model reported in equation (1.47). The relationship between stress and draw ratio predicted by the above model can be easily obtained from the hyperelastic strain energy by partial derivation, for simple tension with $i = j = 1$ it reduces to:

$$\sigma_U = 2\left(C_1 + \frac{C_2}{\lambda_U}\right)\left(\lambda_U - \frac{1}{\lambda_U^2}\right) \tag{3.1}$$

Rearranging equation (3.1) as:

$$\frac{\sigma_U}{2\left(\lambda_U - \frac{1}{\lambda_U^2}\right)} = \sigma^* = C_1 + \frac{C_2}{\lambda_U} \tag{3.2}$$

It is possible to find a linear relation between σ^* and $1/\lambda_U$, in which C_2 is the slope and C_1 the y-intercept. The reduced stress σ^* was evaluated from experimental data and plotted as a function of $1/\lambda$, the resulting curves are reported in figure 3.2(b). NR0 shows the expected linear behaviour up to $1/\lambda_U = 0.3$, above this value a strong deviation was observed. The corresponding strain value was considered to be the upturn onset. Similar behaviour was observed for NR25, although the upturn occurs at lower strain value. NR50 and NR75 show some different behaviour. At small strain a first strong drop was observed that was addressed to the brake-up of the filler network (Payne effect) that is known to form only above a certain filler content due to the filler particles distance and shape [56], above the initial drop a linear regime was observed only for NR50 but not for NR75, for the latter the minimum of the curve was considered as the upturn point. A last remark must be done on the NR75 behaviour; it was the only one compound that shows an inflection point above the upturn. This point, reported with a full triangle in figure 3.2(a), seems to suggest that this compound experience some bulk damage when the chains reach the maximum extension. The upturn point obtained was reported for all the compounds on the stress strain curve in figure 3.2(a), together with the strain induced crystallization (SIC) onset obtained by X-ray diffraction experiments carried out on the same compounds in a previous work [37, 38, 57]. It can be observed that the upturn occurs at lower strain with respect to the SIC onset for all the compounds examined.

3.1.2 Poisson ratio

Using the digital image correlation the transverse strain of the specimen during the simple tension test can be also measured, by which it is possible to calculate a Poisson ratio as it has been defined in equation (1.21). Results are summarized in figure 3.3. At least in the range of measure uncertainty all

the compounds tested showed behaviour in agreement with equation (1.22) that was derivate in the hypothesis of constant volume deformation, with exception for NR75 which showed a slight expansion starting from 200% of applied longitudinal strain. It is agreement with the considerations previously done about the possibility of a bulk damage for this compound when subjected to high strains, in fact even if the onset of volume expansion is found to be above the inflection point of the stress strain curve the difference can be reasonably addressed to the higher sensitivity of the measure on a modulus drop rather than on a volume change measured by the Poisson ratio.

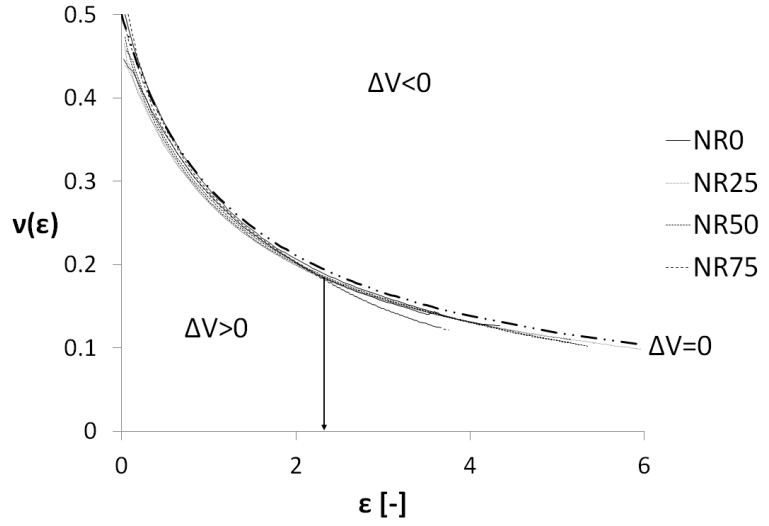

Figure 3.3: *Poisson ratio ν versus longitudinal strain ε during uniaxial extension for natural rubber filled with carbon black.*

3.2 Pure Shear loading

3.2.1 Specimen geometry optimization

The pure shear specimen becomes as more close to the ideal strain state as higher is the ratio between width, w, and height, h_0, what is the correct ratio to be used to obtain reliable results is a topic widely discussed in literature, although the recommended value is always between 8 to 15.

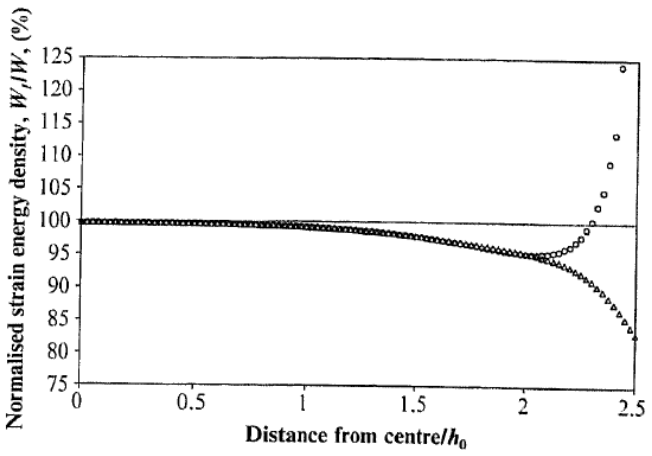

Figure 3.4: *Dependence of the strain energy on the distance from the center of a PS specimen subjected to* 100% *strain (◯ along clamps; △ along center) (image from [51]).*

Treloar in [22] focused attention on the non-ideality of the state of PS deformation for the type of specimen described in section 2.3.1, emphasizing how the material close to the free edges of the specimen is in fact free to contract. Despite having proposed a ingenious technique for correcting the experimental results from edge effects by performing two tests on strips of different width and then subtracting the force of the shorter from that of the wider before calculating the stress, the author concluded that the edge effect on the tensile load was within the experimental error.

Yeoh in [51] also highlights the complex strain field near to the free edge quantifying the size of the perturbed volume of material by using finite elements simulation on pure shear specimens with w/h_0 ratio equal to 5, considering the material behaviour as incompressible Neo-Hookean hyperelastic solid. The main result is reported in figure 3.4, in which the normalized strain energy density was obtained dividing the local value of the strain energy density W by the theoretical strain energy density for an incompressible Neo-Hookean material subjected to the same pure shear strain and the distance from the specimen center along the mid plane and along clamps was normalized with respect to the specimen undeformed height h_0. It can be observed the normalized energy density decreases from the center

towards the free edge of the specimen, which is free to contract and therefore is subject to simple tension. The author also highlights how the perturbed zone change size slightly with increasing applied strain varying between 1,5 and 2 times h_0.

Since no definite conclusion about the correct w/h_0 ratio is well-established a series of tests were performed on strips with various w/h_0 using the digital image correlation to measure the transverse strain, the results are reported in figure 3.5. The transverse strain ε_x is shown as a function of the edge-to-edge distance in percentage of the width w, setting a threshold limit for the transverse strain to -5% is was possible to evaluate volume percentage of the specimen, that can be considered to be under pure shear strain. Results are summarized in table 3.1. It can be observed that the transverse strain

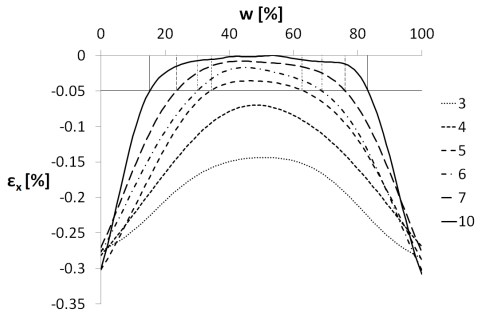

Figure 3.5: *Transverse strain ε_x as a function of the edge-to-edge distance in percentage of the strip width w for different w/h_0 ratios, (*100% *applied strain).*

Table 3.1: *Percentage volume in pure shear strain for speciments with different w/h_0 ratios.*

w/h_0	Volume percentage
3	0
4	0
5	28
6	38
7	52
10	67

obtained in all the specimen in correspondence of the free edge was equal

to -28%, that is the value of the transverse strain for an element subjected to 100% axial strain in simple tension as evaluated by equation (1.23), confirming that the free edge of a pure shear specimen are subjected to uniaxial deformation. Due to results obtained with those preliminary experiments in this work it was decided to use a pure shear specimen with w/h_0 ratio equal to 10, the dimensions of which was already given in section 2.3.1.

3.2.2 Pure shear stress-strain behaviour

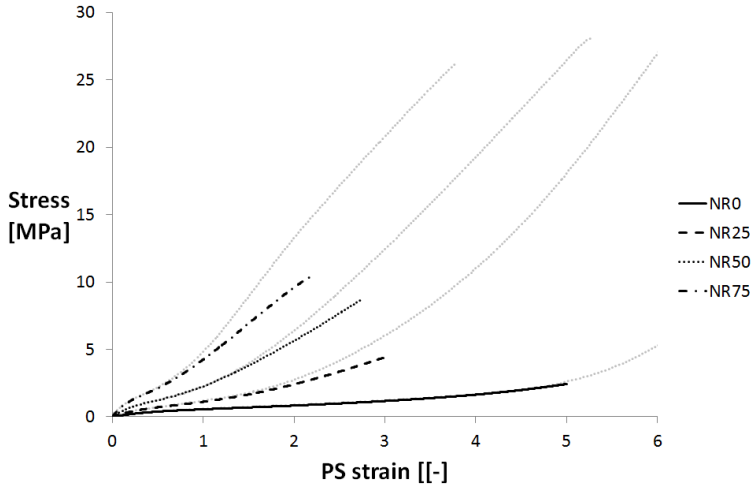

Figure 3.6: *Pure Shear extension - engineering stress versus engineering strain (uniaxial stress-strain behaviours are reported as light grey lines).*

Pure shear tension tests were performed on the compounds described in table 2.1 using specimens reported in figure 2.9(a). Specimens were mounted on the uniaxial Instron dynamometer using the aluminium clamps described in figure 2.9(b) by means of pneumatic grips. The tensile test was carried out with a constant crosshead displacement rate of $30mm/min$. The engineering stress has been calculated in accordance with equation (1.6) using force measured by the load cell and the undeformed area measured before the test, the longitudinal engineering strain was obtained by DIC. The stress-strain behaviours for different compounds are reported in figure 3.6, dotted light grey curves report the uniaxial stress-strain behaviour. It is interesting to underline how the pure shear stress strain behaviour above the upturn

results to be less stiff with respect to the uniaxial behaviour for all the compounds considered, below the upturn the uniaxial and pure shear stress-strain behaviours were the same. The reason of this particular behaviour, that is in contrast with the usual literature data that reports the pure shear behaviour to be equal or stiffer than the uniaxial, is still unknown.

3.3 Biaxial loading

3.3.1 Specimen geometry optimization

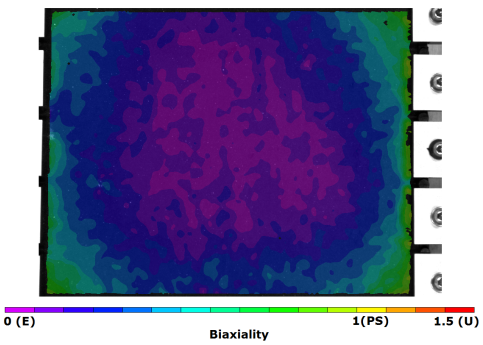

Figure 3.7: *Square specimen biaxiality field when tested without thick edge cuts and holes under* 25% *equibiaxial strain.*

At first the square specimen shown in figure 2.10 but without the cuts on the thick edge and the holes at the end of the cuts was tested. Figure 3.7 reports the biaxiality in the specimen at 25% overall strain It can be observed that equibiaxiality ($biaxiality = 0$, purple in figure 3.7) is present only in a central zone of the specimen. To extend the region of homogeneous strain cuts and holed, as shown in figure 2.10, were introduced. Figure 3.8 shows the specimen at the same 25% overall strain: equibiaxial strain field appears much larger and only near to the holes the strain field results uniaxial.

Another advantage of cuts is that the thick edge becomes discontinuous and does not contribute to the force measurements. Further, as shown in figure 3.9 as equibiaxial applied strain increases in the specimen with edge cuts and holes the strain value in the central area was closer to the applied strain with respect to the specimen with the original geometry.

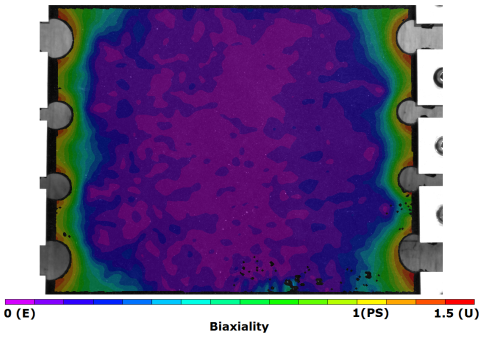

Figure 3.8: *Square specimen biaxiality field when tested with thick edge cuts and holes under 25% equibiaxial strain.*

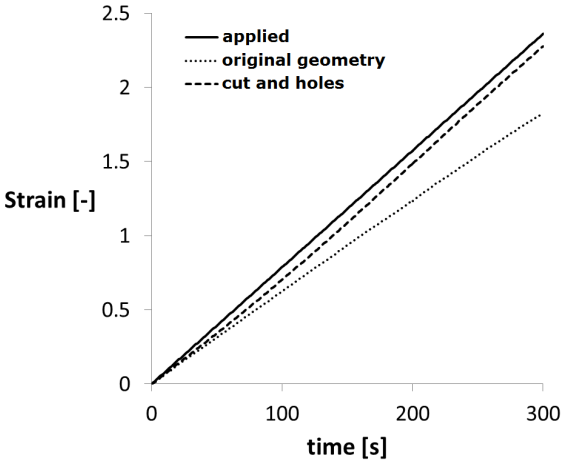

Figure 3.9: *Comparison between applied boundary equibiaxial strain and measures in the center of original and modified square specimen.*

3.3.2 Biaxial stress-strain behaviour

Compounds of table 2.1 were tested in three different biaxial loading conditions, pure shear, biaxial and equibiaxial. Specimens reported in figure 2.10 were mounted on the biaxial clamping system shown in figure 2.6 by means of the interference terminals that fits the thick border of the specimen. For this series of tests y-direction was always the direction of the maximum overall applied strain, x was the orthogonal direction. The tests were performed with constant displacement rate of the motors, the various load configurations were obtained by suitably modifying the relative dis-

placement rates in the x and y directions as shown in table 3.2. Engineering stress was evaluated from boundary forces recorded in both directions by means of equation (1.6), engineering strains was obtained by DIC optical measures in the central zone of the specimen.

Table 3.2: *Displacement rate used for monotonic biaxial tensile tests.*

Load configuration	y direction [mm/s]	x direction [mm/s]
PS	1	0
B05	1	0.5
E	1	1

In order to check the reliability so the stress-strain curves obtained with the new clamping system and square specimen the pure shear stress-strain curves obtained both from pure shear specimen in uniaxial loading and from the square specimen was compared as reported in figure 3.10. It can be observed that the pure shear stress-strain behaviour is well identified using the square specimen, although, due to the presence of holes, the maximum elongation at break on square specimens results to be lower with respect to the value obtained testing the pure shear specimens for all the examined compounds.

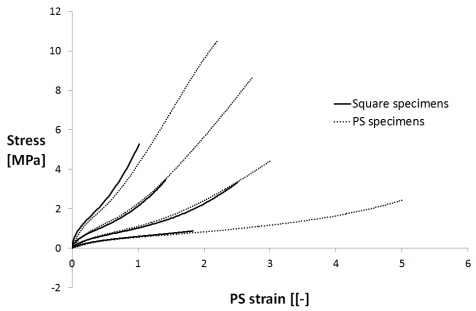

Figure 3.10: *Comparison between the pure shear stress-strain behaviour obtained testing pure shear (dotted line) and square (solid line) specimens.*

Compounds stress-strain behaviour in biaxial loading conditions for the examined compounds were summarized in figure 3.11. In the direction of maximum applied extension (y-direction, left graphs in figure 3.11) the

mechanical behaviour was more rigid as higher was the strain applied in x-direction, passing from pure shear to biaxial to equibiaxial loading. The maximum elongation in y-direction results to be lower as higher the deformation in x-direction. Even if the elongation at break here determined can not be considered as a material property due to the presence of the holes on the specimens those results can be attributed to the maximum extensibility of the molecular network as asserted by Gent in [14], and is in agreement with the hypothesis of a limiting value for the first strain invariant I_1. In the x-direction it can be noted that, as expected, the equibiaxial stress-strain curve results to be exactly the same observed in y-direction. The biaxial stress-strain was more rigid then equibiaxial, but this is only an effect of the lower strain applied, as can be easily understood considering the x-direction stress-strain of the pure shear loading configuration that results infinitely rigid due to the fact that the applied x-strain is equal to 0.

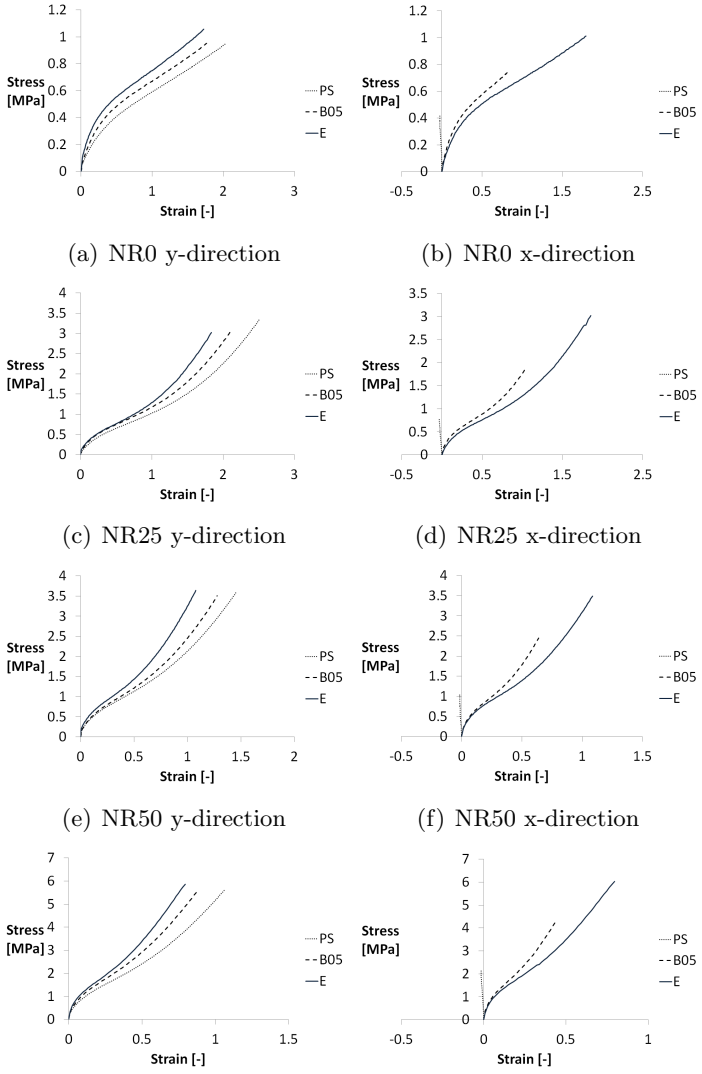

(a) NR0 y-direction (b) NR0 x-direction

(c) NR25 y-direction (d) NR25 x-direction

(e) NR50 y-direction (f) NR50 x-direction

(g) NR75 y-direction (h) NR75 x-direction

Figure 3.11: *Mechanical behavior of compounds in table 2.1 in pure shear (PS), biaxial (B05) and equibiaxial (E) extension.*

3.4 Identified compounds parameters

Using the minimization technique described in section 2.4.1 material parameters of the 3^{rd} order Ogden model were determined by simultaneous fitting of uniaxial, pure shear, biaxial and equibiaxial data sets. In some cases the boundaries given to the parameters, mentioned in section 2.4.1, were partially relaxed in order to achieve better fitting as suggested in [58]. The parameters sets obtained are reported in table 3.3, parameters for NR75 compound are still not available.

Table 3.3: 3^{rd} *order Ogden model materials parameters.*

Compound	μ_1	μ_2	μ_3	α_1	α_2	α_3
NR0	0.036	-0.038	0.391	5.804	5.774	1.959
NR25	0.938	-3.5E-5	0.041	1.002	-5.648	4.306
NR50	1.389	0.237	-1.39E-4	0.779	3.835	-6.956
NR75	-	-	-	-	-	-

Figure 3.12 report a comparison between the experimental data and the model predictions in the case of uniaxial and equibiaxial extension. It can be observed that a good agreement between predicted stress strain behaviour and experimental data was achieved, with exception for NR0 under equibiaxial extension (3.12(b)). Further experiments in more biaxial loading condition as well as repeatability and test set-up optimization can help in a future to obtain more precise representation of the mechanical behaviour.

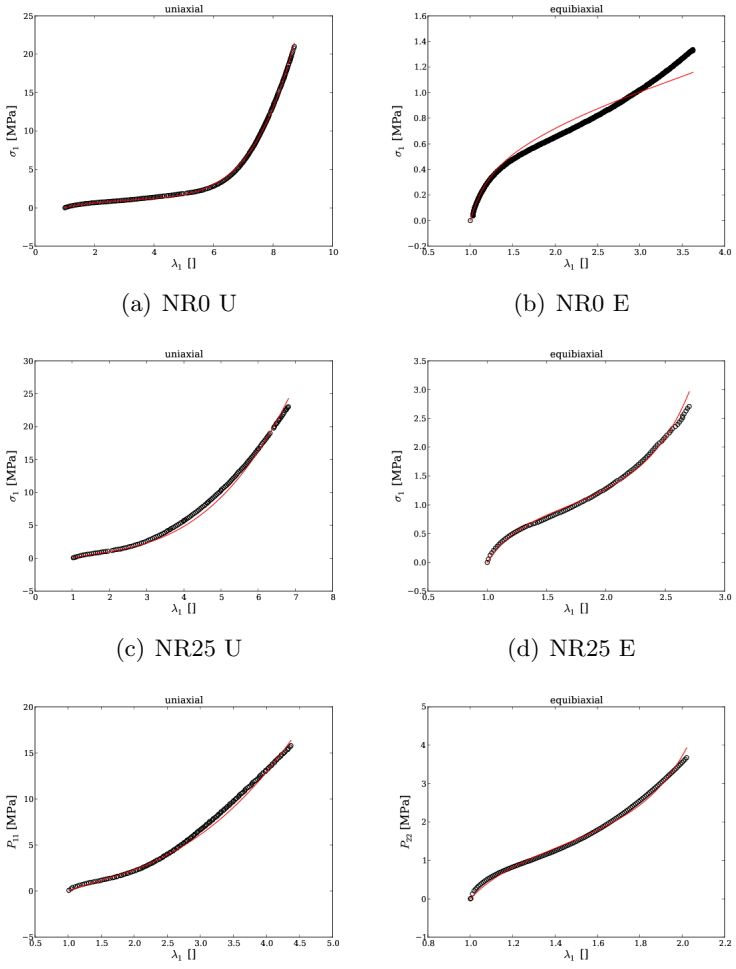

(a) NR0 U (b) NR0 E

(c) NR25 U (d) NR25 E

(e) NR50 U (f) NR50 E

Figure 3.12: *Mechanical behavior of compounds in table 2.1 under uniaxial (left) and equibiaxial (right) extension. 3^{rd} order Ogden model predictions corresponding to material parameters reported in table 3.3 were reported by red lines.*

3.5 Loading-unloading tests

3.5.1 Pure shear

Cyclic loading unloading tests were performed on compounds described in table 2.1. Testing conditions were the same used for PS monotonic tensile tests. Triangular displacement profile was used with $30mm/min$ constant crosshead speed both in loading and unloading, $120s$ were waited between two successive load cycles in order to allow the material to recover part of the residual deformation. Cycles were performed with increasing maximum displacement of $5mm$, corresponding to about 50% maximum strain increase from one cycle to the next one. Engineering stress was evaluated from recorded force cycles in accordance with equation (1.6), engineering strain was evaluated from the crosshead displacement in accordance with equation (1.7). Resulting stress-strain cycles for all the compounds are shown in figure 3.13, carbon black enhances Mullins effect and rise up the residual strain. In figure 3.14 total absorbed (W_t), elastically stored (W_e) and dissipated (W_d) energy densities, evaluated as described in section 2.4.2 are reported. As expected the presence of carbon black rise up the non conservative effects. Those measures will be used in chapter 4 in order to evaluate the elastic component of the tearing energy applied during pure shear fracture tests. In figure 3.15 elastically stored and dissipated energies are reported as a percentage of W_t. The behaviour of the four compounds results to be significantly different, in particular for filled compounds it can be identified a strain level at which the dissipated energy becomes more than half of the total absorbed energy. This level results to be inversely proportional to the amount of carbon black.

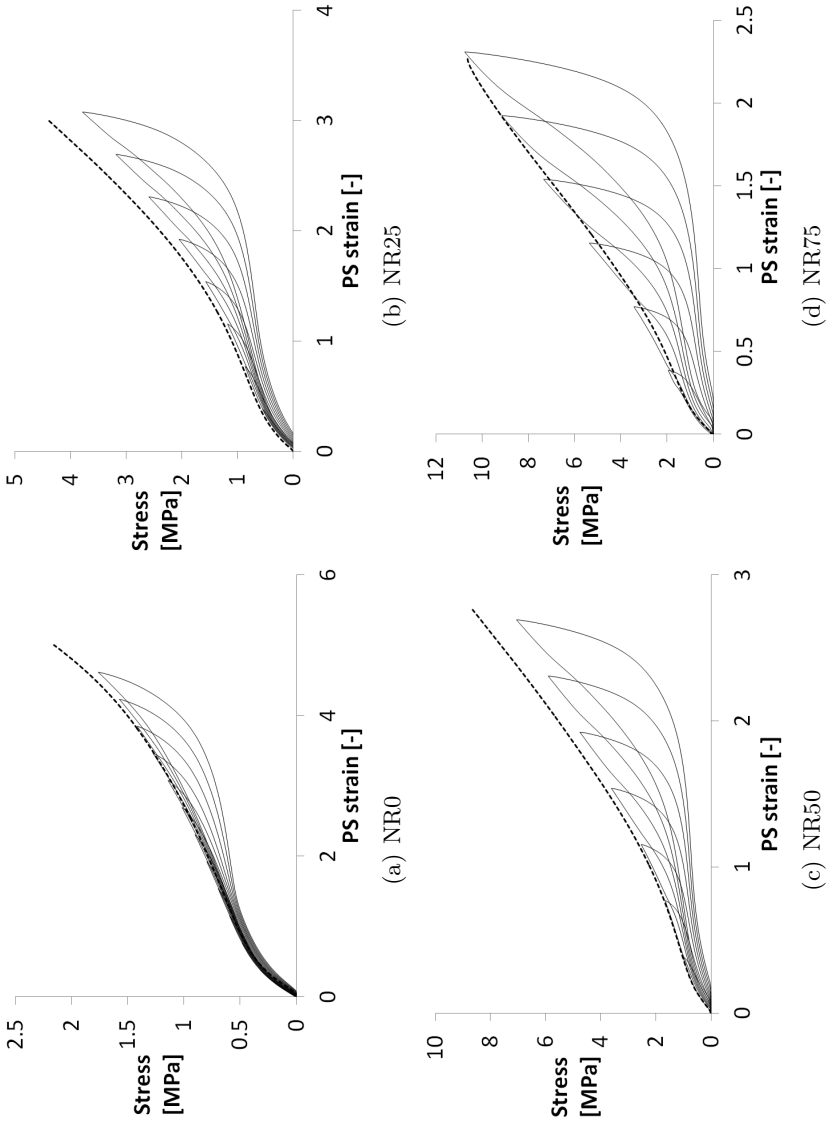

(a) NR0 (b) NR25 (c) NR50 (d) NR75

Figure 3.13: *Stress-strain cycles recorded during PS loading-unloading tests, dashed line is the PS monotonic tensile test.*

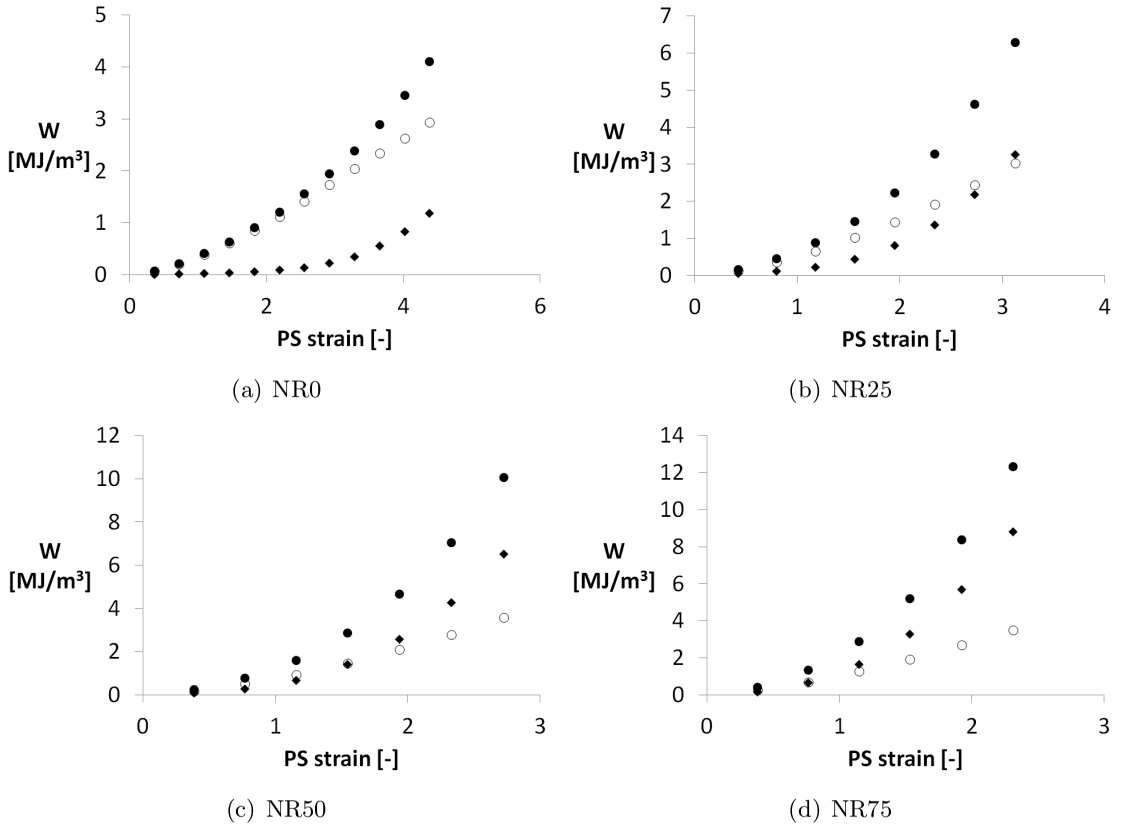

(a) NR0 (b) NR25

(c) NR50 (d) NR75

Figure 3.14: *Strain energy density components in PS loading conditions:* • *Total absorbed energy;* ○ *elastically stored energy;* ◆ *dissipated energy.*

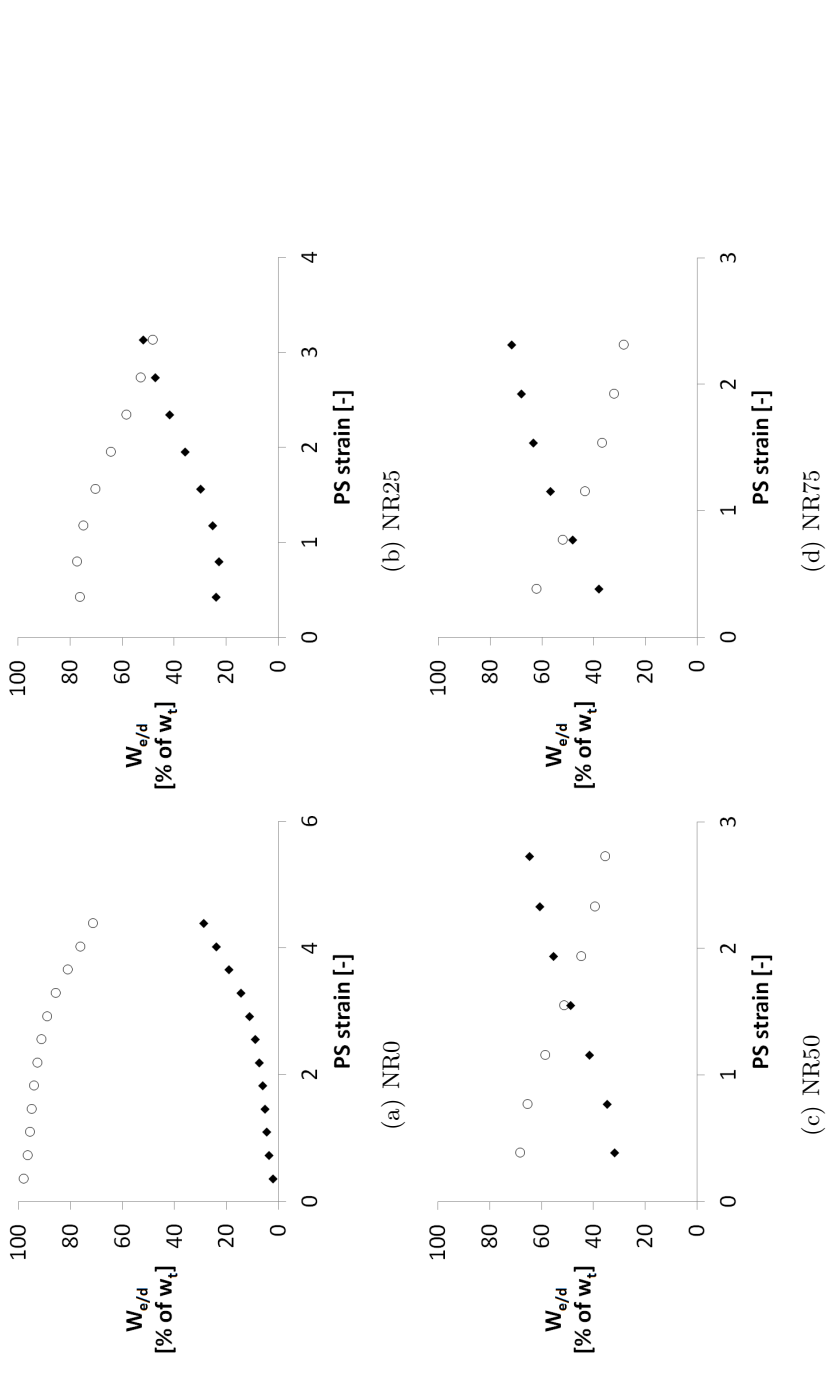

Figure 3.15: *Strain energy density components in PS loading conditions, percentage of W_t: ○ elastically stored energy; ◆ dissipated energy.*

3.5.2 Equibiaxial

Loading-unloading test were also performed in equibiaxial loading conditions on compounds of table 2.1, also in this case triangular displacement cycles have been used symmetrical in both loading directions using a displacement rate of $1mm/s$. Cycles were carried out with increasing maximum relative displacement in steps of $25mm$, corresponding to an increase of the maximum applied strain from one cycle to the next amounting to about 20%. Force displacement cycles were recorded during the test, engineering stress cycles were evaluated from boundary forces in both loading directions in agreement with equation (1.6), engineering strains were evaluated from boundary displacements in agreement with equation (1.7). Stress-strain cycles results to be superimposed in both directions, in figure 3.16 the obtained stress-strain cycles are given always for one direction. Total absorbed energy density W_t and elastically stored energy density W_e were evaluated with the same method described in section 2.4.2 multiplying by two the obtained values for one direction due to the equibiaxial loading condition. Specific dissipated energy W_d was evaluated by the difference between W_t and W_e. Results are reported in figure 3.17.

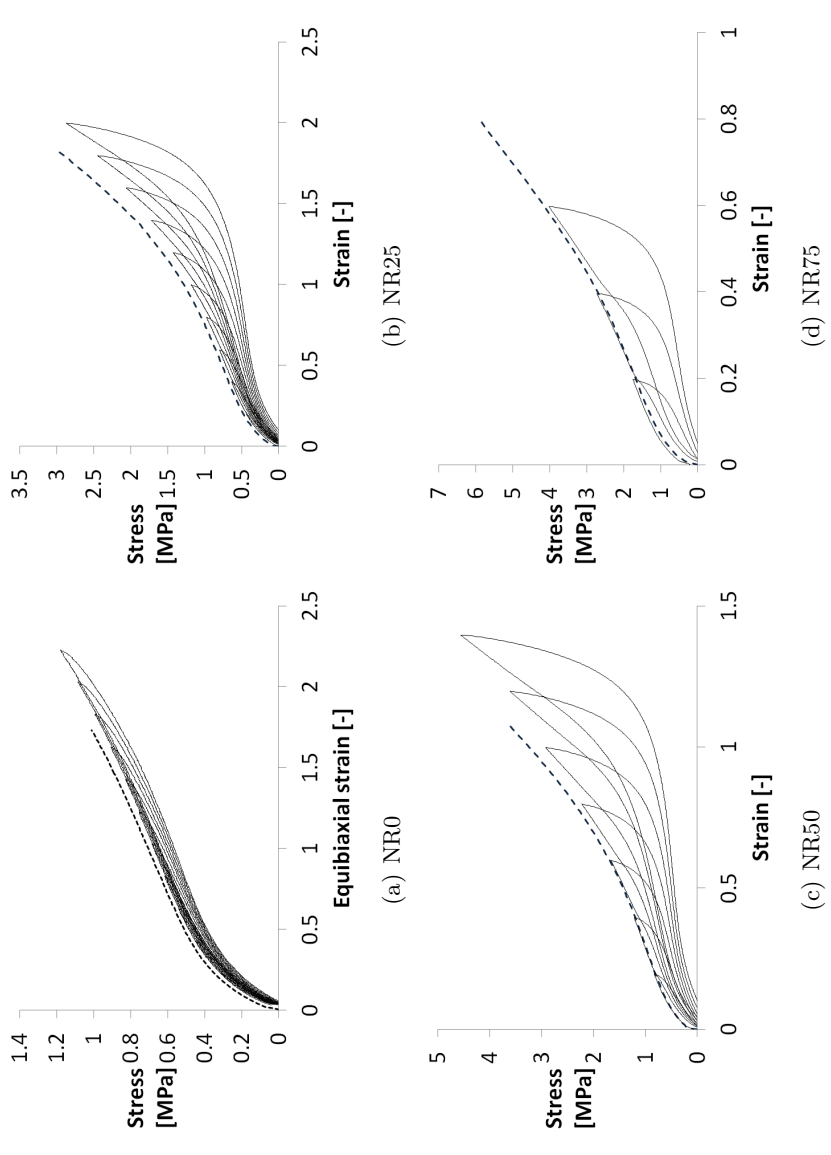

(a) NR0 (b) NR25 (c) NR50 (d) NR75

Figure 3.16: *Stress-strain cycles recorded during E loading-unloading tests, dashed line is the E monotonic tensile test.*

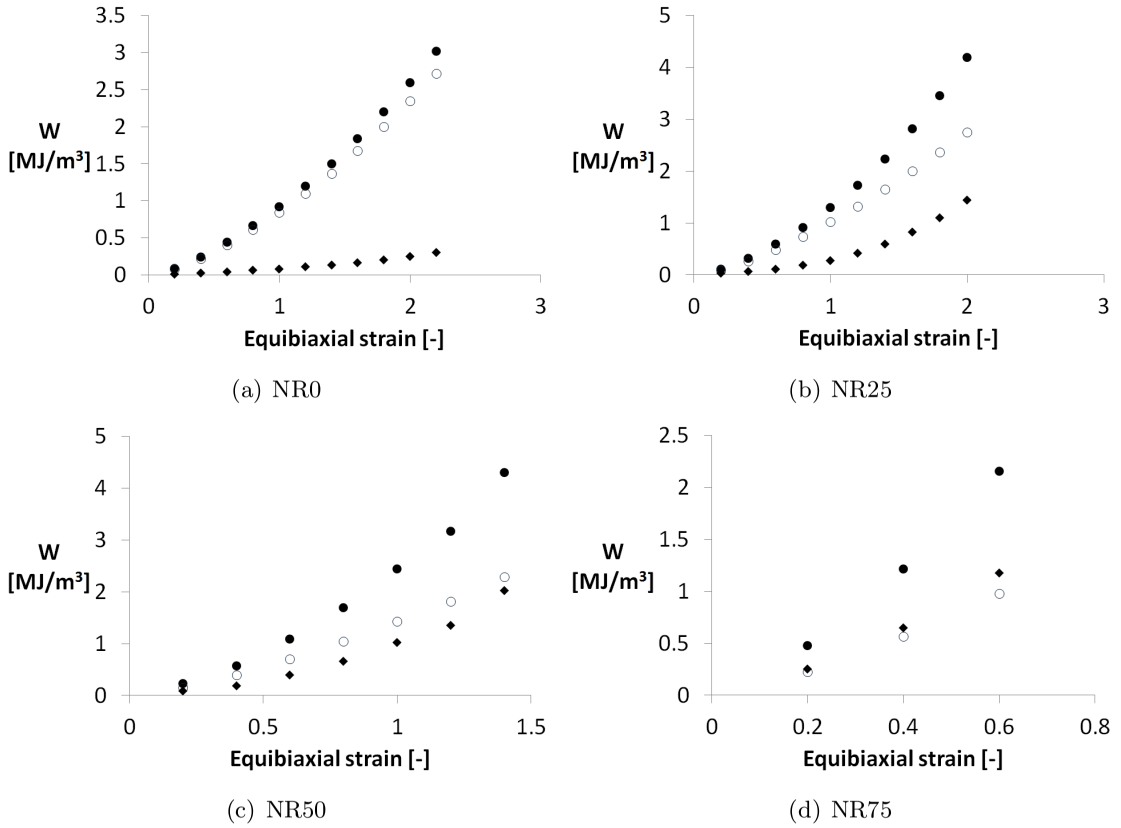

(a) NR0 (b) NR25

(c) NR50 (d) NR75

Figure 3.17: *Strain energy density components in E loading conditions: • Total absorbed energy; ○ elastically stored energy; ◆ dissipated energy.*

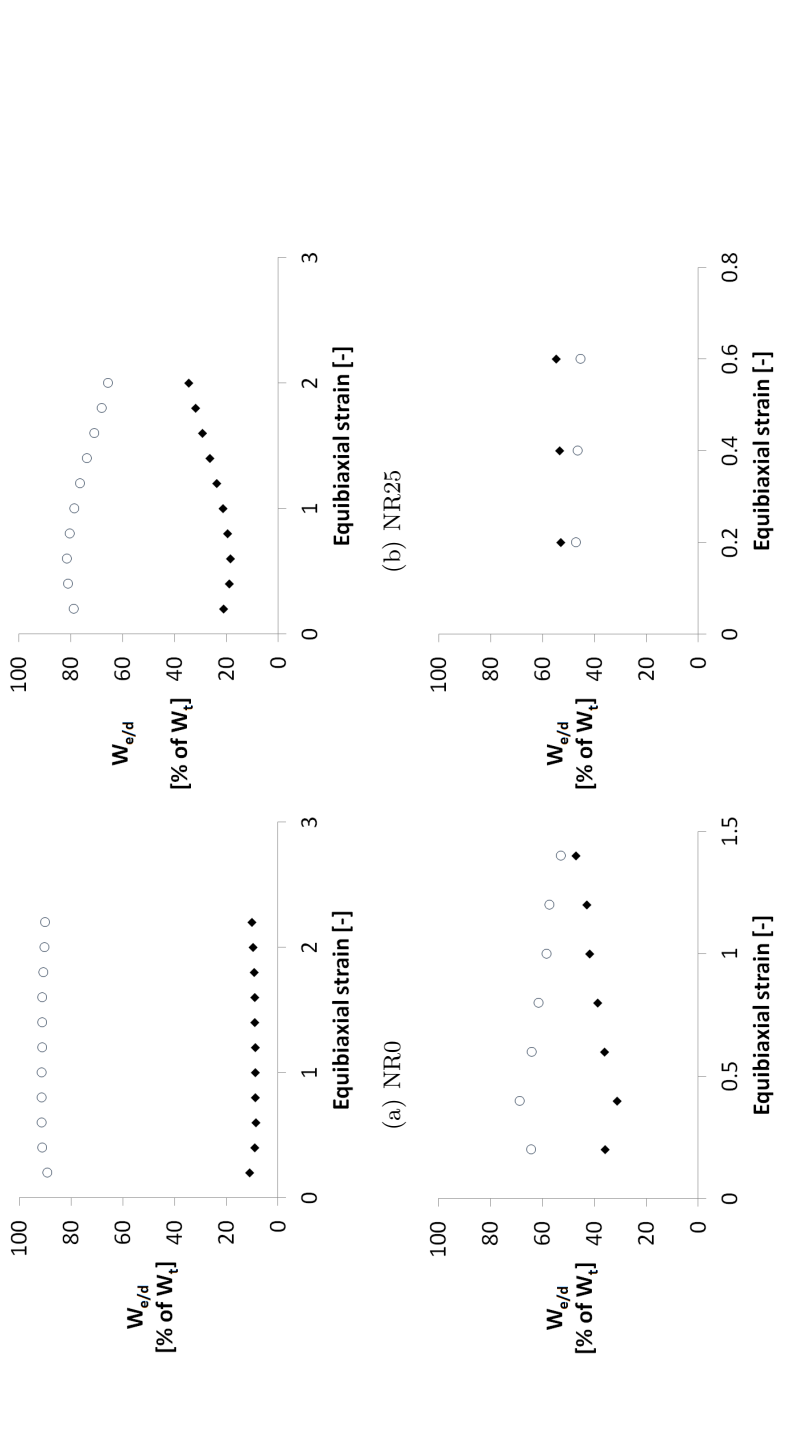

(a) NR0 (b) NR25 (c) NR50 (d) NR75

Figure 3.18: *Strain energy density components in E loading conditions, percentage of W_t: ○ elastically stored energy; ◆ dissipated energy.*

Chapter 4

Quasi-static fracture characterization

4.1 Fracture characterization under pure shear loading

The pure shear fracture tests were performed on compounds reported in table 2.1 with the method described in section 2.5.1.

4.1.1 Preliminary tests

Preliminary fracture tests were carried out on all compounds to verify the actual existence of the four zones described in section 2.5.1, a necessary condition for the evaluation of the tearing energy by means of equation (2.7). Figure 4.1 shows for NR25 the transverse Hencky strain ε_x obtained from digital image correlation at forward onset (overall engineering strain 90%). As can be observed both zones A and B show $\varepsilon_x \approx 0$, as expected for an unloaded zone (A) and a zone under pure shear (B). This confirms that the notch length used was adequate in agreement with the observations of Yeoh [51]. All four compounds examined showed similar behaviour.

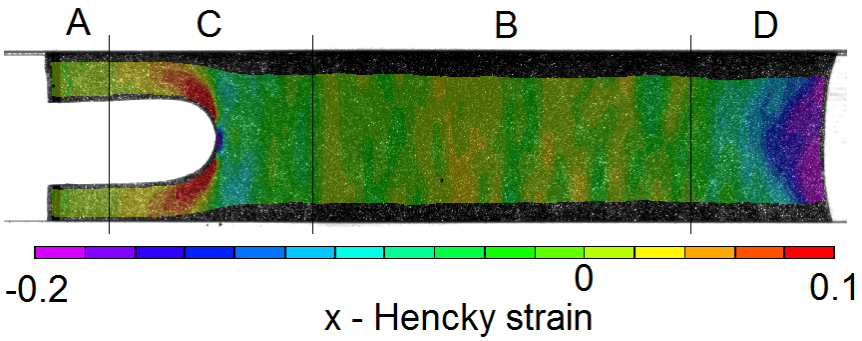

Figure 4.1: *Transverse Hencky strain ε_x at forward crack onset (overall engineering strain 90%) in a fracture test on NR25.*

4.1.2 Fracture phenomenology

For all compounds the fracture phenomenology observed was in line with that reported in the literature. As expected for filled compounds, the onset and propagation of the so-called **sideways cracks** which propagate in the loading direction was observed before fracture onset and propagation along the original crack plane, referred as **forward crack**. The sideways cracks propagation is a well known and widely studied phenomenon of crack deviation mechanism [59–61]. Hamed [62] ascribes crack deviation to strain induced anisotropy in the region of the crack tip, where the high strains align the molecular chains and filler particles in a direction parallel to the applied load.

The forward crack propagation occurred for all specimen tested along the original crack plane without deviations, leading to the catastrophic collapse of the specimen for all the compounds with exception of NR25 that exhibited slower crack propagation. The unfilled natural rubber did not show the phenomenon of sideways crack propagation: the original defect propagated directly along notch plane.

The sideways cracks onset occurs at progressively lower overall applied strain as carbon black content increases, this is probably due to the fact that carbon black acts as a rigid particle enhancing the strain in the rubber matrix. In the vicinity of the crack tip this can lead to higher orientation and strength anisotropy. At the onset of sideways cracks no discontinuity in

the load-displacement curve was observed. Frames from the video recording of the test at the sideways cracks onset are reported in figure 4.2.

(a) NR25 (b) NR50 (c) NR75

Figure 4.2: *Frames from the video recording of the test corresponding to the sideways cracks onset.*

Figure 4.3 reports the frames from video recording of the test at forward crack onset, sideways cracks were highlighted with arrows. It can be observed that the overall applied strain at forward crack onset shows an initial drop going from NR0 to NR25 and then a monotonic increase as carbon black content increases. The overall engineering applied strains ε_{PS} at sideways and forward cracks onset are reported in figure 4.4 as a function of the carbon black content. According to Hamed [63], the increase of ε_{PS} with carbon black content can be attributed to the sideways crack propagation differences between filled compounds. The author asserts that the toughening mechanism in carbon black filled compounds with respect to natural rubber is strictly related to the sideways cracks propagation.

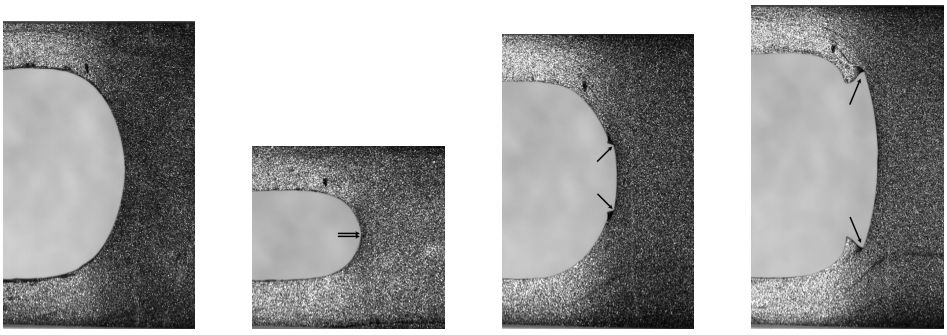

(a) NR0 (b) NR25 (c) NR50 (d) NR75

Figure 4.3: *Frames from the video recording of the test corresponding to the forward crack onset.*

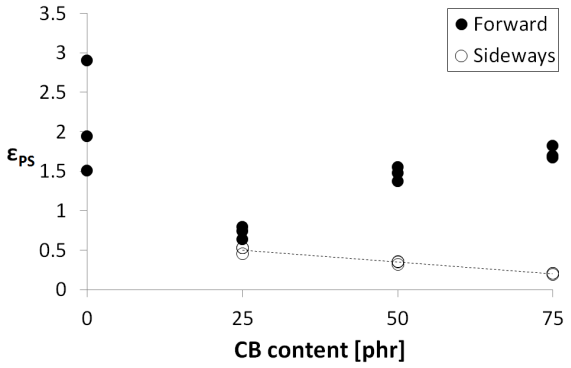

Figure 4.4: *Engineering overall applied strain at forward and sideways cracks onset as a function of carbon black content.*

From the digital image correlation measurements manually selecting the sideways cracks tips during propagation it was possible to reconstruct crack propagation loci on the undeformed specimen configuration as reported in figure 4.5. This procedure was possible only for NR50 and NR75, because sideways cracks in NR25 compounds were too short for the resolution of the analysis. In figure 4.5 the original crack tip was located in the axis origin with the notch in the negative x axis direction (i.e. forward propagation occurs along positive x axis direction). It can be observed that, although the sideways cracks propagate in a direction similar to the loading direction, the undeformed specimen propagation path results not parallel to the vertical direction, the shape observed is in agreement to some similar observations reported in [64]. According to [59,60,62,65] sideways cracks propagate in the direction for which the applied energy release rate is equal to the material resistance. Both quantities depend on the applied strain in the local region near to the crack tip.

The sideways cracks propagation length was also measured and reported in figure 4.6 as a function of carbon black content. As already mentioned, sideways cracks for NR25 were very short at forward crack onset, in figure 4.6 zero propagation length was assigned to this compound. Measurements for the undeformed sideways crack length as a function of carbon black content confirm and quantify the previous qualitative observation.

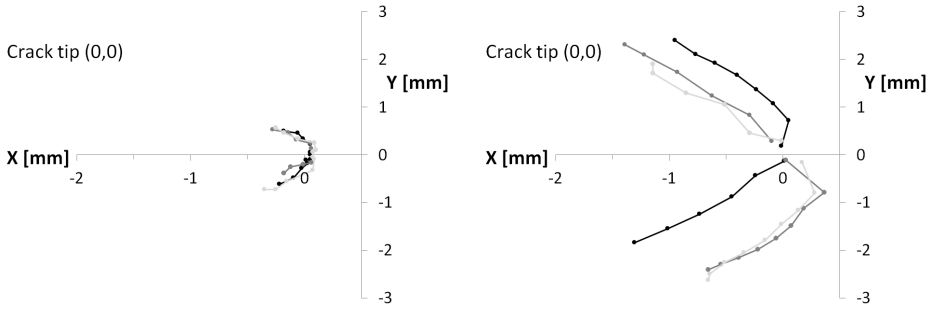

(a) NR50 (b) NR75

Figure 4.5: *Sideways cracks propagation loci in the reference configuration for NR50 and NR75 as revealed by digital image correlation. Different curves are referred to different specimens.*

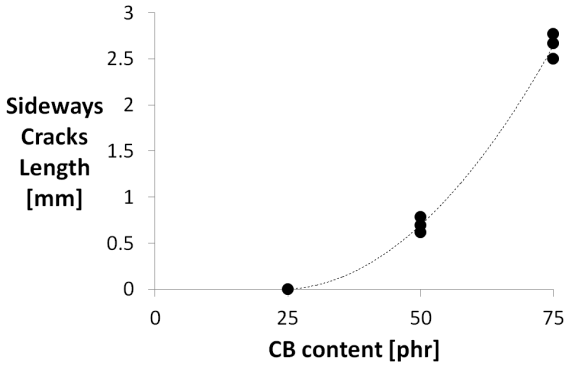

Figure 4.6: *Sideways propagation length at the instant of forward onset as a function of carbon black content.*

4.1.3 Fracture toughness

Using stress-strain characterization data reported in figure 3.14, the critical tearing energy was evaluated both at forward and sideways cracks onset. The overall applied strain at crack onset reported in figure 4.4 were used to evaluate the strain energy density W_{PS} in the uniformly deformed B-zone of the specimen, and the tearing energy evaluated by equation (2.7). Both total and elastic tearing energy were evaluated using the total absorbed energy W_t obtained from monotonic stress-strain characterization and the elastically stored energy W_e obtained from loading-unloading characterization in pure shear loading conditions as reported in figure 3.14. The critical tearing

energy at sideways cracks onset was considered here equal to the applied tearing energy in the forward direction evaluated at the sideways cracks onset.

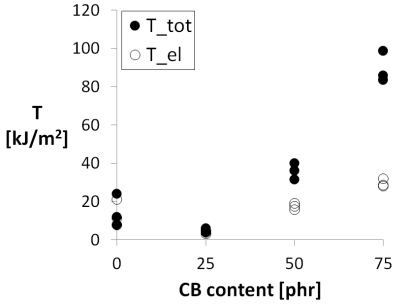

(a) Forward

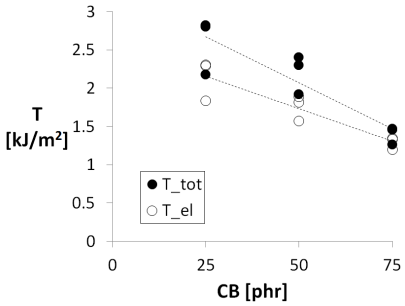

(b) Sideways

Figure 4.7: *Critical tearing energy as a function of the carbon black content for forward (a) and sideways (b) cracks onset.*

Figure 4.7(a) reports the critical tearing energy at forward crack onset, it can be observed that after an initial drop going from NR0 to NR25 the fracture propagation resistance increase as carbon black content increases, both considering the total and the elastic tearing energy. Considering the tearing energy calculated by means of the elastically stored energy T_{el} the difference of tearing energy observed between the different compounds is lower, however, the relative order of toughness does not change confirming that the carbon black has the effect of increasing the rubber resistance to the crack propagation even without considering the energy dissipation required to reach the critical condition of fracture initiation. The critical tearing energy at sideways onset, as reported in figure 4.7(b), is a decreasing function

of the carbon black content. It can be explained by the material orientation near to the crack tip, that is more pronounced as higher the carbon black content is. In this case the difference of the total and elastic tearing energy decreases with carbon black content due to the fact that the sideways cracks propagate at low overall strain, where the dissipations are less pronounced as already discussed in section 3.5.1 and shown in figure 3.15. Both considering T_tot or T_el the compound with the lower fracture toughness was the NR25, this results to be even smaller than that of unfilled natural rubber confirming that the carbon black reinforcement is related not only to sideways cracks onset but also to how much they propagate. The average tearing energies are reported in table 4.1.

Table 4.1: *Tearing energies obtained testing compounds of table 2.1 under pure shear loading.*

	Sideways		Forward	
Compound	T_e $\left[\frac{kJ}{m^2}\right]$	T_t $\left[\frac{kJ}{m^2}\right]$	T_e $\left[\frac{kJ}{m^2}\right]$	T_t $\left[\frac{kJ}{m^2}\right]$
NR0	-	-	13.3 ± 5.7	14.5 ± 6.9
NR25	2.1 ± 0.2	2.6 ± 0.3	3.8 ± 0.5	5.0 ± 0.8
NR50	1.7 ± 0.1	2.2 ± 0.1	17.4 ± 1.4	35.8 ± 3.5
NR75	1.3 ± 0.1	1.4 ± 0.1	29.5 ± 1.6	89.3 ± 6.7

Efforts can be also found in the literature to find a single specimen method for the determination of a fracture parameter for pure shear geometry [66–68] adapting the J-integral approach. J can be evaluated in the case of pure shear fracture test on rubber compounds through the relation:

$$J = \eta \frac{U_i}{b(w-c)} \tag{4.1}$$

where U_i is the area under the force-displacement curve up to the fracture onset, b and w are the specimen thickness and width respectively and c is the original crack length. η is a shape factor that was determined experimentally [66] and by finite element simulations [69, 70] to be equal to 1 for pure shear test configuration.

J-integral was here evaluated in order to have a comparison parameter for fracture toughness obtained from finite elements simulations of the fracture tests in biaxial loading conditions 4.2.3. Figure 4.8 reports the critical tearing energy and the J-integral at forward crack onset as a function of carbon black content. The total tearing energy results to be lower with respect to J for all the compounds examined. This result is not surprising following the conclusions of Kim and Joe, which in [66] argue that "T_c should be smaller than the actual fracture energy (J_c). The variation of the strain energy density in the vicinity of the unconstrained sides of the uncracked specimen has been ignored". This is partially in contrast with the observation about the small effect of the free border in the pure shear specimen observed by Treloar [22].

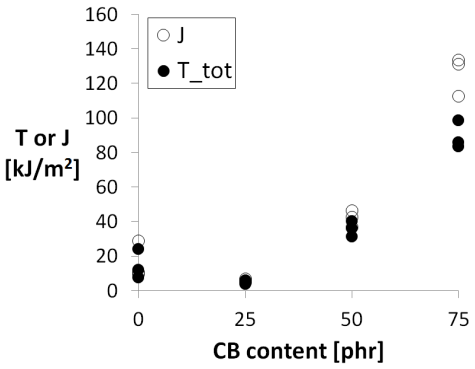

Figure 4.8: *Comparison between tearing energy T and J evaluated by the single specimen method as a function of carbon black content.*

4.1.4 Strain field around the crack tip

The strain field around the crack tip was determined during the pure shear fracture test by means of digital image correlation analysis. Figure 4.9 reports for the studied materials the contour plots of the Hencky strain ε_y, close to the crack tip, for different overall engineering strain levels. The figure is organized as a table, in which columns represents different compounds and rows different overall applied strains. The scale factor is the same for all the pictures, as the color range of the contour plots. For each level of the applied strain the strain range of the contour plot is reported. As long as

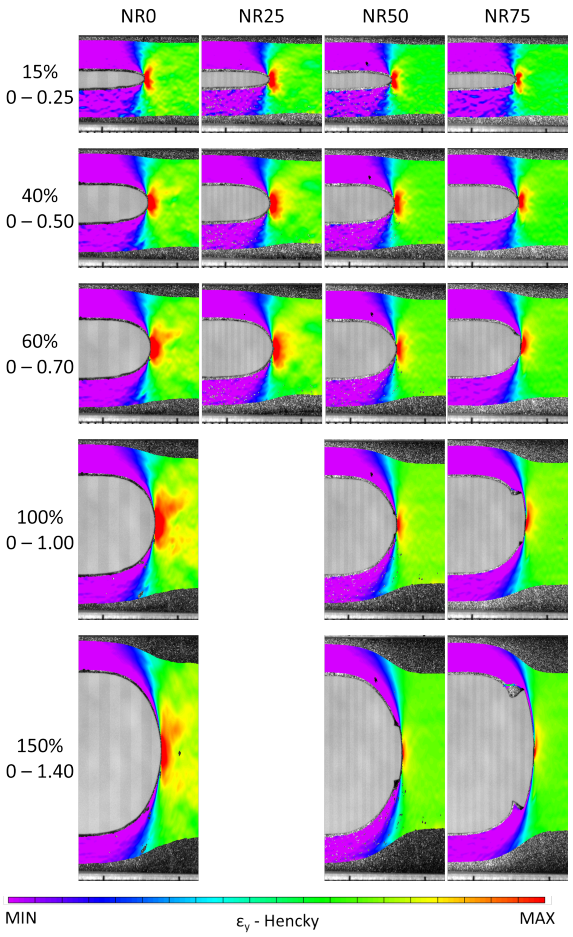

Figure 4.9: *ε_y Hencky strain contour maps at different overall applied engineering strain during pure shear fracture test. For each row the overall applied engineering strain and the Hencky strain contour plot maximum and minimum values are reported.*

the overall applied strain is small $(15-40\%)$, the strain distribution around the crack tip is quite the same for all the compounds examined, even trough the strain intensification zone size slightly decrease as carbon black content increases. As the overall applied strain increases the strain singularity size rapidly increases for NR0 and NR25: the latter compound fails immediately after the sideways cracks onset as already reported in figure 4.4. For NR50 and NR75 compounds higher overall strains can be applied. Sideways cracks propagate significantly before the onset of the forward crack and both the volume of the zone where there is strain intensification and the strain intensification magnitude decrease. Considering the engineering ε_{loc} measured at a certain distance, l, from the crack tip as characteristic of the strain intensification that occur at the crack tip, it is possible to represent the singularity magnitude by the ratio of the local strain ε_{loc} and the overall applied strain ε_{PS}. A value of $0.42mm$ was fixed for l because this value allows to measure the local strain as close as possible to the actual crack tip position: at this distance the sideways cracks propagation do not disturb the digital image correlation analysis.

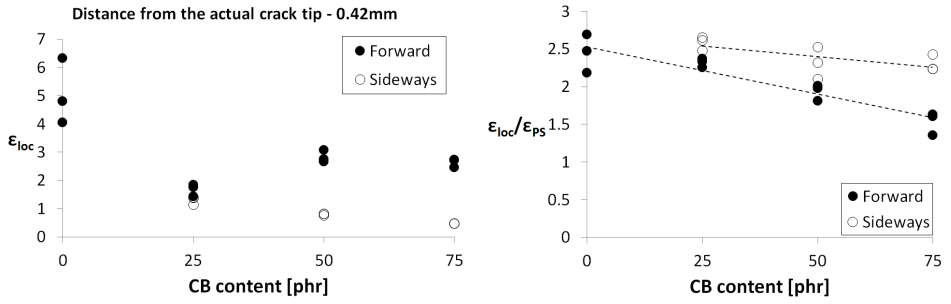

(a) (b)

Figure 4.10: *Analysis of the strain intensification close to the crack tip at forward and sideways cracks onset in pure shear loading fracture tests. a) local strain for different carbon black content; b) Normalized local strain as a function of carbon black content.*

The local strains measured at sideways and forward cracks onset are reported in figure 4.10(a) as a function of carbon black content. The carbon black content dependence of the local strains, ε_{loc}, is similar to that of the overall applied strains ε_{PS} (figure 4.4), although ε_{loc} results to be higher

than ε_{PS}. Figure 4.10(b) reports the ratio between ε_{loc} and ε_{PS} as a function of the carbon black content at sideways and forward cracks onset. It can be observed that at sideways cracks onset this ratio slightly decreases with carbon black content, confirming that the strain intensification at the tip of a crack in filled rubbers is diminished by the presence of carbon black by means of dissipation effects. At forward crack onset the ratio was significantly lower than the value at sideways cracks onset: the sideways cracks propagation reduces both the intensity of the strain field and the relevant deformed zone as mentioned above. This result seems to confirm the beneficial effect of sideways cracks propagation in enhancing rubber toughness as described by Hamed [63, 65], who correlates the reinforcing mechanism of carbon black with the sideways cracks propagation, which changes the geometry of the crack and reduce the stress concentration.

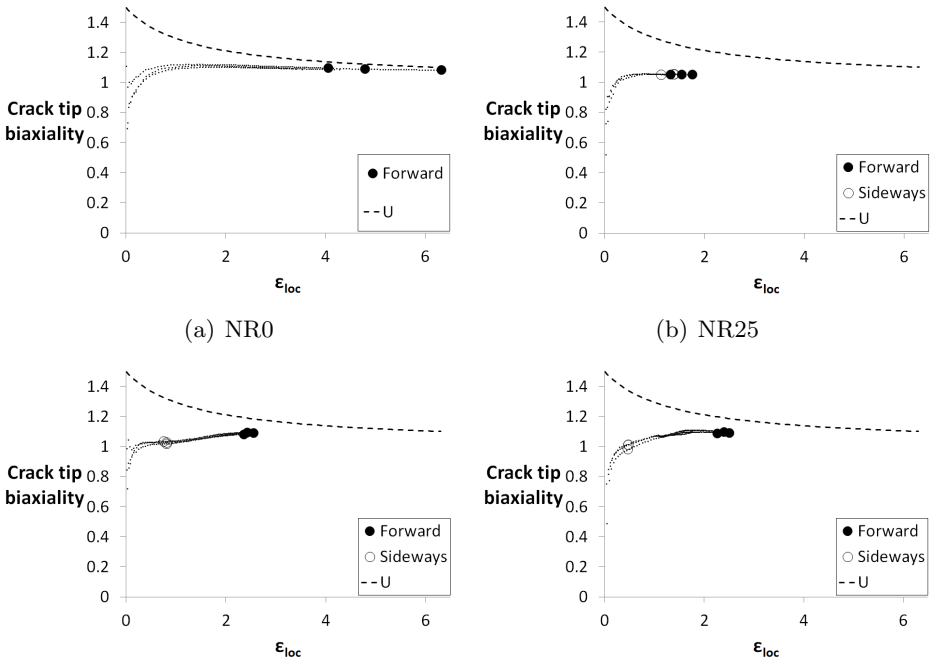

(a) NR0 (b) NR25

(c) NR50 (d) NR75

Figure 4.11: *Crack tip biaxiality as a function of the local strain ε_{loc} during pure shear fracture tests. Dashed line is the strain dependence of the biaxiality predicted for a volume element deformed in uniaxial tensile loading condition.*

The biaxiality (equation (1.20)) at the crack tip during the whole test is

reported in figure 4.11 as a function of the local strain ε_{loc}, together with the biaxiality of a uniaxially deformed volume element. It can be observed that for all the compounds examined at the crack tip there is a biaxial strain state ($biaxiality < 1$) only at relatively small strain ($\varepsilon_{loc} \approx 40\%$), for which the crack was not yet blunted. Then the biaxiality tends to that of a uniaxially deformed volume element of the relevant strain.

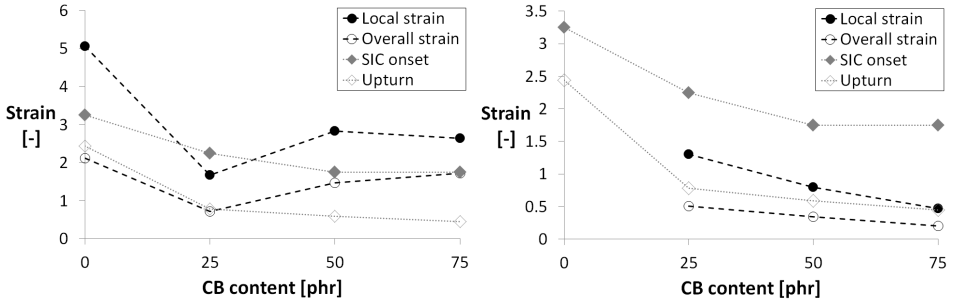

(a) Forward (b) Sideways

Figure 4.12: *Comparison between the overall and local strains at forward (a) and sideways (b) cracks onset with strain thresholds for finite chains extensibility (Upturn) and strain induced crystallization (SIC) onset.*

Local and overall strains can be used to better understand the physical phenomena that occur at the crack tip at sideways and forward cracks onset. Figure 4.12 reports both overall ε_{PS} and local ε_{loc} strain values at forward and sideways cracks onset as a function of carbon black content. On the same graph the strain at stress upturn (Upturn) and the strain at strain induced crystallization onset (SIC) under uniaxial tension (see section 3.1.1) are also reported. As shown above at the onset of forward and sideways cracks the crack tip is almost uniaxially loaded so the strains at stress upturn and at SIC onset relevant to uniaxial tensile test can be compared with these values. It can be observed that at sideways cracks onset (figure 4.12(b)) the overall strain is below the upturn and the local strain is between the upturn and SIC onset. This result suggests that the sideways cracks onset is mainly related to finite chains extensibility. Moreover it results that at the sideways cracks onset, at the crack tip crystallization has not yet occurred. As for the forward crack onset the local strain is higher than the strain for SIC onset,

for all the compounds except for NR25.

4.2 Fracture characterization under biaxial loading

Fracture tests under quasi-static biaxial loading were performed on NR0 and NR50 compounds reported in table 2.1 with the method described in section 2.5.2. In the following different tests under biaxial loading conditions will be named with the pre-drawing λ_x applied in the direction parallel to the crack during the stretching step of the test: for example $\lambda_x = 1$ corresponds to a biaxial test in which no pre-drawing was imposed during the drawing step, $\lambda_x = 2$ means that the specimen was drawn up to 100% along the notch direction during the drawing step and so on. As already mentioned before only a few fracture tests were performed under biaxial loading conditions.

4.2.1 Fracture phenomenology

Two fracture test were performed on the NR0 compound: one with $\lambda_x = 1$ (which are expected to be equivalent to a pure shear fracture test), and one with $\lambda_x = 2$. No sideways cracks propagation was observed for this compound in both tests performed. Frames from the video recording of the tests corresponding to forward crack onset are reported in figure 4.13. The forward onset was simultaneous for both crack tips. It can be observed that the deformed crack eccentricity was significantly different in the two cases examined; crack dimensions a and b were measured. Table 4.2 reports overall and local strains ($0.5mm$ from the actual crack tip) and the crack dimensions a and b in millimeters corresponding to forward cracks onset. The overall applied strain in y-direction strongly decrease from 80% to 4% going from $\lambda_x = 1$ to $\lambda_x = 2$. Also the local strain ε_{yloc} decreases. The local strain in the x-direction ε_{xloc} increases as the applied pre-drawing increases, showing how the crack tip is almost uniaxially deformed for $\lambda_x = 1$ and biaxially deformed for $\lambda_x = 2$ at least considering the minimum distance from the actual position of the crack tip that can be reached with the resolution of the DIC analysis.

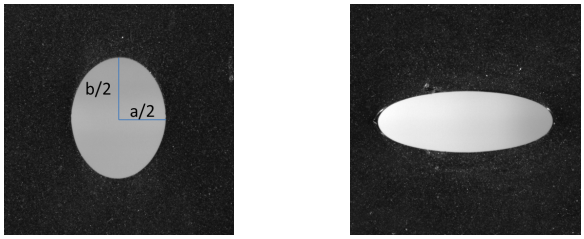

(a) $\lambda_x = 1$ (b) $\lambda_x = 2$

Figure 4.13: *NR0 - Frames from the video recording corresponding to the forward crack onset during fracture tests under biaxial loading condition.*

Four fracture test were performed on the NR50 compound with $\lambda_x = 1 - 1.2 - 1.5 - 2$ respectively. The fracture phenomenology observed was dependent on the applied draw ratio λ_x during the drawing step. As the applied pre-drawing increases the length over which the sideways cracks propagate becomes shorter, for $\lambda_x = 2$ no sideways cracks were observed and the forward cracks propagated directly along notch plane. Figure 4.14 shows the frames at sideways cracks onset. Sideways cracks onset occur with progressively higher crack eccentricity as the applied pre-drawing λ_x increases. Both the overall applied strain ε_{yov} and the local strain ε_{yloc} at sideways cracks onset, reported in table 4.2, decrease as pre-drawing increases, but the latter was always higher than ε_{xloc} showing that the material was oriented in the y-direction at the crack tip when sideways cracks onset occurs. This topic will be more deeply analysed in section 4.2.2. Figure

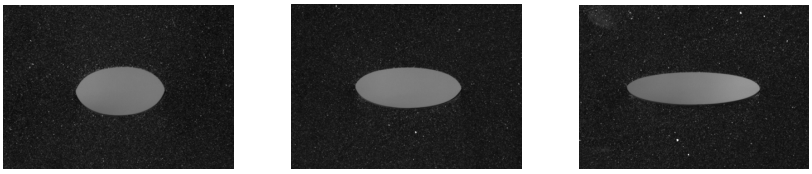

(a) $\lambda_x = 1$ (b) $\lambda_x = 1.2$ (c) $\lambda_x = 1.5$

Figure 4.14: *NR50 - Pictures corresponding to the sideways cracks onset during fracture tests under biaxial loading condition.*

4.15 reports the frames from the video recording of the test corresponding to forward cracks onset. Sideways cracks can be clearly seen for $\lambda_x = 1$ and 1.2,

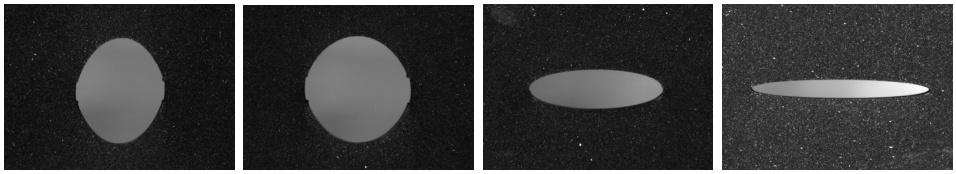

(a) $\lambda_x = 1$ (b) $\lambda_x = 1.2$ (c) $\lambda_x = 1.5$ (d) $\lambda_x = 2$

Figure 4.15: *NR50 - Pictures corresponding to the forward cracks onset during fracture tests under biaxial loading condition.*

but for $\lambda_x = 1.5$ test an image with much magnification would be needed. The crack eccentricity increases regularly with applied λ_x irrespective of the presence of sideways cracks.

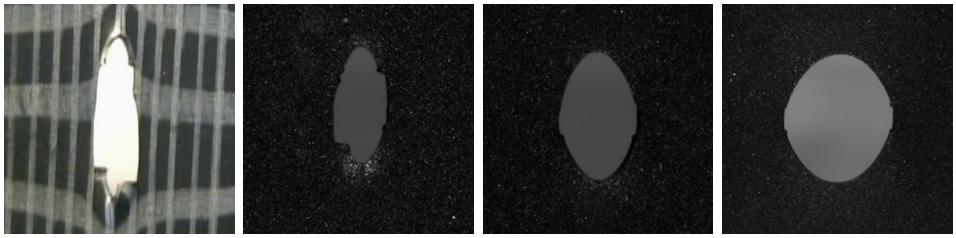

(a) Cross sp. (b) $2c_0 = 4mm$ (c) $2c_0 = 8mm$ (d) $2c_0 = 16mm$

Figure 4.16: *NR50 - Frames from the video recording corresponding to the forward cracks onset for specimens with different crack length, $\lambda_x = 1$. a) Frame corresponding to analogue test performed on cross-shaped specimen (image from [37]) b-c-d) Square specimen.*

The present fracture behaviour is, for both the compounds, qualitatively in agreement with results of a previous work [38] performed on cross-shaped specimens, and reported in appendix B. A difference observed was in the sideways cracks length for the same applied λ_x: it was noticeably shorter for the square specimen without corners here used compared with that of the cross-shaped specimen used in [38]. This could be due to the different initial notch length adopted for the two specimens:$4mm$ for the cross-shaped specimen and $16mm$ for the square one. Two NR50 specimens with central cracks of 4 and $8mm$ were therefore prepared and tested with $\lambda_x = 1$. Frames from video recording of the tests at forward cracks onset are reported in figure 4.16. The sideways cracks length was found to be a function of the

initial crack length, with the $4mm$ crack behaviour similar to cross shaped specimen one. Hence the initial crack length affects the sideways crack propagation, this is probably due to the interaction of the strain fields at the two crack tips. This phenomenon must be studied more in detail in the future in order to find out the minimum initial crack length to be used. Local and overall strains at sideways and forward cracks onset, crack dimensions and eccentricity at sideways cracks onset are reported in table 4.2.

Table 4.2: *Overall and local strains at sideways and forward cracks onset, deformed crack dimensions a and b and corresponding eccentricity e in biaxial fracture tests.*

		Sideways cracks onset				Forward crack onset				Deformed crack dimensions			
Compound	λ_x	ε_{xov}	ε_{yov}	ε_{xloc}	ε_{yloc}	ε_{xov}	ε_{yov}	ε_{xloc}	ε_{yloc}		a [mm]	b [mm]	e
NR0	1	-	-	-	-	0	0.80	-0.18	2.70	•	19.11	23.29	0.42
NR0	2	-	-	-	-	1	0.04	0.76	0.96	•	33.76	11.82	0.80
NR50	1	0.00	0.29	-0.12	0.94	0	0.81	-0.16	1.84	†	15.00	8.23	0.67
NR50	1.2	0.20	0.17	0.08	0.68	0.20	0.81	-0.004	1.72	†	17.82	6.79	0.78
NR50	1.5	0.50	0.09	0.35	0.51	0.50	0.12	0.33	0.69	†	22.61	5.58	0.86
NR50	2	-	-	-	-	1	-0.10	0.92	0.086	•	29.88	2.82	0.95
NR50(4mm)	1	0	0.70	-0.15	1.43	0	1.77	-0.22	2.54	†	3.82	2.08	0.67
NR50(8mm)	1	0	0.60	-0.13	1.17	0	1.39	-0.16	2.11	†	6.44	4.88	0.49

† at Sideways cracks onset
• at Forward cracks onset

4.2.2 Strain fields around the crack tip

Some preliminary analysis of the strain fields around the crack tip have been performed and will be presented in this section although this part of the work is still in progress.

Figure 4.17 reports for the NR0 compound contour plots of the ε_y Hencky strain and biaxiality at forward crack onset for $\lambda_x = 1$ and 2, on the reference specimen-configuration. The ε_y fields are very different in the two cases considered: for the test with no pre-drawing the strain intensification and the volume of the zone where there is strain intensification are larger than in the test with $\lambda_x = 2$. In the latter the strain intensification was confined to a small volume of material near to the crack tip with the surrounding material almost unloaded in y-direction. The biaxiality contour plots show how the material near to the crack tip was subjected to different loading conditions in the two cases: under no pre-drawing the material near to the crack tip results to be almost under uniaxial tension, while for $\lambda_x = 2$ the crack tip was subjected to biaxial tension. On the biaxiality contour plots maximum in-plane principal strain directions are indicated by arrows, it may be a first indication of the material orientation direction but not quantify its magnitude. In the following this direction has been called "orientation". It can be observed that in the case of $\lambda_x = 1$ the material at forward cracks onset is mainly "oriented" uniformly in the y-direction: only the "orientation" along the crack faces is tangent to the faces and the zones above and below the crack appear to be in biaxial extension. Considering $\lambda_x = 2$ the material was "oriented" almost uniformly in the x-direction apart from a small zone at the two crack tips. In figure 4.17, a detail of the biaxiality contour plot near to the crack tip was also reported for the two cases, it can be observed very near to the crack tip the material was "oriented" in the y-direction even in the case of $\lambda_x = 2$.

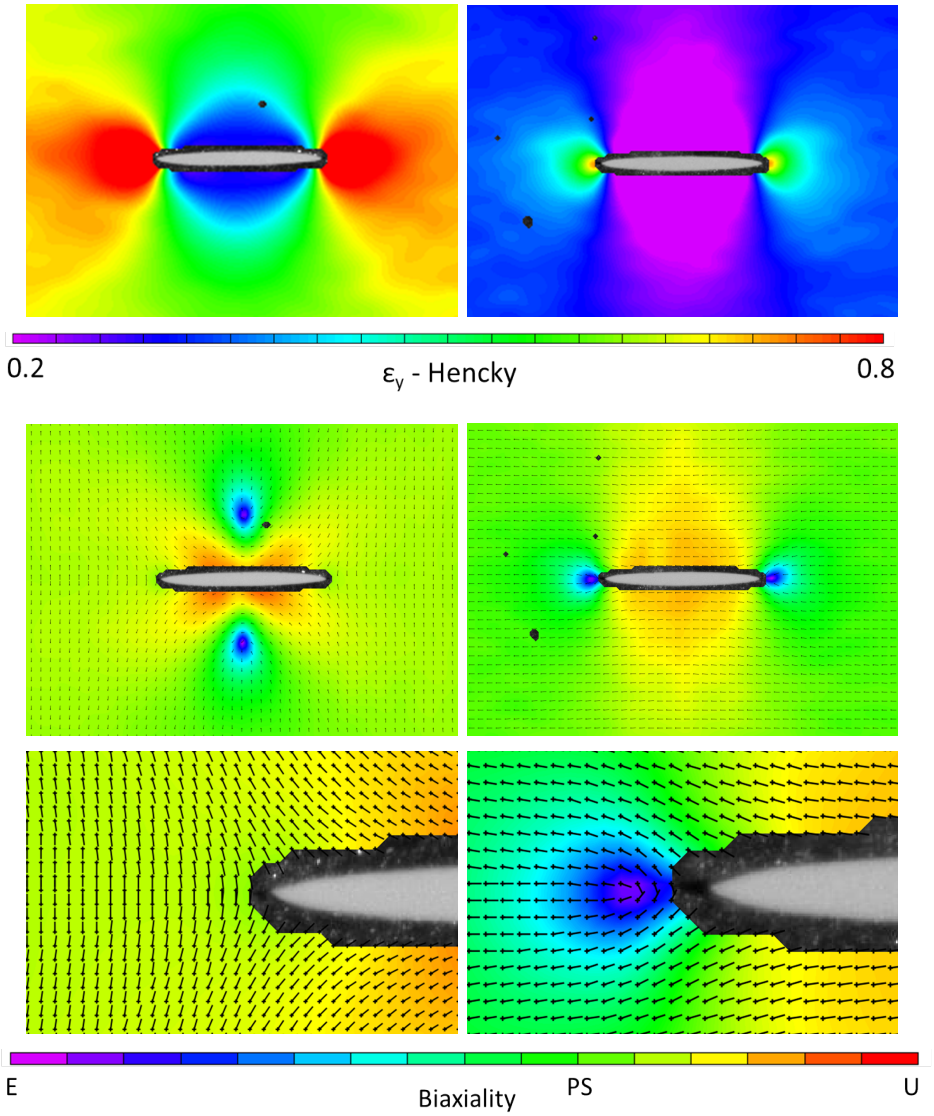

Figure 4.17: *NR0 - ε_y Hencky strain field and biaxiality contour plots for $\lambda_x = 1$ (left) and 2 (right).*

Figure 4.19 reports the biaxiality contour plots near to the crack tip for the NR50 compound both at forward and sideways cracks onset as a function of the applied λ_x. The "orientation" is also reported with arrows. As can be observed at sideways cracks onset it exist at least a small region in front of the crack tip in which the material is "oriented" in the y-direction, even if it is uniaxially deformed for $\lambda_x = 1$ and 1.2 and biaxially deformed for $\lambda_x = 1.5$. The size of the zone in which the material is y-"oriented" decreases as λ_x increases at both sideways and forward cracks onset: for $\lambda_x = 1.5$ only one measure point results to be y-"oriented" in front of the crack tip, for $\lambda_x = 2$ the material at forward crack onset results to be x-"oriented" even in the nearest points to the crack tip that can be analysed with the images resolution here adopted. Figure 4.18 reports the "orientation" angle gamma (with respect to the x-direction) as a function of test time for the nearest measure point to crack tip, sideways cracks onset is also reported as full dots. It can be observed that sideways cracks always occur when the material near to the crack tip is "oriented" in the y-direction ($gamma = 90deg$). This condition is necessary but not sufficient for sideways cracks propagation, in fact for $\lambda_x = 1$ gamma is equal to $90deg$ immediately after the beginning of the test but sideways cracks start to propagate after a while, probably when sufficient energy is available. For $\lambda_x = 1.5$ sideways cracks immediately propagate when gamma reach the value of $90deg$, probably because the energy was already available due to the loading in x-direction applied during the drawing step. Combining the fracture phenomenology observed in section 4.2.1 with those results about material "orientation" it can be concluded that sideways cracks need at least a small amount of "oriented" material in the direction perpendicular to the notch plane in order to propagate and that the propagation length can be related to the size of the y-oriented zone in front of the crack tip. This confirms that the anisotropy induced by orientation is a necessary condition to observe sideways cracks. When the material reach the critical condition for forward crack onset with no y-"oriented" material in front of the crack tip, as is the case for $\lambda_x = 2$, no sideways cracks are observed and the fracture toughness is strongly reduced as will be discussed in section 4.2.3.

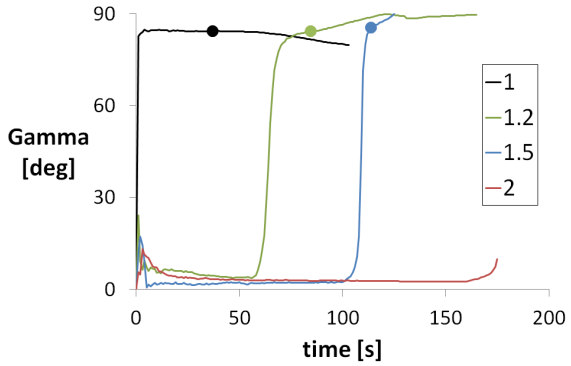

Figure 4.18: *"orientation" angle gamma as a function of testing time; full dots correspond to sideways cracks onset.*

4.2.3 Fracture toughness

The critical energy release rate at forward cracks onset under biaxial loading conditions were evaluated by means of finite element method using the submodel described in section 2.7. Material parameters given in table 3.3 were used to describe the mechanical behaviour of NR0 and NR50 compounds in the model. FEM simulations were performed for all the tests reported in table 4.2, the overall dimensions of the deformed cracks were used in order to check the reliability of the results obtained. Figure 4.20 reports the obtained crack dimensions from FEM simulations as a function of the measured values (reported for each specimen and loading condition in table 4.2). Even if good agreement between predicted and experimental values was found (less than 10% with exception of few cases), it must be underlined that all the points in both horizontal and vertical direction lie below the bisector. This is an indicator that the FEM model response was still stiff. Better agreement was obtained for NR50 compared to NR0, this is probably due to the better fitting obtained for the material mechanical behaviour as discussed in section 3.4.

Tearing energy at forward cracks onset was evaluated by the J-integral. in the finite element model geometry has not been adapted to take into account the propagation of sideways cracks: the obtained values must be considered as an "apparent" value. Table 4.3 reports the obtained J_c values

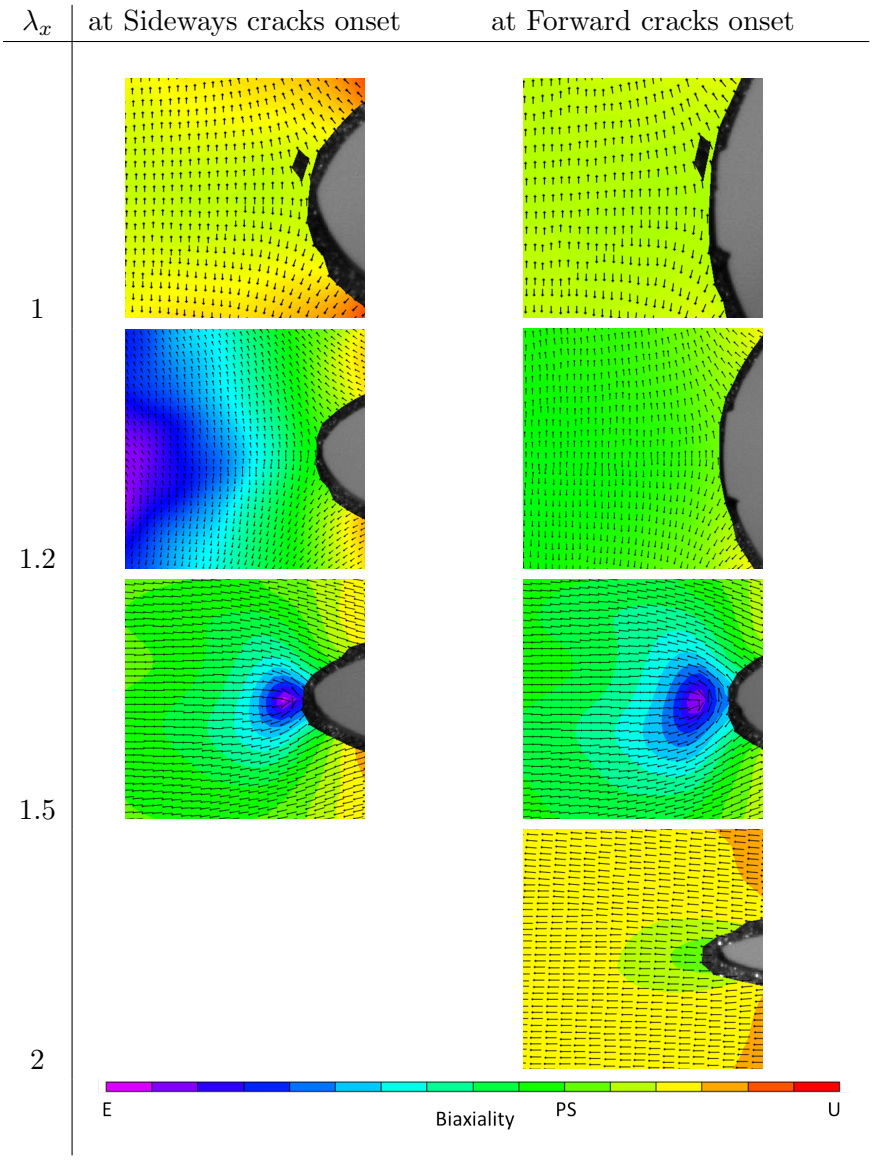

Figure 4.19: *NR50 - Biaxiality contour plots with "orientation" arrows for different applied λ_x at forward and sideways cracks onset.*

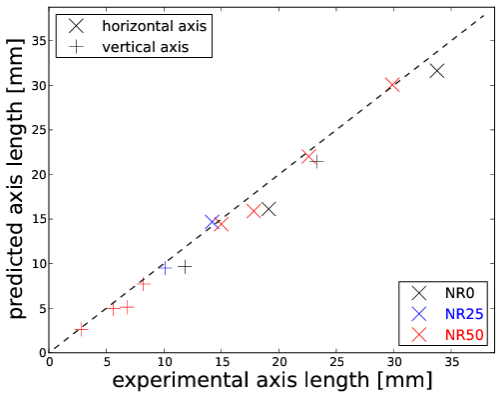

Figure 4.20: *Cracks dimensions obtained from FEM simulations as a function of the measured values for different compounds and biaxial loading configurations, broken line indicates the bisector.*

for the different compounds and biaxial loading conditions. The tearing

Table 4.3: *J_c at forward cracks onset obtained from FEM model for different compounds and biaxial loading conditions.*

Compound	λ_x	$J_c \left[\frac{kJ}{m^2}\right]$
NR0	1	10.1
NR0	2	2.3
NR50	1	21.7
NR50	1.2	21.7
NR50	1.5	1.9
NR50	2	0.6
NR50(4mm)	1	23.4
NR50(8mm)	1	23.4

energy obtained for no pre-drawing test (i.e. $\lambda_x = 1$) at forward propagation was expected to be equal to the total tearing energy obtained from fracture tests in pure shear loading as reported in table 4.1. The obtained values was found to be inside the experimental error for NR0 and slightly lower for NR50, probably due to the fact that the FEM model fail to take in account of sideways cracks propagation. Better results can be probably achieved improving materials stress-strain characterization. For NR0 compound it

can be observed that the J_c value for an imposed $\lambda_x = 2$ was significantly lower ($\approx 23\%$) with respect to the J_c obtained for an imposed $\lambda_x = 1$. NR50 shows a similar trend of the fracture resistance as a function of the imposed pre-drawing λ_x, with the fracture resistance for $\lambda_x = 2$ being only $\approx 3\%$ of the corresponding value obtained with $\lambda_x = 1$. No remarkable difference was found in J_c at forward onset for the specimens with $4mm$ and $8mm$ and $16mm$ crack lengths. This result is interesting because those three specimen differs experimentally in sideways cracks propagation and for the overall applied strains at forward crack onset, but the obtained J_c value does not change even if the FE model does not take in account sideways cracks. Those results are encouraging and can be improved in terms of absolute values and reliability by a more accurate stress strain characterization and including the modified crack geometry in order to take in account for sideways cracks.

Chapter 5

Biaxial dynamic characterization

5.1 Introduction

The overall aim of the research carried out during the period of six months spent at the **"Leibniz-Institute of Polymer Research Dresden e. V. (IPF)"** was to study the rubber properties in biaxial dynamic loading conditions, both for the characterization of the stress-strain behaviour and fatigue crack growth.

The period at the Institute was spent almost in equal parts for the optimization of the testing machine and the test on the rubber compounds properties. Preliminary tests were carried out for the implementation of the digital image correlation, here performed with 2D ARAMIS software, for the acquisition of the load-displacement curves corrected for inertia and friction, and for specimens clamping. After finishing the optimization of the experimental apparatus compounds reported in table 2.3 were characterized in dynamic biaxial stress condition.

5.2 Biaxial tester and testing set-up optimization

5.2.1 Biaxial tester optimization

The dynamic biaxial tester provided by Coesfeld Materilatest, described in section 2.1.2, was a prototype and required quite some work for the development and optimization of both software and hardware. For the first three months of the stay in IPF most of the work has been devoted to the optimization of the biaxial tester itself, in particular, time was spent on the following topics:

- **Images acquisition:** In order to make the system useful for DIC analysis a snapshot function for image acquisition of the undeformed specimen was integrated, and another function was introduced into the software in order to have the possibility to acquire the surface image with top light and the crack image with bottom light in different position with respect to the displacement cycle.

- **Clamping system:** The type of clamping system chosen by Coesfeld, shown in figure 2.5 provides that each clamp slides through a single linear guide. The sliding rails are housed on an aluminium frame with 3 steps, none of the levels of these steps coincides with the plane of force application. This leads to a torsional load on the linear guides that inevitably generates friction, this friction is then recorded by the load cells causing noise on the output signal. The problem of friction was only partially solved by a careful alignment of the clamping system.

  Another problem examined was the effect of the gripping pressure of the clamps on the deformation field measured by DIC. The strain field homogeneity strongly depended on the correct specimen mounting (same pressure on all clamps) and on the pressure applied. Further applying large pressure caused during some preliminary fatigue propagation tests, failure of the specimens at the clamps. Therefore a new gripping system similar to the interference type already described in section 2.3.1 was made. Along with this system a suitable mold for specimens preparation was designed, however, due to the time required for mold production it was available only after the end of my

stay at IPF. The pressure clamps were appropriate for the square specimens obtained from vulcanized plates and were then used for the stress-strain characterization of NR, IR and SBR compounds shown in table 2.3. Once the clamps have been replaced has been necessary to use specimens with thick border that fits the new interference clamps. For this reason, the tests of fatigue crack growth were carried out on specimens with suitable geometry provided by TU Chemnitz, the composition of which was not provided.

- **Inertia forces:** Generated as a result of the cyclic motion of the motors, these forces are due to the interposed position of the load cells between the motor and the clamping system (see figure 2.3). The inertia was corrected by performing cyclic tests without specimen to measure the clamp weight, then the inertia force was evaluated by means of theoretical acceleration profile and compared with the measured value. Real test force readings were then filtered by subtraction of the theoretical inertia force. The obtained filter applied to the measured forces was tested by means of a series of cyclic tensile tests on spring with known stiffness, the results showed that the adopted correction apply from $0.1Hz$ up to $20Hz$;

- **PID control parameters:** The machine originally gave rise to vibrations even below $10Hz$, optimizing the PID it was possible to move the threshold of usability of the biaxial tester above $20Hz$;

5.2.2 Preliminary tests to verify digital image correlation technique

In order to test the capabilities of the ARAMIS software on measuring high strain gradients with the speckle pattern produced on the specimens surface (see section 2.6.1), a series of experiments were performed on SBR compound. Pairs of specimens with different patterns, one with only the central hole and one with a central hole with two opposite notches, have been subjected to similar loading conditions. The resulting strain fields were compared in order to assess whether the DIC software was able to detect the presence

of the notches with the pattern used. After paint and spraying optimization we have obtained the following results.

Specimen with central hole. The specimen was subjected to $2mm$ equibiaxial preload and then an equibiaxial $5Hz$ sinusoidal load cycle was applied with two different stroke levels: 6 and $10mm$. As the specimen is a square with $85mm$ side, applied strains are respectively 9.5% and 14%. These theoretical values can be compared with measured strains far from the hole to have a first validation of the software strain computation. Figure 5.1 reports for the two different overall strains the full-field strain maps and ε_y along the mid plane cross-section for the three applied strain levels corresponding to the preload and the two overall strains applied. The curve highlighted in red corresponds to the adjacent color map. The measured engineering strains in the area away from the hole are 8% and 12% respectively, so it results to be slightly less than the applied strain value. A strain concentration factor (also called normalized strain in what follows) was evaluated as the ratio between the measured local strain and the measured applied strain, this ratio is reported in figure 5.2 as a function of the distance from the hole. It can be highlighted that the strain near to the hole edge results to be 4 times the applied strain.

Specimen with central hole and notch. The presence of the sharp notch gave rise to unstable crack propagation and therefore this series tests were carried out with $2mm$ preload and $5Hz$ sinusoidal displacement cycles with only $4mm$ amplitude. The resulting applied equibiaxial strain was 7%. Under this condition stable crack propagation was observed during the application of cyclic loading. Aramis has proved to be able to measure the strain fields during propagation. Figure 5.3 shows the deformation fields recorded after 70 and $10'000cycles$.

Figure 5.5 reports the comparison of normalized strain intensification obtained in the two experiments described above. Far from defect, the deformation field is dominated by the discontinuity of the cross-section and thus appears to be the same for the two cases examined. Near to the defect the strain field is dominated by the radius of curvature of the crack tip and

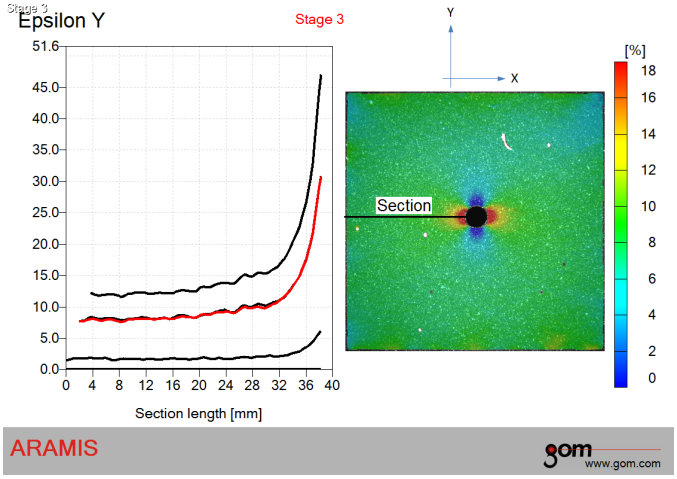

(a)

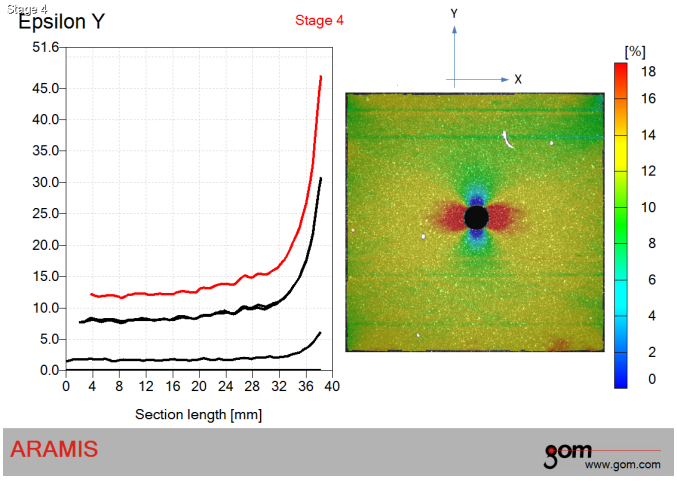

(b)

Figure 5.1: *Full-field y strain for the specimen with central hole, side graphs reports ε_y versus the distance from the specimen border, red line correspond to the adjacent strain field (applied equibiaxial strain: a) 7.5%; b) 14%).*

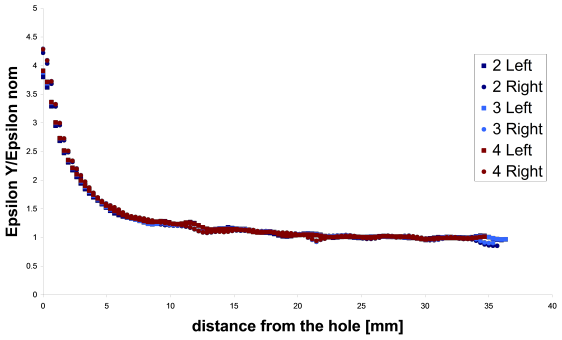

Figure 5.2: *Normalized ε_Y versus distance from the hole for both right and left hole side, numbers refers to different applied strain levels.*

results to be more intense for the sharp crack rather than to the hole. The objective of this series of tests was precisely to optimize the pattern used to measure the effect of a notch on the deformation field at small distances from the defect. The final result was satisfying, in fact near to the sharp crack the measured strain field intensified by 6-12 times while the intensification near to the circular hole edge is only 4 times. Figure 5.4 reports for different cycles during propagation the normalized strain as a function of the distance from the current crack tip position. Results are shown in figure 5.4. In this case the value of normalized deformation measured near the defect varies between 6 and 12 due to the problem of the measurement near to the crack tip. Nevertheless, the software has proved able to follow the strain concentration during crack propagation and showing that, a-part from the maximum value near the crack tip, the strain concentration appears to remain constant and travel together with crack.

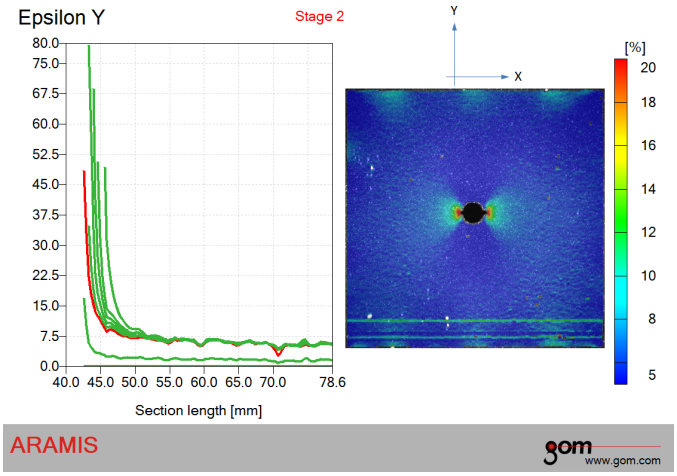

(a)

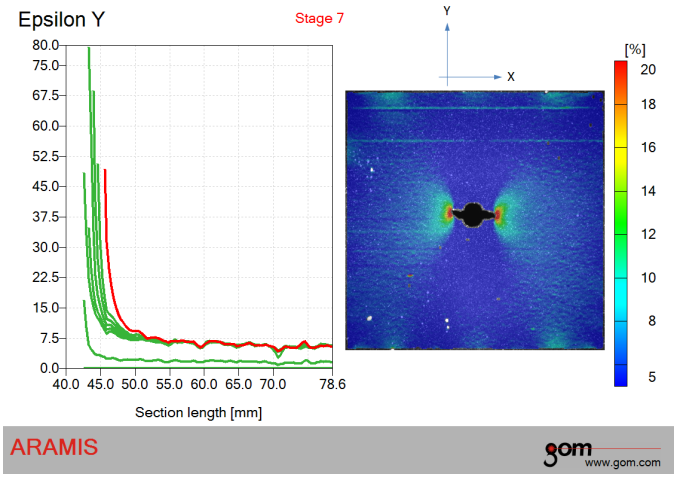

(b)

Figure 5.3: *Full-field y strain for the specimen with central hole and sharp notches, side graphs reports ε_y versus the distance from the specimen border, red line correspond to the adjacent strain field (applied cycles: a) 70; b) 10000).*

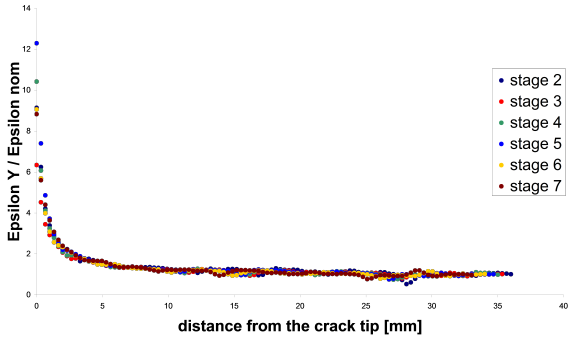

Figure 5.4: *Normalized ε_Y versus distance from the crack tip for specimen with hole and notches, stages numbers refers to different propagation lengths.*

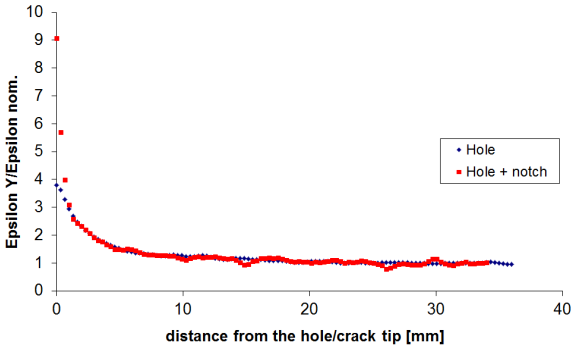

Figure 5.5: *Normalized ε_y versus distance from the hole/crack tip for both specimen with hole and with hole and notches.*

5.3 Dynamic stress-strain characterization of NR IR and SBR compounds

5.3.1 Testing conditions

A tension-tension sinusoidal $1Hz$ displacement was applied. An initial fixed displacement of $1mm$ was given in both directions to all specimens. The amplitude of the cyclic displacement was varied as reported in table 5.1. Results will be given in terms of engineering stress and strain.

Uniaxial Due to the unavoidable noise of the force signal and the low reaction force of the single strip specimen used for the uniaxial test described

Table 5.1: *Cyclic displacement amplitude and corresponding applied strain.*

Cycle Amplitude $[mm]$	Applied strain [%]
10	≈ 13
20	≈ 25
30	≈ 36
40	≈ 48
50	≈ 60

in section 2.3.2, three identical specimens were mounted together in parallel on the biaxial tester. So the stress-strain curve obtained was an average curve between that relevant to each specimen. In the following we refer to those three specimens as the uniaxial specimen. After that specimen was mounted 100 preconditioning cycles was applied at maximum strain ($\approx 60\%$) to ensure the overcoming of strain softening phenomena that always occurs during the first cycles. After that the characterization test was started: the specimen was subjected to 60 loading-unloading cycles for each strain level and the force-displacement cycle was recorded each 10 cycles.

Pure Shear and equibiaxial For both tests the same square specimen was used for each compound; it was mounted on the biaxial tester and then preconditioned with 100 cycles at the maximum equibiaxial strain. First the equibiaxial tests were performed. In this series of test displacement cycles amplitude given in table 5.1 were used in both directions symmetrically.

The pure shear tests were performed on the same specimen after the equibiaxial tests applying displacement cycles only in one direction. Just to ensure that the pure shear stress-strain curves obtained were not affected by fatigue/damage of the matrix due to the cyclic loading-unloading during equibiaxial tests, a further equibiaxial test at 60% strain was performed on each specimen after the end of the pure shear tests (this test will be referred as last test).

Even if the compounds had been cycled for 100 times at the maximum strain, during the tests at different strain levels of table 5.1 a slight decrease

of the maximum stress was observed during the first 4 cycles. To avoid the influence of this effect in the following the results shown will be always referred to the 55^{th} cycle.

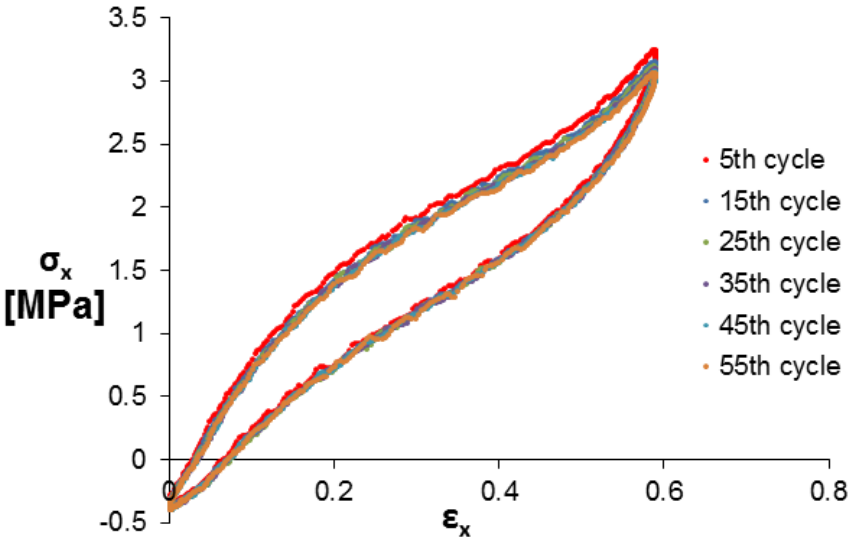

Figure 5.6: *Cyclic softening observed during first cycles of characterization tests.*

5.3.2 Results

Results of dynamic stress-strain characterization on NR, IR and SBR compound will be now reported and briefly commented. For each material a comparison between mechanical behaviour in different loading condition will be given for the cycle with maximum applied strain and the energy densities evaluated by equations (2.3)(2.4)(2.5).

Figure 5.7(a) reports results from uniaxial tests, it can be noted that dissipation occurs even at low strain. Even using three specimens in parallel connection data for uniaxial loading remains seriously affected by noise due to the low strip specimens reaction forces compared to the full scale of the load cell.

Figure 5.8(a) reports data for pure shear loading cycles. With the larger square specimen forces are higher and noise is less important.

Figure 5.9(a) reports data for equibiaxial loading cycles. Results are

given only for one direction, but the recorded stress strain cycles in both directions were identical. The curve labelled "last test" as mentioned above refers to the equibiaxial control test performed after the end of the characterization tests in PS loading and it can be observed that it coincides with the previous cycling at the same strain.

For IR and SBR compounds similar results were obtained.

Figures 5.10(a) 5.11(a) 5.12(a) report a comparison of mechanical behaviour in different loading conditions for NR, IR and SBR respectively. Materials results to be stiffer passing from uniaxial, to pure shear, to equibiaxial loading conditions, showing a greater propensity to the phenomenon of strain hardening (upturn) under equibiaxial loading conditions. For NR and IR the increase in stiffness passing from U to PS loading conditions seems to be due to higher of elastically stored energy, in fact the dissipated energy is almost the same. The SBR rubber shows a small increase of dissipation passing from U to PS.

In figure 5.13 the mechanical behaviour of the three characterized compounds is compared with respect to the three loading conditions considered. NR and IR rubbers gave virtually indistinguishable results, probably due to the fact that the maximum deflection reached during this series of characterization tests is below the threshold of strain induced crystallization. The SBR was found to be the stiffer in all loading conditions, it shows the highest value of residual strain both in loading and unloading and a greater propensity to dissipation of energy. This last point can be examined in more detail by means of the percentage energy components calculated from the equation (2.6) and shown in Figure 5.14. The results for the IR compound will be omitted as they are identical to those observed for the NR compound. All the compounds considered have shown an increase of $W_e\%$ as the maximum applied strain increases in the case of U loading and less markedly in PS, this increase shows a trend to plateau on reaching a maximum value equal to approximately 80% for NR and IR, and to 70% for the SBR. In the case of E loading for all the compounds a constant value of $W_e\%$ was observed, equal to the maximum observed in the other two cases.

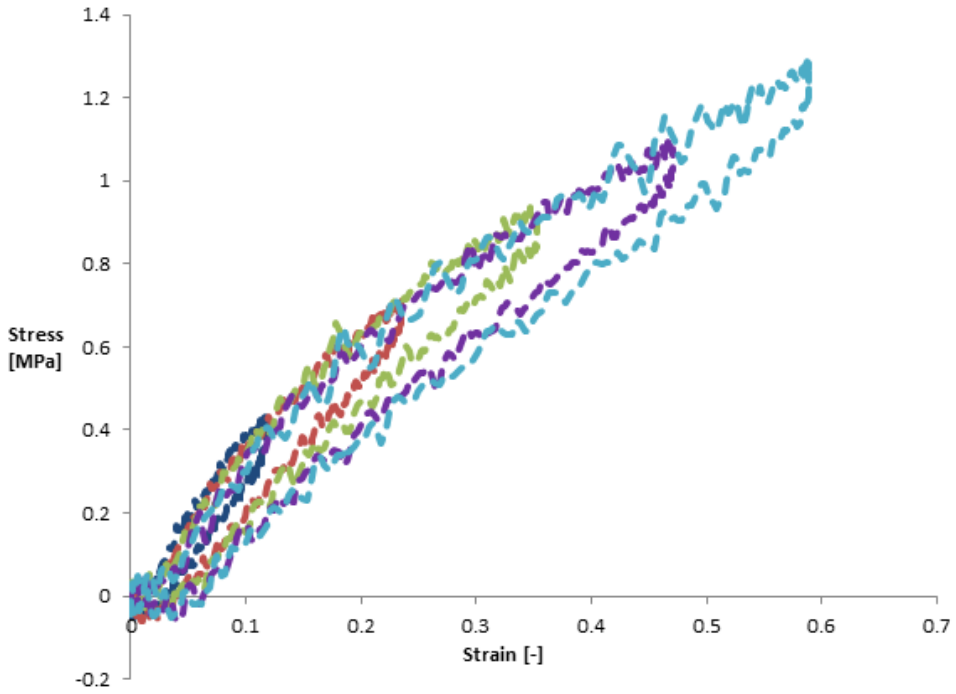

(a)

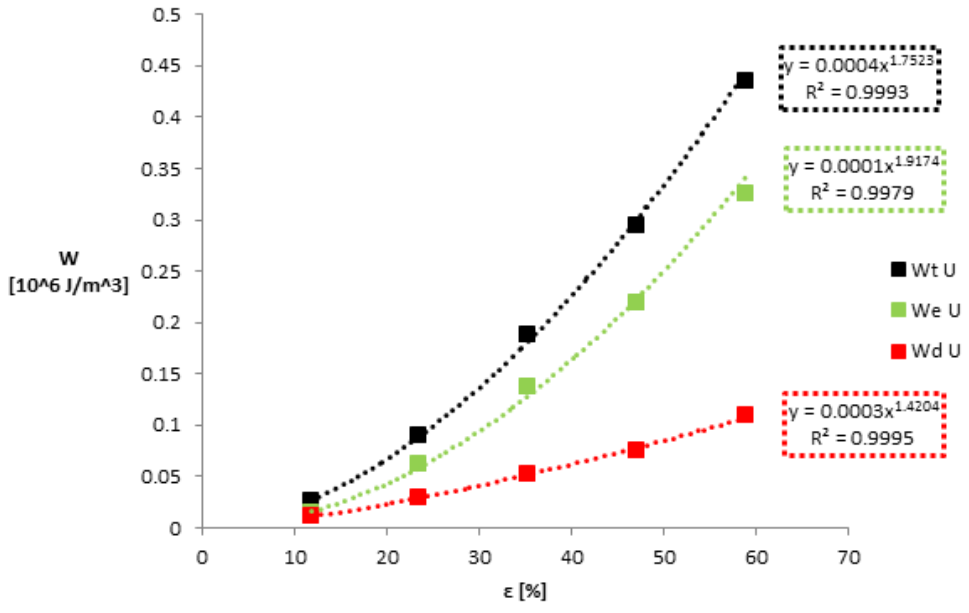

(b)

Figure 5.7: *NR U dynamic loading characterization. a) stress-strain cycles; b) energy density components.*

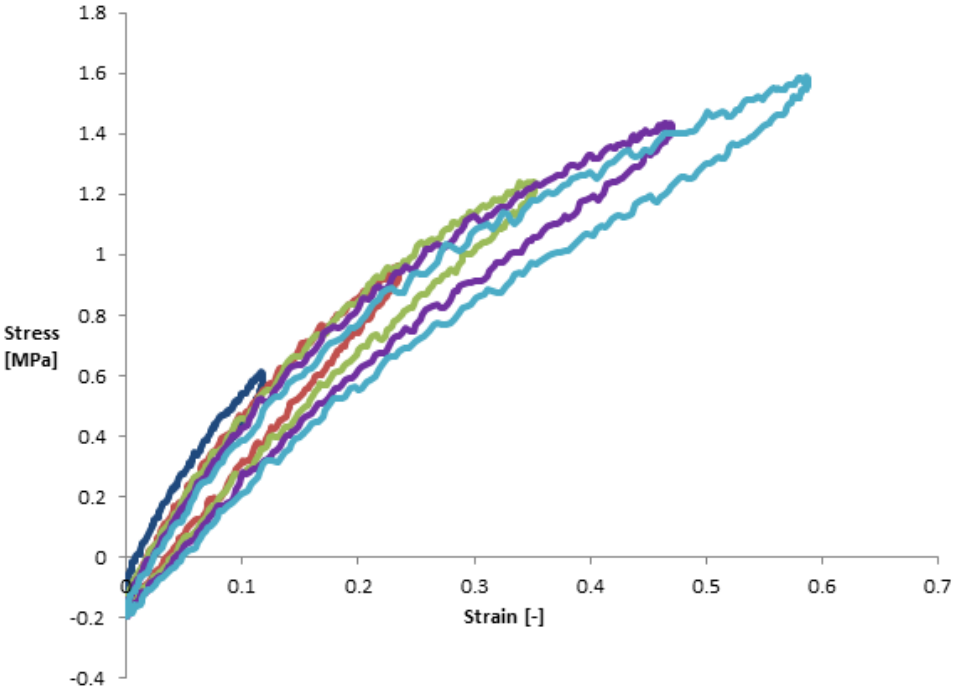

(a)

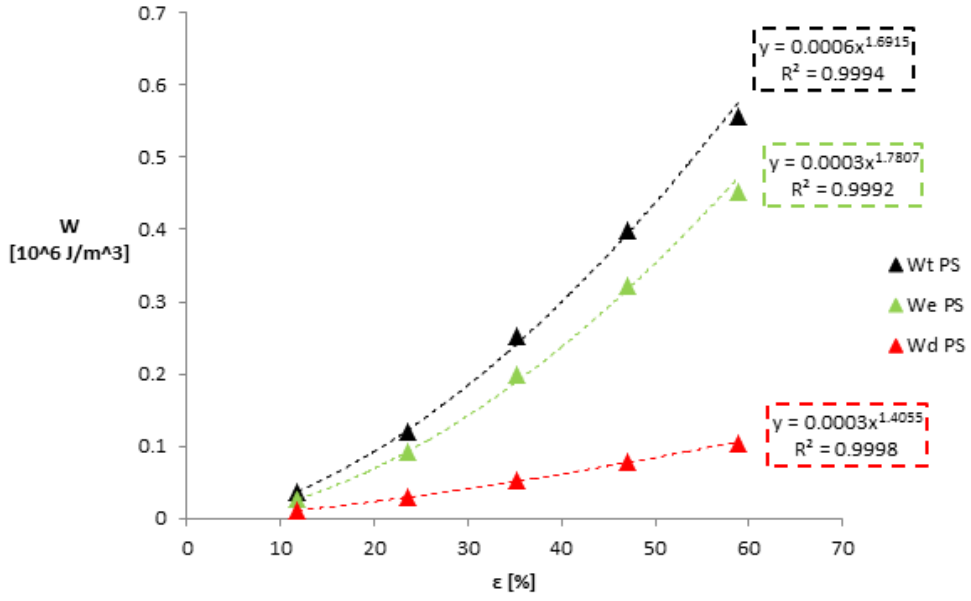

(b)

Figure 5.8: *NR PS dynamic loading characterization. a) stress-strain cycles; b) energy density components.*

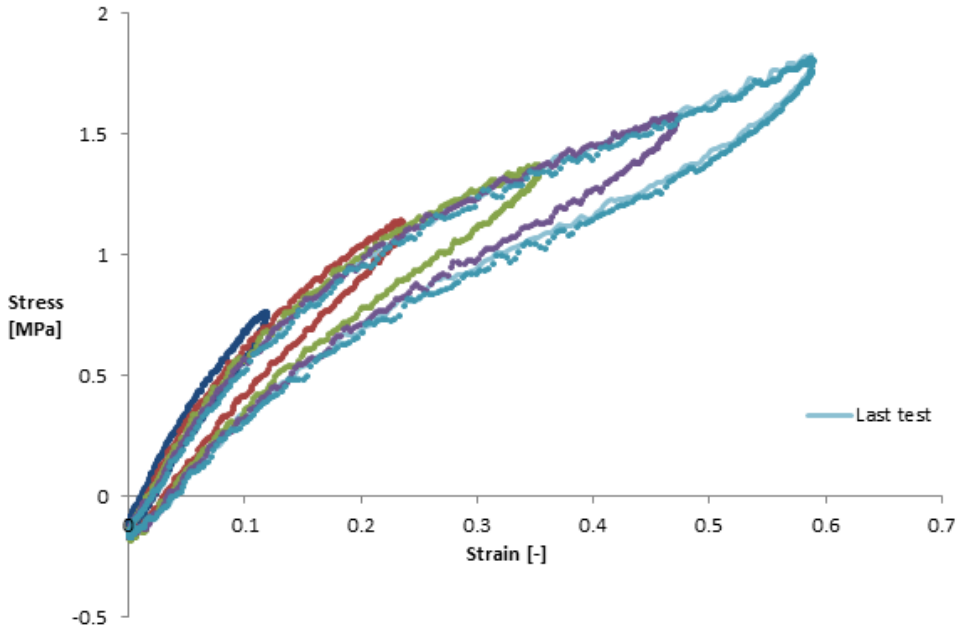

(a)

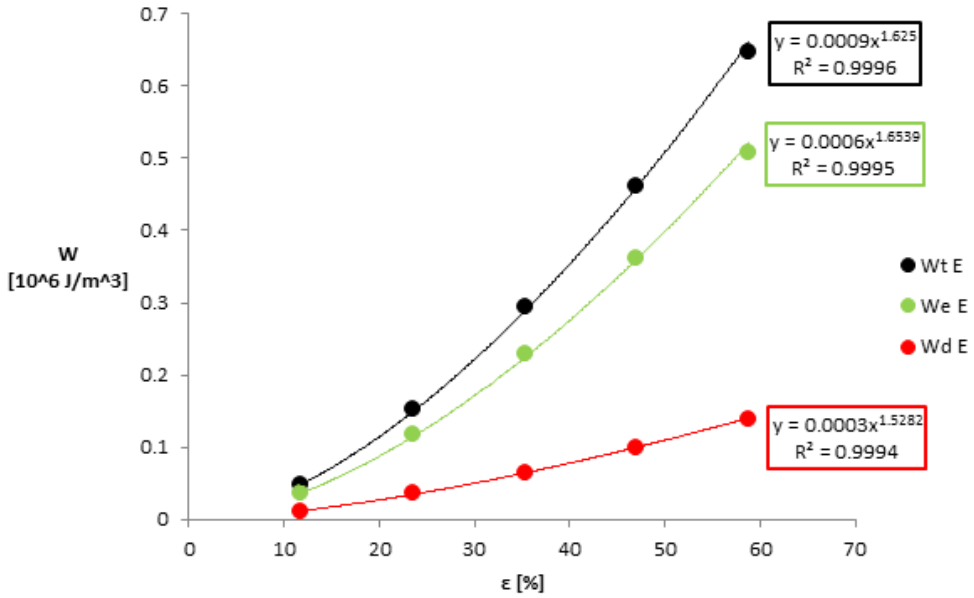

(b)

Figure 5.9: *NR E dynamic loading characterization. a) stress-strain cycles; b) energy density components.*

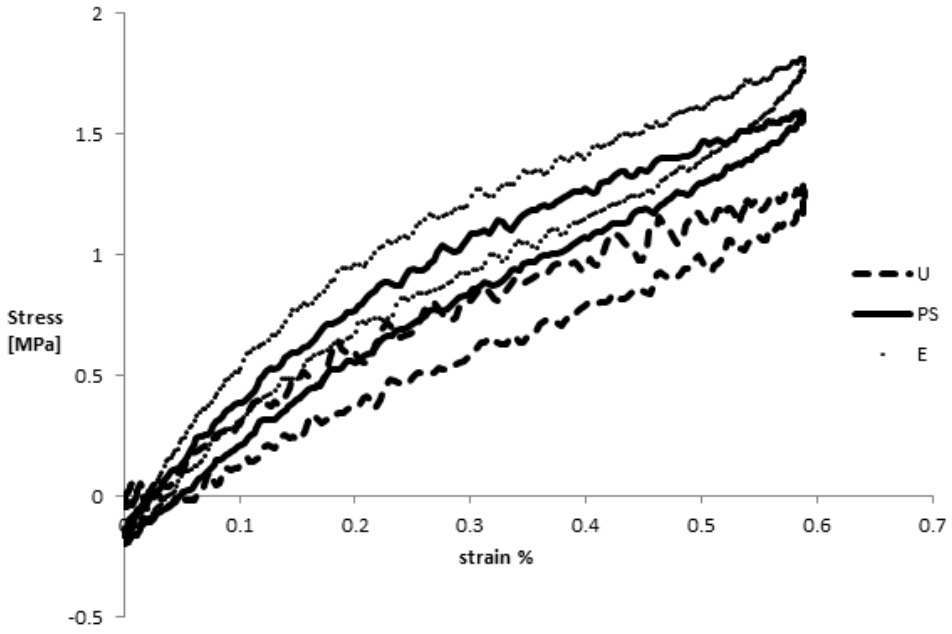

(a)

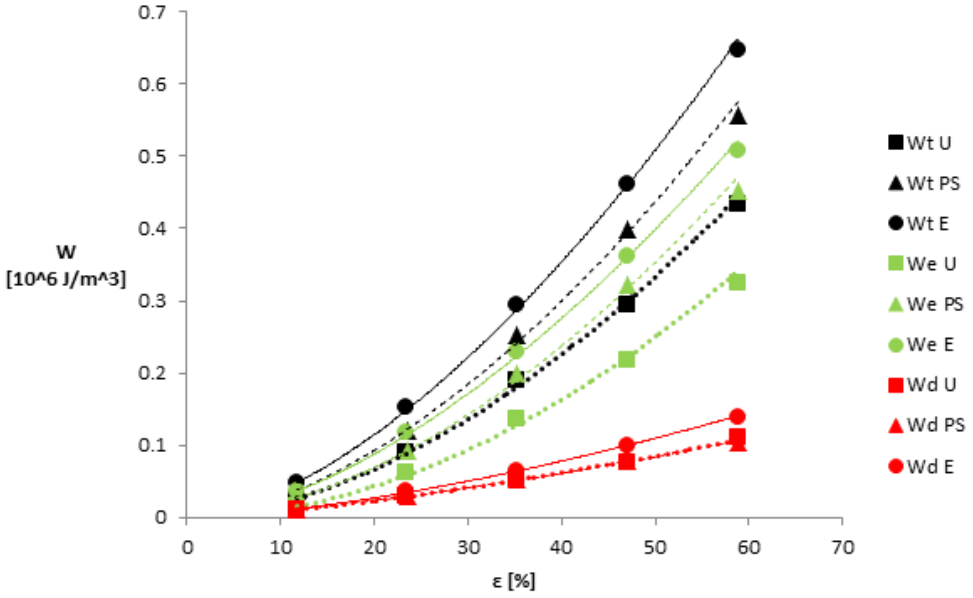

(b)

Figure 5.10: *Comparison between mechanical behaviour in different loading conditions for NR compound. a) stress-strain cycles; b) energy density components.*

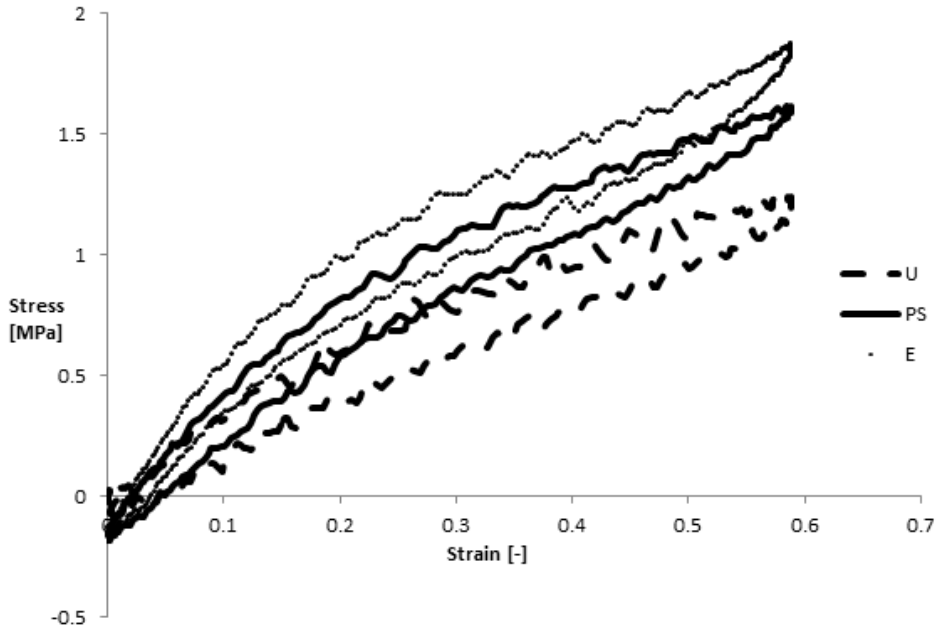

(a)

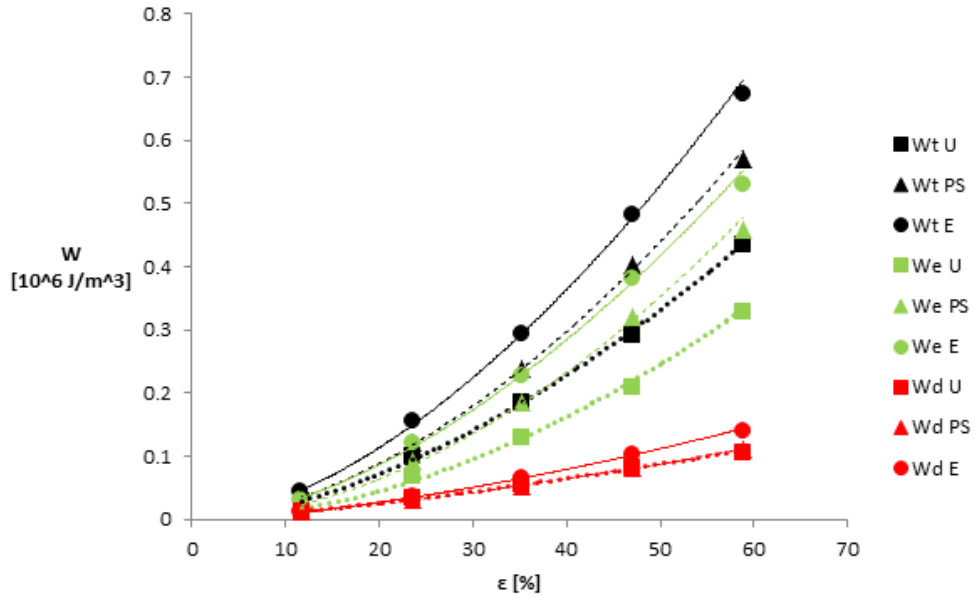

(b)

Figure 5.11: *Comparison between mechanical behaviour in different loading conditions for IR compound. a) stress-strain cycles; b) energy density components.*

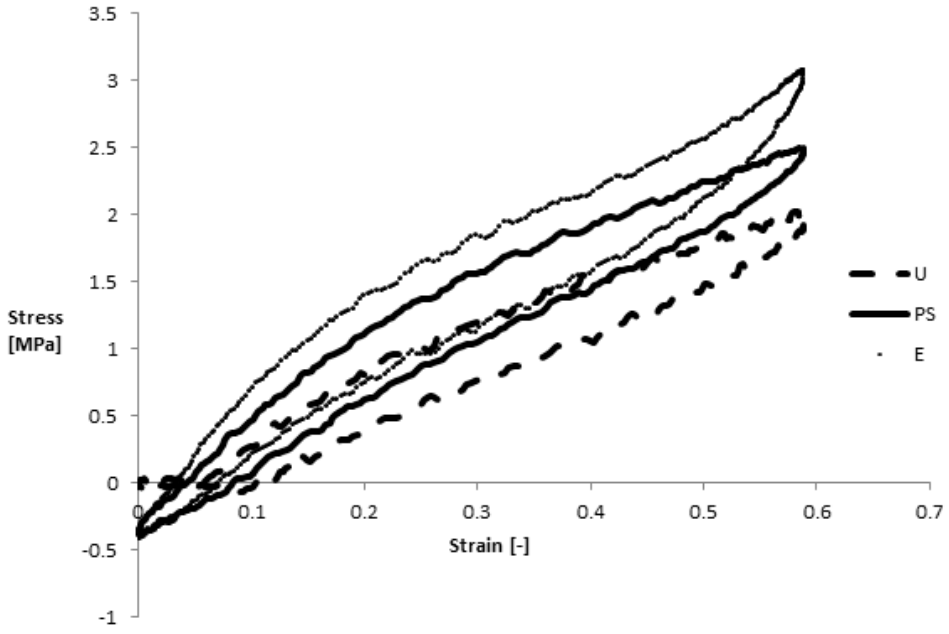

(a)

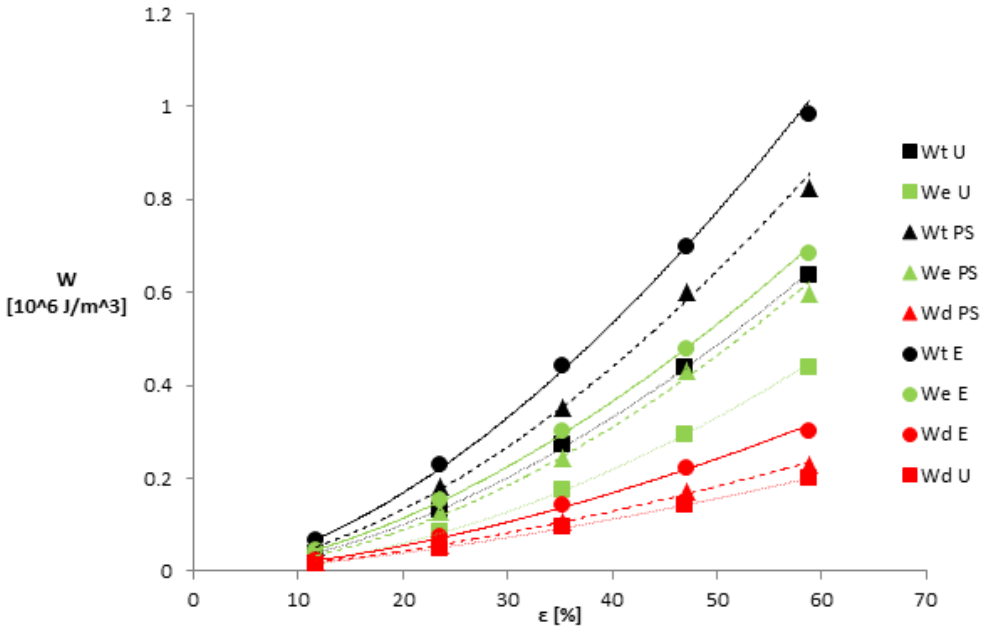

(b)

Figure 5.12: *Comparison between mechanical behaviour in different loading conditions for SBR compound. a) stress-strain cycles; b) energy density components.*

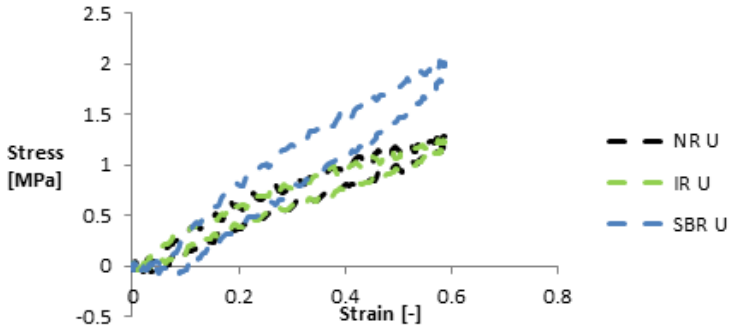

(a)

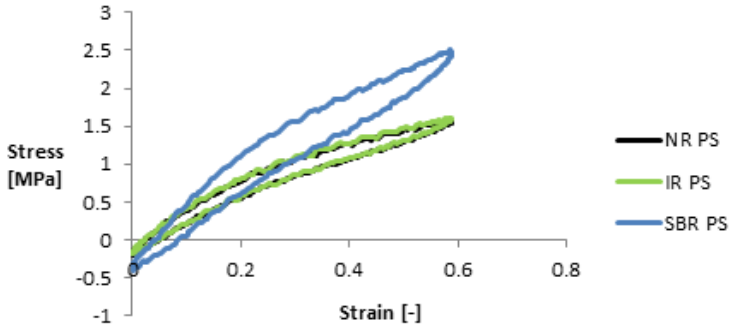

(b)

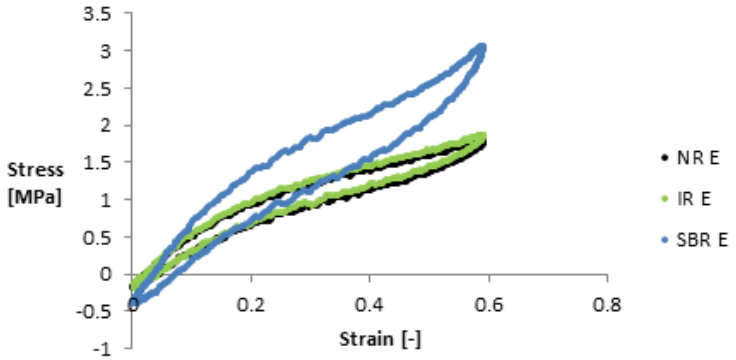

(c)

Figure 5.13: *Comparison between mechanical behaviour of NR IR and SBR rubbers when subjected to uniaxial (a), pure shear (b) and equibiaxial (c) dynamical loading conditions.*

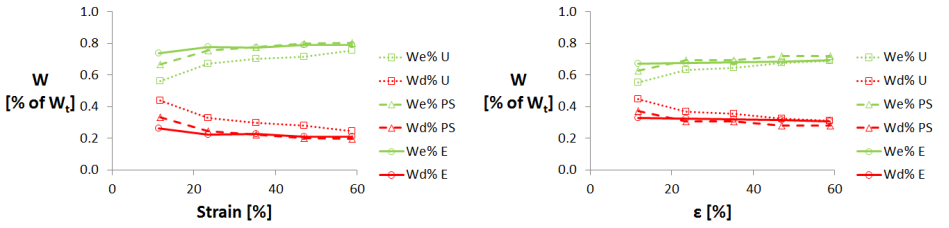

(a) (b)

Figure 5.14: *Elastically stored energy density W_e and dissipated energy density W_d as a percentage of W_t for different strain levels and loading conditions. a)NR and IR b)SBR.*

5.4 Dynamic stress-strain and fatigue characterization of Ch compound

As already explained in the introduction to this chapter the test of propagation of the defect in dynamic loading conditions was performed on a specimen of a different material than those just described, called Ch compound. The specimens used were squares of side $110mm$ thickness $2mm$ and with circular edges of radius $2mm$ needed for mounting of the specimen with the new interference clamps. Being the maximum displacement of the motors of the machine a fixed quantity, the larger size of this specimen results in a reduction of the maximum strain that can be applied from 60% to 33%.

5.4.1 Dynamic stress-strain characterization

The stress-strain behaviour was characterized in 32 different biaxial loading conditions schematically summarized in figure 5.15. Sinusoidal displacement profiles were used with frequency equal to $1Hz$, no preload was used. Before the beginning of the characterization tests the specimen was preconditioned by application of 500 load cycles at maximum equibiaxial strain. The stress-strain curves for each load configuration were recorded after 100 load cycles in order to reach a stationary behaviour. In figure 5.16 the stress strain curves recorded for maximum strain cycles (33%) are reported, transverse strain increasing from 0% (PS) to 33% (E). Increasing the transverse strain applied, the material is progressively stiffer and shows a progressive tendency

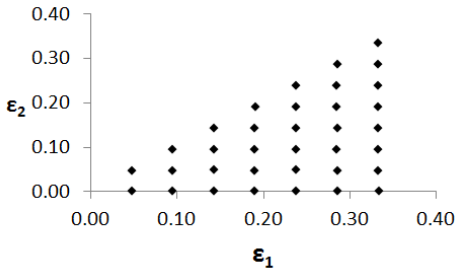

Figure 5.15: *Loading configurations used for Ch compound characterization.*

to the phenomenon of strain hardening.

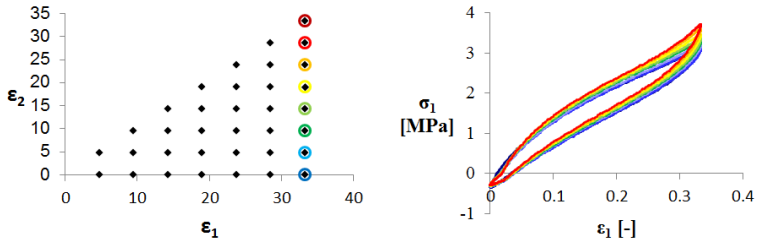

(a) (b)

Figure 5.16: *Stress strain cycles recorded for Ch compound passing from PS (blue) to equibiaxial (red) configurations.*

Due to the large number of test performed results will be given directly in terms of elastically stored strain energy density W_e by means of the three-dimensional plot shown in figure 5.17(a), it reports W_e as a function of the applied strain configuration $(\varepsilon_1; \varepsilon_2)$. Experimental values of W_e as a function of applied strain configuration were then fitted with Gent's model (section 1.5 equation (1.49)), the resulting parameters were $E = 6.25MPa$ and $I_m = 80$. As can be seen in figure 5.17(b) there is a fairly good agreement between experimental data and model prediction.

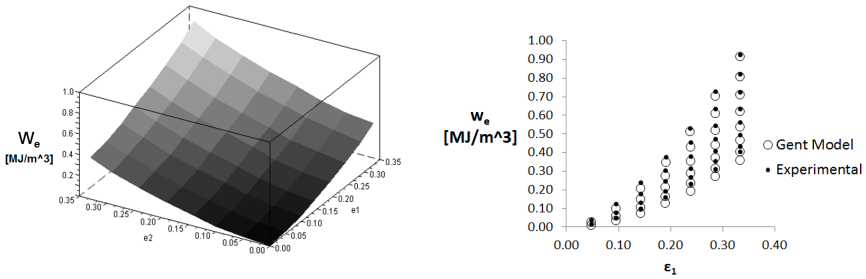

(a) (b)

Figure 5.17: *Results of characterization tests for Ch compound: a) W_e as a function of $(\varepsilon_1; \varepsilon_2)$; b) Experimental data and Gent model prediction, projection on $\varepsilon_2 = 0$ plane.*

5.4.2 Fatigue crack growth

5.4.2.1 Testing conditions

For crack propagation test on Ch compound specimen were first subjected to preconditioning of $500 cycles$ of equibiaxial deformation with sinusoidal displacement profile, amplitude $35mm$ ("$\varepsilon = 33\%$") and frequency $1Hz$. After preconditioning the specimens were notched on a single edge to a depth of $30mm$ using a sharp razor blade, specimen was then mounted on the biaxial tester with the notch oriented as direction 2. Two tests were performed, one in PS and one in biaxial loading conditions. For both tests a sinusoidal $1Hz$ displacement cycle was applied, the amplitudes of the cycles used in the two loading directions are reported in table 5.2. Note that for the biaxial loading condition the applied strain parallel to the original notch was chosen to be higher with respect to the strain applied in the perpendicular direction.

5.4.2.2 Tearing energy evaluation from DIC data

The problem of assessing the energy release rate resulting from the propagation of a defect in a specimen is one of the central arguments with which one must deal in the study of fracture properties of the rubbers and materials in general. If the specimen has a geometry such that it is possible to calculate

Table 5.2: *Fatigue crack propagation. Displacement cycles amplitude and corresponding applied strain.*

	Direction 1		Direction 2	
	Cycle Amplitude	ε	Cycle Amplitude	ε
Load case	$[mm]$	$[\%]$	$[mm]$	$[\%]$
Pure shear	30	≈ 27	0	0
Biaxial	20	≈ 18	35	≈ 32

directly the tearing energy applied by some theoretical assumptions, as in the case of pure shear specimen [48] or strip with edge cut in simple tension [71], the problem has a simple solution. In the case of fatigue tests on a square specimen, however, these simplifications cannot be done and the calculation of the energy release rate becomes more complicated. Generally the problem is solved by finite element analysis. In this part of the work an attempt has been made to develop a technique for the direct calculation of the tearing energy from experimental data, based on the measurement of the variation of the deformation field resulting from the propagation of the defect. The proposed method has the advantage of being independent from the specimen geometry, provided that there are suitable conditions to perform a measurement of the strain field by the technique of digital images correlation. The method introduced here is schematically shown by the flowchart in figure 5.18, and is applicable only to the case of plane stress. It consists of recording the images of the specimen surface during the propagation of the defect by which it is possible to determine the strain field using the digital image correlation. Once the strain field is obtained for a generic cycle an elastic strain energy density value can be associated to each measurement point through the constitutive model obtained from characterization tests. The total elastic energy contained in the specimen in a given cycle can be easily calculated by summing the strain energy density values obtained for each measure point (index i of the sum in the flowchart runs over measure points) and multiplying this sum by the elementary volume ΔV, the value of which is determined by the square of the spacing between the measures (square grid) multiplied by the specimen thickness. This meas-

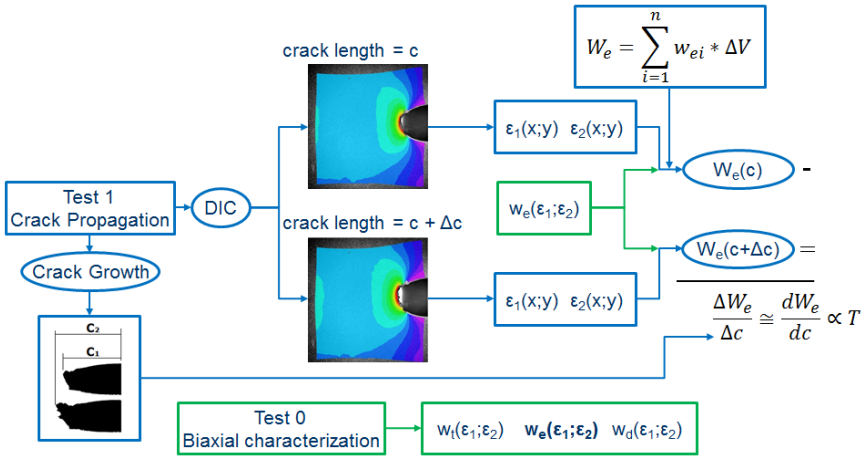

Figure 5.18: *Flowchart of the proposed technique for tearing energy evaluation from strain full-field measured by DIC.*

ure of the total elastic energy contained in the specimen must be repeated on two cycles images that differs only for the crack length, the difference of the total elastic energy between the two frames ΔW_e will therefore be the variation of elastic energy due the crack growth Δc measured as described in section 2.5.3. If the work done by the external forces can be considered to be constant, as it is the case here being images collected always in motion inversion point of the sinusoidal displacement cycle (i.e. at maximum displacement), the difference in elastic energy content measured between two cycles is proportional to the tearing energy through its definition:

$$T = -\frac{1}{t}\left(\frac{\partial W_e}{\partial c}\right)_L \tag{5.1}$$

where t is the specimen thickness, c is the crack length and L is the work of external forces. Method accuracy in energy release rate calculation depends essentially on the accuracy with which the constitutive model used represents the mechanical behaviour of the material.

5.4.2.3 Results

The technique described in section 5.4.2.2 was used to calculate the tearing energy applied in the two tests of fatigue crack growth described in section

5.4.2.1, crack growth rate was obtained as described in section 2.5.3. The results obtained are summarized in table 5.3. In order to obtain feedback

Table 5.3: *Fatigue crack propagation tests. Measured tearing energy and crack growth rate.*

Load case	T $\left[\frac{kJ}{m^2}\right]$	$\frac{dc}{dN}\left[\frac{mm}{cycle}\right]$
Pure shear	4.37	$7.8 * 10^{-4}$
Biaxial	1.2	$1.2 * 10^{-3}$

regarding the reliability of the technique used for the calculation of the tearing energy it was decided to carry out a comparison of the results obtained on Ch compound in the two load configurations with data from Harbour, Fatemi and Mars [72] related to fatigue crack growth test performed on pure shear specimens of natural rubber and SBR filled with carbon black. Results of this comparison are reported in figure 5.19. The results obtained from the test in pure shear loading conditions are in line with literature data, while in biaxial loading conditions (with maximum applied deformation parallel to the original crack) was found an higher crack growth rate even though the applied tearing energy was lower, confirming the effect of load biaxiality on fatigue crack propagation.

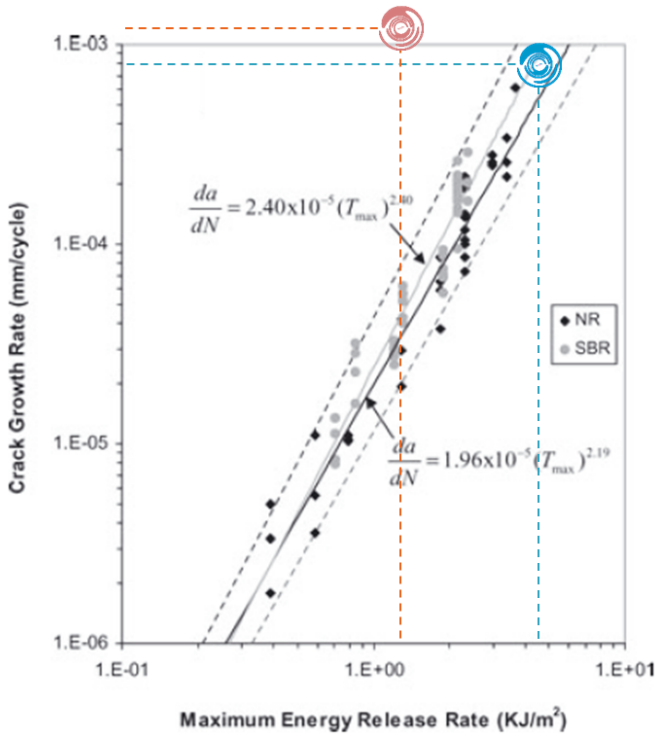

Figure 5.19: *Comparison between the experimental fatigue crack propagation of Ch compound (blue PS, red Biaxial) with literature data for carbon black filled NR and SBR under PS loading condition. (Image adapted from [72]).*

Chapter 6

Conclusive remarks

In this work the fracture behaviour of carbon black filled rubber compounds under both quasi-static and dynamic biaxial loading conditions was studied. The work was divided in two main areas: one concerning the study of the fracture phenomenology, most widely developed in the case of quasi-static loading conditions and one concerning the development of techniques for evaluating the tearing energy in the case of complex shape specimens such as that used for biaxial testing.

In chapter 4 the fracture phenomenology observed for both pure shear and biaxial loading conditions was reported and widely investigated by means of digital image correlation technique. Local strain fields around the crack tip were directly observed, and the effect of the sideways cracks propagation in reducing the strain intensification highlighted in the case of pure shear loading conditions. The phenomenon of sideways cracks propagation was also studied by means of biaxial loading fracture tests: it was highlighted that local orientation is a necessary condition for sideways cracks propagation. Identifying the material orientation with the maximum principal strain direction, at sideways cracks onset the material was found to be always oriented in the direction normal to the notch plane at least in a small zone in front of the crack tip. The results obtained in biaxial loading condition were only limited and regard only two of the four compounds (NR0 and NR50), the extension of the performed study to different compounds and rubber matrix can be an interesting topic for future research.

The digital image correlation analysis can be improved by changing the specimens patterning technique going from the actual airbrush paint spring to the talc powder deposition that was recognized in some recent literature works to be an optimum system to be used with rubbers. Also the image resolution used for biaxial testing can be improved by reducing the area analysed on the specimen to obtain more information about the material near to the crack tip.

The digital image correlation was also used for specimen optimization, for the determination of the Poisson ratio as shown in chapter 3 and for the determination of the tearing energy with two different techniques: for quasi-static tests using the displacement field obtained as a boundary condition for the FE simulation as shown in chapter 4 and for dynamic tests using the variation of the strain field measured due to the crack propagation as shown in chapter 5. Both techniques for the evaluation of the tearing energy have advantages and shortcomings: the FE method requires an accurate description of the geometry and is very sensitive to the constitutive model calibration, the DIC based method require high resolution images of the specimen during crack propagation that cannot be recorded for fast propagating cracks. Both methods need an accurate calibration of the constitutive behaviour of the material in order to be applied.

The stress-strain characterization techniques used in quasi-static and dynamic loading conditions were rather different. For dynamic loading condition the maximum strain reached was moderate ($\varepsilon < 60\%$) and the fitting procedure results to be easier than in the case of quasi-static loading, for which the maximum strain considered was higher ($\varepsilon > 500\%$). The characterization methods used in this work can be improved under different pointy of view. The dynamic stress-strain behaviour used for the evaluation of the tearing energy with the technique discussed at the end of chapter 5 could be better described by a more complicated model than the simple hyperelastic model here considered and further, data should be collected up to higher maximum strain in order to minimize errors in the determination of the strain energy density of the highly deformed elements near to the crack tip. The quasi-static stress strain characterization can be improved by performing tests in more biaxial loading conditions in order to obtain a more

accurate constitutive equation for the material.

Appendix A

Biaxial clamping system

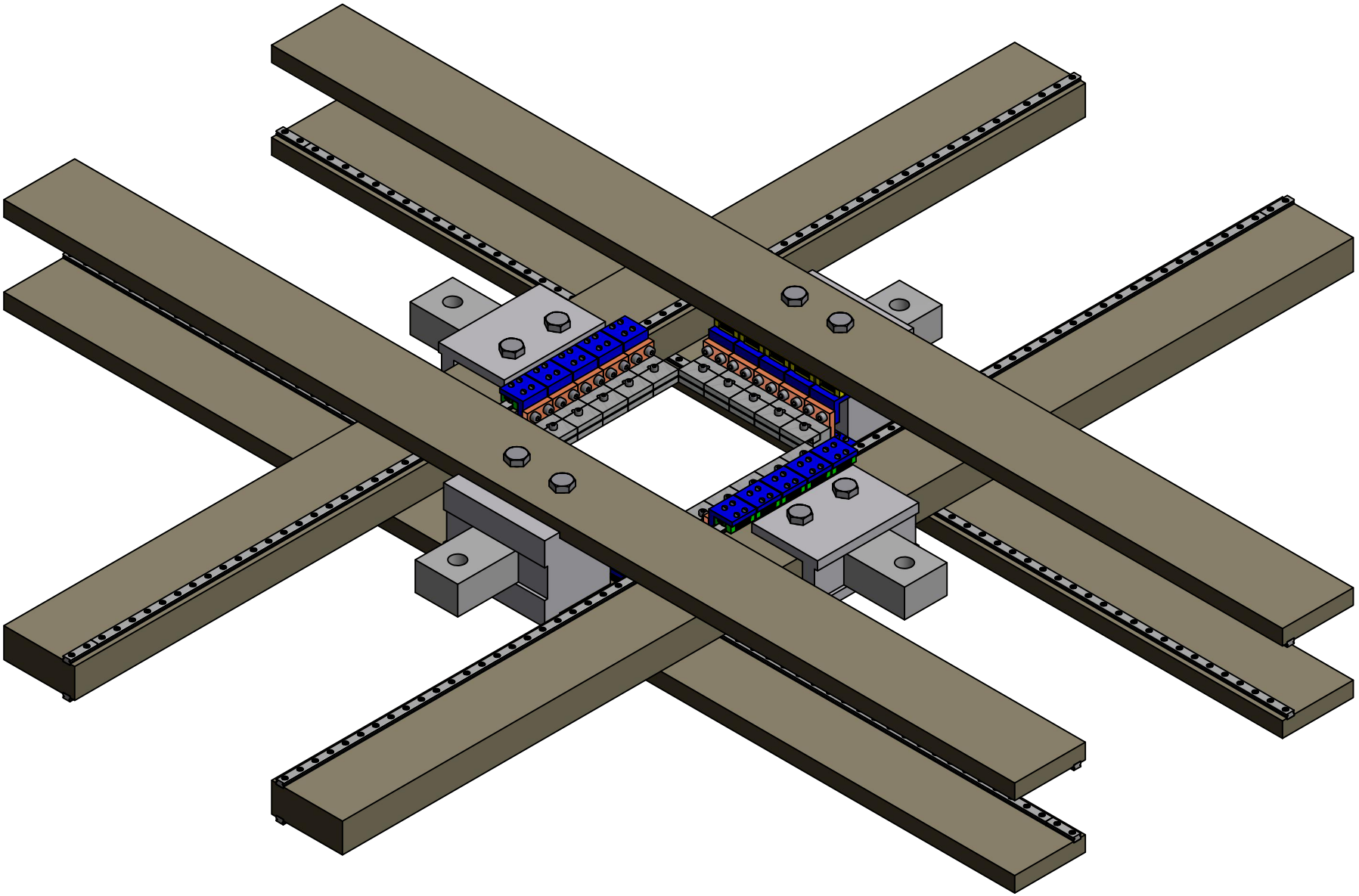

DRAWN Alessandro Calabrò	08/11/2012	Calabrothers Corp.	
CHECKED Ing. Roberto Calabrò		PROJECT	
DESCRIPTION Assieme		Biaxial Clamping System	
Q.TY 1			
APPROVED		SIZE A2	COMPONENT NUMBER / REV
		SCALE	SHEET 1 OF 1

PARTS LIST			
ITEM	QTY	PART NUMBER	DESCRIPTION
1	1		Barra singola
2	1		Afferraggio per barra singola
3	1		Connessione per biassiale
4	10		Carrello a ricircolo di sfere M7
5	10		Piastrina ad L
6	5		Piastrina clamp
7	5		Clamp bottom
8	5		Clamp top
9	2	ISO 4032 - M10	Hexagon nuts, style 1 - Product grades A and B
10	2	ISO 4014 - M10 x 60	Hexagon head bolt - product grades A and B
11	1	ISO 10642 - M10 x 30	Hexagon Socket Countersunk Head Screw-1 - Product grade A
12	2	ISO 7089 - 10 - 140 HV	Plain washers - Normal series - Product grade A
13	2		Binario a ricircolo di sfere M7
14	134	ISO 4762 - M2 x 6	Hexagon Socket Head Cap Screw
15	25	ISO 4762 - M4 x 10	Hexagon Socket Head Cap Screw
16	5	ISO 4762 - M3 x 10	Hexagon Socket Head Cap Screw
17	40	ISO 1207 - M2 x 6	Slotted cheese head screws - Product grade A

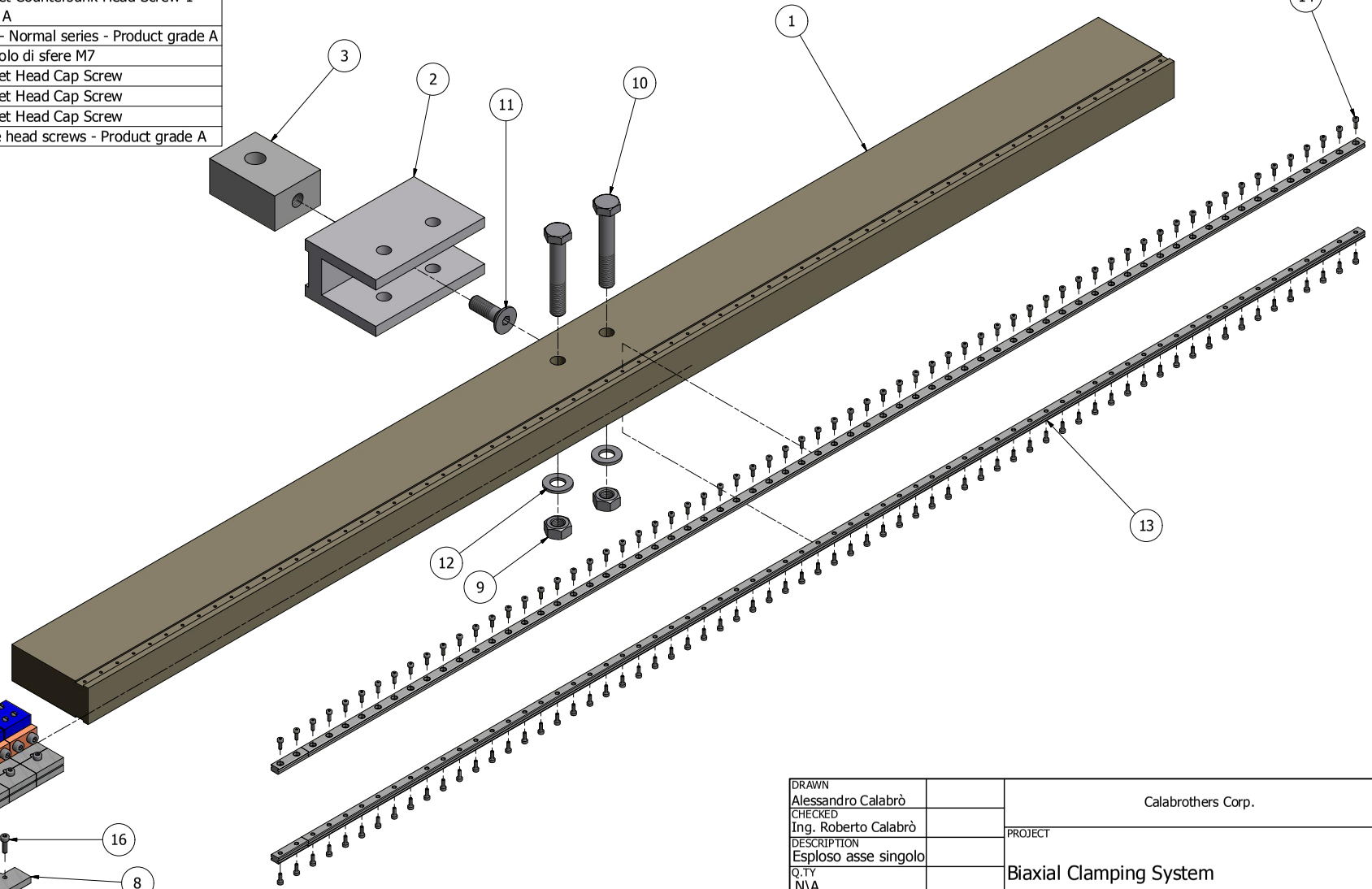

DRAWN: Alessandro Calabrò		Calabrothers Corp.	
CHECKED: Ing. Roberto Calabrò		PROJECT: Biaxial Clamping System	
DESCRIPTION: Esploso asse singolo			
Q.TY: N\A			
APPROVED		SIZE: A2	COMPONENT NUMBER
		SCALE	REV: 1
			SHEET 1 OF 1

PARTS LIST

ITEM	QTY	PART NUMBER	DESCRIPTION
1	2		Barra doppia
2	1		Afferraggio per barre doppie
3	1		Connessione per biassiale
4	10		Carrello a ricircolo di sfere M7
5	10		Piastrina ad L
6	5		Piastrina clamp
7	5		Clamp bottom
8	5		Clamp top
9	2	ISO 4032 - M10	Hexagon nuts, style 1 - Product grades A and B
10	2	ISO 4014 - M10 x 100	Hexagon head bolt - product grades A and B
11	1	ISO 10642 - M10 x 50	Hexagon Socket Countersunk Head Screw-1 - Product grade A
12	2	ISO 7089 - 10 - 140 HV	Plain washers - Normal series - Product grade A
13	2		Binario a ricircolo di sfere M7
14	134	ISO 4762 - M2 x 6	Hexagon Socket Head Cap Screw
15	25	ISO 4762 - M4 x 10	Hexagon Socket Head Cap Screw
16	5	ISO 4762 - M3 x 10	Hexagon Socket Head Cap Screw
17	40	ISO 1207 - M2 x 6	Slotted cheese head screws - Product grade A

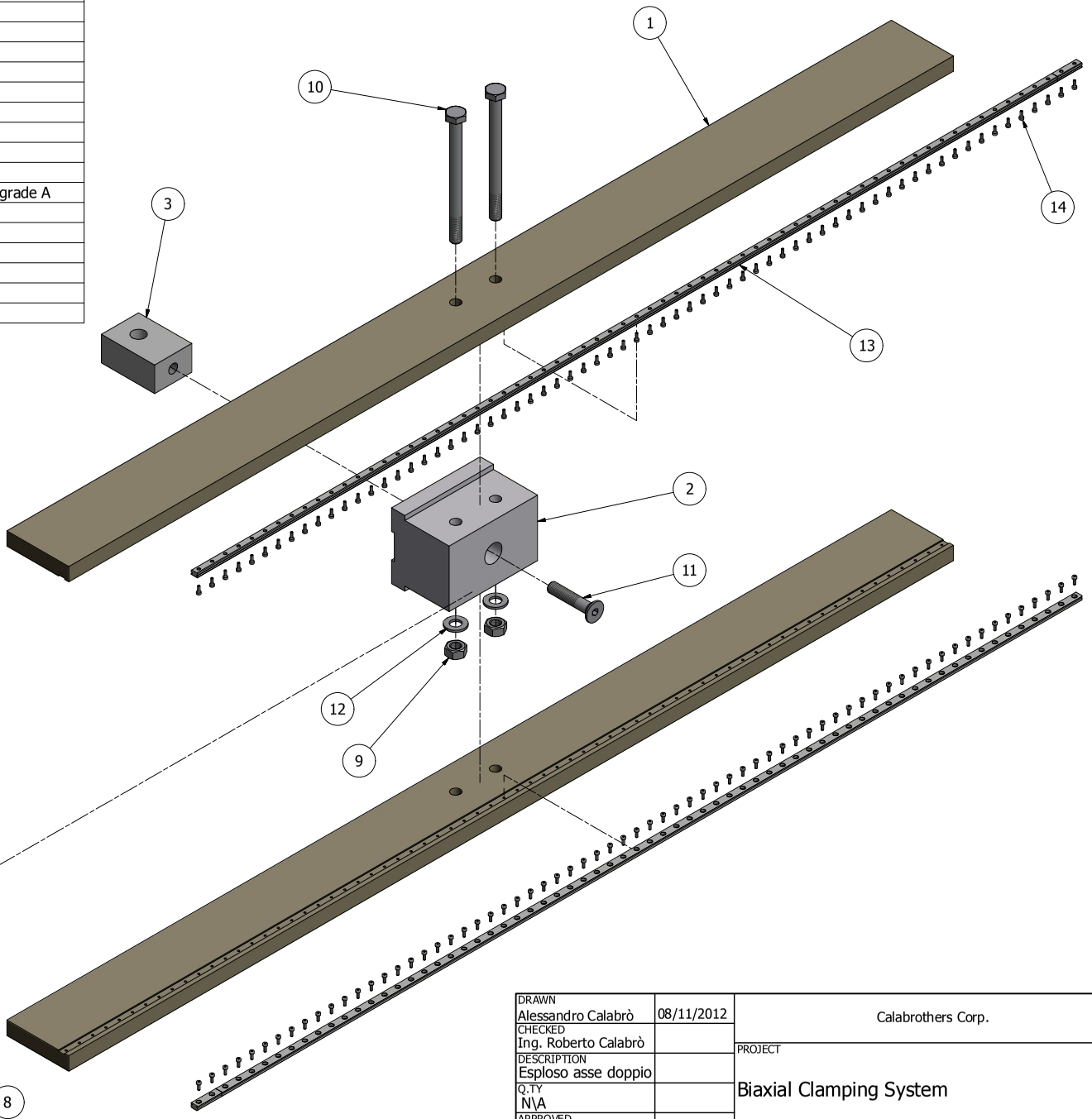

DRAWN Alessandro Calabrò	08/11/2012	Calabrothers Corp.	
CHECKED Ing. Roberto Calabrò		PROJECT	
DESCRIPTION Esploso asse doppio		Biaxial Clamping System	
Q.TY N\A			
APPROVED			
		SIZE A2 / COMPONENT NUMBER / REV	
		SCALE / SHEET 1 OF 1	

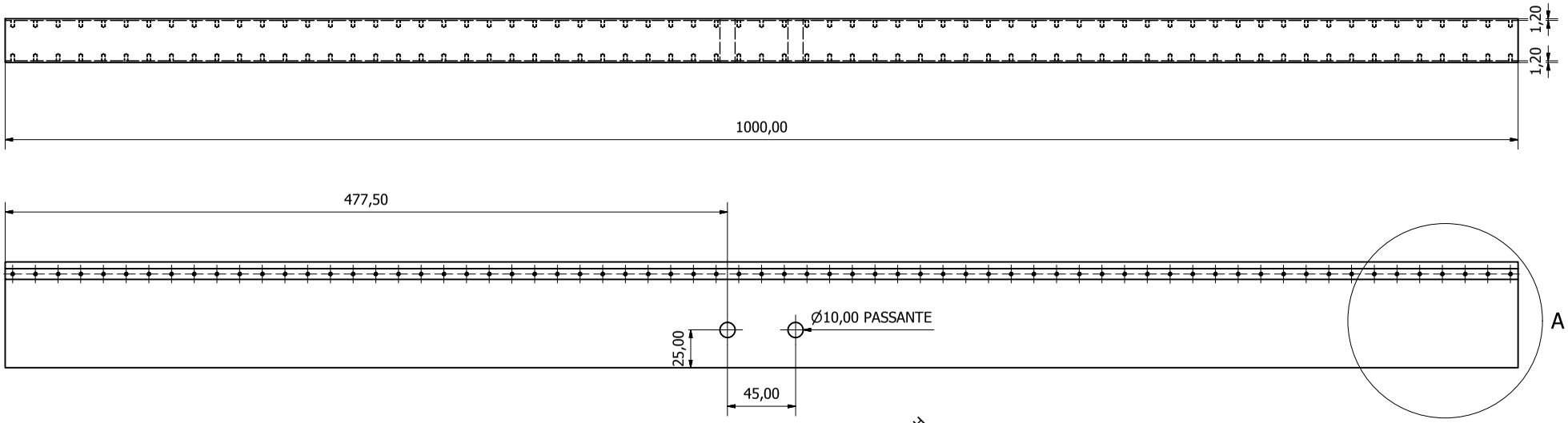

A (2 : 1)

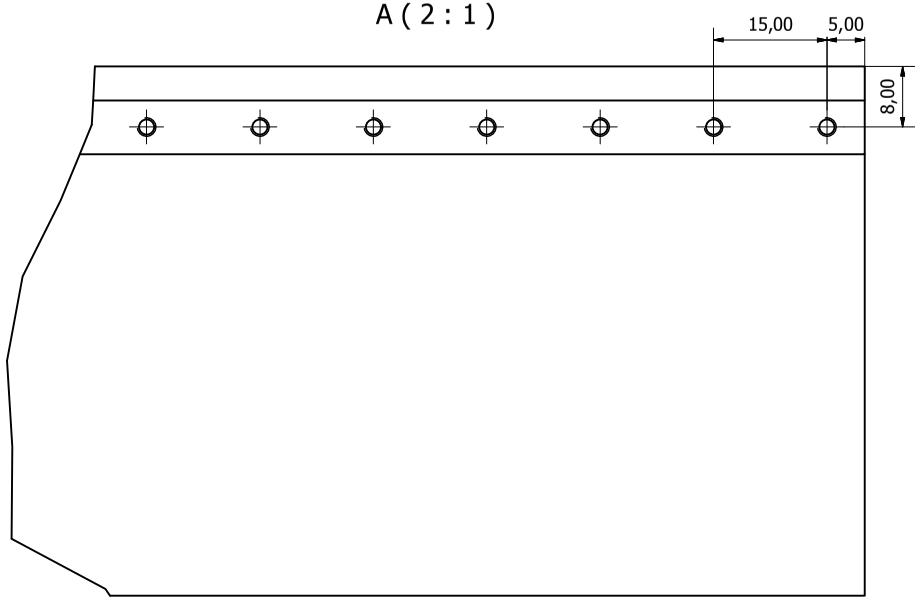

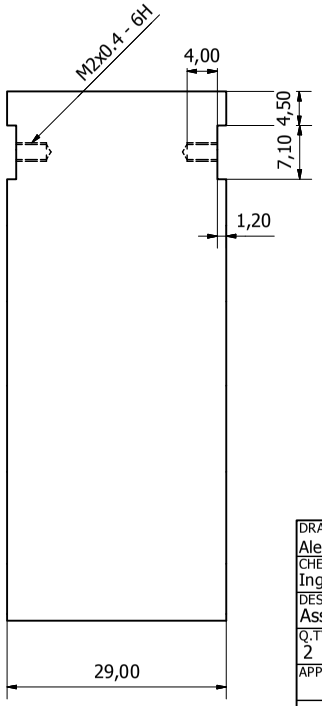

DRAWN Alessandro Calabrò	08/11/2012	Calabrothers Corp.	
CHECKED Ing. Roberto Calabrò		PROJECT	
DESCRIPTION Asse singolo		Biaxial Clamping System	
Q.TY 2			
APPROVED		SIZE A2	COMPONENT NUMBER / REV
		SCALE	SHEET 1 OF 1

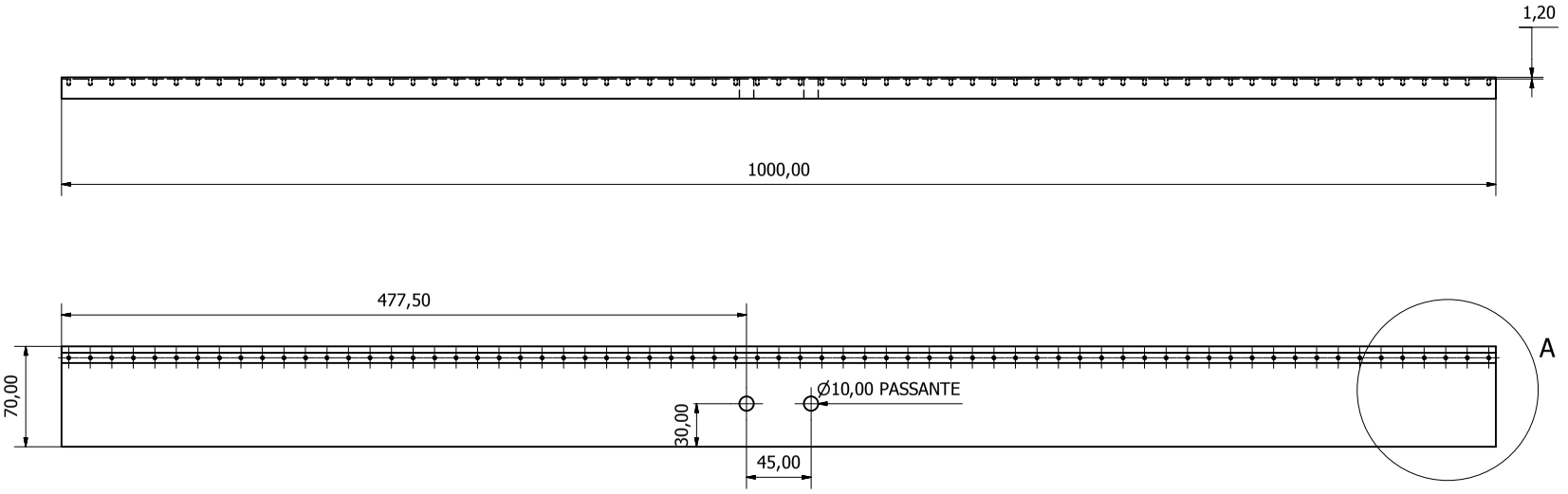

A (2: 1)

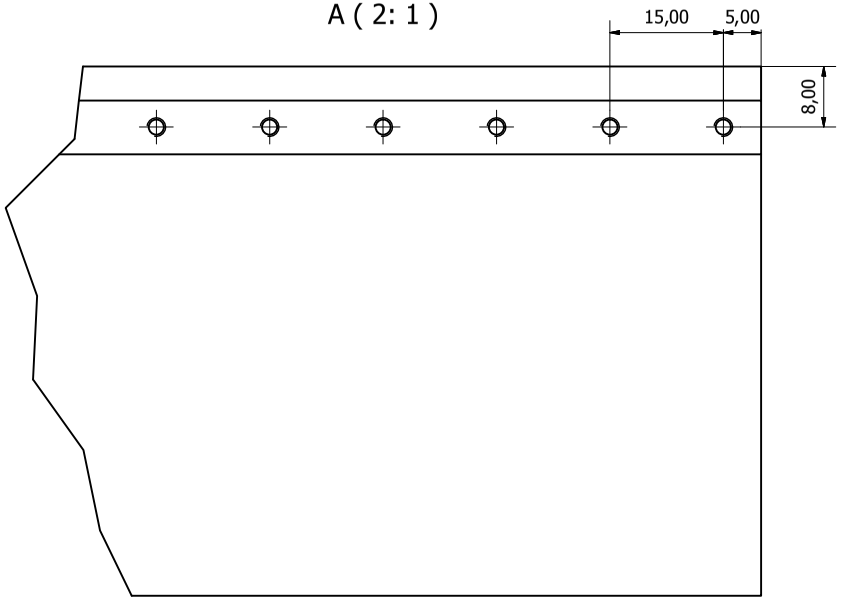

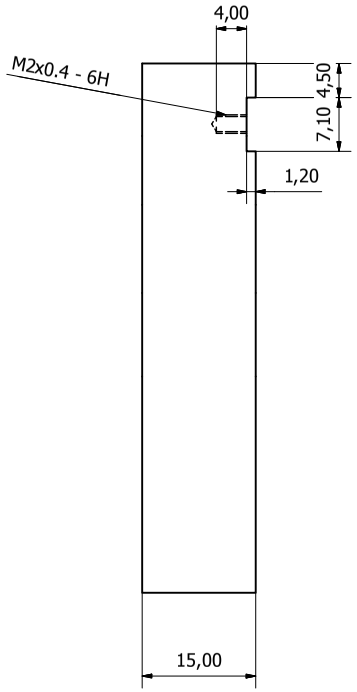

DRAWN Alessandro Calabrò	08/11/2012	Calabrothers Corp.
CHECKED Ing. Roberto Calabrò		PROJECT
DESCRIPTION Asse doppio		Biaxial Clamping System
Q.TY 2		
APPROVED		
		SIZE A2 / COMPONENT NUMBER / REV
		SCALE / SHEET 1 OF 1

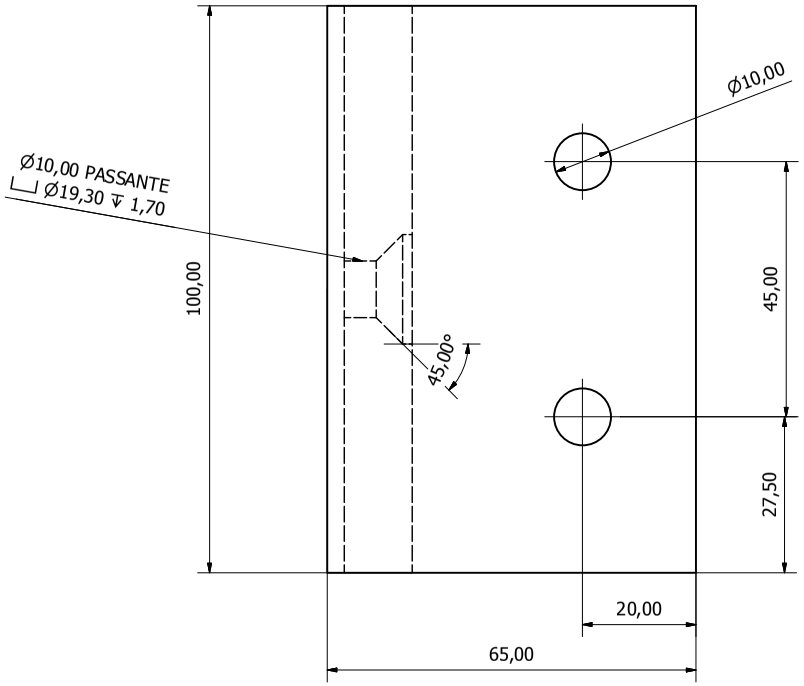

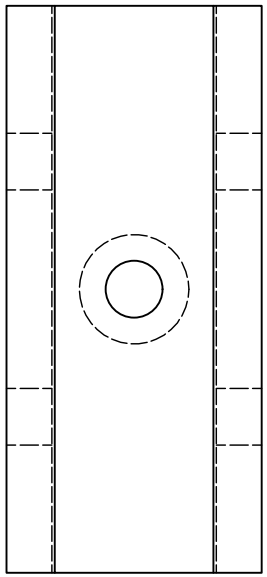

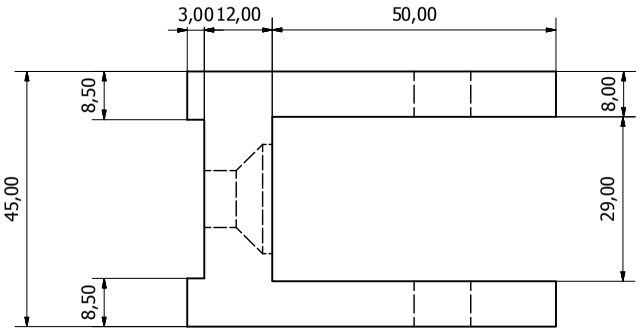

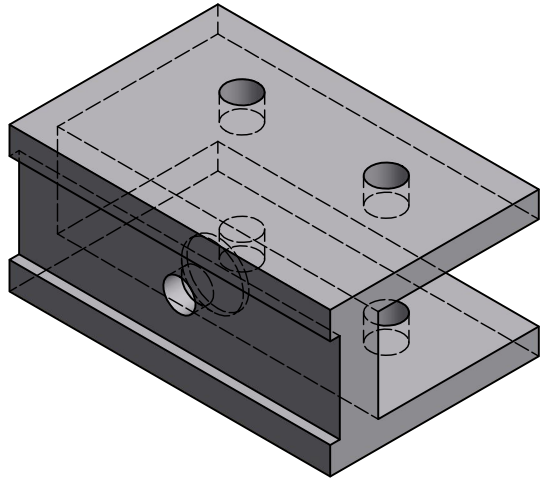

DRAWN Alessandro Calabrò	08/11/2012	Calabrothers Corp.		
CHECKED Ing. Roberto Calabrò		PROJECT		
DESCRIPTION Aff. asse singolo		Biaxial Clamping System		
Q.TY 2				
APPROVED		SIZE A2	COMPONENT NUMBER	REV
		SCALE	SHEET 1 OF 1	

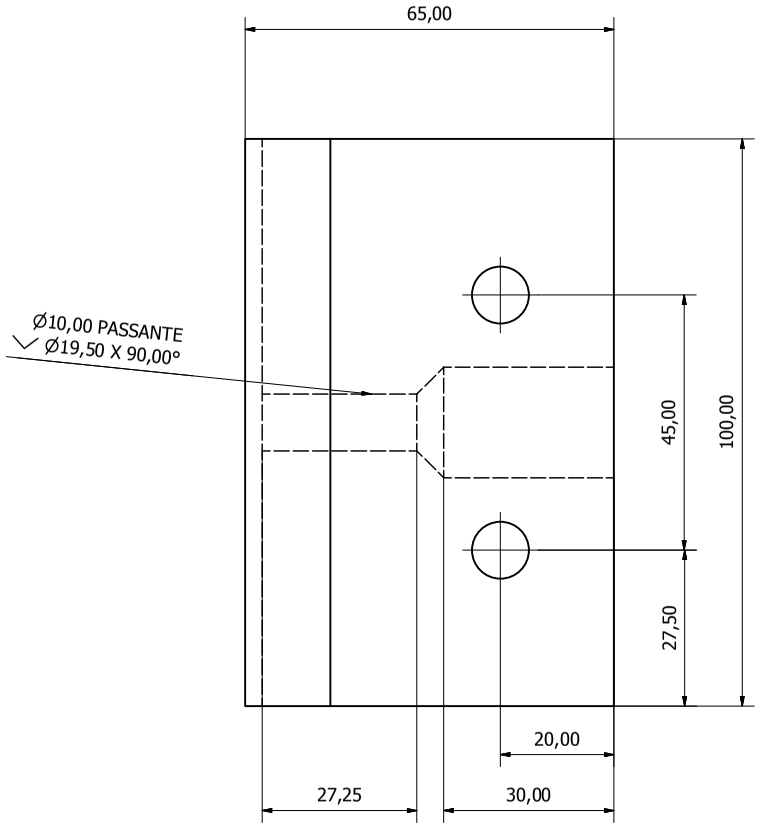

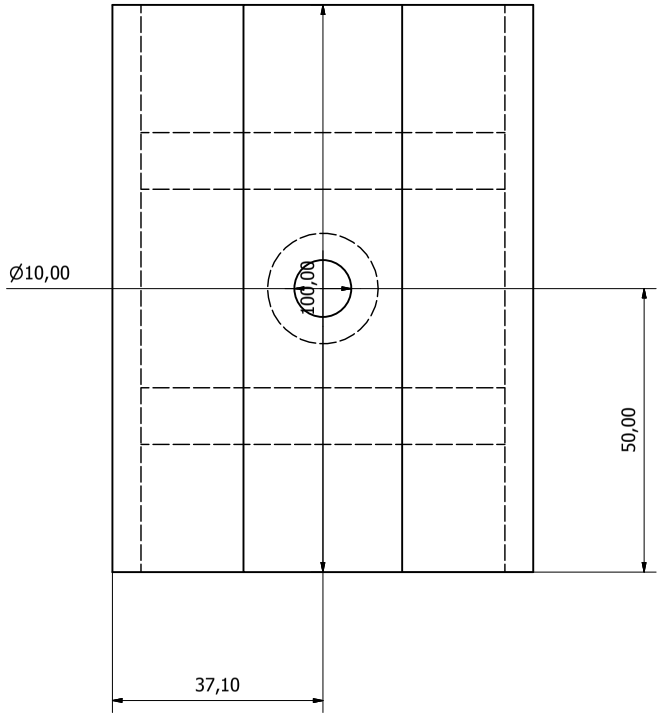

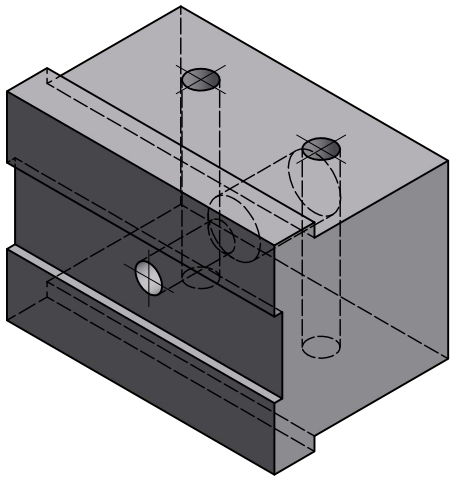

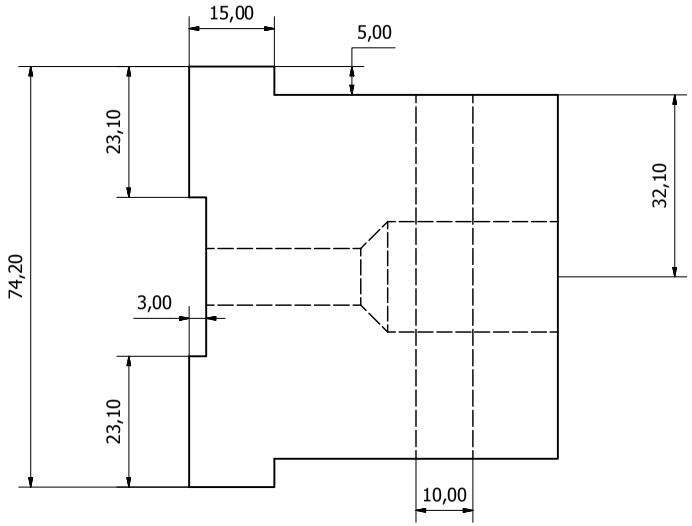

DRAWN Alessandro Calabrò	08/11/2012	Calabrothers Corp.	
CHECKED Ing. Roberto Calabrò		PROJECT	
DESCRIPTION Aff. asse doppio		Biaxial Clamping System	
Q.TY 2			
APPROVED			
		SIZE A2 / COMPONENT NUMBER / REV	
		SCALE / SHEET 1 OF 1	

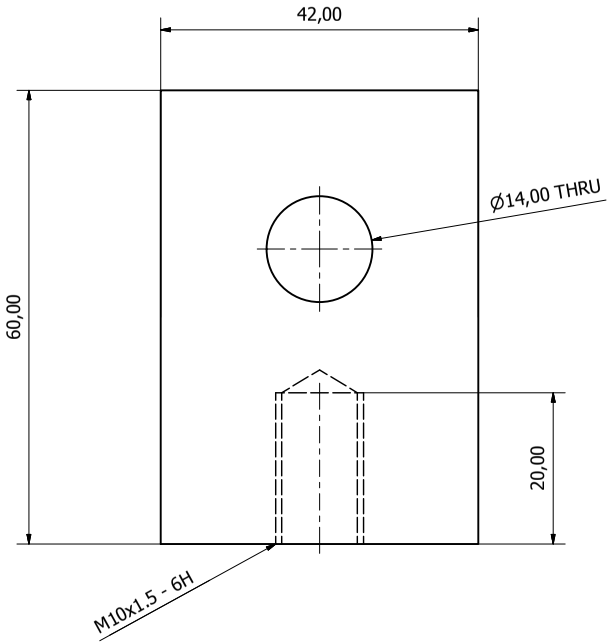

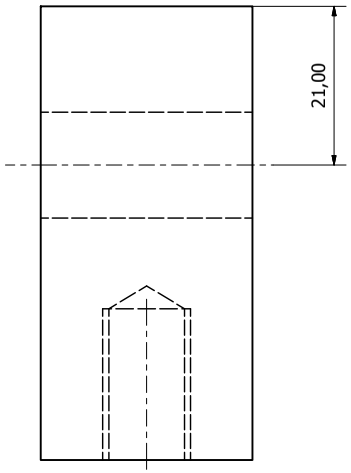

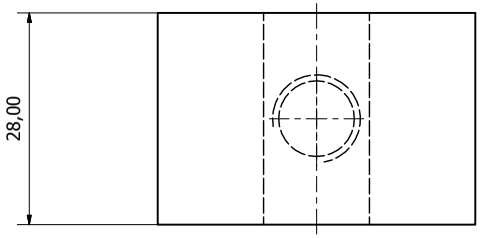

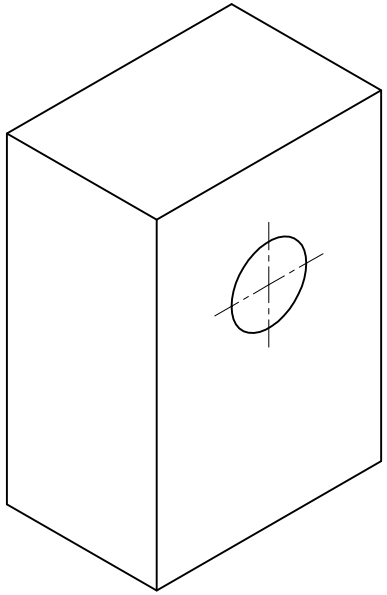

DRAWN Alessandro Calabrò	07/06/2012	Calabrothers Corp.		
CHECKED Ing. Roberto Calabrò		PROJECT Biaxial Clamping System		
DESCRIPTION Conn. biassiale				
Q.TY 4				
APPROVED		SIZE A2	COMPONENT NUMBER 9	REV
		SCALE	SHEET 6 OF 12	

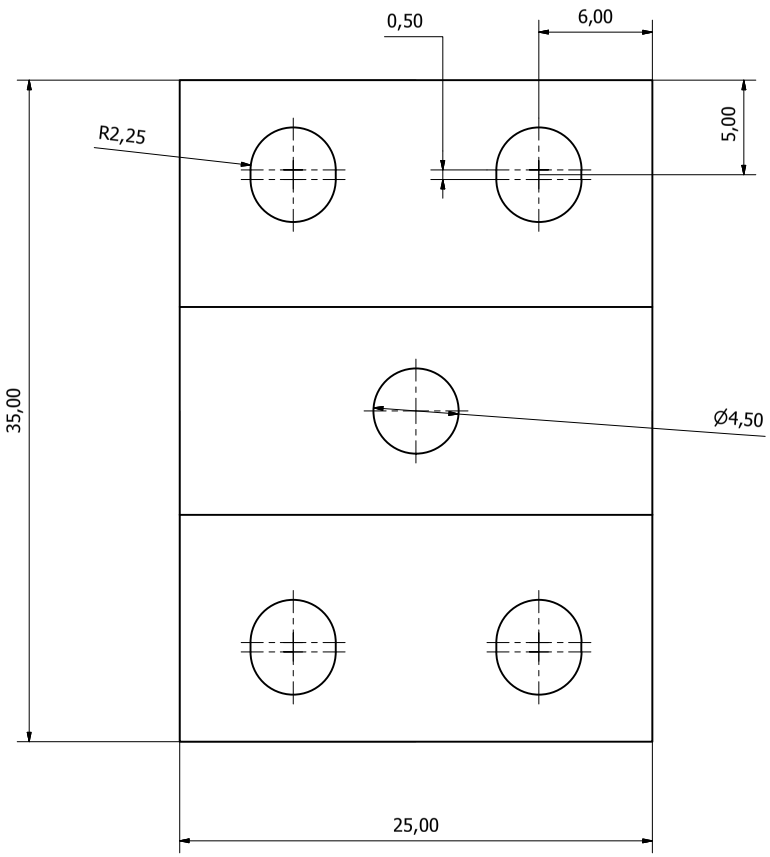

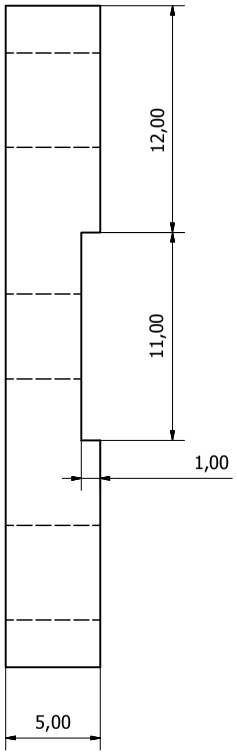

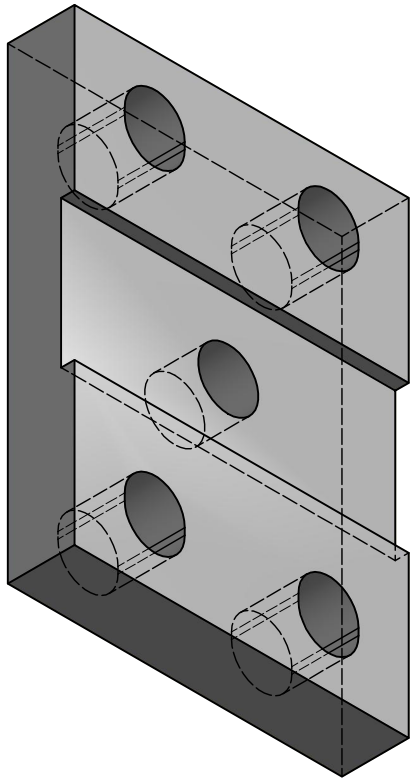

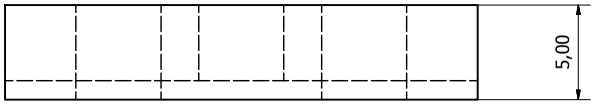

DRAWN Alessandro Calabrò	08/11/2012	Calabrothers Corp.	
CHECKED Ing. Roberto Calabrò		PROJECT	
DESCRIPTION Piastrina		Biaxial Clamping System	
Q.TY 20			
APPROVED			
		SIZE A2 / COMPONENT NUMBER / REV	
		SCALE / SHEET 1 OF 1	

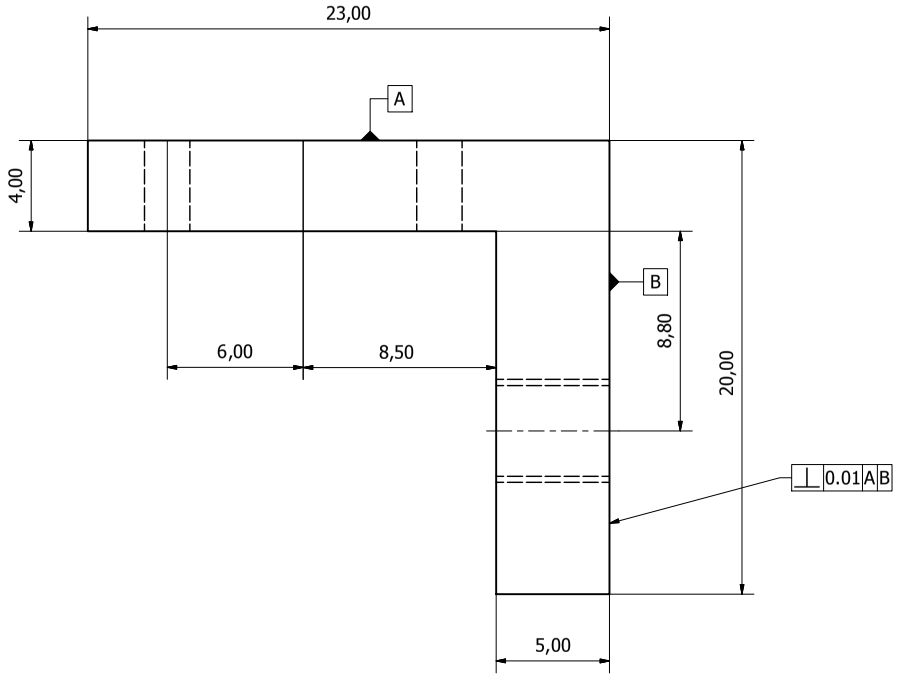

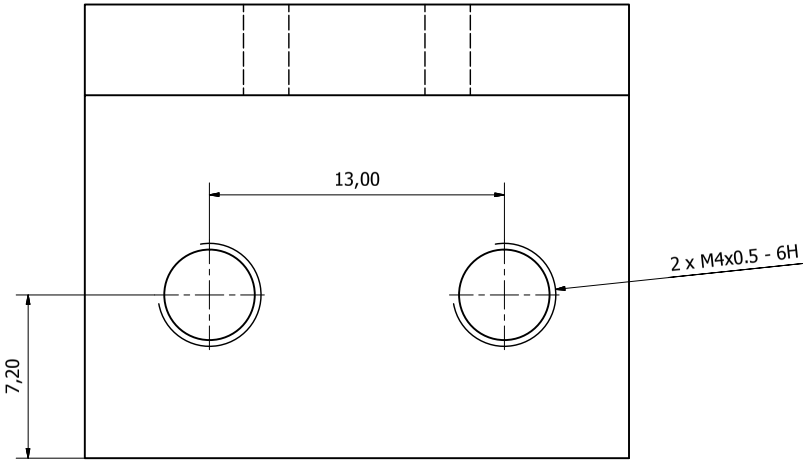

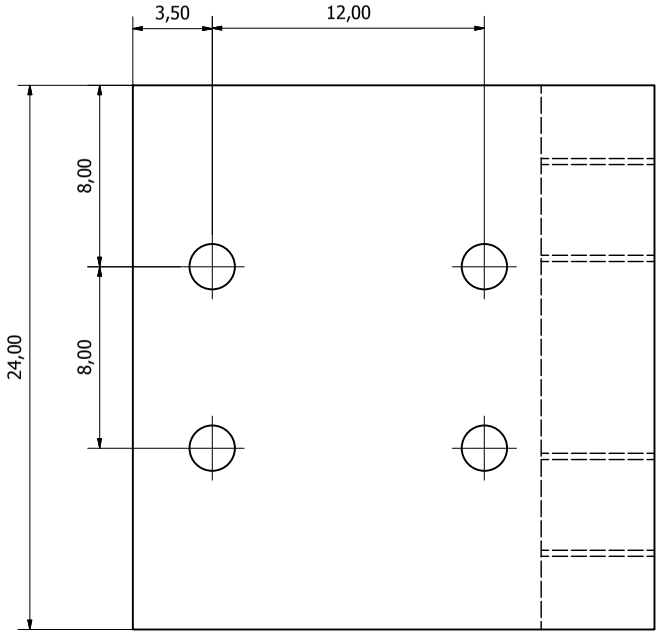

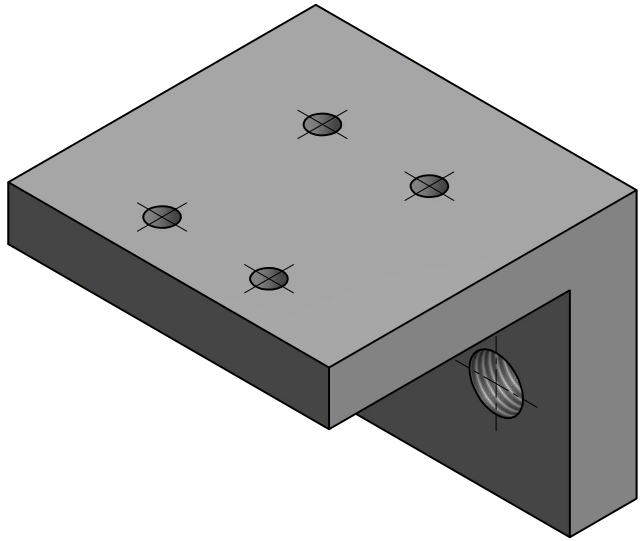

DRAWN Alessandro Calabrò	08/11/2012	Calabrothers Corp.
CHECKED Ing. Roberto Calabrò		PROJECT
DESCRIPTION Sq. asse doppio		Biaxial Clamping System
Q.TY 20		
APPROVED		
	SIZE A2	COMPONENT NUMBER / REV
	SCALE	SHEET 1 OF 1

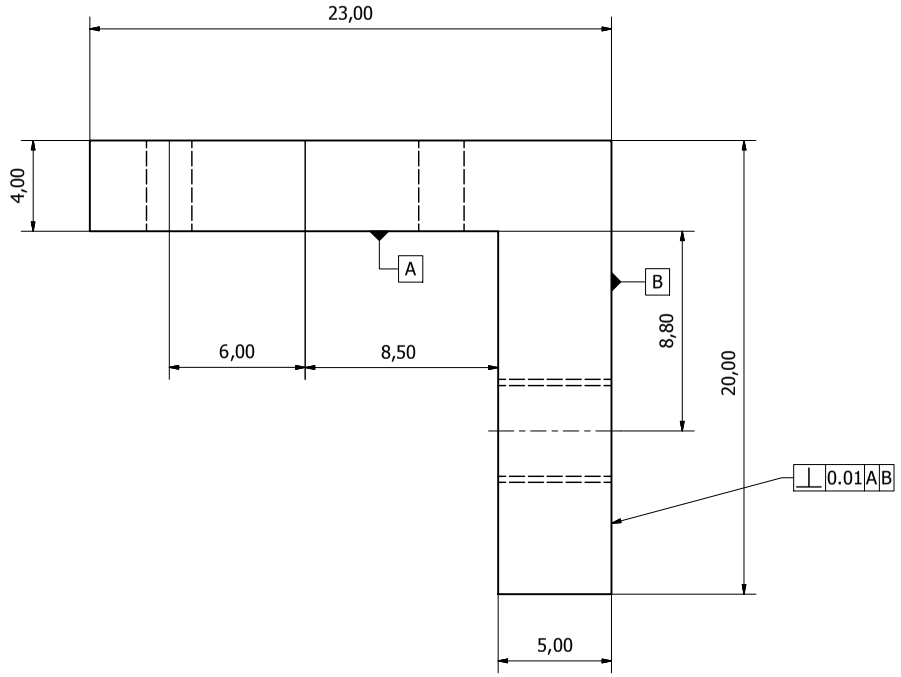

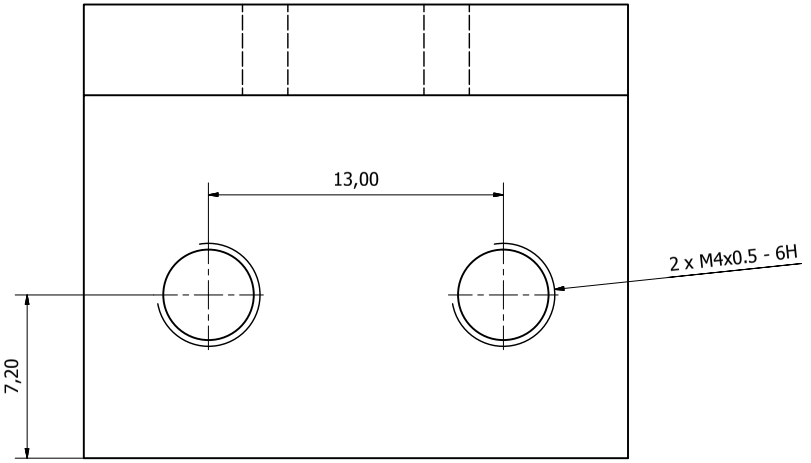

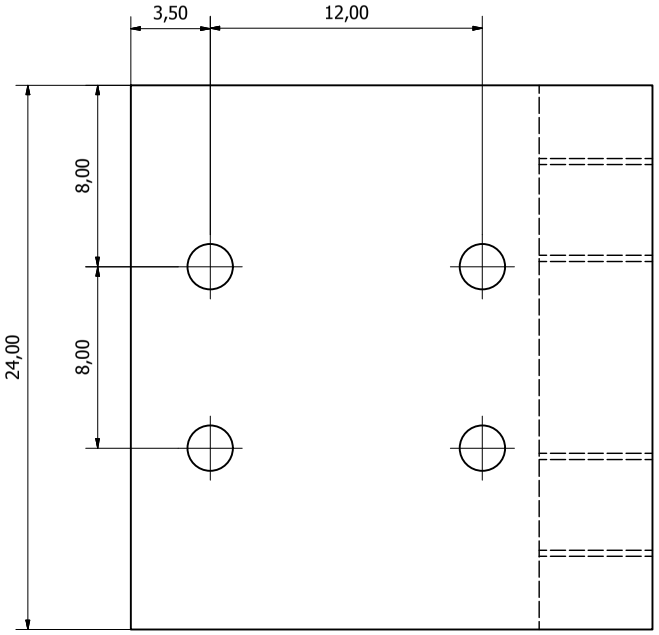

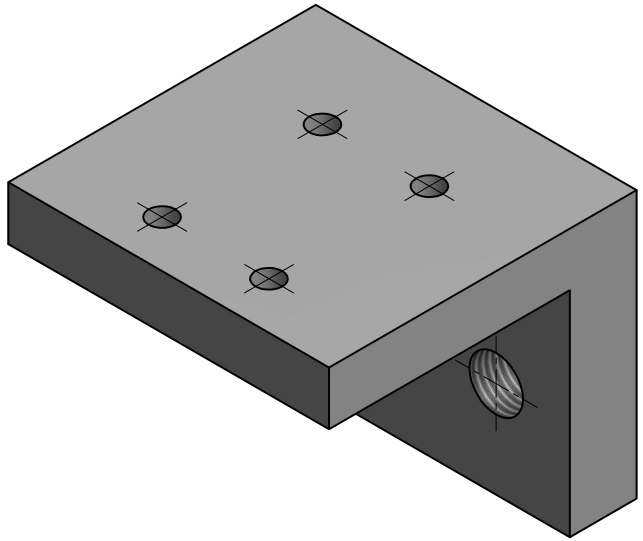

DRAWN Alessandro Calabrò	08/11/2012	Calabrothers Corp.
CHECKED Ing. Roberto Calabrò		PROJECT
DESCRIPTION Sq. asse singolo		Biaxial Clamping System
Q.TY 20		
APPROVED		
	SIZE A2	COMPONENT NUMBER / REV
	SCALE	SHEET 1 OF 1

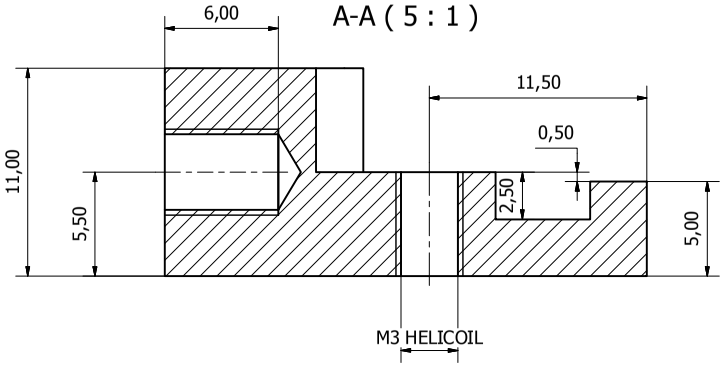

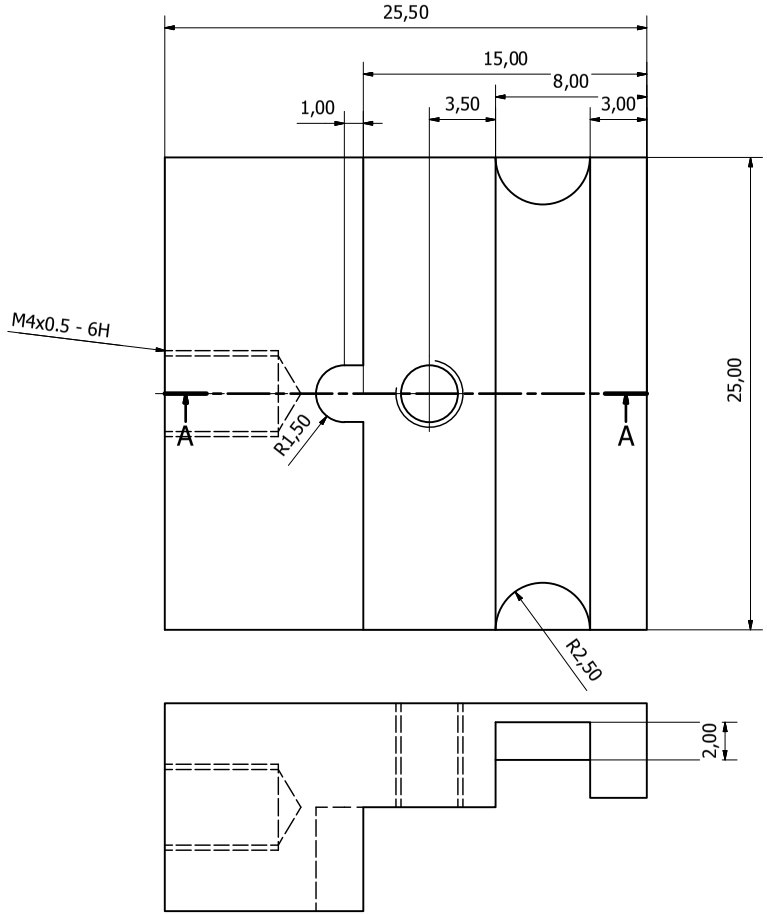

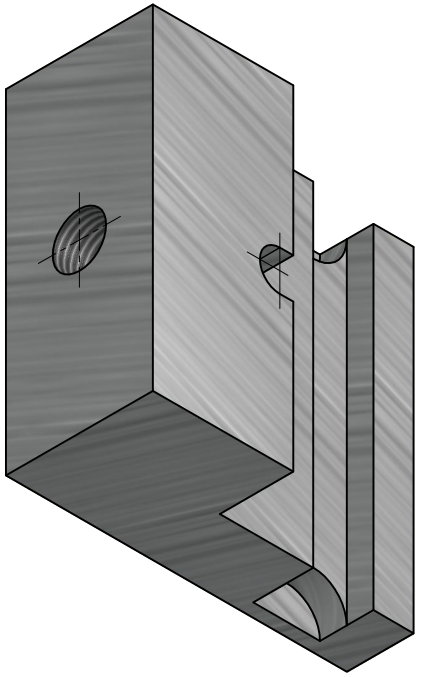

DRAWN Alessandro Calabrò	08/11/2012	Calabrothers Corp.	
CHECKED Ing. Roberto Calabrò		PROJECT	
DESCRIPTION Clamp bottom		Biaxial Clamping System	
Q.TY 20			
APPROVED		SIZE A2	COMPONENT NUMBER / REV
		SCALE	SHEET 1 OF 1

A-A (6 : 1)

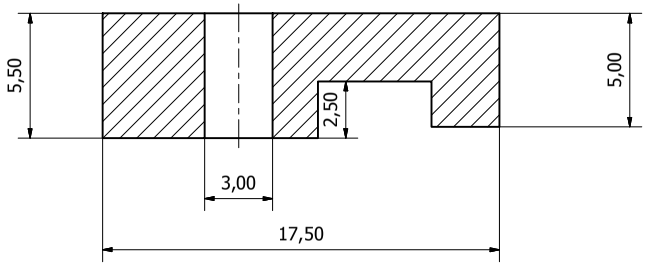

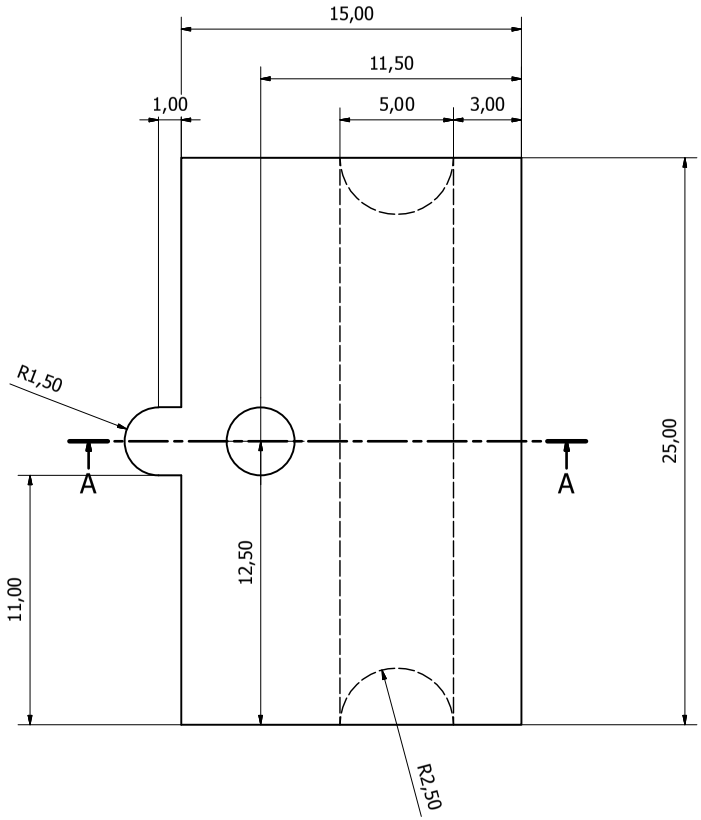

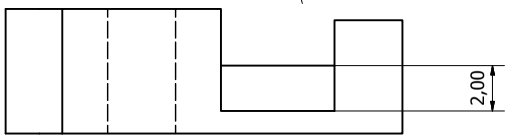

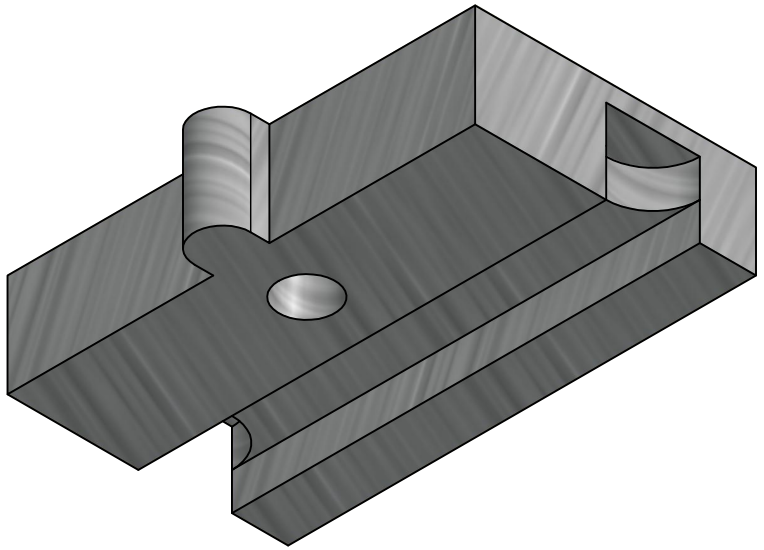

DRAWN Alessandro Calabrò	08/11/2012	Calabrothers Corp.	
CHECKED Ing. Roberto Calabrò		PROJECT	
DESCRIPTION Clamp top		Biaxial Clamping System	
Q.TY 20			
APPROVED			
		SIZE A2 / COMPONENT NUMBER	REV
		SCALE	SHEET 1 OF 1

PARTS LIST			
ITEM	QTY	PART NUMBER	DESCRIPTION
1	1	Semistampo inferiore	
2	1	Semistampo superiore	
3	8	Piastrina di posizionamento	
4	2	Spina	
5	16	Vite M3	

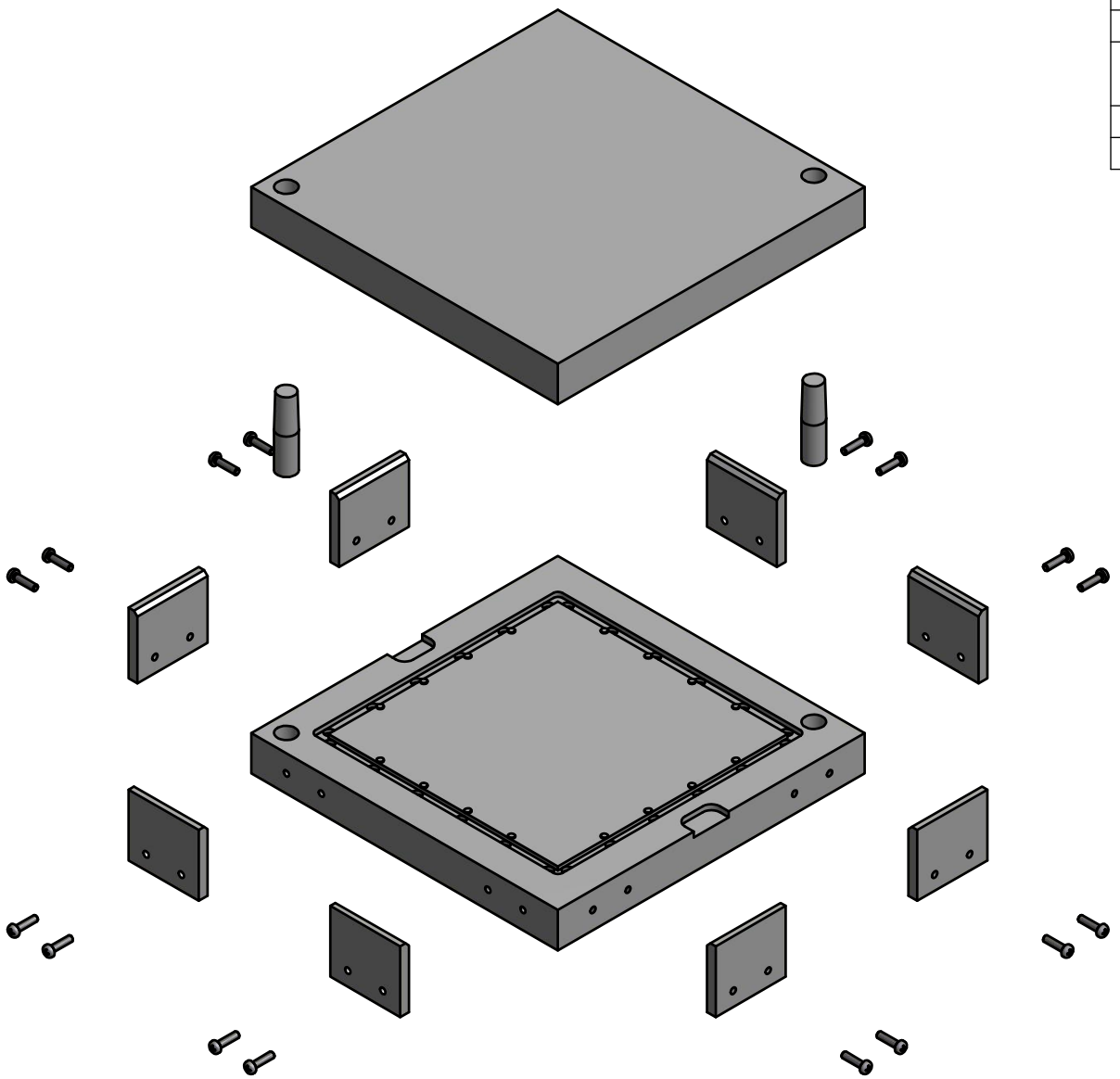

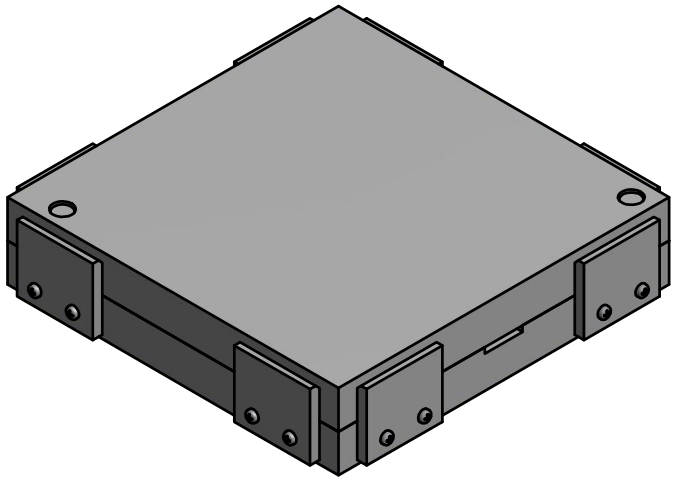

Designed by	Checked by	Approved by	Date		Date	
A.Calabrò	R.Calabrò				11/12/2012	

Calabrothers Corp.	Semistampo superiore		
	Esploso	Edition	Sheet 1 / 1

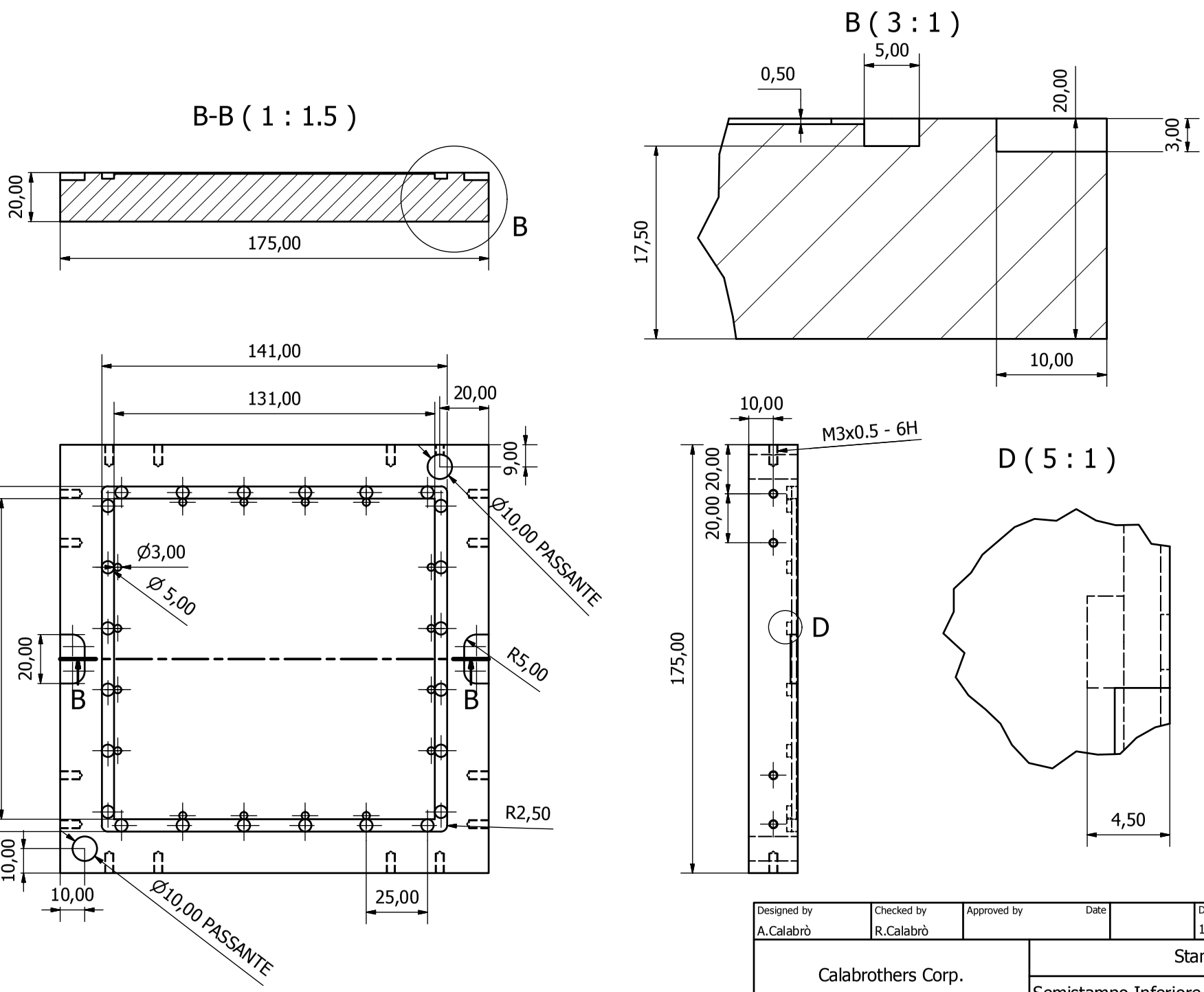

Designed by	Checked by	Approved by	Date		Date	
A.Calabrò	R.Calabrò				11/12/2012	

Calabrothers Corp.	Stampo		
	Semistampo Inferiore	Edition	Sheet 1 / 1

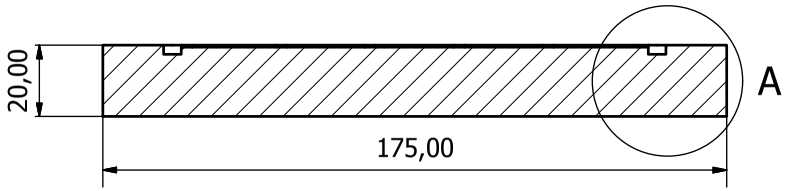

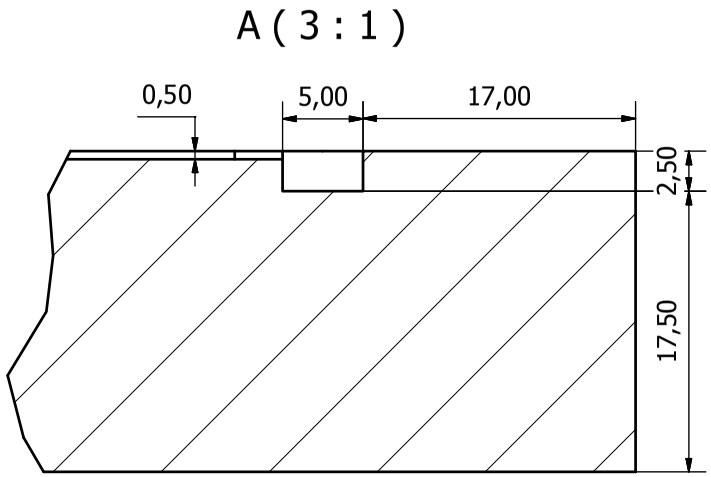

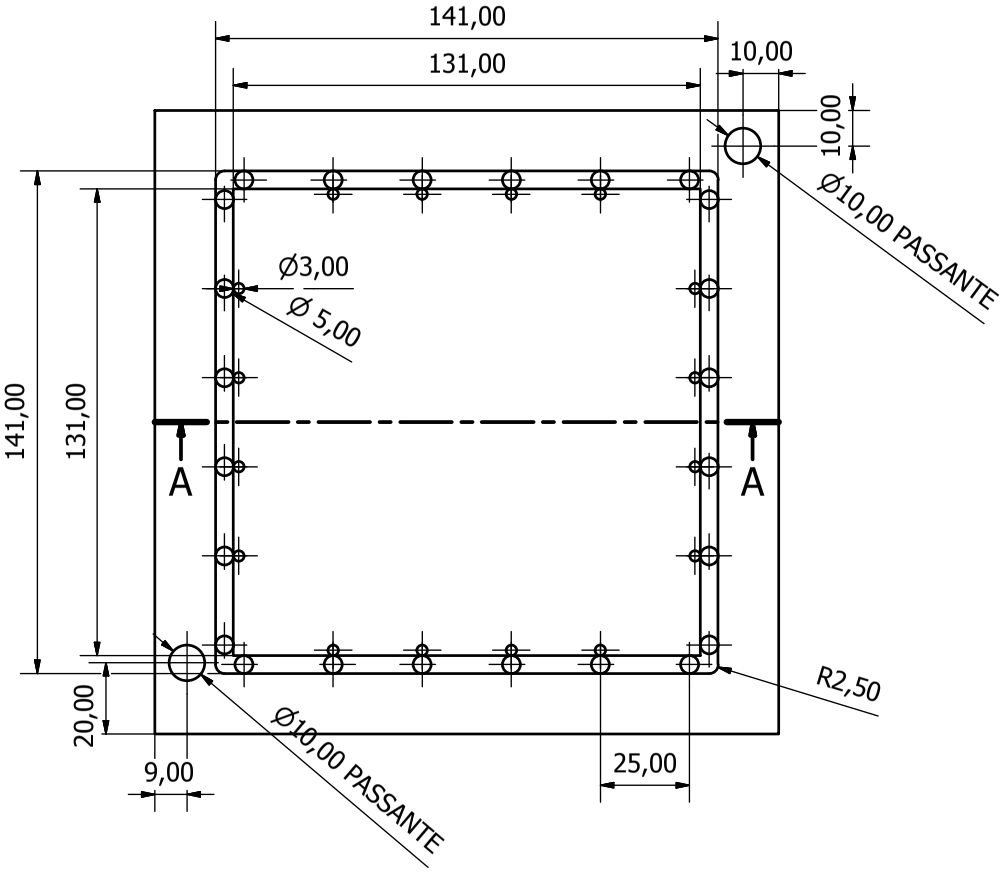

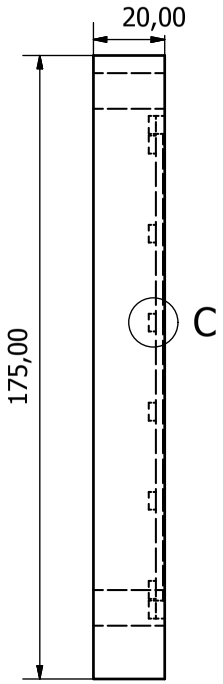

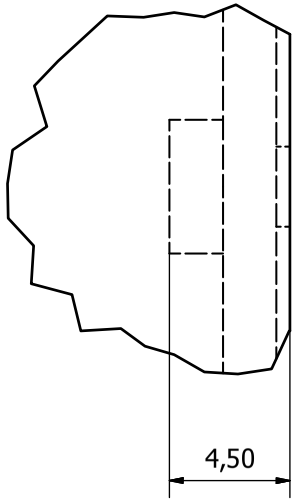

Designed by	Checked by	Approved by	Date		Date	
A.Calabrò	R.Calabrò				11/12/2012	

Calabrothers Corp.	Stampo		
	Semistampo superiore	Edition	Sheet 1 / 1

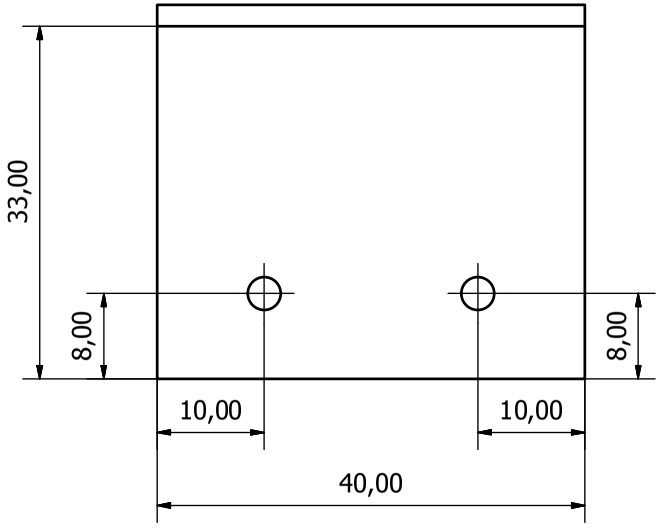

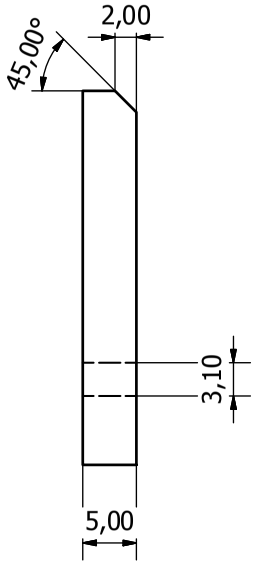

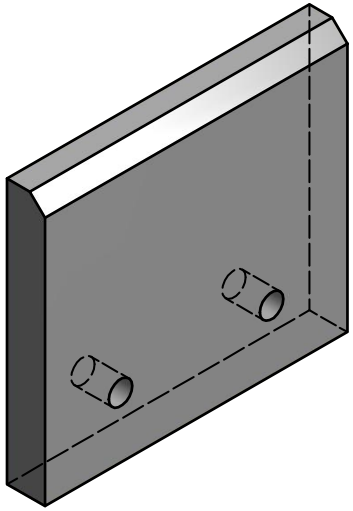

Designed by	Checked by	Approved by	Date		Date	
A.Calabrò	R.Calabrò				11/12/2012	

Calabrothers Corp.	Stampo		
	Piastrina di centraggio	Edition	Sheet 1 / 1

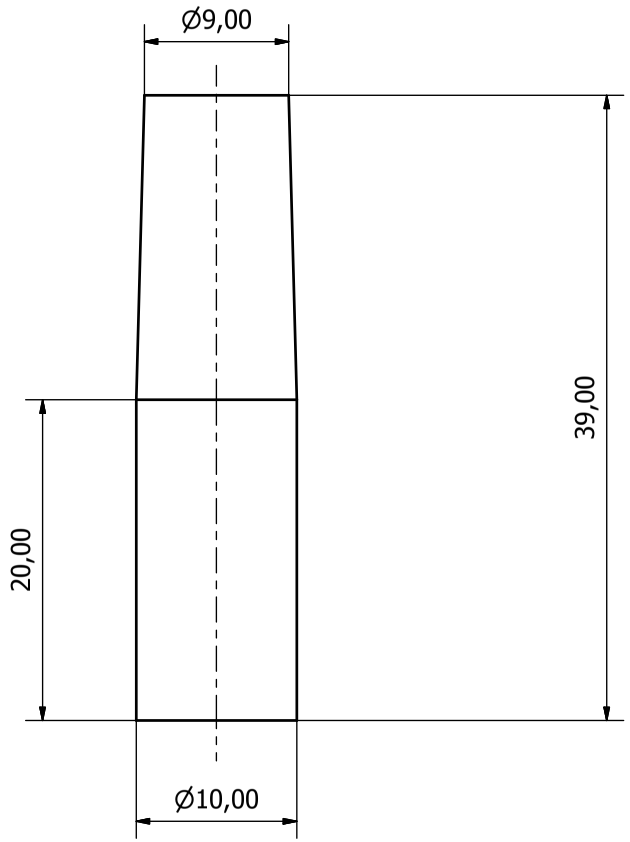

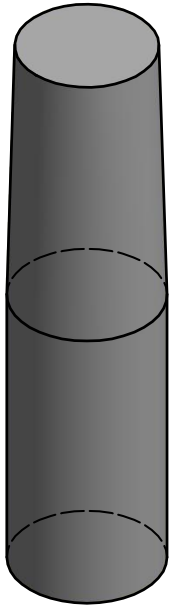

Designed by A.Calabrò	Checked by R.Calabrò	Approved by Date		Date 11/12/2012	
Calabrothers Corp.	Stampo Spina		Edition	Sheet 1 / 1	

Appendix B

Publications

Effect of Molecular Orientation on the Fracture Behavior of Carbon Black-Filled Natural Rubber Compounds

CLAUDIA MARANO, ROBERTO CALABRÒ, MARTA RINK

Politecnico di Milano-Dipartimento di Chimica, Materiali e Ingegneria Chimica "Giulio Natta", Milano, Italy

Received 12 November 2009; revised 22 April 2010; accepted 23 April 2010
DOI: 10.1002/polb.22054
Published online in Wiley InterScience (www.interscience.wiley.com).

ABSTRACT: The fracture behavior of carbon black-filled natural rubber compounds, differing in filler content, was studied performing tensile tests in biaxial loading conditions, using a central notched cross-shaped specimen. The test consisted of two steps: a drawing step was initially performed loading the specimen in the direction parallel to the notch plane, up to different draw ratios, and then the specimen was loaded in the direction normal to the notch plane up to fracture. Using a fracture mechanics approach, the fracture toughness was evaluated as a function of the draw ratio applied in the drawing step. A correlation between the fracture phenomenology observed and molecular orientability and orientation was attempted. © 2010 Wiley Periodicals, Inc. J Polym Sci Part B: Polym Phys 48: 1509–1515, 2010

KEYWORDS: biaxial test; fracture; orientation; rubber; strenght anisotropy

INTRODUCTION It is known that crack deviation from the notch plane occurs when fracture tests in mode I are performed on natural rubber compounds reinforced with carbon black:[1–3] the crack does not propagate along the notch plane (forward direction), but two small cracks form parallel to the loading direction (sideways cracks) and then, starting from one of these, a crack propagates across the specimen. From a finite element analysis, Gent et al.[4] found that, in a rubber sheet with a small edge-crack loaded in mode I, the applied energy release rate for crack propagation in the loading direction, G_s, is significantly lower than that for a crack propagating along the notch plane, G_f. The ratio $\frac{G_s}{G_f}$ was found to be 0.4 and 0.6 for strains equal to 0.20 and 2, respectively. From this analysis it derives that, for crack propagation to occur in the loading direction, there must be strength anisotropy at the crack tip: material resistance for crack propagation in the sideways direction (parallel to the loading direction) must be much lower than the crack propagation resistance in the forward direction (along the notch plane). Similar results are reported in ref. 5 in which an energy-based criterion for the deflection along the loading direction of a short crack previously introduced orthogonally to the loading direction in a anisotropic rubber laminate was proposed. It was found that under plane strain conditions, the ratio $\frac{R_{co\perp}}{R_{ad//}}$ between the material cohesive bulk energy, $R_{co\perp}$, and the interface adhesive energy, $R_{ad//}$, has to be lower than $4\pi(1-\nu^2)$, where ν is the material's Poisson ratio, to allow the crack to divert along the interface.

The reinforcing action of carbon black has been attributed to this crack deviation mechanism,[6] in relation to its ability to create a high degree of orientation. Carbon black particles acting as physical crosslinks and amplifying the local strains induce high strength anisotropy at the crack tip where large strains are present as a consequence of stress concentration.[7–10]

Many authors have studied the relation between crack deviation propensity and material and testing variables. The effects of crosslink density and crack length on crack growth in natural rubber vulcanizates with and without carbon black were analyzed in refs. 2 and 3. The tear energy dependence on temperature and crosslink density of different carbon black-filled rubbers was measured in ref. 11. Natural rubber compounds having different carbon black contents up to 75 phr were studied in ref. 1: a critical carbon black content, above which crack deviation along the loading direction occurs, was found and, further, it was observed that the compound with 50 phr of carbon black showed the highest strength.

This study is part of a wider research work in which the fracture mechanics approach has been applied to study the effect of carbon black content on the fracture behavior of natural rubber vulcanizates. Some of the obtained results were presented in ref. 12 and will be shortly published in another article. Tensile tests in pure-shear configuration were performed, using an optimized specimen geometry, which favors the crack propagation to occur along the notch plane. In the filled compounds, the onset and propagation of sideways cracks, parallel to the loading direction, was always observed before the failure of the specimen due to the propagation of a forward crack, along the notch plane direction.

Correspondence to: C. Marano (E-mail: claudia.marano@polimi.it)
Journal of Polymer Science: Part B: Polymer Physics, Vol. 48, 1509–1515 (2010)

The unfilled compound (pure natural rubber) never showed sideways cracks formation.

In this work, the fracture mechanics approach was applied to study the fracture behavior of the same carbon black-filled natural rubber compounds, performing tensile tests on a biaxial dynamometer using a central notched cross-shaped specimen. A stress intensity factor at fracture initiation was determined as a function of the draw ratio applied in the direction parallel to the notch plane. The dependence of the fracture phenomenology and fracture resistance on the applied draw ratio and the carbon black content was analyzed. The propensity for crack deviation from the notch plane was also considered.

EXPERIMENTAL

Materials and Test Specimens

The materials, natural rubber (NR0) and carbon black-filled natural rubber (NR25, NR50, and NR75), provided by Bridgestone, have been crosslinked by sulfur vulcanization. The filled natural rubber compounds contain 25, 50, and 75 g of carbon black N330 per hundred grams of rubber (phr). The relevant filler volume fractions are $\varphi_{NR25} = 0.12$, $\varphi_{NR50} = 0.21$, and $\varphi_{NR70} = 0.29$. Plates (200 × 170 × 3 mm) were compression molded at 160 °C and 8 MPa for 15 min so as to assure complete sulfur vulcanization.

Cross-shaped specimens (Fig. 1) were cut from the plates, and a 4-mm long central notch was introduced with a sharp razor blade. To minimize the sample deformation outside the biaxially loaded zone, reinforced rubber was properly placed on the uncured compound and then cured together with it. A 45-μm-thick polytetrafluoroethylene sheet was used to avoid the crosslinking between the reinforcing rubber and the compounds in the central part of the specimen.

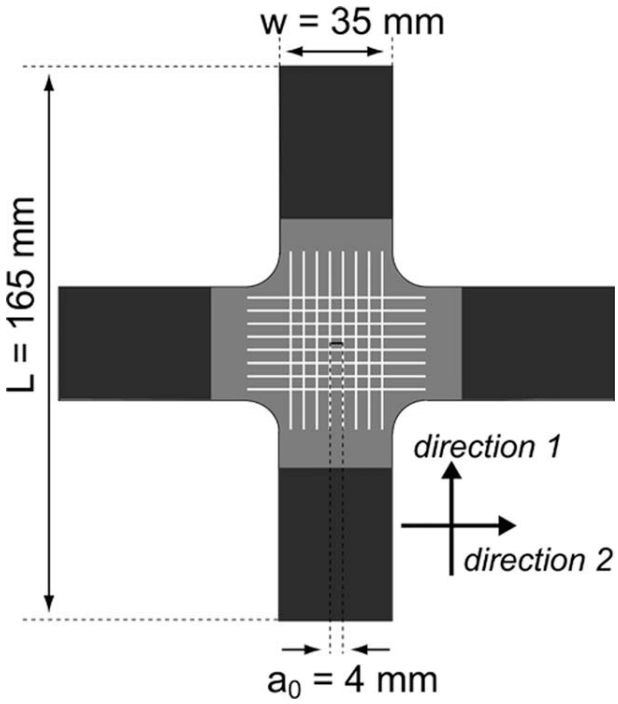

FIGURE 1 Test specimen geometry (dark gray: reinforced rubber). The specimen thickness, *b*, is 3 mm.

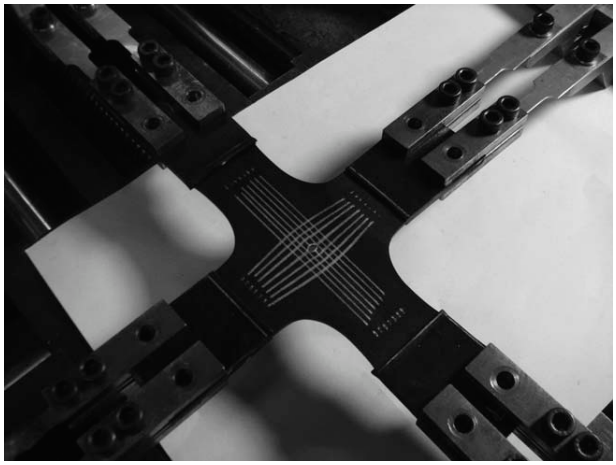

FIGURE 2 Test configuration.

Fracture Test and Data Analysis

Tests were performed on a displacement-controlled biaxial dynamometer developed at LaBS, Politecnico di Milano,[13] and made available for this research. Test configuration is shown in Figure 2. Tests were video recorded, and local displacements were measured through a grid drawn on the biaxially loaded zone of the specimen. In each test, the sample was at first drawn, at 100 mm/min, along a direction parallel to the notch plane (direction 2), up to a given draw ratio $\lambda_2 = (1–2.5)$ and then loaded perpendicularly to the notch plane (direction 1), at 30 mm/min, up to fracture. In the following, these two steps will be also referred to as the drawing and the loading step, respectively. Test procedure and load trends are schematically depicted in Figure 3. The load measured in direction 2, P_2 was let to relax down to a fairly constant value before loading in direction 1.

The fracture mechanics approach was applied to evaluate fracture resistance. Considering the intersection between the two bars of which the cross is formed as a sheet with a central crack under two mutually perpendicular uniform stresses remote from the crack, the stress intensity factor at fracture initiation, K_{Ic}^*, can be calculated as follows:

$$K_{Ic}^* = \sigma_c \sqrt{\pi \cdot a} \tag{1}$$

in which $2a = \lambda_2 \cdot a_0$ is the notch length after the specimen has been stretched up to λ_2 in direction 2 (a_0 mm is the initial notch length), and σ_c is the true stress applied, at crack onset, in direction 1, that was obtained by dividing the applied load by the effective cross section. The latter was

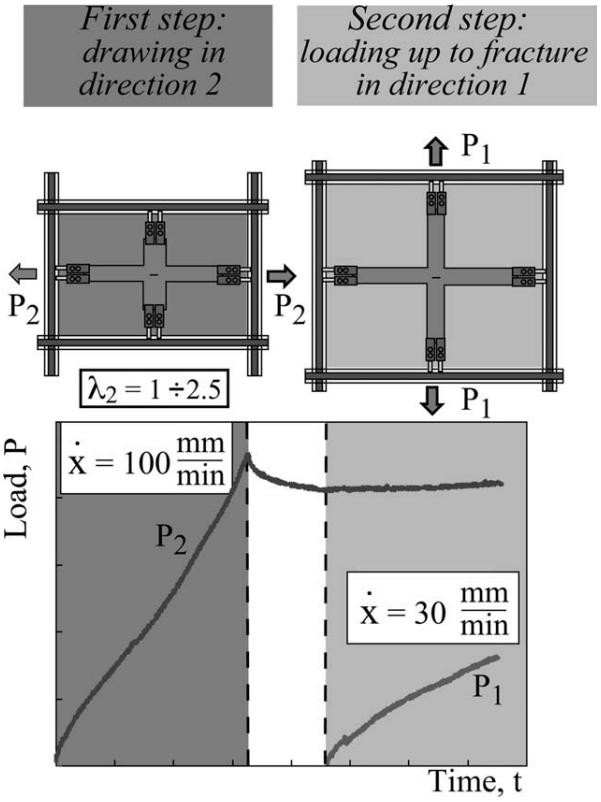

FIGURE 3 Test procedure (see text).

obtained by dividing the initial cross section by the draw ratio λ_1 at crack initiation.

λ_2 was measured locally, at the notch tip, through image analysis, as the ratio $\lambda_2 = \frac{l_2}{l_2^0}$ between the grid lines distance in direction 2 at each time, l_2, and the relevant distance in the undeformed specimen, l_2^0.

Fracture onset was detected from the video recordings of the tests. Two drawbacks to the application of this approach must be considered: one regards test configuration as eq 1 is valid for a sheet with a central crack under biaxial normal stress and the other regards material behavior because the stress intensity factor is defined in the case of linear elastic materials. As for the test configuration, from the video recordings it was observed that deformations in the intersection between the two bars of the cross-shaped specimen are quiet uniform as expected for the configuration considered. As for the material behavior, the compounds here considered are elastic but nonlinear; however, within the deformations taking place in the tests, this approach can be considered as a first approximation and the asterisk, used on the stress intensity factor calculated, indicates this.

RESULTS AND DISCUSSION

Fracture Phenomenology

The tests' video recording permitted to analyze the phenomenology of the fracture process in the different compounds. For the unfilled material NR0, when a specimen is loaded in direction 1, a crack propagates in the forward direction (along the notch plane), irrespective of the draw ratio, λ_2, applied in direction 2.

For the carbon black-filled compounds (NR25, NR50, and NR75), the fracture phenomenology resulted to be dependent on the draw ratio applied in the direction 2. When a sufficiently high value of the draw ratio λ_2 was applied in the drawing step, the slow propagation of a crack parallel to the notch plane (forward crack) was always observed during the following loading step. In Figure 4, a sequence of frames from the video recording of a test performed at a high value of the draw ratio applied in direction 2 ($\lambda_2 = 1.9$) is reported for the compound NR75, as an example. When a low value of the draw ratio λ_2 was applied, a more complex

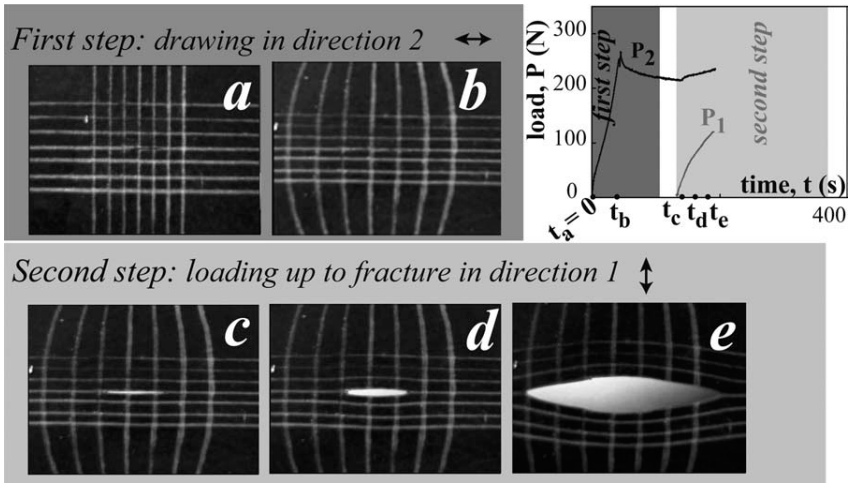

FIGURE 4 Frames from the video recording of a test on NR75 at $\lambda_2 = 1.9$ corresponding to (a) the beginning and (b) the end of the drawing step, in which load is applied parallel to the notch plane, (c) a point immediately after the beginning of the loading step (in direction 1), (d) the onset of the forward crack, and (e) a frame during its propagation. P2 and P1 are the loads applied during the drawing (direction 2) and the loading (direction 1) steps, respectively.

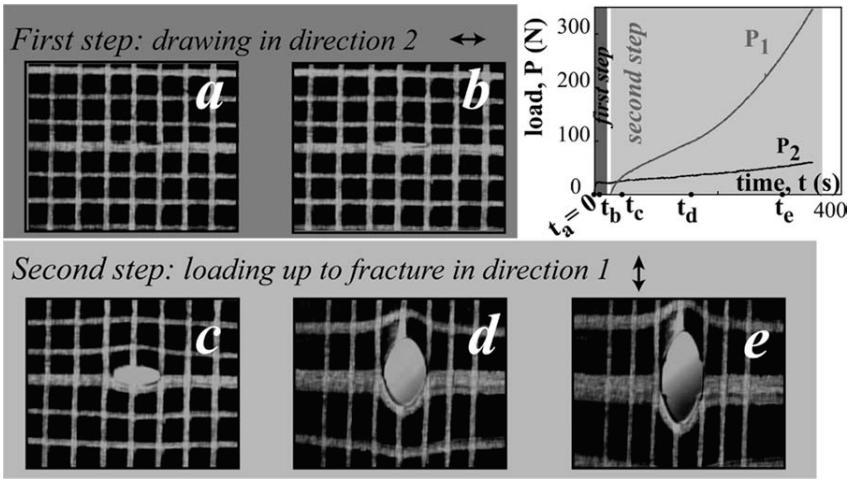

FIGURE 5 Frames from the video recording of a test on NR50 at $\lambda_2 = 1.2$ corresponding to (a) to the beginning and (b) the end of the drawing step, in which load is applied parallel to the notch plane, (c) a point immediately after the beginning of the loading step (in direction 1), (d) the onset of sideways cracks, and (e) just before the catastrophic propagation of the forward crack. P2 and P1 are the loads applied during the drawing (direction 2) and the loading (direction 1) steps, respectively.

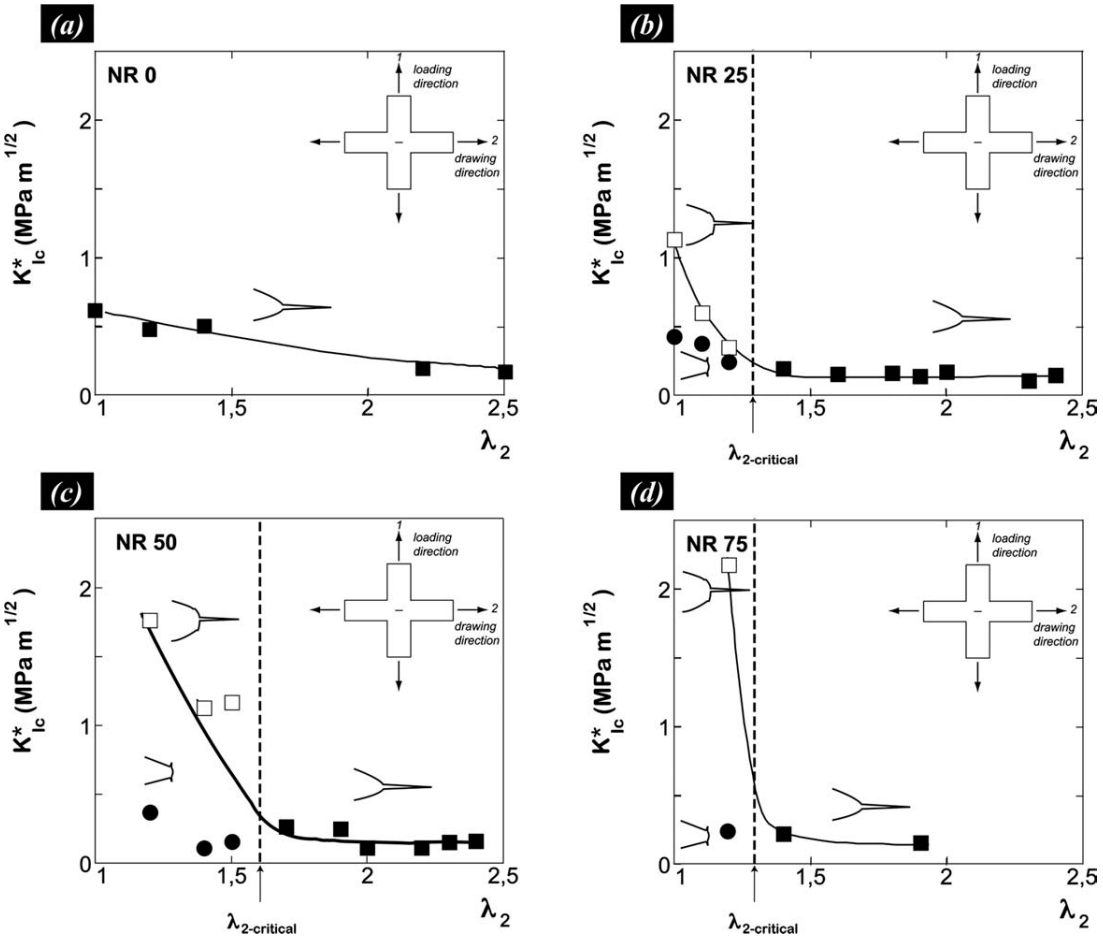

FIGURE 6 Stress intensity factor at fracture initiation, K^*_{Ic}, as a function of draw ratio in direction 2, λ_2, for different carbon black contents: (a) unfilled rubber, (b) 25 phr, (c) 50 phr, and (d) 75 phr. Full circles, onset of sideways cracks followed by a forward crack (open squares). Full squares, onset of a forward crack only (see text).

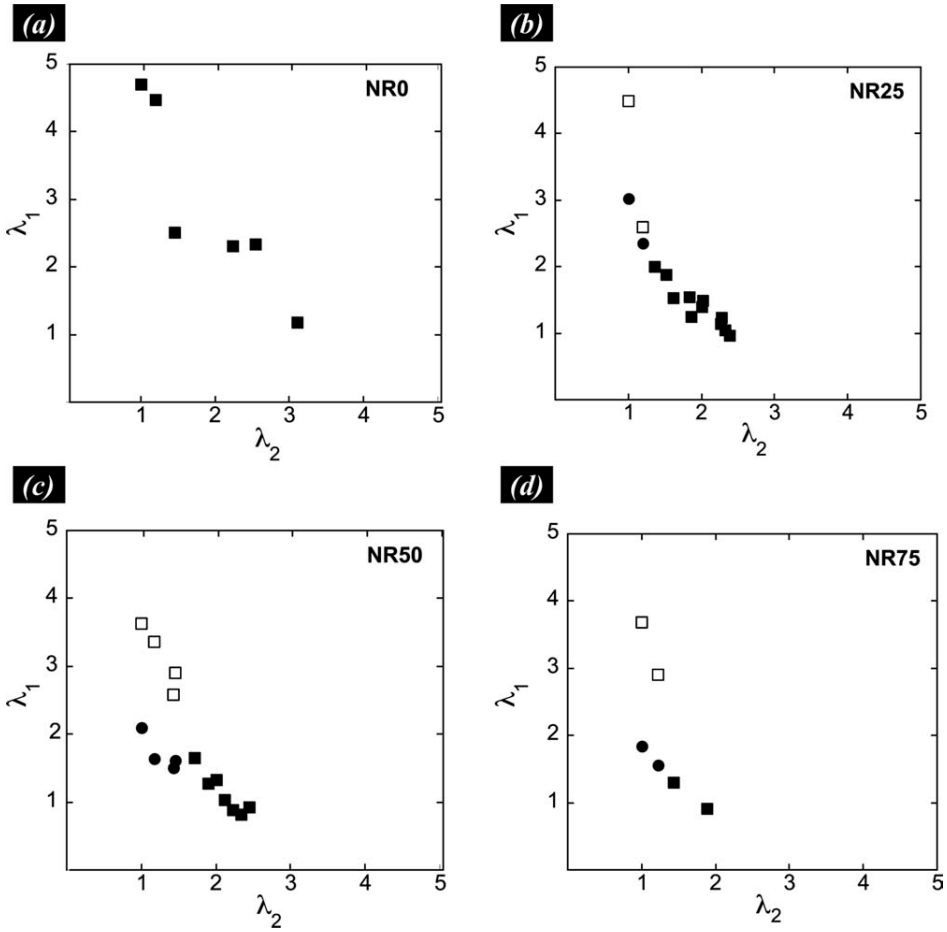

FIGURE 7 Draw ratio in direction 1, λ_1, as a function of draw ratio in direction 2, λ_2, for different carbon black contents: (a) unfilled rubber, (b) 25 phr, (c) 50 phr, and (d) 75 phr. Full circles, onset of sideways cracks followed by a forward crack (open squares). Full squares, onset of a forward crack only (see text).

fracture phenomenology, similar to that shown in pure shear tests reported in ref. 12, was observed. In Figure 5, a sequence of frames from the video recording of a test performed at $\lambda_2 = 1.5$ is shown for the compound NR50 as an example: in this case, during the loading step, the onset of cracks parallel to the loading direction 1 (sideways cracks) always occurred before the catastrophic propagation of a forward crack, parallel to the drawing direction 2, took place.

Fracture Resistance

Stress intensity factor, K^*_{Ic}, was calculated, according to eq 1, at the onset of forward cracks and, when present, also at the onset of sideways cracks. The results are shown in Figure 6(a–d), where K^*_{Ic} is plotted versus the applied draw ratio λ_2 for all the studied compounds. Sketches of the notch tip after the onset of sideways and forward cracks are also reported in Figure 6(a–d) to help the reader.

The unfilled compound NR0 never showed sideways cracks and the fracture strength, measured at the forward crack onset, when loading in direction 1, resulted to be slightly decreasing towards a constant value as the draw ratio applied in direction 2 increases (Fig. 6a).

For the carbon black-filled compounds, it can be observed that at high values of the draw ratio λ_2, where fracture occurs due to propagation of a forward crack only, K^*_{Ic} is quite constant irrespective of the applied draw ratio [full squares in Fig. 6(b–d)], indicating that further drawing in direction 2 does not change fracture resistance when load is applied in direction 1. Moreover, in this draw ratio range, K^*_{Ic} resulted to be not significantly dependent on the carbon black content. At low values of the applied draw ratio λ_2, for which sideways cracks (propagating perpendicularly to the notch plane, along the direction 1) were observed, it resulted that fracture resistance measured at the onset of the sideways cracks [full circles in Fig. 6(b,c)] is not very dependent on the draw ratio and just slightly higher than the strength at high λ_2, and the values of K^*_{Ic} measured at the onset of the forward cracks that subsequently propagated parallel to the notch plane, along the drawing direction [open squares in Fig. 6(b–d)] indicate, instead, that the ultimate material's strength increases as the draw ratio decreases. Further, at

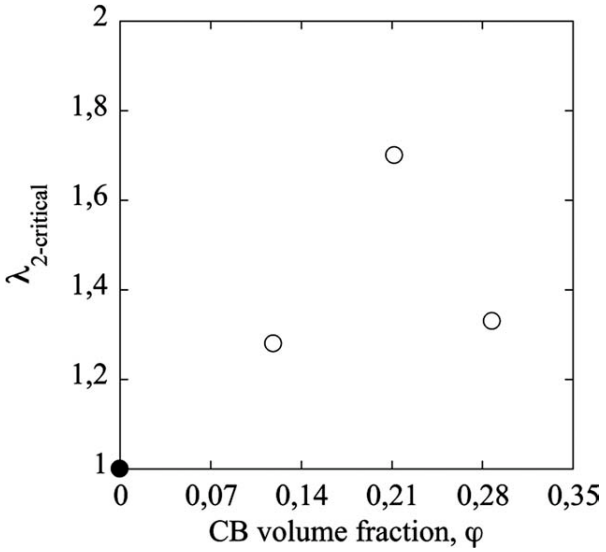

FIGURE 8 Critical draw ratio as a function of filler content. For natural rubber that never showed sideways cracks, a critical draw ratio $\lambda_{2-\text{critical}} = 1$ was considered (full circle).

low values of draw ratio, the ultimate strength increases with the CB content. The results relevant to tests without prestretching in direction 2 ($\lambda_2 = 1$) are in agreement with those found on the same materials of this work, using the pure shear test configuration.[12]

From the data reported in Figure 6(b–d), a critical value of the draw ratio applied in the drawing step $\lambda_{2-\text{critical}}$ was determined for each filled compound: it is the minimum value of the draw ratio that has to be applied parallel to the notch plane so that only a forward crack propagates and it was obtained as the mean between the value of λ_2 of the last specimen showing sideways cracks and that of the first one showing only the propagation of a forward crack.

Figure 7 reports the draw ratios, λ_1, in the loading direction at sideways and/or forward crack onset as a function of the applied draw ratio λ_2 (symbols as in Fig. 6). The draw ratio λ_1 was measured locally, at the notch tip, through image analysis, as the ratio $\lambda_1 = \frac{l_1}{l_1^0}$ between the grid lines distance in direction 1 at each time, l_1, and the relevant distance in the undeformed specimen, l_1^0. It resulted that in all cases in which sideways cracks were present, the value of the ratio $\frac{\lambda_1}{\lambda_2}$ at sideways cracks onset was larger than one. Nevertheless, for NR0 and in some cases for NR25, the propagation of only a forward crack occurred also in the case where $\frac{\lambda_1}{\lambda_2}$ was larger than one: in these cases, although the material strength was deformed in the loading direction 1, the strength anisotropy induced was evidently not sufficient for sideways cracks to occur.

In Figure 8, the critical draw ratio, $\lambda_{2-\text{critical}}$, is plotted versus the carbon black content, φ. A nonmonotonic trend is observed: $\lambda_{2-\text{critical}}$ reaches a maximum value for the compound with 50 phr of CB ($\varphi = 0.21$).

It has to be mentioned that, for each of the studied compounds, the obtained $\lambda_{2-\text{critical}}$ is significantly lower than the relevant draw ratio at the strain-induced crystallization onset, which was measured[12] from wide-angle X-ray scattering experiments as a function of carbon black content and is reported in Table 1.

Therefore, $\lambda_{2-\text{critical}}$ has not to be related to strain crystallization but rather to molecular orientability and reorientability during deformation. In this sense, it can be thought that to suppress the formation of sideways cracks, it is necessary to reach a certain molecular orientation. The critical draw ratio, $\lambda_{2-\text{critical}}$, is not a direct measure of molecular orientation since the presence of carbon black causes an amplification of the strain in the rubber molecules and can also modify their orientability.[14] During deformation, chains between chemical and physical crosslinks orient, but, as strain increases, bonds between rubber chains and carbon black may break and the chains may recoil loosing the achieved orientation.[10] These phenomena are dependent on carbon black content.

As for strain amplification, it can be taken into account adopting Nielsen's model,[15]

$$\lambda_{2-\text{corrected}} = \left[\frac{\lambda_2 - 1}{\left(1 - \varphi^{\frac{1}{3}}\right)}\right] + 1 \qquad (2)$$

which considers rubber and filler particles in a series arrangement and perfectly linked to rubber molecules.

The orientability of the different compounds was considered to be proportional to $1/\lambda_{\text{cryst\_onset}}$ in the hypothesis that crystallization occurs at constant molecular orientation.

The product of the actual draw ratio $\lambda_{2-\text{corrected}}$ by the orientability $1/\lambda_{\text{cryst\_onset}}$ was thus adopted as an estimate of molecular orientation. In Table 2, the critical draw ratio $\lambda_{2-\text{critical}}$ and the molecular orientation $\lambda_{2-\text{corrected}} \cdot 1/\lambda_{\text{cryst\_onset}}$ are reported for the different compounds. It can be observed that the molecular orientation at the critical draw ratio is different for the different compounds: it shows the same nonmonotonic trend as $\lambda_{2-\text{critical}}$.

TABLE 1 Draw Ratio at Crystallization Onset for the Different Compounds, as Measured by WAXS Experiments

Compound	NR0	NR25	NR50	NR75
Draw ratio at crystallization onset, $\lambda_{\text{cryst\_onset}}$	4.25 ± 0.25	3.25 ± 0.25	2.75 ± 0.25	2.75 ± 0.25

TABLE 2 Values of Critical Draw Ratio, $\lambda_{2-\text{critical}}$, and Molecular Orientation, $\lambda_{2-\text{corrected}} \cdot 1/\lambda_{\text{cryst\_onset}}$, for the Different Compounds

Compound	NR0	NR25	NR50	NR75
$\lambda_{2-\text{critical}}$	1	1.35 ± 0.16	1.7 ± 0.22	1.32 ± 0.11
$\lambda_{2-\text{corrected}} \cdot 1/\lambda_{\text{cryst\_onset}}$	0.2	0.5	1.0	0.7

To interpret these results, it is necessary to consider that during the loading step perpendicular to the notch plane, the strength anisotropy at the notch tip changes: in fact the molecules can be thought to loose their orientation in the drawing direction (direction 2) while orienting in the loading direction. Therefore, the tendency to give rise to sideways cracks when loading in direction 1 should be linked to the propensity of the molecular chains to reorient in direction 1 during loading.

From the results in Figure 7, it can be hypothesized that, increasing the carbon black content up to a volume fraction of 0.21, the propensity of the molecular chains to reorient in direction 1 during the loading step increases and therefore the draw ratio, $\lambda_{2-\text{critical}}$, that has to be applied to avoid sideways cracks, is higher for NR50 ($\varphi = 0.21$) than for NR25. At higher filler content ($\varphi = 0.28$), $\lambda_{2-\text{critical}}$ decreases suggesting that for the compound NR75 reorientation of the molecules in the loading direction is more difficult.

CONCLUSIONS

The aim of this work was to evaluate the fracture resistance of filled natural rubber compounds as a function of molecular orientation, using biaxially loaded notched specimens. The orientation was induced by specimen prestretching parallel to the notch plane. It was possible to determine the resistance to crack propagation only above a certain value of prestretching, because below this value crack deviation from the notch plane was always observed.

It was found that fracture resistance along a plane parallel to the notch plane is fairly constant irrespective of the applied prestretch and does not significantly depend on the carbon black content. Further, from a qualitative evaluation of molecular orientation, it turned out that the minimum molecular orientation required to avoid sideways cracks is different for the different compounds.

A deeper understanding of the observed phenomena is in progress through a quantitative evaluation of molecular orientation as a function of the strain history and its relation to material resistance.

This work was supported by Bridgestone Technical Center Europe, Roma. The authors thank the Bridgestone technical staff for the helpful discussion.

REFERENCES AND NOTES

1 Hamed, G. R.; Al-Scheneper, A. A. Rubber Chem Technol 2002, 76, 436–460.

2 Hamed, G. R.; Rattanasom, N. Rubber Chem Technol 2001, 75, 323–332.

3 Hamed, G. R.; Rattanasom, N. Rubber Chem Technol 2002, 75, 935–941.

4 Gent, A. N.; Razzaghi-Kashani, M.; Hamed, G. R. Rubber Chem Technol 2003, 76, 122–131.

5 Kendall, K. Proc R Soc Lond A 1975, 344, 287–302.

6 Gent, A. N.; Kim, H. J. Rubber Chem Technol 1978, 51, 35–44.

7 Gent, A. N.; Zhang, L.-Q. Rubber Chem Technol 2002, 75, 923–934.

8 Trabelsi, S.; Albouy, P. A.; Rault, J. Macromolecules 2002, 35, 10054–10061.

9 Hamed, G. R. Rubber Chem Technol 1991, 64, 493–500.

10 Hamed, G. R. Rubber Chem Technol 1994, 67, 529–536.

11 De, D.; Gent, A. N. Rubber Chem Technol 1996, 69, 834–850.

12 Boggio, M. Fracture Behaviour of Carbon Black Filled Natural Rubber, Ph.D. Thesis; Politecnico di Milano: Milano, Italy, 2010.

13 Quaglini, V.; Corazza, C.; Poggi, C. Compos A 2008, 39, 1331–1342.

14 Bakobza, L.; Rapoport, O. J Appl Polym Sci 2002, 85, 2301–2316.

15 Nielsen, L. E. Mechanical Properties of Polymers and Composites; Marcel Dekker, Inc.: New York, 1974; Vol. 2, Chapter 7.

Biaxial fracture testing of rubber compounds

F. Caimmi, R. Calabrò, C. Marano & M. Rink
Dipartimento di Chimica, Materiali e Ingegneria Chimica "Giulio Natta" Politecnico di Milano, Milano, Italia

ABSTRACT: In this work the fracture toughness of natural rubber compounds under biaxial tensile loading condition was evaluated determining the J-integral by finite element analysis. To this aim a sound constitutive equation from tests under simple well-identified stress states such as tensile and plane strain test configurations was first determined for the studied materials. The models were then validated through the numerical simulation of both tensile tests under more complex stress states and of fracture tests in pure shear test configuration. The method was then applied to biaxial fracture tests previously performed.

1 INTRODUCTION

In a previous work (Marano et al. 2010) tensile tests under biaxial loading conditions were performed using a central notched cross-shaped specimen to study the fracture behaviour of carbon black-filled natural rubber compounds. The test consisted of two steps: a drawing step was initially performed loading the specimen in the direction parallel to the notch plane, up to different draw ratios, and then the specimen was loaded in the direction normal to the notch plane up to fracture. The fracture mechanics approach was applied to evaluate fracture toughness as a function of the draw-ratio set in the drawing step, showing a dependence of toughness on the draw ratio, at least for low draw ratios. As a fracture mechanics parameter a stress intensity factor was determined considering the central part of the cross-shaped specimen as a biaxially loaded infinite plate. This approach has several shortcomings. First, the part of the specimen under biaxial load is not easily identified and the stress at the boundaries is, thus, not precisely known. Further, the high strains and the highly non-linear behaviour of the material imply strong limitations in applying the stress intensity factor, whose use can therefore lead to misleading results.

The present work aims at determining an energy based parameter, such as J-integral, for this test configuration by means of numerical simulation via finite element (FE) method. In order to obtain sensible data, several steps are needed, namely: identification of a constitutive law, validation of its predictive capabilities and finally calculation of the J-integral at fracture from the experimental load data.

In the first part of this work a sound constitutive equation was determined, for each of the studied materials, from tests under simple well identified stress states such as uniaxial and plane strain tensile configurations. In this work it was *a priori* decided to focus on hyper-elastic material models to describe rubber mechanical response; among the various models available, see *e.g.* (Holzapfel 2000), Ogden model was selected due to its ability to carefully reproduce the experimental data.

In the second part tensile tests under more complex stress states, that is the tensile loading of a cross-shaped specimen, and fracture tests in pure shear configuration (Boggio 2010) were carried out and the experimental results compared to numerical simulation predictions for model validation. It is worth to highlight that non-linear material models bring up a number of issues. In particular, in the material parameters identification step, the non-linear optimization problem to be solved in order to identify the material constants may have multiple solutions, depending also on the number of experimental tests used for fitting; such a multiplicity can lead to very different numerical solutions when these solutions are used to solve some given boundary value problem (Ogden et al., 2004). The experimental validation step on some further configuration is therefore mandatory in order to obtain sound results and to be confident in the actual predictive capabilities of the identified law.

The FE method was then applied to the tests previously performed in (Marano et al. 2010).

2 EXPERIMENTAL STUDY

2.1 *Materials*

Natural rubber (NR0) and carbon black-filled natural rubber (NR50), kindly provided by Bridgestone, containing 50 g of carbon black N330 per hundred grams of rubber (phr), which corresponds to a volume fraction of 0.21. Plates having a thickness, *B*, between 1.5 and 3 mm were compression moulded at 160°C and 8 MPa for 15 min, so as to assure complete sulphur vulcanization.

2.2 *Tests for materials' constitutive equation determination*

Tests in uniaxial and plane strain tensile configurations were performed to determine the constitutive equations of the studied materials. The tests were carried out at 23°C on a INSTRON 1185 dynamometer, at a nominal strain rate of 1.5 min^{-1}. A video-extensometer was used for strain measurement both in the loading and in the transverse direction.

Dumbbell specimens were used for uniaxial tensile test.

The plane strain tensile stress state was obtained subjecting rectangular specimens 30 mm high and having 3 x 98 mm^2 section subjected to uniaxial loading.

2.3 *Tests for model validation*

Test under biaxial tensile configuration were performed on a displacement-controlled biaxial dynamometer developed at LaBS, Politecnico di Milano, and made available for this research. Cross-shaped specimens, shown in Figure 1, were used. Parts in dark grey are made of reinforced rubber, which is vulcanized together with the rubber compound during the compression moulding process. During testing, deformation of the reinforced part of the specimen can be neglected. The tests were carried out at 23°C, drawing the sample at 30 mm/min in direction 1 and 2 simultaneously. Samples surface was sprayed with a target pattern in order to obtain a deformation field through the digital image correlation technique.

Fracture tests in pure shear test configuration were performed using a notched version of the specimen described in 2.2 for plane strain test. Notches 30 mm length were introduced with a cutter and sharpened with a razor blade. To ensure that crack propagates along the notch plane a groove was cut on both sides of the PS specimen. The ratio of the actual specimen thickness on the notch plane to that in the ungrooved region was about 0.6.

The tests were carried out under the same conditions as for the tests in 2.2.

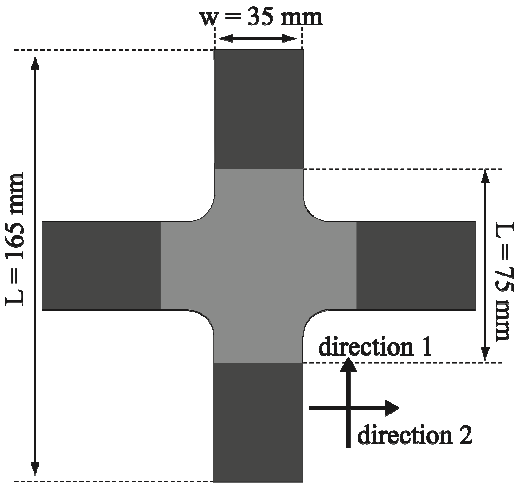

Figure 1. Test specimen geometry (dark gray: reinforced rubber).

Material fracture toughness was evaluated as follows:

$$J = \eta\left(\frac{a}{W}\right)\frac{U}{B_C}(W-a) \tag{1}$$

where η = dimensionless factor which for ungrooved pure shear specimen is equal to 1 (Hocine et al. 2003), (Kim & Joe, 1989); B_c = the thickness of the grooved sample; W = the specimen width; a = the crack length; U = the fracture input energy.

Pure shear fracture tests are thoroughly described in (Boggio et. al 2011).

2.4 *Fracture test*

The numerical simulation was applied to the fracture tests reported in (Marano et al. 2010), which are shortly described in the following. Tensile tests under biaxial loading conditions were performed using the cross-shaped specimen described in 2.3 in which a 4 mm long central notch was introduced with a sharp razor blade. The test was video-recorded to determine fracture initiation time. To measure a local (near tip) draw ratio, hereafter denoted simply as λ_2, a grid was drawn on the biaxially loaded zone of the specimen. (Marano et. al 2010). The test consisted of two steps: the sample was first drawn, at 100 mm/min, along a direction parallel to the notch plane (direction 2), up to a given draw ratio λ_2 (in the range 1–2.5) and then loaded perpendicularly to the notch plane (direction 1), at 30 mm/min, up to fracture. Test procedure and load trends are schematically depicted in Figure 2. The load measured in direction 2, P_2 was let to relax down to a fairly constant value before loading in direction 1.

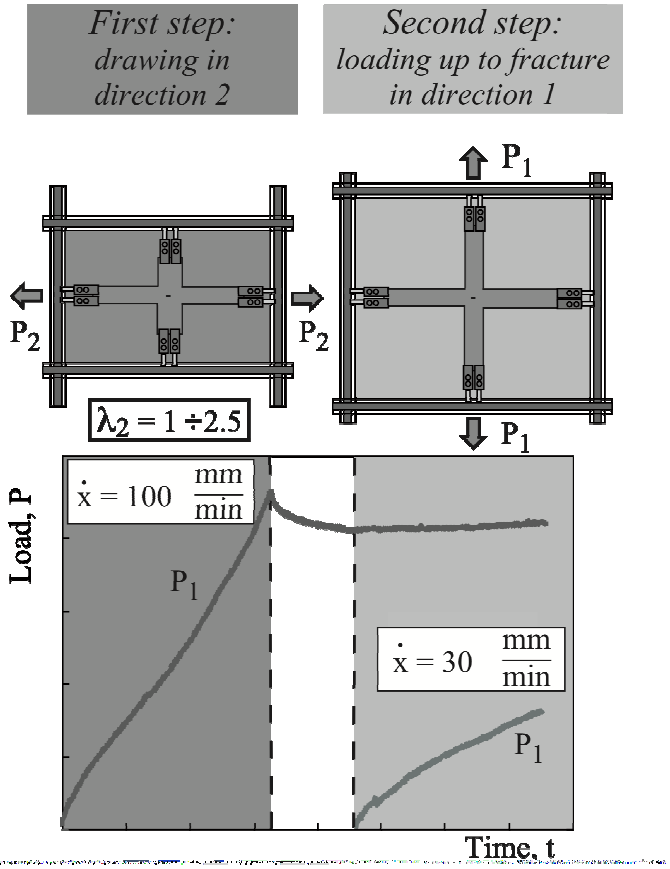

Figure 2 Procedure of the fracture test on cross-shaped sample.

Note that this is a pure Mode I fracture test, due to specimen symmetry and loading configuration. In the studied materials molecular orientation induced by deformation is expected to give rise to strength anisotropy and to a dependence of toughness on λ_2, at variance with what one would anticipate if the materials were isotropic linear elastic.

3 MODELING

3.1 *Constitutive model*

As mentioned earlier, at this stage of the research work, the description of material behaviour was deliberately restrained to the class of hyper-elastic materials. In this class, Ogden's celebrated hyper-elastic material model was selected (Ogden, 1972). Among the various modifications of the model proposed in literature, the one implemented in the FE software ABAQUS (Dassault Systèmes, 2010) was selected for obvious convenience, as ABAQUS is the software used for FE simulation.

In ABAQUS Ogden's model is expressed in terms of a hyper-elastic strain energy function as

$$\Psi = \sum_{i=1}^{N} \frac{2\mu_i}{\alpha_i}\left(\bar{\lambda}_1^{\alpha_i^2} + \bar{\lambda}_2^{\alpha_i^2} + \bar{\lambda}_3^{\alpha_i^2} - 3\right) + \sum_{i=1}^{N} \frac{1}{D_i}(J-1)^{2i} \quad (2)$$

where the first summation represents the deviatoric part of the mechanical response and the second the volumetric one. λ_j (j=1,2,3) are the principal stretches, while $\bar{\lambda}_j$ are the deviatoric principal stretches *i.e.*

$$\bar{\lambda}_j = J^{-1/3}\lambda_j \quad (3)$$

with J being the volume ratio, *i.e.* the determinant of the deformation gradient.

In equation (2) N is the number of terms in the summations, and is a fit parameter. μ_i, α_i and D_i are material constants to be identified; the μ_i are related to G, the shear modulus of the material in the reference configuration (*i.e.* $\sum_i \mu_i = G$) while the D_i are related to volumetric expansion.

To model NR0, material incompressibility was assumed and thus all of the D_i were set to zero. As to NR50, experimental data obtained on the lateral contraction of plane strain specimens indicated that the such material was compressible, thus to obtain a good fit a volumetric term was inserted in the model, *i.e.* D_1 was not set to zero, while for i>1 the D_i were set to zero also for NR50. With such a choice, D_1 can be directly related to bulk modulus, K, in the reference configuration by the relation K=2/ D_1 (Dassault Systèmes, 2010).

Identification of material constants can be performed directly by ABAQUS using the least-square method (Dassault Systèmes, 2010). ABAQUS internal algorithms were used for NR50. With NR0 ABAQUS was unable to obtain fits corresponding to thermodynamically stable materials over the whole range of experimental deformations considered in this work. Thus an *ad-hoc* identification routine was written; the routine minimizes the square of the Euclidean distance between the experimental stress-strain response (simultaneously for plane strain and uniaxial tests) and the one calculated at varying material parameters. The optimization was constrained by imposing that the tangent stiffness matrix be positive for λ=1,2,3,4 and 5 for uniaxial loading, plane strain loading and biaxial loading. The need to impose the positive definiteness at various levels of strain comes from the fact that for Ogden materials the tangent stiffness matrix depends on deformation, as it can be readily verified by calculating it from (2) . While this procedure does not rigorously grant the obtainment of a stable material for all possible stress states and for every possible level of deformation from the identification routine, in this work it was enough to give a stable material for biaxial, uniaxial and plane strain stress states at every level of nominal deformation among those reached during the experiments.

3.2 *FE models*

In this work two finite element models were used and implemented in the ABAQUS FE code (Dassault Systèmes, 2010). The first model was used to

reproduce the behaviour of pure shear fracture specimens. It is a 3D model reproducing only one quarter of the specimen; the need to use a 3D model arise from the presence of the groove in the specimens. Velocity is prescribed on the top part of the boundary, while symmetry conditions are imposed on the other faces. Simulations were run up to the experimentally determined fracture time. Notches were modelled as region with unconstrained boundary displacements. 20-nodes brick element with reduced integration and mixed formulation (C3D20RH in ABAQUS, helpful in the case of incompressible materials) were used to model most of the specimen. In a region having a radius of 5 mm around the crack front fully integrated elements were used. Near the crack tip typical element edge dimension was 0.05 mm. A total of about 7000 elements were used in the model.

The second one is the model for the cross-shaped specimen. It is a plane stress 2D model of the specimen in Figure 1; both reinforced rubber and unreinforced rubber were modelled. Reinforced rubber was modelled as isotropic liner elastic material with modulus 720 MPa (measured from uniaxial tensile tests), while unreinforced rubber was modelled with the Ogden model previously described. Only a quarter of the specimen was modelled due to symmetry. At the boundary (edges of the cross arms) a velocity corresponding to the crosshead displacement rate was prescribed in the case of un-notched biaxial specimens used for validation, while, for easiness, a stress corresponding to the fracture initiation load was prescribed in the case of fracture specimens. 8-noded rectangular element with reduced integration and mixed formulation were used for most of the model; elements with standard displacements formulation were used to model the reinforced rubber regions. In the tip region fully integrated elements were used. A total of 15500 were used in the model.

The J-integral was determined as a line integral using the ABAQUS built-in routine, thus avoiding the need to obtain accurate stress fields at the tip.

4 RESULTS AND DISCUSSION

4.1 *Constitutive law identification*

Stress-strain curves obtained in uniaxial tensile and plane strain tests together with the identified constitutive laws are reported for NR0 and NR50 in figures 3 (a) and (b) respectively.

Very good agreement exists between the identified law and the experimental data.

For the NR0 material it has been found that a three terms Ogden strain energy was needed to find a good fit to the experimental data. In the case of NR50 two terms gave a better results than three terms. As recalled earlier, in this case a single volumetric term corresponding to a Poisson's ratio of 0.4 was needed to obtain a good fit (see 3.1); the value was determined from lateral strain measurements and supplied directly to the identification routine.

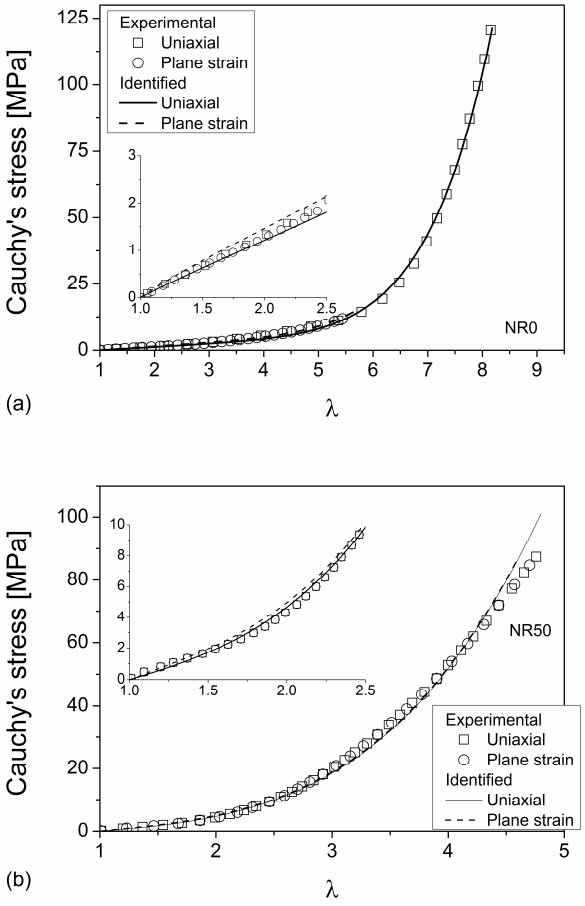

Figure 3 Experimental and identified stress-strain behaviour in terms of true stress/stretch ratio. Insets show the initial region of the plot. (a) NR0. (b) NR50.

4.2 *FE models validation*

In Figure 4 some representative predictions from the FE models of the pure shear fracture specimens are given in terms of load-displacement traces recorded up to the fracture load. Excellent agreement was obtained for NR0 predictions while the agreement for NR50 is slightly less satisfactory. In particular, the initial compliance is not correctly reproduced nor is the strain hardening behaviour, which begins to show itself at crosshead displacements of about 11 mm.

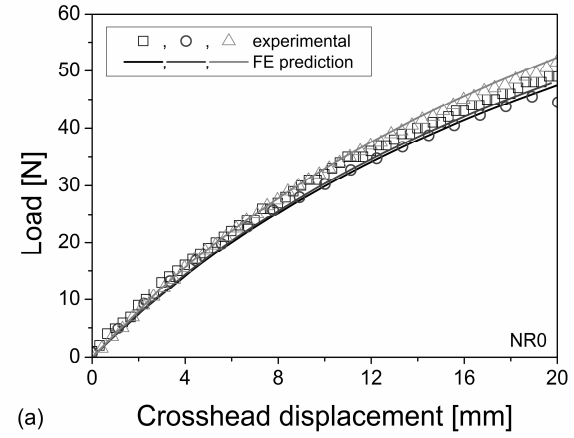

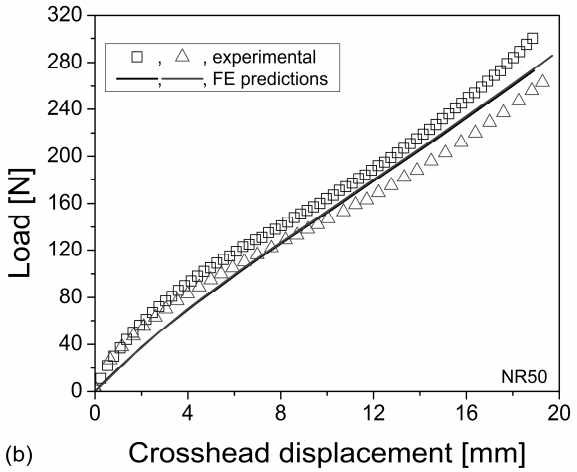

Figure 4 Load-displacement traces for pure-shear fracture specimens. Various experimental samples are shown (symbols) together with the respective FE prediction. Corresponding greytones indicate results for the same sample. (a) NR0. (b)NR50.

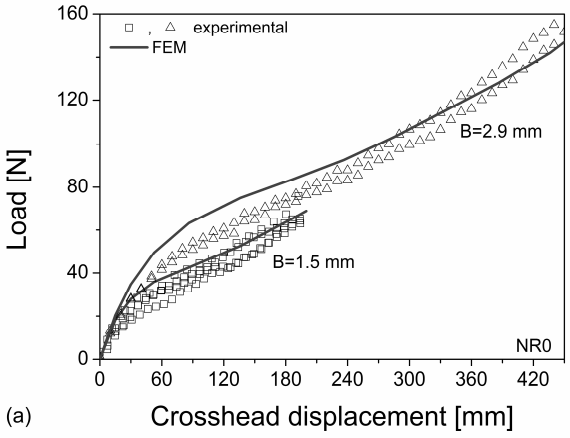

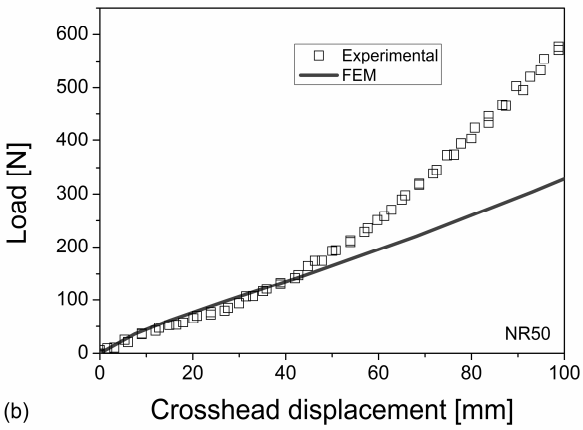

Figure 5 Load-displacement traces for the un-notched cross-shaped specimens. Various experimental samples are shown (symbols) together with the respective FE prediction (a) NR0. Samples with different thickness are shown (b)NR50. Samples thickness is 1.5 mm.

Prediction for the un-notched cross-shaped specimen are shown in Figures 5 and 6. For NR0 the agreement is more than satisfactory in terms of predictions of both the load-displacement trace (Fig. 5a) and the strain field (an example of the comparison between the prediction and some measurements is given in Figure 6).

In the case of NR50 (Fig. 5b) a good agreement could be obtained only at low forces. The FE model clearly fails to catch the abrupt increase in stiffness shown by the experiments. Whether this is due to a problem with the FE model of the cross-shaped specimen (arising at high loads and therefore unnoticed for NR0) or to a problem with the identified constitutive model is at present unclear. As to this last hypothesis, it is worth remembering that the larger the number of experimental data available for fitting, the better are the predictive capabilities of Ogden's model (Ogden et al. 2004). It is thus possible that better results could be obtained by increasing the number of experimental stress states used as inputs for the identification procedure. Further investigation is currently underway.

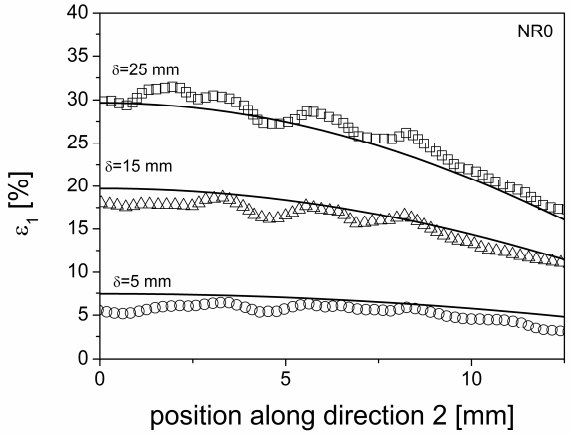

Figure 6 Nominal strain along direction 1, ε_1, vs. position for NR0 cross-shaped unnotched samples. (solid lines: calculated via FE; symbols: measured via DIC). Reference system origin is in the symmetry center of the specimen. δ= crosshead displacement. Specimen thickness *B*=1.5 mm

4.3 *J-integral determination*

Due to the unsatisfactory results obtained with the validation of the NR50 models, J-integral calcula-

tions were performed only for NR0. The results from such calculations are shown in Figure 7.

A strong decrease of J with the draw ratio can be observed thus confirming the qualitative trends obtained in (Marano et. al. 2010) and showing the sensitivity of rubber toughness to deformation induced structural anisotropy.

Toughness at λ_2=1 is about 30 kJ/m^2. From pure shear fracture tests on the same material (Boggio 2010) a value of 23±1 kJ/m^2 was obtained at similar nominal strain rate. Further tests are underway to asses the repeatability of the cross-shaped fracture tests.

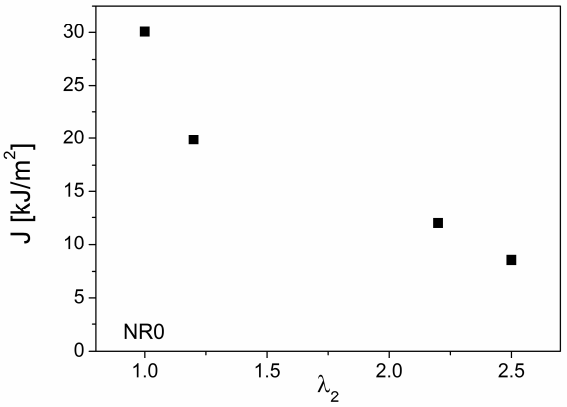

Figure 7 Natural rubber fracture toughness as a function of the transverse draw ratio for cross-shaped fracture specimens.

5 CLOSING REMARKS

An *ad-hoc* identification and validation technique to identify Ogden's model parameters was developed and applied to predict the fracture toughness of natural rubber compounds under a special biaxial loading condition.

The identification of Ogden's parameters from plane strain and uniaxial tests seemed straightforward. Anyway it was possible to find a set of parameters actually able to predict the response of the material under very different loading conditions only for NR0. In the case of NR50 the predictions were much less satisfying. The reasons for such a disagreement may lay in every step behind the validation one:

-Ogden's model was actually unable to catch the behaviour of the carbon-black-filled material;

- the number of stress-states used for identification was insufficient;

- the intrinsic problems arising in non-linear optimization prevented the finding of a parameter set corresponding to the actual material behaviour.

Nonetheless the technique was successfully applied to calculate from the experimental data a fracture parameter for natural rubber (NR0) as a function of the applied draw ratio, confirming the actual dependence on transverse strain of natural rubber fracture toughness.

ACKNOWLEDGMENTS

F.C. gratefully acknowledges partial support by Italy's Consorzio Interuniversitario Nazionale per la Scienza e la Tecnologia dei Materiali (INSTM) through grant ID/DB234.

REFERENCES

Boggio, M. 2010. Ph.D. Thesis. Fracture Behaviour of Carbon Black Filled Natural Rubber; Politecnico di Milano, Milano, Italy

Boggio, M., Marano, C., Rink, M.2011. Time-Dependence of Fracture Beahviour of Carbon Balck Filled Natural Rubber. 7th Europen Conference on Constitutive Models for Rubber (ECCMR7), Dublin, Ireland.

Dassault Systèmes Simulia Corp. 2010. ABAQUS/ Analysis User's Manual, version 6.10. Providence, RI, USA.

Holzapfel G.A., *Nonlinear Solid Mechanics* ([n.p]: Wiley, 2000).

Marano C., Calabrò R. & Rink M. 2010. Effect of Molecular Orientation on the Fracture Behavior of Carbon Black-Filled Natural Rubber Compounds. *Journal of Polymer Science: Part B: Polymer Physics*, 48: 1509–1515.

Ogden R.W., Large Deformation Isotropic Elasticity: On the Correlation of Theory and Experiment for Compressible Rubberlike Solids, *Proceedings of the Royal Society of London. Series A, Mathematical and Physical Sciences*, 328 (1972), 567-83.

Ogden R.W., Saccomandi G. & Sgura I., Fitting hyperelastic models to experimental data, *Computational Mechanics*, 34 (2004), 484-502.

Mechanical characterization of carbon black filled NR/BR compounds from small strains up to fracture

E. Cazzoni, R. Calabrò, C. Marano, M. Rink
Politecnico di Milano, Dipartimento di Chimica, Materiali e Ingegneria Chimica "Giulio Natta", Milano, Italy
G. Barbaglia
Bridgestone Technical Center Europe S.p.A., Castel Romano, Roma, Italy

ABSTRACT: In this research filled natural rubber (NR), butadiene rubber (BR) and a 50/50 NR/BR blend, having different carbon black (CB) contents, were studied. Dynamic-mechanical characterization, tensile tests were carried out. Fracture tests using notched pure shear test specimens were also performed. The fracture mechanics approach was applied so as to determine J-integral at crack onset. Fracture phenomenology was analysed from video-recordings of the tests. It was observed that 'sideways' cracks propagating at the crack tip in the loading direction before the onset of a 'forward' crack propagating along the notch plane and which are responsible for high toughness values develop for rubber contents above 35 phr of rubber for NR and the NR/BR blend, while for BR a larger carbon black content is required.

1 INTRODUCTION

The largest application of rubbers is in the tire industry, among the many requirements of the final product, three fundamental ones are rolling resistance, wet skid (or grip) and wear. All three are complex properties of the product and determined by different intrinsic properties of the compounds adopted. Generally the optimization of a rubber compound to obtain the best performance of the tire is a difficult task since improving one requirement may be detrimental for another one. Performance of a given rubber compound depends on both the nature of the rubber matrix and the type and content of filler. Carbon black filled blends of natural and butadiene rubbers are widely used.

Natural rubber (NR) is known to exhibit numerous outstanding properties, such as good oil resistance, low gas permeability, improved wet grip and rolling resistance, coupled with high strength (Kaushik 2010). Polybutadiene (BR) is frequently found in treads, sidewalls, and some casing components of the tire because it offers good abrasion resistance, and tread wear performance and enhances resistance to cut propagation. BR can also be blended with natural rubber, and many authors have reported that such compositions give improved fatigue and cut growth resistance (Mezynski & Rodgers 1993).

A wide variety of particulate fillers are used in the rubber industry for various purposes, of which the most important are reinforcement, reduction in material costs and improvements in processing (Tinker & Jones 1998). Reinforcement is primarily the enhancement of strength and strength-related properties, abrasion resistance, hardness and modulus (Heinrich & Kluppel 2002).

As known from the literature (Massie 1993 & Sircar 1973), the NR/BR blend is heterogeneous and exhibits a two-phase morphology. The aim of this work is to compare the mechanical behaviour of the blend with those of its two components. The dynamic-mechanical properties, the tensile behaviour and fracture behaviour of natural rubber (NR), butadiene rubber (BR) and a 50/50 NR/BR blend, having different carbon black (CB) contents, were studied.

2 EXPERIMENTAL DETAILS

2.1 Materials

Natural rubber, polybutadiene and a 50/50 NR/BR blend filled with four different contents (15, 35, 50 and 70 phr) of carbon black N134 were studied. NR and BR compounds were prepared also without carbon black (CB), but this was not possible for the NR/BR blend. All compounds were vulcanized with sulphur in a compression molding press at 160°C and 8 MPa for 15 minutes. All materials were pro-

vided by Bridgestone Technical Center Europe S.p.A.

2.2 *Dynamic Mechanical Analysis*

The dynamic-mechanical properties of the compounds were measured with an RSA III analyser. The experiments were performed in tension applying a static deformation on which a dynamic strain having an amplitude of 0.05% of the static deformation and a frequency of 10 Hz was superposed. The static deformation was increase by steps from 0.05% up to about 300%. Prismatic specimens having cross-section 10x2 mm^2 and the gauge length of 40 mm were adopted.

2.3 *Uniaxial tensile tests*

Uniaxial tensile tests were performed at displacement rate 50 mm/min, using dumbbell specimens having 2 mm thickness and a gauge length of 16 mm.

2.4 *Fracture tests*

Fracture tests were performed so as to apply the fracture mechanics approach. Pure shear (PS) specimens were adopted to determine J-integral values at fracture onset. Figure 1 reports the specimen geometry and its relevant dimensions. The specimen is obtained and vulcanized in a purposely-made mold, it is grooved on both sides to promote crack propagation along the notch plane. The notch was introduced with a razor blade just before the test. All tests were performed on an Instron 1185 screw driven dynamometer at a displacement rate of 50 mm/min. Fracture tests were video recorded to determine cracks onset, to observe fracture phenomenology and the crack tip shape and size during the test.

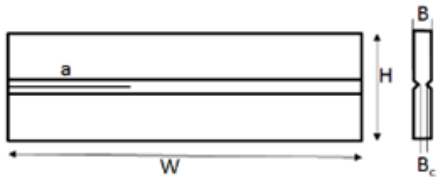

a	W	H	B	B_c	
34	98	30	2	1.4	[mm]

Figure 1. Pure shear specimen with relevant dimensions.

The fracture toughness, expressed as J-integral, was evaluated at cracks onset from the load displacement curves using the expression:

$$J = \eta \frac{U}{B_c(W - a_0)}$$

in which U is the strain energy, B_c is the notch plane thickness, a_0 the initial notch length, W the specimen width and η a dimensionless factor which depends on specimen geometry and test configuration. For the PS specimen geometry used in this work it has been found both from experimental and a numerical analysis that $\eta = 1$ (Ait Hocine, Nait Abdelaziz & Imad 2002.) (Kim & Joe 1989).

3 RESULTS AND DISCUSSION

3.1 *Dynamic-mechanical analysis*

Figure 2 reports the storage modulus E' as a function of the applied static strain for NR at different filler contents. All curves show a decrease in E' as strain increases until a minimum is reached after which an increase in modulus takes place. Also BR and the NR/BR blend show the same trend. The decrease in modulus at relatively low strains reflects dissipative filler-filler and filler-polymer interactions. The level of the minimum is determined by the degree of chemical and 'physical' crosslinks and the contribution of the rigid CB inclusions Finally the increase in E' after the minimum is related to reaching the maximum chain extensibility and strain induced crystallization (Bokobza 2001).

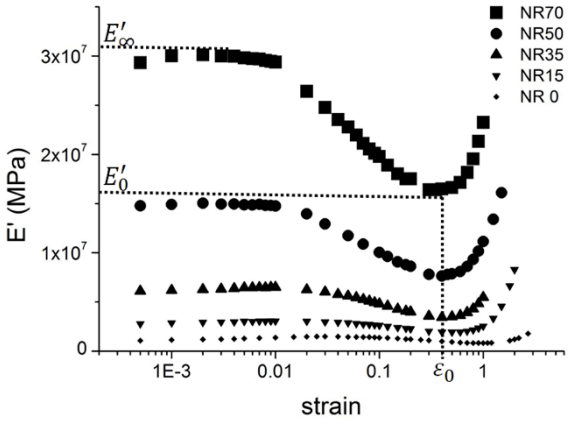

Figure 2. DMA results for natural rubber

From the storage modulus-strain graphs as those in Figure 2 the drop in modulus $\Delta E' = E'_\infty - E'_0$ for each material was determined and is plotted in Figure 3 as a function of CB content. It can be observed that at low CB contents the three rubbers have similar $\Delta E'$ while for 50 and 70 phr CB the blend shows the highest change in modulus indicating a larger filler-filler and/or filler-rubber interaction.

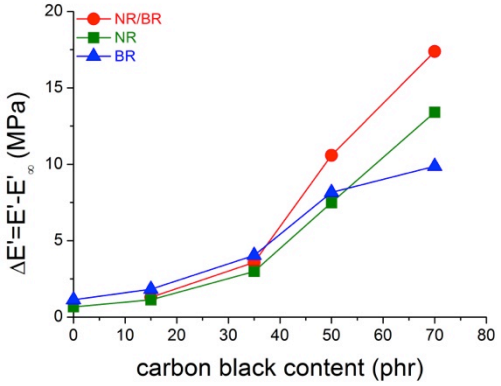

Figure 3. Modulus drop as a function of carbon black content.

Figure 4 reports the strain at which E' reaches the minimum E'_0 for the three rubbers as a function of CB content. This strain, which gives an indication of the strain necessary to reach the molecular chains extensibility limit, is linked to the strain induced crystallization onset and it is expected to decrease as CB content increases because interactions between CB and the polymer act as further crosslinks. No significant difference in trend among the three rubbers is observed, even if a slightly higher value of strain is found for BR, except for the highest CB content (70 phr), but this value has to be confirmed. The higher value for BR can be thought to be due to the fact that SIC for this rubber requires larger strains (Marano, Mohammadpoor, Rink 2013).

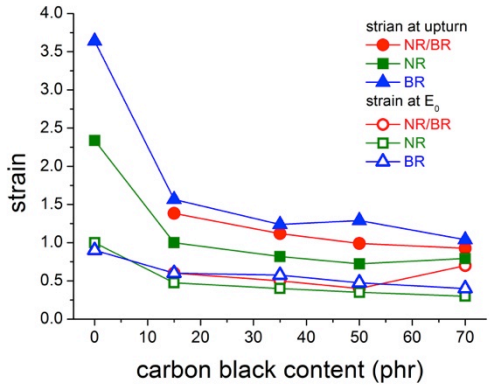

Figure 4. Strain at E_0 (from DMA)(open symbols) and strain at upturn (from uniaxial test)(filled symbols) as a function of carbon black content.

3.2 *Tensile behaviour*

Figure 5 shows the stress strain curves of the NR, BR and their 50/50 blend for the different CB contents. All three materials show a similar trend, typical for reinforced rubbers: first softening linked to non affine deformation (in the unfilled materials) and also the disruption of filler-filler and filler-rubber interactions for the filled ones, then at higher strains an up-turn followed by strain hardening due to limited chain extensibility and strain induced crystallization (SIC). For the unfilled BR failure took place before the turn-up occurred.

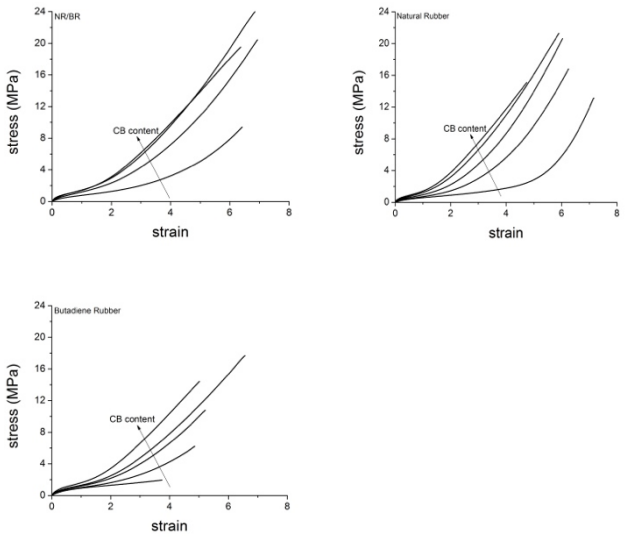

Figure 5. Stress-strain curves from uniaxial tests of NR/BR blend, NR and BR with different content of carbon black.

Figure 6 reports the strain, the stress and the overall energy at rupture for the three materials as a function of CB content.

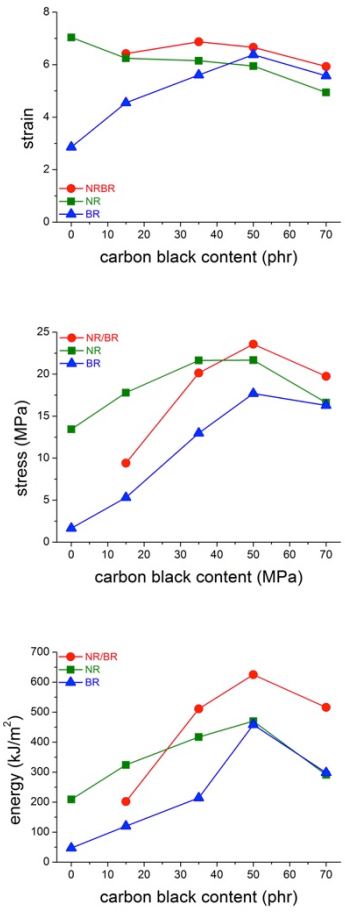

Figure 6. Strain, stress and energy at break for NR/BR, NR and BR as a function of carbon black content.

The ultimate strain seems to decrease as CB content increases for the blend and natural rubber, while for the butadiene rubber at the lower contents it increases as carbon black content increases. For all the materials, the stress at break and the overall energy increase as CB content increases up to 50 phr then, for 70 phr both decrease. Further, stress and energy at high CB content are higher for the blend. From these results the NR/BR blend with 50 phr CB would seem the best material with regard to failure.

Following the Mooney-Rivlin (MR) equation (Mark 1985), often stress-strain data are analysed through the plot of the 'reduced stress':

$$\sigma^* = \frac{\sigma}{(\lambda - \lambda^{-2})}$$

as a function of $1/\lambda$. In which σ is the nominal stress and λ the extension ratio. From the MR equation a straight line would be expected. Filled rubbers deviate from this trend: at low strain, a decrease in the stress is attributed to the Payne effect, at high strain, an upturn in the stress due to the limited chain extensibility and strain induced crystallization. Also the unfilled materials may show this upturn as they reach their chain extensibility limit, but it is at higher deformations (Bokobza, 2001).

Figure 4 also reports the deformation at which the upturn occurs as a function of CB content. Both, the deformation at the upturn in the uniaxial tensile curves and the deformation at which the material reaches E_0 in DMA, represent the strain at which the chain extensibility limit is reached. As expected, the two strains show the same trend: the blend has an intermediate behaviour between that of natural rubber and butadiene rubber, the latter has a greater chain extensibility and this is more evident from the tensile tests. The absolute strain values from the two tests are different probably due to the different strain rate of the two tests.

3.3 *Fracture behaviour*

Two different types of fracture phenomenology were observed. In the first one, as is usually expected in mode I test configurations as the PS test is, a crack propagates from the initial notch along the notch plane perpendicularly to the applied load. In the second one, first, from the tip of the initial notch, two cracks initiate and propagate in opposite directions, symmetrically and parallel to the applied load direction. At the onset of these cracks, named sideways cracks, no discontinuity in the load displacement curve is observed. With further increase of the overall applied deformation, the sideways cracks propagate in a steady way until the onset of a crack (forward crack) and its propagation along the grooved notch plane. The forward crack propagation is unstable and may occur in one or two steps until the failure of the whole specimen takes place. The adopted geometry, allowed to well separate the sideways cracks onset from the forward crack onset. The two unfilled compounds (NR and BR) show only a forward crack propagating along the notch plane. When CB is added to either rubber or to the blend, at a certain level of filler, the sideways crack phenomenology occurs. The formation of sideways cracks was observed for NR and the NR/BR blend for carbon black content above 35 phr while for BR this was observed above 50 phr of CB. The formation of sideways cracks is known to give much higher toughness and this is linked to the much larger strains which may be reached at the crack tip before catastrophic fracture occurs (Gent & De 1996) (Hamed & Park 1999) (Hamed & Al-Sheneper 2002). Sideways cracks develop as a consequence of strength anisotropy at the crack tip which arises as a consequence of molecular orientation and stress induced crystallization at the crack tip (Gent, Razzaghi-Kashani & Hamed 2003).

Figure 7 shows for the three types of rubber pictures taken at the onset of sideways and forward cracks for 35 and 50 phr CB. It can be observed that the deformation at the onset of the forward crack for the BR with 35 phr CB (photogram 'e'), for which no sideways cracks form, is very similar to the deformation at the onset of the sideways cracks in the BR with 50 phr CB (photogram 'd'). Nevertheless, in the latter material after the onset of the sideways cracks, the crack tip "blunts", and very high strains are reached before a forward crack initiates and catastrophically propagates through the whole uncracked ligament.

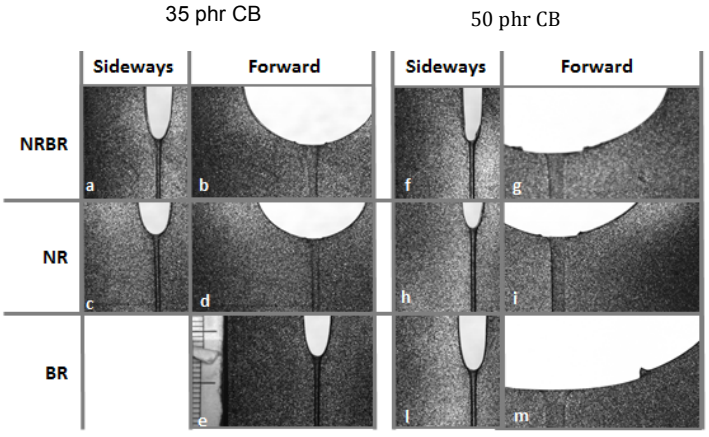

Figure 7. Onset of sideways and forward for NR, BR and NR/BR with 35 and 50 phr of carbon black.

From Figure 7 it can also be observed that as CB content increases the local deformation at the crack tip at sideways crack onset decreases (compare photograms 'a' with 'f' and 'c' with 'h'). Work is in progress to quantify this by digital image correlation, but overall specimen strain reported in Figure 8 confirm this trend: CB contributes to the crosslink density in the compound and therefore lower strains

are required to give the anisotropy necessary for sideways cracks to occur.

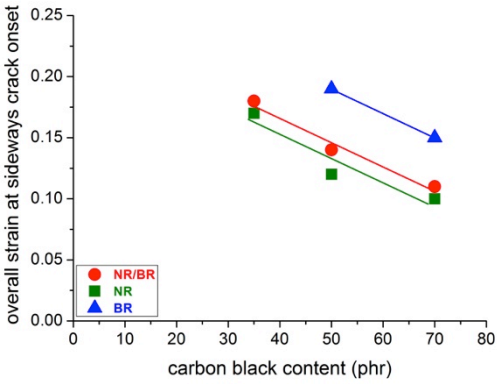

Figure 8. Onset of sideways and forward for NR, BR and NR/BR with 35 and 50 phr of carbon black.

Figures 9 and 10 show the trend of J-integral at forward and sideways cracks onset respectively as a function of CB content for the two parent rubbers and the blend. It can be observed that if sideways cracks do not form the value of J at forward crack onset is low, while if they form J becomes larger and increases as CB content increases. This is particularly marked for BR for which a slightly different fracture phenomenology was observed: for a given CB content, sideways cracks propagate much further than in the case of NR or the blend. It appears that for BR a larger energy, and also larger strains (Figure 8) are required to obtain the onset of sideways cracks, probably because orientation is more difficult in this rubber, but once they occur their propagation is favoured. It has been previously reported (Hamed, Kim & Gent 1996) that sideways cracks are more easily observed in CB filled NR and the NR/BR blend rather than in BR. As previously mentioned SIC occurs at higher strains for BR and therefore probably at a given strain level, orientation and the consequent strength anisotropy at the crack tip are less significant for BR with respect to NR at the same CB content. Nevertheless, when CB content is sufficient for sideways cracks to initiate it seems that the strength anisotropy is larger for this material and forward crack propagation occurs at much higher strains and relevant J values. As for the blend, it needs less CB to show the fracture phenomenology with sideways cracks when compared with BR (35 phr instead of 50 phr). Even if the blend is two phased it has been found that the crystallization of BR is favoured in the blend (Marano, Mohammadpoor, Rink 2013): this may contribute to the change in the fracture mechanism for the blend at lower CB content (35 phr) with respect to BR.

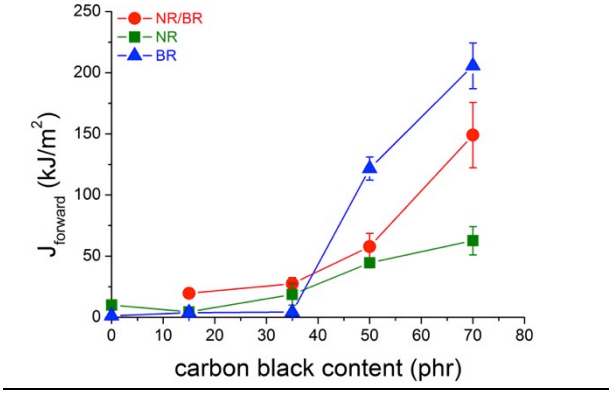

Figure 9. J integral at forward onset for NR, BR and NR/BR as a function of CB content.

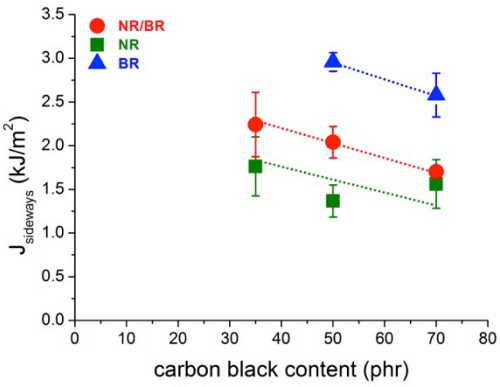

Figure 10. J integral at sideways onset for NR, BR and NR/BR as a function of CB content.

4 CONCLUDING REMARKS

In this work carbon black filled 50/50 NR/BR blends have been studied, from small strains up to fracture, in comparison with its two parent materials. The blend often showed an intermediate behaviour between that of its components. Nevertheless, depending on the property considered and the CB content, a better performance of the blend was also observed. The main findings are:

- From the drop in the storage modulus with the applied strain, it seems that, at the highest CB contents, the filler-filler and/or the filler-rubber interaction is stronger for the blend.

- From the uniaxial tests it turns out that the blend has a better behaviour at failure (both ultimate stress and overall energy are larger) for the highest CB contents.

- Fracture mechanics tests evidenced two types of phenomenology, one in which a crack propagates directly in mode I and the other, giving higher toughness values, in which the crack "blunts" as consequence of the formation of the "sideways" cracks. Unfilled materials show only the first type, above a

given CB content the filled rubbers can show the second phenomenology (35 phr CB for NR and the blend, 50 phr for BR). In any case the onset of "sideways" cracks appears more difficult (higher energy and strains) for BR. Up to 35 phr CB the blend is tougher than its components, while at higher contents its toughness is intermediate.

Measurements of local strains with digital image correlation are in progress to better understand the deformation mechanisms occurring at the crack tip so as to obtain significant structure to properties relations.

5 REFERENCES

Ait Hocine, N., Nait Abdelaziz, M. & Imad, A. 2002. Fracture problems of rubbers: J -integral estimation based upon η factors and an investigation on the strain energy density distribution as a local criterion. *International Journal of Fracture* 117(1): 1-23.

Bokobza, L. 2001. Reinforcement of elastomeric networks by fillers. *Macromol. Symp.* 169(1): 243-260.

Gent, A.N. & De, D. 1996. Tear strength of carbon-black-filled compounds. *Rubber Chem Technol* 69(5): 834-850.

Gent, A.N. & Razzaghi-Kashani & Hamed G.R. 2003. Why do cracks turn sideways. *Rubber ChemTechnol*,76:122–131.

Hamed G.R. & Al-Sheneper A.A. 2002. Effect of carbon black concentration on cut growth in NR vulcanizates *Rubber Chem Technol* 76: 436-459.

Hamed, G.R, Kim, H.J. & Gent, A.N. 1996. Cut Growth in Vulcanizates of Natural Rubber, cis-Polybutadiene, and a 50/50 Blend during Single and Repeated Extension. *Rubber Chem. Technol.* 69(5): 807-818.

Hamed, G.R. & Park, B.H. 1999. The Mechanism of Carbon Black Reinforcement of SBR and NR Vulcanizates. *Rubber Chem Technol* 72(5): 946-959.

Heinrich, G. & Kluppel, M. 2002. *Reinforcement of elastomers*. Published by Elsevier Science Ltd.

Kaushik, P. 2010. Influence of carbon blacks on butadiene rubber/high styrene rubber/natural rubber with nanosilica: Morphology and wear. *Materials & Design* 31(3): 1156-1164.

Kim, B.H. & Joe, C.R. 1989. On the ratio (Φ) of the J-integral to the total work done per unit uncracked area. *Engineering Fracture Mechanics* 32(6): 953-963.

Marano, C., Mohammadpoor, Sh. & Rink, M. 2013. Characterization of high cis-content polybutadiene compounds differing in cis-content and molecular weight distribution. *EC-CMR 2013*.

Mark, J.E. 1985. Recent Studies of Rubberlike Elasticity. *Polymer Journal* 17(1): 265-269.

Massie, J.M. & Hirst, R.C. 1993. Carbon Black Distribution in NR/Polybutadiene Blends. *Rubber Chem Technol* 66(2): 276-285.

Mezynski, S.M. & Rodgers M.B. 1993. Heavy Duty Truck Tire Materials and Performance. *Kautschuk Gummi Kunststoffe* 46: 718–726. Frankfurt.

Sircar, A.K. & Lamond, T.G. 1973. Carbon Black Transfer in Blends of Cis-Poly(Butadiene) with Other Elastomers. *Rubber Chem Technol* 46(1): 178-191.

Tinker, A.J. & Jones, K.P. 1998. *Blends of natural rubber, novel techniques for blending with specialty polymers*. London: Chapman & Hall.

Bibliography

[1] K. Cornish. Similarities and differences in rubber biochemistry among plant species. *Phytochemistry*, 57:1123–1134, 2001.

[2] A. N. Gent. Elastic instabilities in rubber. *International Journal of Non-Linear Mechanics*, 40:165–175, 2005.

[3] A. N. Gent. *Engineering with Rubber.* Library of Congress catalogin-in-Publication Data, HANSER publishers, Munich, 2nd edition, 2001.

[4] L. Chevalier; Y.Marco. Tools for multiaxial validation of behavior laws chosen for modeling hyper-elasticity of rubber-like materials. *Journal of Polymer Engineering and Science*, 42(2):280–298, 2002.

[5] K. C. Valanis; R. F. Landel. The strain-energy function of a hyperelastic material in terms of the extension ratios. *Journal of Applied Phisics*, 38:2997–3002, 1967.

[6] R. W. Ogden. *Non-linear elastic deformations.* ISBN 0-486-69648-0. Dover Publications, 1984.

[7] R. S. Rivlin. Large elastic deformations of isotropic materials. IV. Further developments of the general theory. *Philos. Trans. Roy. Soc. Lond. Ser.*, A 241:379–397, 1948.

[8] R. S. Rivlin. *"Large elastic deformation" in Rheology, Theory and Applications*, volume 1, Chap. 10. Academic, New York, 1956.

[9] J. E. Mark; B. Erman; F. R. Eirich, editor. *The science and technology of rubber.* ELSEVIER academic press, 3rd edition, 2005.

[10] L. R. G. Treloar. *The Phisics of Rubber Elasticity.* Oxford University Press, 1975.

[11] R. W. Ogden. Large deformation isotropic elasticity: on the correlation of theory and experiment for incompressible rubberlike solids. *Proc. R. Soc. Lond.*, 326(1567):565–584, 1972.

[12] R. W. Ogden; G. Saccomandi; I. Sgura. Fitting hyperelastic models to experimental data. *Computational Mechanics*, 34:408–502, 2004.

[13] R. W. Ogden. Large deformation isotropic elasticity: on the correlation of theory and experiment for compressible rubberlike solids. *Proc. R. Soc. Lond.*, 328:567–583, 1972.

[14] A. N. Gent. Extensibility of rubber under different types of deformation. *The Society of Rheology, Inc. J. Rheol.*, 49:271–275, January/February 2005.

[15] A. N. Gent. A new constitutive relation for rubber. *Rubber Chemistry and Technology*, 69:59–61, 1996.

[16] R. S. Rivlin; D. W. Saunders. Large elastic deformations of isotropic materials. VII. Experiments on the deformation of rubber. *Phil. Trans. R. Soc. Lond. A*, 243:251–288, 1951.

[17] L. J. Hart-Smith. Elasticity parameters for finite deformations of rubber-like materials. *Zeitschrift fur angewandte Mathematik und Physik*, 17:608–626, 1966.

[18] M. Kaliske; G. Heinrich. An extended tube-model for rubber elasticity: Statistical-mechanical theory and finite element implementation. *Rubber Chemistry and Technology*, 72:602–632, 1999.

[19] M. Kaliske G. Heinrich. Theoretical and numerical formulation of a molecular based constitutive tube-model of rubber elasticity. *Comput. Theo. Polym. Sci.*, 7:227, 1997.

[20] E. Arruda; M. C. Boyce. A three-dimensional model for the large stretch behavior of rubber elastic materials. *J. Mech. Phys. Solids*, 41(2):389412, 1993.

[21] G. Marckmann; E. Verron. Comparison of hyperelastic models for rubber-like materials. *Rubber Chemistry and Technology*, 79:835–858, 2006.

[22] L. R. G. Treloar. Stress-strain data for vulcanised rubber under various types of deformation. *Trans. Faraday Soc.*, 40:59–70, January 1944.

[23] S. Kawabata; M. Matsuda; K. Tei; H. Kawai. Experimental survey of the strain energy density function of isoprene rubber vulcanizate. *Macromolecules*, 14:154–162, January 1981.

[24] G. Palmieri; M. Sasso; G. Chiappini; D. Amodio. Mullins effect characterization of elastomers by multi-axial cyclic tests and optical experimental methods. *Mechanics of Materials*, 41:1059–1067, 2009.

[25] C. S. Woo; W. D. Kim; H. S. Park. Finite element analysis and design of rubber specimen for mechanical test. *Constitutive models for rubber VII, proceedings of the* 7^{th} *European Conference on Constitutive Models for Rubber, ECCMR, Dublin, Ireland, 20-23 September 2011*, pages 439–443, 2012.

[26] C. W. Extrand; A. N. Gent. Strenght under various modes of deformation. *International Journal of Fracture*, 48:281–297, 1991.

[27] T. Gulon; E. Toussaint; J.B. Le Cam; N. Promma; M. Grdiac. A new characterisation method for rubber. *Polymer Testing*, 28:715–723, 2009.

[28] J. M. Chenal; L. Chazeau; L. Guy; Y. Bomal; C. Gauthier. Molecular weight between physical entanglements in natural rubber: A critical parameter during strain-induced crystallization. *Polymer*, 48:1042–1046, 2007.

[29] J. M. Chenal; C. Gauthier; L. Chazeau; L. Guy; Y. Bomal. Parameters governing strain induced crystallization in filled natural rubber. *Polymer*, 48:6893–6901, 2007.

[30] J. Rault; J. Marchal; P. Judeinstein; P. A. Albouy. Stress-induced crystallization and reinforcement in filled natural rubbers: 2H NMR study. *Macromolecules*, 39:8356–8368, 2006.

[31] S. Toki; I. Sics; B. S. Hsiao; M. Tosaka; S. Poompradub; Y. Ikeda; S. Kohjiya. Probing the nature of strain-induced crystallization in polyisoprene rubber by combined thermomechanical and in situ x-ray diffraction techniques. *Macromolecules*, 38:7064–7073, 2005.

[32] S. Murakami; K. Senoo; S. Toki; S. Kohjiya. Structural development of natural rubber during uniaxial streching by in situ wide angle x-ray diffraction using a synchrotron radiation. *Polymer*, 43:2117–2120, 2002.

[33] S. Toki; I. Sics; S. Ran; L. Liu; B. S. Hsiao. Molecular orientation and structural development in vulcanized polyisoprene rubbers during uniaxial deformation by in situ synchrotron x-ray diffraction. *Polymer*, 44:6003–6011, 2003.

[34] S. Toki; T. Fujimaki; M. Okuyama. Strain-induced crystallization of natural rubber as detected real-time by wide-angle x-ray diffraction technique. *Polymer*, 41:5423–5429, 2000.

[35] L. Mullins. Effect of stretching on the properties of rubber. *Journal of Rubber Research*, 16:275–289, 1947.

[36] L. Mullins; N.R. Tobin. Theoretical model for elastic behaviour of filler-reinforced vulcanized rubbers. *Rubber Chemistry and Technology*, 30:551–571, 1957.

[37] R. Calabro'. Studio dell'effetto dell'orientazione molecolare sul comportamento a frattura della gomma naturale caricata con nero fumo. Master's thesis, Politecnico di Milano, AA 2008-2009 (in italian).

[38] C. Marano; R. Calabro'; M. Rink. Effect of molecular orientation on the fracture behavior of carbon black-filled natural rubber compounds. *Journal of Polymer Science: Part B: Polymer Physics*, 48:1509–1515, April 2010.

[39] F. Caimmi; R. Calabro'; C. Marano; M. Rink. Biaxial fracture testing of rubber comppounds. In *Constitutive models for rubber VII, proceedings of the* 7^{th} *European Conference on Constitutive Models for Rubber,*

ECCMR, Dublin, Ireland, 20-23 September 2011, volume 8, pages 449–454, 20-23 September 2012.

[40] ASTM D 3053:2008. *Standard Terminology relating to Carbon Black.*

[41] B. Rodgers; W. Waddel. *The science of rubber compounding.* Science and Technology of Rubber, 3rd edition, 2005.

[42] ISO 1183-1:2004(E). *PlasticsMethods for determining the density of noncellular plasticsPart 1: Immersion method, liquid pyknometer method and titration method.*

[43] O. H. Yeoh. Fracture mechanics of bond failure in the "pure shear" test piece. *Rubber Chemistry and Technology*, 76:483–494, 2003.

[44] K. Miller. Testing elastomers for hyperelastic material models in finite element analysis. Technical report, Axel Products, Inc.

[45] K. Deb, A. Pratap, S. Agarwal, and T. Meyarivan. A fast and elitist multiobjective genetic algorithm: Nsga-ii. *Evolutionary Computation, IEEE Transactions on*, 6(2):182 –197, apr 2002.

[46] Ruben Perez, Peter Jansen, and Joaquim Martins. pyOpt: a Python-based object-oriented framework for nonlinear constrained optimization. *Structural and Multidisciplinary Optimization*, 45:101–118, 2012. 10.1007/s00158-011-0666-3.

[47] S. Reese and P. Wriggers. Material instabilities of an incompressible elastic cube under triaxial tension. *International Journal of Solids and Structures*, 34(26):3433 – 3454, 1997.

[48] R. S. Rivlin; A. G. Thomas. Rupture of rubber. I. Characteristic energy for tearing. *Journal of Polymer Science*, 10(3):291–318, 1952.

[49] G.R. Irwin. Onset of fast crack propagation in high strength steel and alluminium alloys. *Segamore Research Conference Proceedings*, 2:289–305, 1956.

[50] A.A. Griffith. The phenomena of rupture and flow in solids. *Philosophical Transaction, series A*, 221:163–198, 1920.

[51] O. H. Yeoh. Analysis of deformation and fracture of 'pure shear' rubber testpiece. *Plastics, Rubber and Compounds*, 30(8):389–397, 2001.

[52] M. A. Sutton; J.-J. Orteu; H. W. Schreier. *Image correlation for shape, motion and deformation measurements.* Springer, 2009.

[53] B. Pan; H. Xie; Z. Wang; K. Qian; Z. Wang. Study on subset size selection in digital image correlation for speckle patterns. *Optics Express*, 16(10), May 2008.

[54] C. Feichter; Z. Major; R. W. Lang. Deformation analysis of notched rubber specimens. *Strain*, 42:299–304, 2006.

[55] S. Mzabi; D. Berghezan; S. Roux; F. Hild; C. Creton. A critical local energy release rate criterion for fatigue fracture of elastomers. *Journal of Polymer Science Part B: Polymer Phisics*, 49:1518–1524, 2011.

[56] G. Heinrich; M. Kluppel; T. A. Vilgis. Reinforcement of elastomers. *Current Opinion in Solid State and Materials Science*, 6:195–203, 2002.

[57] M. Boggio. *Fracture behaviour of carbon black filled natural rubber.* PhD thesis, Politecnico di Milano, A.A. 2009.

[58] P. A. Przybylo and E. M. Arruda. Experimental investigations and numerical modeling of incompressible elastomers during non-homogeneous deformations. *Rubber Chemistry and Technology*, 71(4):730–749, September 1998.

[59] A. N. Gent; M. Razzaghi-Kashani; G. R. Hamed. Why do cracks turn sideways? *Rubber Chemistry and Technology*, 76:122–131, 2002.

[60] G. R. Hamed. Tearing of vulcanized rubber. *Rubber Chemistry and Technology*, 78:548–553, 2005.

[61] T. Horst; B. Lauke; G. Heinrich. Application of configurational forces in the context of a kinked crack. *Proc. Appl. Math. Mech.*, 6:173–174, 2006.

[62] G. R. Hamed. Molecular aspects of the fatigue and fracture of rubber. *Rubber Chemistry and Technology*, 67:529–536, 1994.

[63] G. R. Hamed; A. A. Al-Sheneper. Effect of carbon black concentration on cut growth in NR vulcanizates. *Rubber Chemistry and Technology*, 76:436–460, 2003.

[64] G. R. Hamed; H. J. Kim; A. N. Gent. Cut growth in vulcanizates of natural rubber, *Cis*-polybutadiene,and a 50/50 blend during single and repeated extension. *Rubber Chemistry and Technology*, 69:807–818, 1996.

[65] G. R. Hamed; B. H. Park. The mechanism of carbon black reinforcement of SBR and NR vulcanizates. *Rubber Chemistry and Technology*, 72:946–959, 1999.

[66] B. H. Kim; C. R. Joe. Single specimen test method for determining fracture energy (J_c) of highly deformable materials. *Engineering Fracture Mechanics*, 32(1):155–161, 1989.

[67] N. Ait Hocine; M. N. Abdelaziz; H. Ghfiri; G. Mesmaque. Evaluation of the energy parameter J on rubber-like materials: Comparison between experimental and numerical results. *Engineering Fracture Mechanics*, 55:919–933, 1996.

[68] N. Ait Hocine; M. N. Abdelaziz; G. Mesmacque. Experimental and numerical investigation on single specimen methods of determination of J in rubber materials. *International Journal of Fracture*, 94:321–338, 1998.

[69] N. Ait Hocine; M. N. Abdelaziz. A new alternative method to evaluate the J-integral in the case of elastomers. *International Journal of Fracture*, 124:72–92, 2003.

[70] N. A. Hocine; M. N. Abdelaziz; A. Imad. Fracture problems of rubbers: J-integral estimation based upon factors and an investigation on the strain energy density distribution as a local criterion. *International Journal of Fracture*, 117:1–23, 2002.

[71] H. W. Greensmith. Rupture of rubber x: The change in stored energy on making a small cut in test piece held in simple extension. *Journal of Applied Polymer Science*, 7:993, 1964.

[72] R. J. Harbour; A. Fatemi; W. V. Mars. Fatigue crack growth of filled rubber under constant and variable amplitude loading conditions. *Fatigue Fract. Engng. Mater. Struct.*, 30:640–652, 2007.